Spectrally efficient coded transmissions for wireless and satellite applications

Charbel Abdel Nour

To cite this version:

Charbel Abdel Nour. Spectrally efficient coded transmissions for wireless and satellite applications. Information Theory [cs.IT]. enst-bretagne, 2008. English. NNT : . tel-01883652

HAL Id: tel-01883652
https://hal.science/tel-01883652

Submitted on 28 Sep 2018

N^o d'ordre : 2007telb0046

THÈSE

présentée à

l'ECOLE NATIONALE SUPERIEURE DES TELECOMMNUNICATIONS DE BRETAGNE

en habilitation conjointe avec l'Université de Bretagne Sud

pour obtenir le grade de

DOCTEUR DE L'ENST BRETAGNE

Mention : *Sciences pour l'Ingénieur*

par

Charbel ABDEL NOUR

Spectrally efficient coded transmissions for wireless and satellite applications

---

soutenue le 31 janvier 2008 devant la commission d'examen :

Composition du Jury :

Directeurs de thèse	: Claude BERROU, Directeur d'Études, ENST Bretagne
	: Emmanuel BOUTILLON, Professeur, UBS
Encadrant	: Catherine DOUILLARD, Professeur, ENST Bretagne
Rapporteurs	: Tor AULIN, Professeur, Université de Chalmers
	: Hikmet SARI, Professeur, SUPÉLEC
Examinateur	: Jean Francois HELARD, Professeur, INSA de Rennes

Contents

Introduction

THIS manuscript provides solutions and results obtained in the context of two unrelated studies having only one common ground consisting of coded modulations. It is logically divided into two main parts:

The first part entitled "Turbo coded modulations and fading channels" is inspired by the results reported in literature where the quasi-optimality of turbo codes associated with high order M-ary modulations over fading channels remains to be proven. In fact, previous simulations have shown wider gaps to capacity for this type of association when compared to the error correcting performance over Gaussian channels. From this observation, in addition to the increasing demands for wireless applications, our interest in turbo coded high order modulations over fading channels saw the light. We had the opportunity later on to apply the results of our study in the context of the Digital Video Broadcasting, Terrestrial, Second Generation (DVB-T2).

The second part entitled "Coded continuous phase modulation schemes for satellite transmissions" presents the results of a study motivated by the advantages of this type of modulation schemes over non-linear channels. It was intended to investigate enhanced digital transmission techniques for broadband satellite digital transmissions with continuous phase modulations. The aspects that have been addressed include signal selection (frequency pulse type and duration, modulation index, alphabet size) and forward error correcting code selection in order to optimize the performance over typical satellite links. Afterwards, the results of this study have been applied in the context of a European Space Agency (ESA) funded project initiated in January of 2006.

Part I

Turbo coded modulations and fading channels

Market driven telecommunication systems push toward further development of wireless applications. Numerous technical aspects should be considered, like for example source coding, channel coding, interleaving, frame synchronization, phase detection and modulation issues. We restrict ourselves to studying methods intended to improve throughput and reliability in the context of channel coding and modulation. These latter are greatly affected by the transmission medium. For wireless applications, the fading channel represents the model that fits real world test measurements.

On one hand, higher throughputs can be achieved by spectrally efficient systems. On the other hand, designing reliable applications is generally attained thanks to the introduction of Forward Error Correcting (FEC) solutions. Consequently, in this part of the manuscript, we investigate FEC solutions for spectrally efficient systems over fading channels.

Important efforts have been undertaken in the field of channel coding to approach the theoretical limits established by Shannon in [1, 2]. One of the important landmarks was the invention of turbo codes in 1993 by Berrou *et al* [3]. Afterwards, approaching the channel capacity over Gaussian channels for antipodal signaling was within reach. These results were extended for high order modulations [4, 5] where turbo codes have proven once more their quasi-optimality in approaching theoretical limits.

Thanks to the flourishing demand for wireless applications, turbo codes over fading channels have already found their way into literature. A quick review of published results have shown that the performance over fading channels of coded high order modulations in terms of probability of error suffers from greater gaps to capacity and high error floors when compared to the performance over Gaussian channels.

The goal of this part of the manuscript is to propose high order turbo coded modulation schemes over fading channels improving previously published results in literature and approaching further the channel capacity established by Shannon. It is organized in two chapters as follows:

- Chapter 1 provides the necessary technical background for the study, including an introduction to fading channels followed by their mathematical description, the computation of the theoretical limits, a review of existing works on coded modulations over fading channels and simulation results showing the error correcting performance of turbo codes over fading channels.
- Chapter 2 describes an innovative technique intended for doubling the diversity order of turbo coded high order modulations over fading channels. This contribution is based on introducing simple modifications to the modulator and demodulator. In order to fully take advantage of the proposed technique, an additional iterative processing is introduced at the receiver side. Finally, conclusions and future work perspectives are given.

CHAPTER 1

Coded modulations and fading channels

THIS chapter sets the basis for an in-depth comprehension of factors acting on error correcting performance of coded modulations over fading channels. Once achieved, innovative contributions intended to improve existing systems can follow.

We start from the basics by introducing fading channels and defining the channel model adopted in the rest of the study. Afterwards, theoretical limits consisting of the Shannon channel capacity and the underlying frame size penalty are investigated. The remaining sections offer a review of existing coded modulation solutions designed for fading channels. They offer as well an accurate identification of the parameters with great influence on coded performance over fading channels.

1.1 The fading channel model

A key component in the design of wireless systems is the wireless channel model. It has to provide an accurate description of the effects of the channel on the system behavior and performance. First of all, we briefly recall the main physical phenomena that induce fading effects over the propagation channel. Then, we provide the detailed mathematical description of the flat fading channel model that we have adopted in our study.

1.1.1 General description of fading channels

In a wireless communication system, the signals may travel through multiple paths between a transmitter and a receiver causing what is called multipath propagation [6]. Due to the multiple paths, the receiver observe variations of amplitude, phase and angle of arrival of the transmitted signal. These variations originate the phenomenon referred to as *multipath fading*. The variations are usually classified according to the fading scale [6]: one distinguishes *large-scale* and *small-scale* fading. Fig. 1.1 shows a simplified diagram of the one in [6] describing the different fading manifestations, their interaction and the associated specific types of degradations.

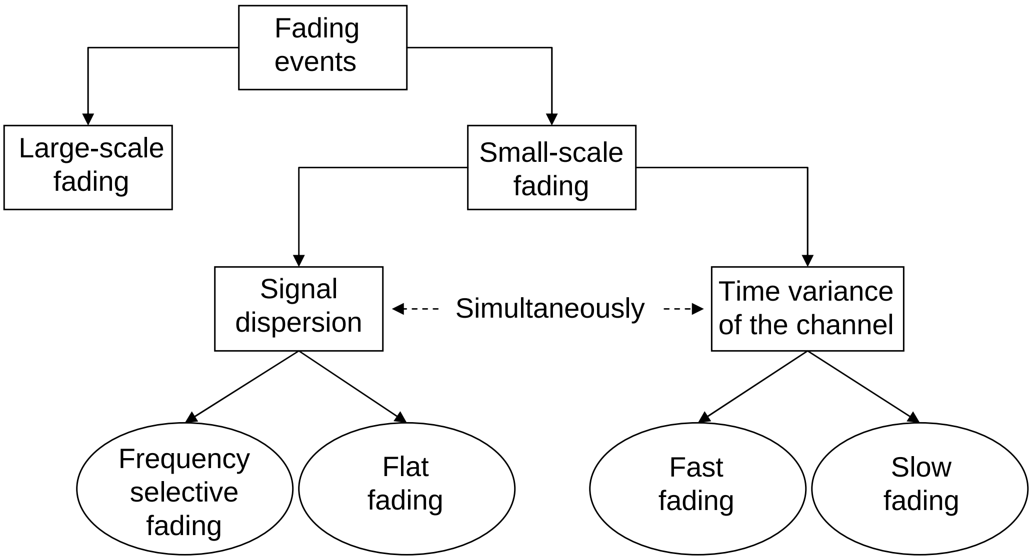

Figure 1.1 — Fading types and their corresponding manifestations

Large-scale fading refers to the degradation caused by the presence of physical objects of considerable size (like hills, buildings, forests) in the wireless signal path. The receiver is said to be shadowed by these obstacles. This type of fading can be modeled through the estimate of a *path loss* as a function of the distance between the transmitter and the receiver. this model can be divided into a mean loss and a Log-normal probability density function (pdf) variation around this mean.

Small-scale fading events describe changes in the separation between a transmitter and a receiver. They can be caused by the mobility of the transmitter or the receiver as well as by the crossing by any physical object of the line of sight path stretching between them. The rate of change of the propagation conditions accounts for the fading rapidity. Small-scale fading results into important variations of signal amplitude and phase. It shows itself in two distincts mechanisms: time-spreading of the signal or *signal dispersion*, and *time variant behavior* of the channel. When there is no predominant line of sight between the transmitter and receiver, the fluctuation of the signal envelope is Rayleigh distributed. Small-scale fading is then referred to as *Rayleigh fading.* When there is a predominant line of sight between the transmitter and the receiver the fluctuations are statistically described by a Rician pdf.

As shown in fig. 1.1, the signal dispersion manifestation leads to *frequency selective fading* and *flat fading* degradations. From the time domain point of view, frequency selective fading occurs when the maximum spread in time of a symbol is greater than the duration of the symbol. Consequently, this fading degradation is also known as channel induced *intersymbol interference.* From the frequency domain point of view, frequency selective fading occurs when the spectral components of a signal are affected in different ways by the channel. In particular, frequency selective fading occurs when the channel coherence bandwidth, i.e. the channel bandwidth in which all components experience approximately the same fading characteristics, is smaller than the signal bandwidth. When the channel characteristics are approximately flat for all frequencies, the degradation is referred to as flat fading.

Fig. 1.1 also shows the degradation types due to the channel time variance. These are *fast* and *slow fading.* From the time domain point of view, fast fading refers to the condition in which the channel coherence time i.e. the time interval during which the channel response is invariant is smaller than the symbol duration.

Fast fading in the frequency domain is directly related to the Doppler effect [6, 7, 8]. The Doppler frequency f characterizes the maximum Doppler frequency shift of the signals in a mobile environment. It is computed as

$$f = \frac{v}{\lambda} \tag{1.1}$$

where v is the relative velocity between the transmitter and the receiver and λ is the wavelength of the transmitted signal. Thus, from the frequency domain point of view, fast fading occurs when the signal bandwidth is less than the maximum frequency Doppler shift.

Any wireless radio signal transmitted over large physical distances is subject to both large as well as small-scale fading types. Since, large-scale fading affects only the average strength of the received signal, it will not be considered in the rest of our study. Thus, we will restrict ourselves to small-scale fading and precisely to flat fading. The flat fading channel is a typical channel encountered in many wireless environments. For instance, many systems such as Wireless Fidelity (IEEE 802.11) (WiFi), Worldwide Interoperability for Microwave Access (IEEE 802.16) (WiMax), Digital Audio Broadcasting (DAB), or Digital Video Broadcasting, Terrestrial (EN 300 744) (DVB-T) can be modeled as flat fading channels, since they call for the Orthogonal Frequency Division Multiplexing (OFDM) technique that has the capability to transform frequency selective channels into parallel flat fading channels.

1.1.2 Mathematical model for flat fading channels

In this section, we will derive the mathematical equations suited for describing the flat fading channel model with its associated slow fading time variance manifestation based on the previous works of [7, 8, 9]. An interesting observation is that the pdf of the fading process follows well known mathematical distributions. The resulting description is referred to as "the fading channel model" in the rest of this study.

The mathematical model according to [9] assumes that the received field at the receiver is made up of a number of horizontally traveling plane waves, with random amplitudes and phase angles, arriving from different locations. The phases of the waves are uniformly distributed between 0 to 2π. The amplitudes and phases are considered to be independent. Assuming a moving vehicle with constant velocity v, fig. 1.2 describes the model where the vehicle is moving in the x-direction.

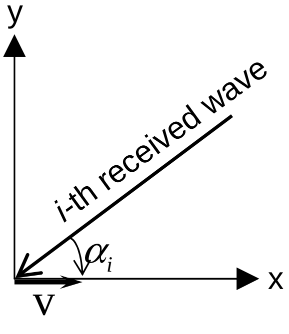

Figure 1.2 — A mobile receiver and an incoming wave

The motion of the vehicle introduces a Doppler shift Δf_i of the frequencies in every received wave:

$$\Delta f_i = \beta v cos(\alpha_i) \tag{1.2}$$

where $\beta = \dfrac{2\pi}{\lambda}$.

$S(t)$ being the transmitted complex signal having a carrier frequency f_0 modulated by a baseband complex signal $x(t)$, it can be written as:

$$S(t) = x(t)\exp(j2\pi f_0 t) \tag{1.3}$$

For a transmission over a multipath channel with m distincts waves, and omitting the additive white Gaussian noise at the input of the receiver, the received signal can be expressed as:

$$S'(t) = \sum_{i=1}^{m} a_i(t)S(t-\tau_i(t)) = \sum_{i=1}^{m} a_i(t)\exp(-j2\pi f_0\tau_i(t)) \cdot x(t-\tau_i(t))\exp(j2\pi f_0 t) \tag{1.4}$$

where $a_i(t)$ and $\tau_i(t)$ represent the attenuation and the delay of the path wave i. The baseband version $y(t)$ of the received signal $S'(t)$ can be written as:

$$y(t) = \sum_{i=1}^{m} c_i(t)x(t-\tau_i(t)) \tag{1.5}$$

with

$$c_i(t) = a_i(t)\exp(-j2\pi f_0\tau_i(t)) \tag{1.6}$$

$c_i(t)$ represents the lowpass (after filtering) channel impulse response for wave i. $a_i(t)$ and $\varphi_i(t) = -2\pi f_0\tau_i(t)$ denote the envelope and the phase of the corresponding lowpass channel response. From equ. 1.2, the Doppler shift is bounded to $\pm\beta v$ which is in practice small when compared to the carrier frequency. Assuming m is large or equivalently having a large number of incoming uncorrelated waves the central limit theorem can be applied for a statistical modeling of the overall channel response $c(t) = \sum_{i=1}^{m} c_i(t)$. It follows that $c(t)$ becomes a complex mutually independent Gaussian process as follows:

$$c(t) = p(t) + jq(t) = \rho(t)\exp(j\varphi(t)) \tag{1.7}$$

where $p(t)$ and $q(t)$ are independent Gaussian processes having the same variance σ^2. The enveloppe is then $\rho(t) = \sqrt{p(t)^2 + q(t)^2}$ and the phase $\varphi(t)$ of $c(t)$ is taken uniformly distributed in $[0, 2\pi]$.

If we suppose that $p(t)$ and $q(t)$ are centered, the fading enveloppe $\rho(t)$ is then Rayleigh distributed with the following pdf:

$$\begin{cases} P_{\rho(t)}(u) = \dfrac{u}{\sigma^2} \exp\left(-\dfrac{u^2}{2\sigma^2}\right) & \text{for } u \geq 0 \\ \\ P_{\rho(t)}(u) = 0 & \text{for } u < 0 \end{cases} \tag{1.8}$$

For simulation purposes, the normalized Rayleigh distribution is generally adopted, i.e. $E\{\rho(t)\} = 1$, which leads to:

$$\begin{cases} P_{\rho(t)}(u) = 2u \exp\left(-u^2\right) & \text{for } u \geq 0 \\ \\ P_{\rho(t)}(u) = 0 & \text{for } u < 0 \end{cases} \tag{1.9}$$

When a line of sight path arrives to the receiver with an average power of m_p, the enveloppe is Rice-Nakagami distributed with the following expression for the pdf:

$$\begin{cases} P_{\rho(t)}(u) = \dfrac{u}{\sigma^2} \exp\left(-\dfrac{u^2 + m_p^2}{2\sigma^2}\right) I_0\left(\dfrac{m_p u}{\sigma^2}\right) & \text{for } u \geq 0 \\ \\ P_{\rho(t)}(u) = 0 & \text{for } u < 0 \end{cases} \tag{1.10}$$

where $I_0(.)$ represents the Bessel function of the first kind and order 0.

In the case of a flat fading channel, the maximum value taken by the delay $\tau_i(t)$ is small when compared to the signal symbol period T. As a consequence, $x(t - \tau_i(t))$ can be approximated by $x(t)$. The received signal $y(t)$ can be rewritten as:

$$y(t) = x(t) \sum_{i=1}^{m} c_i(t) = x(t)c(t) \tag{1.11}$$

Introducing the additive complex white Gaussian noise $b(t)$, the received signal can be expressed as:

$$y(t) = \rho(t) \exp(j\varphi(t)) x(t) + b(t) \tag{1.12}$$

From the signal space viewpoint [10] after filtering, the received discrete time signal y_n at time period n can be written as a function of the discrete time transmitted signal x_n, channel response envelope ρ_n, channel response phase φ_n and gaussian noise b_n such that:

$$y_n = \rho_n \exp(j\varphi_n) x_n + b_n \tag{1.13}$$

In our study we mainly focus on the Rayleigh flat fading channel model (fading distribution of ρ_n follows equ. 1.9) assuming perfect Channel State Information (CSI) and perfect phase estimation at the receiver. Consequently, the phase shift of φ_n can be compensated and the received discrete time faded signal used in our study becomes:

$$y_n = \rho_n x_n + b_n \tag{1.14}$$

1.2 Theoretical limits for transmissions over fading channels

1.2.1 Capacity computation

In this section we focus on the computation of the Shannon's capacity for the most widely used digital modulation schemes over fading channels. When compared to the Gaussian channel case, the capacity for fading channels with perfect CSI is nothing else but the averaging of the conditional capacity for Gaussian channels with respect to the probability density function of the fading amplitude [11]:

$$C = \int_0^\infty C_g(\rho) P_f(\rho) d\rho \tag{1.15}$$

where $P_f(\rho)$ is the fading distribution and $C_g(\rho)$ is the conditional capacity with the following expression for an M-ary transmission scheme:

$$C_g(\rho) = \max_{p(X)} \sum_{i=1}^{M} \int_{-\infty}^{\infty} \cdot_{D \text{ times over y}} \cdot \int_{-\infty}^{\infty} P_i(Y/X,\rho) \log_2 \left[\frac{P_i(Y/X,\rho)}{P_i(Y/\rho)} \right] dy_1 ... dy_D \tag{1.16}$$

where

- D represents the number of signal space dimensions for the transmitted symbols.
- $p(X)$ designates the probability distribution of the transmitted M-ary D-dimensional symbols X.
- $Y = (y_1, ..., y_D)$ denotes the corresponding received symbol.
- $P_i(.)$ is the conditional probability of (.).

In this study we are mainly interested in 2-dimensional modulation schemes ($D = 2$) such as Quadrature Amplitude Modulation (QAM) for which we assume an equiprobable distribution for the M-ary constellation signals. This assumption also holds for Phase Shift Keying (PSK) Modulation schemes. When a Rayleigh distributed fading is considered:

$$C = \int_{0}^{\infty} 2\rho \exp(-\rho^2) C_g(\rho) d\rho \tag{1.17}$$

with

$$\begin{aligned} C_g(\rho) = \log_2 M &- \frac{1}{M \cdot \log(2) \cdot \pi N_0} \sum_{i=1}^{M} \int_{-\infty}^{\infty}\int_{-\infty}^{\infty} \frac{\|Y - \rho X_i\|^2}{N_0} \exp\left(\frac{\|Y - \rho X_i\|^2}{N_0}\right) dy_I dy_Q \\ &- \frac{1}{M \cdot \pi N_0} \sum_{i=1}^{M} \int_{-\infty}^{\infty}\int_{-\infty}^{\infty} \exp\left(\frac{\|Y - \rho X_i\|^2}{N_0}\right) \log_2\left(\sum_{i=1}^{M} \exp\left(\frac{\|Y - \rho X_i\|^2}{N_0}\right)\right) dy_I dy_Q \end{aligned} \tag{1.18}$$

where:

- N_0 represents the single sided continuous time spectral density of the white additive Gaussian noise.
- X_i is the transmitted QAM constellation signal.
- I and Q denote the in-phase and quadrature components in signal space.

For an in-depth derivation of the capacity computation the reader is referred to [11]. The computation of the capacity for fading channels is quite cumbersome, but with the proper usage of numerical integration methods and precisely the Romberg method [12], it is possible to compute accurately the capacity curves. The results of the computation are plotted in fig. 1.3 for QAM schemes and in fig. 1.4 for PSK schemes in the case of Rayleigh flat fading channel.

1.2.2 Achievable optimal coded performance

Channel capacity represents the tightest upper bound on the amount of information that can be reliably transmitted over a communication channel. Nevertheless, its computation assumes the transmission of infinite length blocks, assumption far from the actual transmission conditions in many practical real world applications. The transmission of finite length blocks induces a penalty on the achievable error correcting performance. A way of estimating the extent of this penalty over Gaussian channels has already been proposed in [13]. This method is based on the previous work of Shannon introduced in [2] where the so-called *sphere-packing*

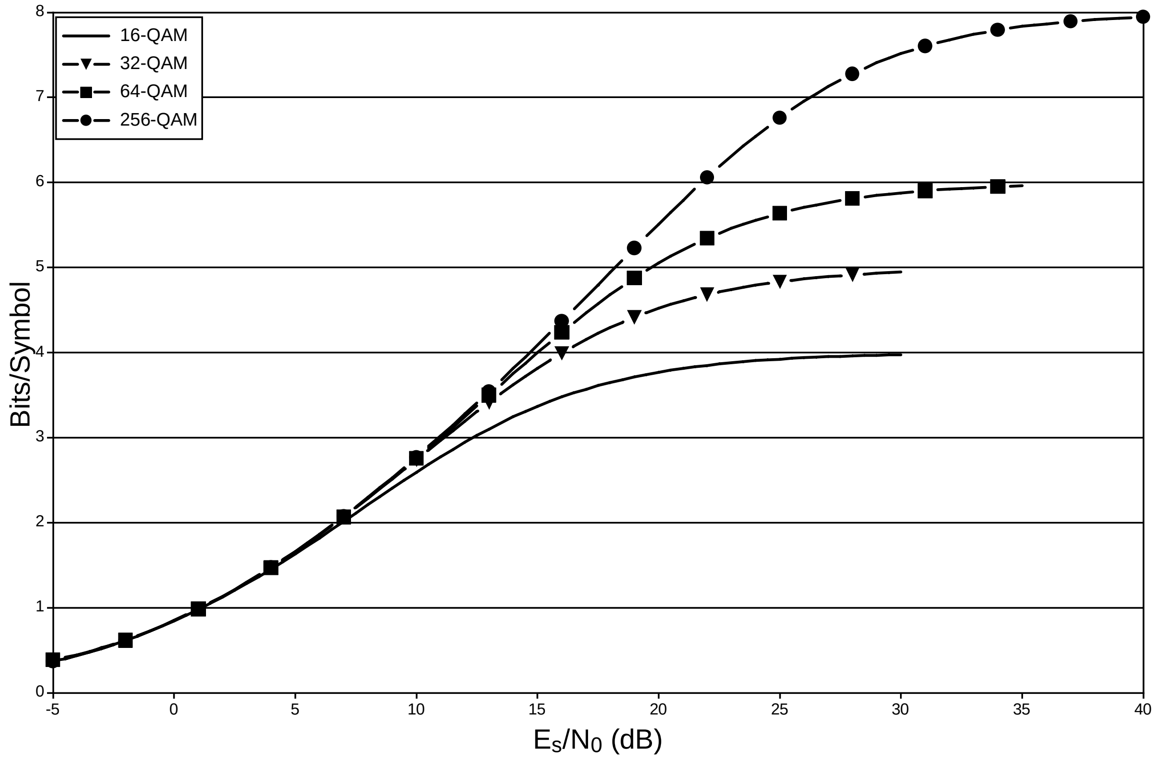

Figure 1.3 — Shannon capacity for QAM schemes over Rayleigh flat fading channels

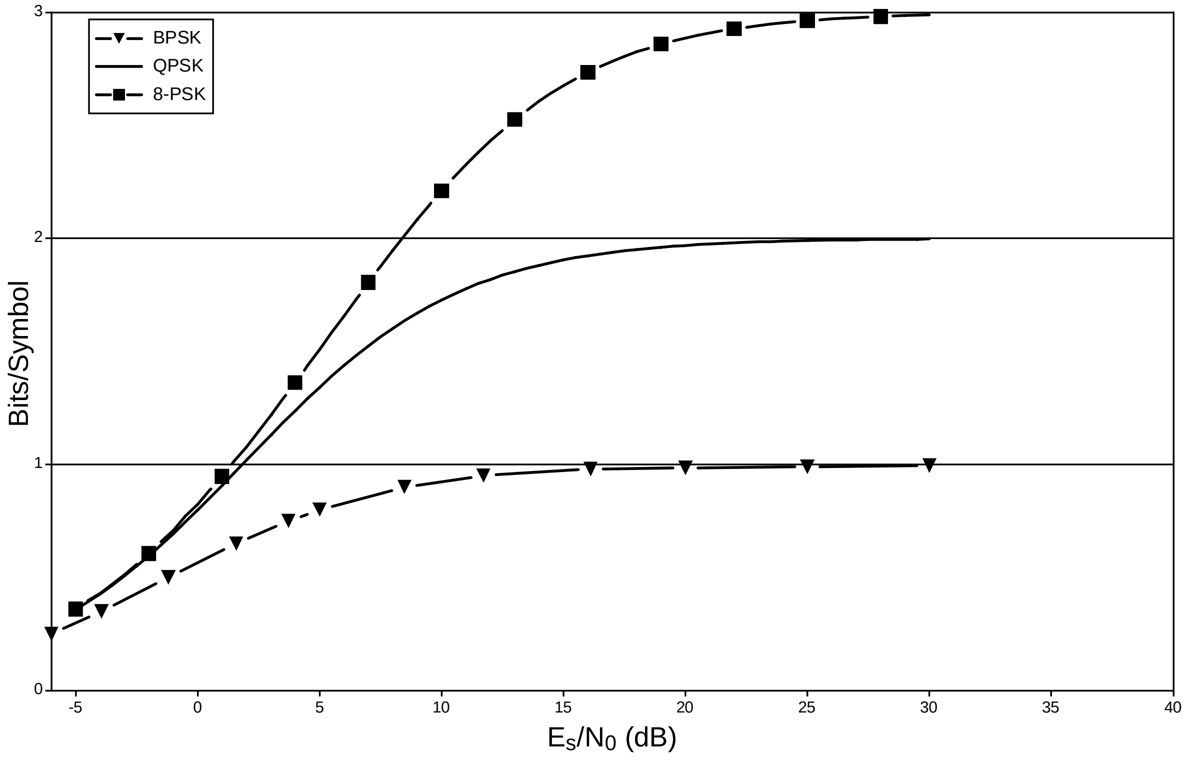

Figure 1.4 — Shannon capacity for BPSK to 8-PSK schemes over Rayleigh flat fading channels

lower *bound* on the probability of error is derived as a function of the average Signal To Noise Ratio (SNR), the target spectral efficiency and the frame size. This bound is computed for transmission over Gaussian channels.

The derivation goes through a geometrical approach in signal space (see fig. 1.5). In fact, modulated codewords of N symbols are assumed to have equal energy (PSK schemes) and are assimilated to N-dimensional vectors. For covenience, Shannon used in his derivation an optimal code in terms of 'spatial separation' for which the codeword (vectors) are taken uniformely distributed over an $N-$dimensional sphere in signal space. The bound on the probability of error then corresponds to the probability for the received vector to be moved by an additive $N-$dimensional Gaussian noise outside the pyramid surrounding the transmitted original vector $\mathbf{c}$. The pyramidal form surrounding a transmitted vector corresponds to what is known as the voronoi region of the vector. A Voronoi region associated to an N-dimensional point is the set of points closer to that point than any other. The measure of closeness is based on the definition of the distance measure.

As the bound in [2] is a function of the frame size, it can be used in order to have an insight on the effect of the frame size over error correction for spherical codes. Note that even the most powerful codes in terms of error correction do not attain neither the optimum spatial distribution nor the equal codeword energy characteristic of spherical codes. Consequently, the accuracy of the computed penalty via the lower bound depends on the considered code and its closeness to the characteristics of a spherical code. It was shown in [14] by means of simulation that for codeword sizes exceeding 100 bits, the bound estimate is asymptotically accurate as it predicts values of the probability of error quite close to the simulation values for quasi-optimal codes like turbo codes [15].

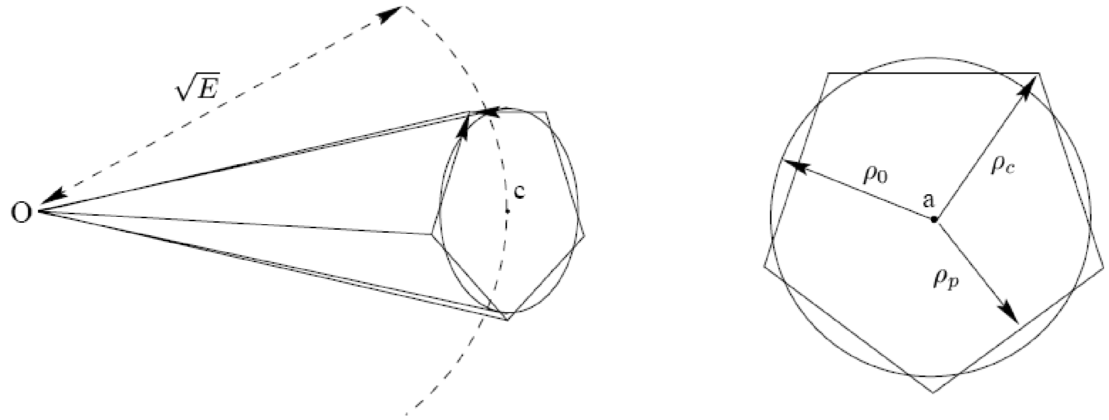

Figure 1.5 — Geometrical representation of the solid angle associated to a codeword

Unfortunately, the extension of this work in order to evaluate the block length penalty over fading channels is not straightforward. In fact, in the original paper by Shannon, an essential mathematical assumption was made in the described geometrical approach: the effect of adding N Gaussian variables to N orthogonal components on the probability of error is modeled by a statistical distribution known as the *$t-$student distribution*. This assumption cannot be extended to fading channels mainly because of the introduction of the $N-$dimensional Rayleigh distributed fading amplitudes in the computation of the bound. Despite these difficulties, some work was undertaken in [16, 17] on the subject. This work is based on a Voronoi region study. However, in order to carry out the bound computation for fading channels, the authors of [16, 17] had to make specific mathematical assumptions that turned out to be questionable, as stated by the authors themselves. These assumptions are not discussed here and the reader is referred to [16, 17] for further details. Due to the lack of accuracy in the provided estimate in [16, 17] we have only used the capacity values for comparison with the theoretical limits in the rest of the study.

1.3 Coded modulations over flat fading channels

Bandwidth being a limited asset for most telecommunciation applications, one of the most important criteria for the design of a communication system is an efficient usage of the available frequency spectrum. Multiple ways for increasing this efficiency exist from using high order modulation schemes to carefully choosing the pulse shape. Another important aspect is transmission reliability. The most common way of building reliable applications relies on the introduction of FEC codes.

We start by a brief review of previous studies on coded modulations designed for fading channels then identify the main factors acting on error correcting performance. We proceed afterwards to a detailed study of particular types of coded modulation schemes representing the state of the art solutions over fading channels. They include schemes with simple outer codes and more powerful error correcting codes like turbo codes.

1.3.1 A brief review of previous studies

Since Ungerboeck's work on Trellis Coded Modulation (TCM) [18], it has been generally accepted that modulation and coding should be combined in a single entity for improved performance. Several results followed this line of thought, as documented by a considerable body of work aptly summarized and referenced in [19].

As a brief summary of [19], we note that TCM schemes were also proposed for fading channels. Under the assumption that transmitted symbols were interleaved with a depth exceeding the coherence time of the fading process, new codes were designed for fading channels in the purpose of inducing maximum *diversity* in the transmission system. This implied in particular that parallel transitions should be avoided in the code trellis, and that increasing the constraint length of the code should lead to increased diversity.

A notable departure from Ungerboeck's paradigm was proposed by Viterbi *et al* [20] in 1989. In this so-called *pragmatic approach*, coded modulation schemes are generated by pairing an M-ary signal set with a binary convolutional code offering large free Hamming distance. This approach implied giving up the joint code/modulation concept in favor of two separate entities. One should mention that for non-Ungerboeck systems, i.e. those separating modulation and coding, the cumulated Euclidean distance along a trellis path is proportional to the Hamming distance. With a reasoning based on this concept, Zehavi in [21] first recognized that the code diversity, and hence the reliability of coded modulations over Rayleigh fading channel, can be improved by introducing bitwise interleaving at the encoder output and by using an appropriate soft-decision bit metric as an input to the Viterbi decoder. This technique, now called Bit-Interleaved Coded modulation (BICM), makes the code diversity order equal to the smallest number of distinct bits along an error event, rather than equal to the number of distinct modulated symbols as in TCM. The BICM concept will be detailed in section 1.3.3.

One of the interesting findings in [21] was that, over fading channels, combining demodulation and decoding as in the TCM approach is not appropriate. This result prompted the study whose results are presented in a comprehensive fashion in [22] and [23]. An advantage of the BICM approach lies in its robustness, since changes in the physical channel do not greatly affect the receiver structure. Thus, BICM provides good performance over fading channel as well as over AWGN channel and, consequently, over Rice fading channel, which can be seen as intermediate between these two.

Before detailing the BICM approach, we first describe the main factors acting on the error correcting performance for coded modulations.

1.3.2 Factors acting on the error correcting performance of coded modulations over fading channels

It has been established that the optimum design criterion acting on TCM performance over Gaussian channel is the maximization of the free Euclidean distance [18]. Over fading channels, different factors influence error correcting performance. On the basis of an analytical asymptotic performance analysis, we are going to identify these factors as pointed out in [24].

The average bit error probability at the output of the fading channel is upper bounded by the union bound:

$$P_b \leq \sum_{\mathbf{v}\in\varsigma}\sum_{\hat{\mathbf{v}}\in\varsigma} a(\mathbf{v},\hat{\mathbf{v}})p(\mathbf{v})P(\mathbf{v}\rightarrow\hat{\mathbf{v}}) \tag{1.19}$$

where $a(\mathbf{v},\hat{\mathbf{v}})$ is the number of bit errors occuring when the sequence $\mathbf{v}$ is transmitted and the sequence $\hat{\mathbf{v}} \neq \mathbf{v}$ is chosen by the decoder, $p(\mathbf{v})$ is the *a priori* probability of transmitting $\mathbf{v}$ and ς is the set of all coded sequences. $P(\mathbf{v}\rightarrow\hat{\mathbf{v}})$ represents the Pairwise Error Probability (PEP) corresponding to the probability that the decoder chooses sequence $\hat{\mathbf{v}}$ while sequence $\mathbf{v}$ has been transmitted.

For memoryless channels, the channel probabilities satisfy:

$$P_N(\boldsymbol{\gamma}|\mathbf{v},\boldsymbol{\rho}) = \prod_{n=1}^{N} P(\gamma_n|v_n,\rho_n) \tag{1.20}$$

where $\boldsymbol{\gamma}$ corresponds to the received bit sequence. Under the Maximum Likelihood (ML) assumption, the detection metric can be expressed as:

$$met(\boldsymbol{\gamma},\mathbf{v},\boldsymbol{\rho}) = \ln P_N(\boldsymbol{\gamma}|\mathbf{v},\boldsymbol{\rho}) = \sum_{n=1}^{N} met(\gamma_n,v_n,\rho_n) \tag{1.21}$$

Consequently, the PEP can now be written as:

$$P(\mathbf{v}\rightarrow\hat{\mathbf{v}}) = P\{met(\gamma_n,\hat{v}_n,\rho_n) \geq met(\gamma_n,v_n,\rho_n)|\mathbf{v}\} \tag{1.22}$$

Applying the Chernoff bound, the PEP becomes [25]:

$$P(\mathbf{v}\rightarrow\hat{\mathbf{v}}) \leq \prod_{n\in\eta} E\left\{\exp\left(\lambda\left[met(\gamma_n,\hat{v}_n,\rho_n) - met(\gamma_n,v_n,\rho_n)\right]\right)|\mathbf{v}\right\} \tag{1.23}$$

where E{} is the averaging operation, λ represents the Chernoff bound parameter and η stands for the set of all n where $v_n \neq \hat{v}_n$. In the case of coherent detection with perfect CSI, the metric $met(\gamma_n,v_n,\rho_n)$ is defined as [24]:

$$met(\gamma_n,v_n,\rho_n) = -\left|\gamma_n - \rho_n v_n\right|^2 \tag{1.24}$$

resulting into a PEP conditioned on the fading amplitude ρ that can be written as [26]:

$$P(\mathbf{v}\rightarrow\hat{\mathbf{v}}|\rho) \leq \prod_{n\in\eta} \exp\left[-\lambda\rho_n^2\left|v_n - \hat{v}_n\right|^2(1-2\lambda N_0)\right] \tag{1.25}$$

where N_0 represents the power spectral density of the Gaussian noise. Since N_0 is independent of n, $\lambda_{optimum} = \dfrac{1}{4N0}$ and the conditioned PEP becomes:

$$P(\mathbf{v} \to \hat{\mathbf{v}}|\rho) \leq \exp\left\{-\frac{E_s}{4N_0} d^2(\mathbf{v}, \hat{\mathbf{v}})\right\} \tag{1.26}$$

where

$$d^2(\mathbf{v}, \hat{\mathbf{v}}|\rho) \triangleq \sum_{n \in \eta} \rho_n^2 \left|\mathbf{v} - \hat{\mathbf{v}}\right|^2 \tag{1.27}$$

represents the *weighted* Euclidean distance between the two symbol sequences $\mathbf{v}$ and $\hat{\mathbf{v}}$. In order to obtain the PEP, we need to average equ. 1.26 with respect to the fading distribution. The averaged weighted Euclidean distance with respect to a Rician distribution becomes:

$$\begin{aligned} d^2(\mathbf{v}, \hat{\mathbf{v}}) &= \sum_{n \in \eta} \left[\frac{K \cdot |v_n - \hat{v}_n|^2}{1 + K + \frac{E_s}{4N_0} |v_n - \hat{v}_n|^2} + \frac{1}{\frac{E_s}{4N_0}} \ln \left(\frac{1 + K + \frac{E_s}{4N_0} |v_n - \hat{v}_n|^2}{1 + K} \right) \right] \\ &= \sum_{n \in \eta} \left[d_{1n}^2 + d_{2n}^2 \right] \end{aligned} \tag{1.28}$$

where K is the Rician fading coefficient. Despite the rather complex aspect of equ. 1.28, it provides an insight on the factors that dictate error correcting performance over Gaussian as well as over fading channels.

For $K = \infty$, the Rician channel amounts to the classical Gaussian channel (no fading) and equ. 1.28 becomes:

$$d^2(\mathbf{v}, \hat{\mathbf{v}}) = \sum_{n \in \eta} \left[d_{1n}^2 + 0 \right] = \sum_{n \in \eta} |v_n - \hat{v}_n|^2 \tag{1.29}$$

Notice that $d^2(\mathbf{v}, \hat{\mathbf{v}})$ reduces to the classical sum of the squared Euclidean distances along the error event path. Consequently, the PEP over Gaussian channel is obtained by replacing in equ. 1.26 the value of $d^2(\mathbf{v}, \hat{\mathbf{v}})$ obtained in 1.29:

$$P(\mathbf{v} \to \hat{\mathbf{v}}) \leq \exp\left\{-\frac{E_s}{4N_0} \sum_{n \in \eta} |v_n - \hat{v}_n|^2\right\} \tag{1.30}$$

One interesting observation from equ. 1.30 is that the error probability decreases exponentially with E_s/N_0 over Gaussian channel, where the main optimization criterion is the Euclidean distance along the error path.

For Rayleigh fading channel, we have $K = 0$ and the corresponding weighted Euclidean distance becomes:

$$d^2(\mathbf{v}, \hat{\mathbf{v}}) = \sum_{n\in\eta} \left[0 + d_{2n}^2\right] = \sum_{n\in\eta} \frac{1}{\frac{E_s}{4N_0}} \ln\left(1 + \frac{E_s}{4N_0} \left|v_n - \hat{v}_n\right|^2\right) \tag{1.31}$$

For large values of E_s/N_0, we can re-write the upper bound on the PEP as in [26] by applying the Chernoff bound:

$$P(\mathbf{v} \to \hat{\mathbf{v}}) \leq \frac{1}{\prod\limits_{n\in\eta} \frac{E_s}{4N_0} \left|v_n - \hat{v}_n\right|^2} \tag{1.32}$$

Equ. 1.32 shows that:

- Over fading channels, the probability of bit errors decreases with the E_s/N_0 term raised to the power n_d, n_d being the cardinality of η. This is in contrast with findings over Gaussian channel where the probability of bit error decreases exponentially with E_s/N_0.

- This probability of error is inversely proportional to the product of the squared Euclidean distances along the error path of length n_d.

It is important to notice here that the longer the shortest error path, the larger the product of the distances along that path and the better the code will perform even though the minimum Hamming distance of the code is not achieved along this path.

Recalling that the *diversity order* is defined as the minimum number of distinct components between any two sequences, since n represents the positions where $v_n \neq \hat{v}_n$, it is referred to as the diversity order of the coded modulation. When n increases, the probability of bit error rapidly decreases with E_s/N_0. Consequently, **maximizing the diversity order represents the most important design criterion over fading channels**.

In the following section, we introduce BICM as a mean of increasing the diversity order, thus improving error correcting performance with respect to TCM schemes.

1.3.3 The Bit-Interleaved Coded Modulation (BICM)

First introduced by Zehavi in [21], BICM offered a considerable improvement in error correcting performance for coded modulations over fading channels compared to the previously existing techniques.

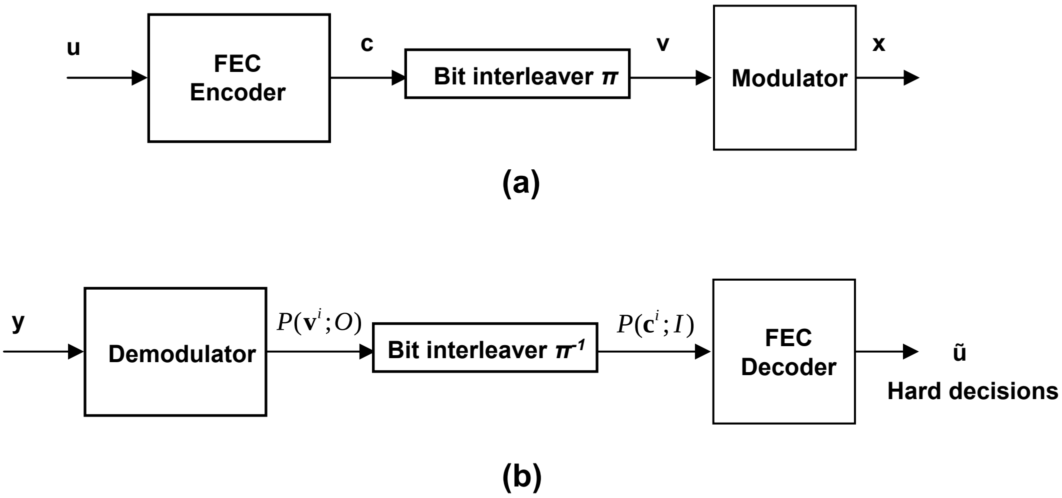

Figure 1.6 — Transmitter (a) and receiver (b) in the BICM approach.

1.3.3.1 System description

The BICM transmitter shown in fig. 1.6 (a) is a serial concatenation of an encoder, a bit interleaver π and a memoryless modulator. The pragmatic coded modulation approach is therefore adopted.

The information frame $\mathbf{u}$ is encoded via a binary outer code. The encoded sequence $\mathbf{c}$ is then interleaved by π and the resulting interleaved sequence $\mathbf{v}$ is mapped to a succession of complex modulation symbols $\mathbf{x}$. At the discrete time signaling interval t, m bits of the interleaved sequence are mapped to symbol x_t chosen from a 2^m-ary constellation by an m-bit signal label μ_m.

$$x_t = \left\{ (x_t^I, x_t^Q) \in \chi \right\} \tag{1.33}$$

where x_t^I and x_t^Q represent respectively the in-phase and quadrature components of $\mu_m(v_t)$ at the signaling interval t. χ represents the possible set of constellation signals.

If we define $i = \{0, .., m-1\}$ and let N_s be the frame size as a number of discrete time modulation symbols, the interleaving function for every interleaved bit respects:

$$\pi(mt + i) = mt' + i \tag{1.34}$$

where t and $t' \in [1, N_s]$. In other words, the interleaving function is a modulo m mathematical operation that divides the coded sequence into m subsequences. This type of interleaver is known as an inline interleaver [27]. Then for every subsequence corresponding to the function relating t' to t, classical interleaving functions can be used. From the wide available choice, we can mention the probabilistic *uniform interleaving* [28] as it offers an insight on the average performance of the BICM and the *S-random interleaving* [29] as it guarantees a minimum spreading of the successive bits. Note that the frame size is supposed to be sufficiently long so that the interleaving function is considered to break any existing correlation between the m subsequences.

Bits-to-symbol mapping represents an important parameter for coded modulation. It greatly affects the bit error correcting performance. Different strategies can be adopted. They include:

- Set Partitionning (SP), a mapping designed to maximize the Euclidean distance of the coded modulation taking into account the trellis structure of the code and is therefore constrained by the characteristics of the outer code. In the case of BICM, the interleaver introduces randomness between the code and the modulation breaking any means of joint optimization. Consequently SP mapping is not suited for BICM.
- Gray mapping, characterized by only one different bit between one constellation point and all of its neighbors. This feature minimizes the bit error probability at the output of the demodulator. Consequently, when code and modulation are separate entities, at the transmitter side as well as at the receiver side as in fig. 1.6, Gray mapping offers the lowest bit error probability of all mapping types. Therefore Gray mapping is adopted in the rest of this section.

At the receiver side (see fig. 1.6 (b)), the demodulator (that we also call demapper in this report) provides probabilities on transmitted bit sequence $\mathbf{v}^i$, $i = \{0, .., m-1\}$. At signal time t, the probability of error on bit v_t^i noted $P(v_t^i = b|\mathbf{y}; O)$ is expressed as follows:

$$P(v_t^i = b|\mathbf{y}; O) = \sum_{x_t \in \chi} P(x_t|y_t) = \sum_{x_t \in \chi} P(y_t|x_t) \cdot P(x_t) \tag{1.35}$$

where $b = \{0, 1\}$ and $P(x_t)$ designates the *a priori* probability of transmitting x_t. Assuming a perfect estimation of the CSI, the soft information at the output of the demodulator can be rewritten as:

$$P(v_t^i = b|\mathbf{y}; O) = \sum_{x_t \in \chi} \frac{1}{\sigma\sqrt{2\pi}} \cdot \exp\left(-\frac{\left|y_t^I - \rho_t x_t^I\right|^2 + \left|y_t^Q - \rho_t x_t^Q\right|^2}{2\sigma^2} \right) \cdot P(x_t) \tag{1.36}$$

where σ^2 represents the gaussian noise variance and ρ_t the amplitude of the fading. $P(x_t)$ being unavailable at the receiver, an equally likely assumption is adopted. After deinterleaving, $P(c_t^i = b|\mathbf{y}; O)$ constitutes the input of the Soft Input (SI) decoder which delivers hard decisions related to the transmitted information bits.

1.3.3.2 Reasons behind the improvement in performance with respect to TCM

The improved performance of BICM with respect to TCM can be explained through the analysis of the PEP of equ. 1.32. In order to do so, let us consider the 8PSK modulation as an example [21].

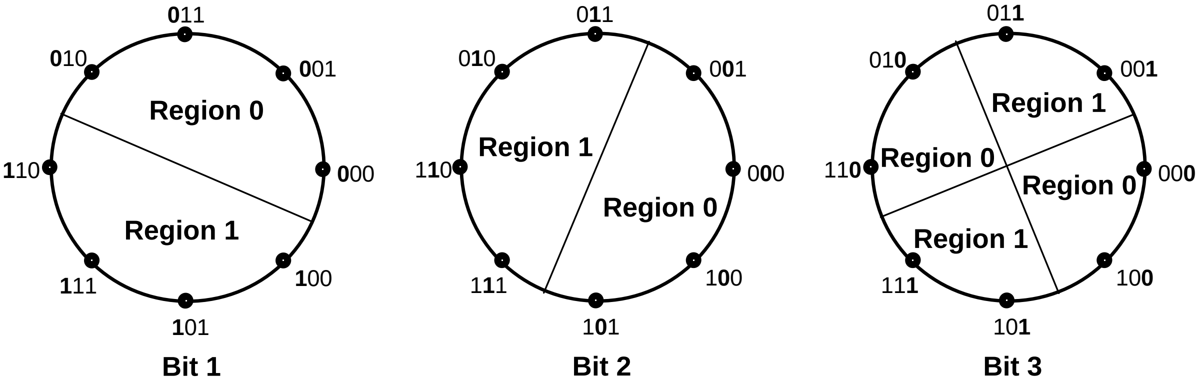

Figure 1.7 — Decision regions for the 3 distincts binary modulations corresponding to a Gray mapped 8PSK modulation.

Since the interleaver π is divided into m sub-interleaving functions and is supposed to operate on a bit stream of sufficiently long size to remove any existing correlation, the 8PSK modulation can be seen as 3 independent binary modulations. The introduction of a BICM bit interleaver induces a random bitwise mapping. Constrained by the 8PSK modulation, the induced random mapping proves to be suboptimum in terms of minimum Euclidean distance between constellation points. Consequently, BICM suffers from a lower minimum Euclidean distance when compared to TCM (see fig 1.7).

Nevertheless, the BICM 8PSK being equivalent to 3 independent binary modulations, the corresponding 3 bits at the input of the FEC decoder become uncorrelated and an error on one of the bits does not enduce any consequence on the remaining two bits. We can say that the FEC decoder only sees uncorrelated binary error events instead of symbol error events in the case of TCM. Consequently, the optimization criterion for the BICM scheme relies on minimizing the number of binary error events. It can be achieved by increasing the separation in number of distincts bits between the transmitted sequence and the potentiel challenging error sequences or, in other words, by optimizing the diversity order between the transmitted and any other potentiel candidate bit sequence. This bit separation is lower bounded by the outer code minimum Hamming distance $d_{H_{\min}}$. The diversity order becomes then $n_d \geq d_{H_{\min}}$.

When applying equ. 1.32 for BICM, as $n_d \geq d_{H_{\min}}$, a greater diversity order is achieved by BICM when compared to TCM at the price of a decay of the Euclidean distance. This latter is compensated though, as the probability of errors decreases rapidly with increasing values of n_d.

For example, let us consider a BICM scheme based on the association of a Recursive Systematic Convolutional (RSC) code with a Gray-mapped 8PSK modulation. The code is the (1,15/13) in the octal generator form [30]. For the Ungerboeck's 8-state trellis-coded 8PSK, we have $n_d = 3$ and $d^2_{E-TCM}(\mathbf{v}, \hat{\mathbf{v}}) = |v_n - \hat{v}_n|^2 = 4.59$ [18] whereas for the proposed BICM, $n_d \geq d_{H_{\min}} = 4$ and $d^2_{E-BICM}(\mathbf{v}, \hat{\mathbf{v}}) = 2.34$. This leads to the following pairwise bit error probabilities over Rayleigh fading channel:

$$\begin{aligned} P_{TCM}(\mathbf{v} \rightarrow \hat{\mathbf{v}}) &\leq \frac{1}{\left(\frac{E_s}{4N_0}\right)^3 \cdot (4.59)^3} \\ &\leq \frac{1}{96.70 \cdot \left(\frac{E_s}{4N_0}\right)^3} \end{aligned} \tag{1.37}$$

and

$$\begin{aligned} P_{BICM}(\mathbf{v} \rightarrow \hat{\mathbf{v}}) &\leq \frac{1}{\left(\frac{E_s}{4N_0}\right)^4 \cdot (2.34)^4} \\ &\leq \frac{1}{29.98 \cdot \left(\frac{E_s}{4N_0}\right)^4} \end{aligned} \tag{1.38}$$

The PEPs of equ. 1.37 and equ. 1.38 lead to a crossing for the bit error probabilities curves of TCM and BICM at $E_b/N_0 = 12.9$ dB corresponding to a probability of 4.10^{-3}. Before the crossing, TCM offers best error correcting performance whereas BICM outperforms TCM for E_b/N_0 values greater than 12.9 dB with a slope decreasing as a power of 4 with E_s/N_0 or E_b/N_0. The crossing value depends on the outer code minimum Hamming distance: the higher the minimum Hamming distance $d_{H_{\min}}$, the earlier the crossing.

A further improvement to BICM schemes has been afterwards proposed by Li and Ritcey in [31]. Taking advantage of the so-called *turbo principle* [15], they proposed iterative processing between the decoder and the demodulator of the BICM receiver in order to improve the overall performance of the scheme. This technique, called (BICM-ID) is presented in the next section.

1.3.4 The Bit-Interleaved Coded Modulation with Iterative Demodulation BICM-ID

1.3.4.1 System description

After the seminal paper on turbo codes [15], the iterative decoding principle has been extended to other functions than error correction in transmission systems in order to improve their overall performance. This was the case of BICM systems with the introduction of iterative demodulation [31].

As iterative processing between the decoder and the demodulator is introduced, they have to be able to exchange extrinsic information [15, 32]. Consequently, the original BICM receiver of fig. 1.6 (b) has to be modified in order to incorporate two Soft Input Soft Output (SISO) [33] modules for the demodulator and the decoder as shown in fig. 1.8.

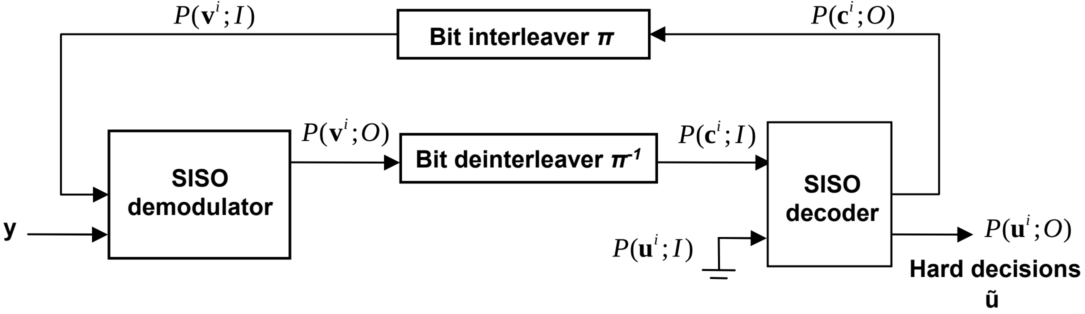

Figure 1.8 — Structure of the BICM-ID receiver.

In a BICM-ID scenario, the SISO decoder provides soft extrinsic output information $P(c_t^i;O)$ that is interleaved by the same permutation π as at the transmitter side. The interleaved soft information $P(v_t^i;I)$ is forwarded to the input of the demodulator to constitute the symbolwise *a priori* information $P(x_t)$ of equ. 1.36 by applying:

$$P(x_t) = P(\mu_m(v_t^0, v_t^1, ..v_t^{m-1}); I) = \prod_{\substack{l \neq i \\ l=0}}^{m-1} P(v_t^l; I) \tag{1.39}$$

As far as the interleaving function is concerned, it has to respect the constraints given by equ. 1.34 for classical BICM. However, as stated in [34], the interleaving function design assuring optimum error correcting performance still remains an open issue. Nevertheless the authors of [34] propose design guidelines for the interleaver construction offering good error correcting performance to the system:

- The use of an inline bit interleaver.

- The bits issued from the same coding instance should not be mapped into the same modulation symbol.
- The succeeding bits at the output of encoder should be spread in order to avoid localized error bursts for the feedback when iterative demodulation is introduced.

All guidelines listed above can be completely satisfied by an inline S-random interleaver if the spreading factor S constraint is applied to the bits originating from the same coding instance as well as the successive bits at the output of the encoder.

Another important modification with respect to BICM concerns bits-to-symbol mapping. Since a joint processing of modulation and code is performed at the receiver side through iterative demodulation, mapping design has to be reconsidered. In fact, in light of the *a priori* information available at the demodulator input, the maximization of the iterative process gain becomes the design criterion for the mapping. Numerous studies aimed at optimizing signal mapping for BICM-ID using a convolutional code exist in the literature: [35], [34, 36] and recently [37] and [38].

Among the main conclusions of these studies, Gray mapping has been shown to offer negligeable iterative gain and is consequently not suited for these schemes. The so-called Semi Set Partitionning (SSP) mapping – described in the next section – is shown to be well suited for iterative schemes, and consequently, improves error rate performance with respect to other mapping types.

As an illustration example of the superior performance of BICM-ID with respect to BICM for convolutional codes, we have compared the corresponding average Bit Error Rate (BER) performance of a rate 2/3 8-state $(1, 13/15)$ convolutionally coded 8-PSK. Fig. 1.9 shows the simulation results for the transmission of 4,000-information bit frames over Rayleigh fading channel for

- A classical Gray-labeled BICM scheme
- A SSP-labeled BICM-ID scheme with 8 iterations.

Observing fig. 1.9, we can confirm that BICM offers significant improvement in error correcting performance when compared to classical BICM. The Gray-mapped BICM-ID curve is not displayed in the figure since it shows quasi-identical performance to the Gray-mapped BICM scheme.

1.3.4.2 Reasons behind the performance improvement with respect to BICM

BICM-ID being a particular case of BICM, it offers high diversity order with respect to TCM at the price of a loss in intersignal Euclidean distance. If we assume error free feedbacks to the

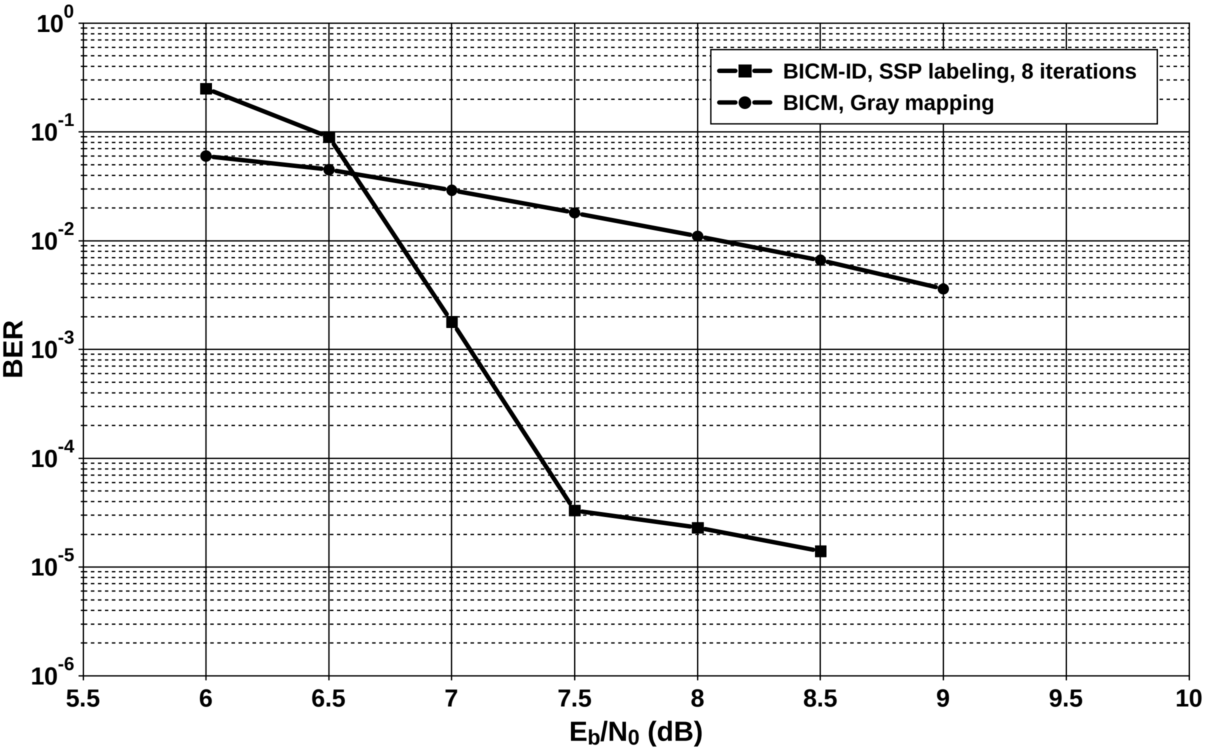

Figure 1.9 — BER comparison of $R = 2/3$, $K = 4000$ bits (1,15/13) CC 8PSK BICM-ID and BICM.

demodulator, we can illustrate the effect of iterative demodulation. This assumption holds asymptotically as feedbacks from the decoder tend to error free feedbacks for high SNRs.

When the soft information $P(v_t^i; O)$ related to the i^{th} bit of symbol x_t is computed, the feedbacks on the other bits of the same transmitted symbol are assumed to be perfect. Consequently the potential bit error to be committed concerns only bit i. In order to minimize the residual probability of error, maximum separation for bit i between symbols where its value is 0 and symbols where its value is 1 should be achieved. The resulting procedure increases the Euclidean distance conditioned by incoming *a priori* soft information from the outer decoder d^2_{E-C} called *conditional Euclidean distance.*

Fig. 1.10 presents the SSP mapping that maximizes d^2_{E-C} for an 8PSK BICM-ID scheme. For example, for bit 1 and symbol 111, if perfect feedbacks are assumed for the remaining two bits, the challenging constellation signal neighbor is represented by the symbol having the same values of bits 2 and 3 (bit $2 = 1$ and bit $3 = 1$) and the value 0 for the considered bit 1 (challenging symbol $= 011$). A suitable mapping for BICM-ID is then the one designed for maximum separation of a symbol and its challenger (symbol 111 and its challenger 011 for bit 1 for example). However, due to the spatial distribution of the 8PSK modulation considered in this example, maximum bitwise separation consisting of antipodal signaling could not be attained for bits 2 and 3.

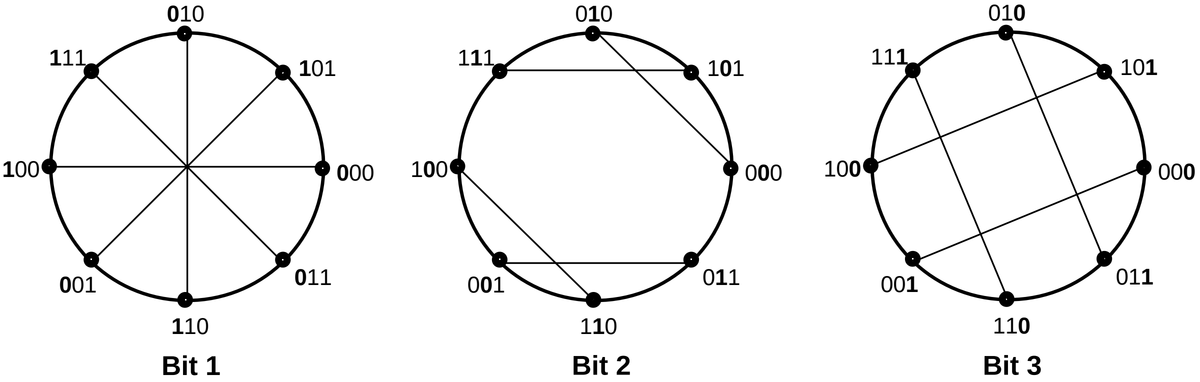

Figure 1.10 — Constellation signals and their corresponding remaining neighbor when perfect feedback is assumed for SSP labeled 8PSK.

Increasing conditional Euclidean distance implies lowering the PEP of BICM-ID with respect to BICM. If we consider once again the example of section 1.3.3.2 for SSP-mapped BICM-ID, we have $n_d = 4$ and $d^2_{E-C} = 12$ resulting into the following PEP:

$$\begin{aligned} P_{BICM-ID}(\mathbf{v} \rightarrow \hat{\mathbf{v}}) &\leq \frac{1}{\left(\frac{E_s}{4N_0}\right)^4 \cdot (12)^4} \\ &\leq \frac{1}{20736 \cdot \left(\frac{E_s}{4N_0}\right)^4} \end{aligned} \tag{1.40}$$

When compared to the PEP of TCM in equ. 1.37 and of BICM in equ. 1.38, the PEP of BICM-ID of equ. 1.40 offers an important improvement by lowering the error rate for chosen value of the SNR. Note that for actual receivers, the soft feedbacks from the outer code tend to error-free feedbacks only for values of E_b/N_0 exceeding the convergence threshold of the iterative process. For lower values of E_b/N_0, SSP-mapped BICM-ID suffers from the increased number of constellation signal neighbors and presents worse error correcting performance than BICM. Nevertheless the crossing point generally corresponds to high values of BER as in the example of fig. 1.9.

In this section, we have recalled the main results of [31] showing that the introduction of iterative demodulation significantly improves the error correcting performance of BICM schemes. However, when simple codes such as convolutional codes are used in BICM schemes, high error floors and large gaps to capacity are observed. For example, for the scheme simulated in fig. 1.9, the error floor occurs at a BER of 10^{-5} and a gap of 2 dB to capacity (at 5.38 dB) for a BER as high as 10^{-4} is seen. The next logical step of this study involves the investigation of more powerful codes such as turbo codes.

1.3.5 Turbo coded modulation schemes

1.3.5.1 Brief review of previous work

Turbo coded modulation schemes being a particular case of coded modulation, two main approaches exist:

1. A joint coding and modulation approach inspired by the TCM principle. First introduced in [4], the Turbo Trellis-Coded Modulation (TTCM) is oriented towards an optimization of the Euclidean distance along the error path of the code trellis. Since it is a TCM-based approach, it produces quasi-optimum results in terms of error correction over Gaussian channels, but significantly suffers from a lack of diversity over Rayleigh fading channels.
2. A separate coding and modulation approach inspired by the BICM principle called *turbo BICM*. First introduced in [5], it is based on the pragmatic approach of Viterbi *et al* [20] and offers greater flexibility when compared to TTCM thanks to a simpler puncturing procedure as the modulation and coding are treated separately. This flexibility comes at a cost in performance ranging from 0.3 to 0.5 dB over Gaussian channels explained by the non-optimized Euclidean distance. However, over fading channels, turbo BICM enjoys greater diversity than TTCM and consequently as pointed out in section 1.3.2 offers improved error correcting performance of several dBs.

As we are interested in obtaining best performance over fading channels, we will mainly focus on turbo BICM. Among the previous works on turbo BICM in literature, we only cite the pioneer works done by:

- Le Goff *et al* [5] which considered fully-interleaved Rayleigh channels for bandwidth efficient turbo coded schemes.
- Junk [39] which showed results for a reduced complexity decoding scheme over a fully-interleaved Rayleigh fading channel.
- Hall and Wilson [40] which treated turbo coded BPSK signaling over fully-interleaved and exponentially correlated Rayleigh fading channels.

The cited articles assume theoretical fully-interleaved fading channels. This channel model is non realistic as in-phase and quadrature components of the transmitted signal are supposed to fade independently. In real world applications, the transmitted constellation signal is subject to the same fading over the I and Q axes as described in section 1.1.2.

We have opted for studying turbo BICM in the context of the realistic channel model adopted in [22]. The error simulation performed are in compliance with the approach in [5] adapted for the realistic channel model and the results obtained will serve as a reference for the rest of our study.

1.3.5.2 Turbo Bit-Interleaved Coded Modulation (TBICM)

System description First introduced in [5], Turbo Bit-Interleaved Coded Modulation (TBICM) represents an extension of BICM to turbo codes. Based on the pragmatic approach, TBICM replaces the outer FEC code of fig. 1.6 by a powerful turbo code. High spectral efficiencies can be obtained by varying the modulation order M and the outer code rate R. This latter is achieved by means of puncturing.

At the transmitter side (see fig. 1.11), TBICM reproduces the same steps undertaken by BICM.

At the receiver side (see fig. 1.12), similarly to BICM, the demodulator computes soft information on the transmitted bits that will be fed to the turbo decoder after deinterleaving. This latter adopts iterative processing, exchanging extrinsic information between its two constituents. After a predefined number of iterations, hard decisions are made.

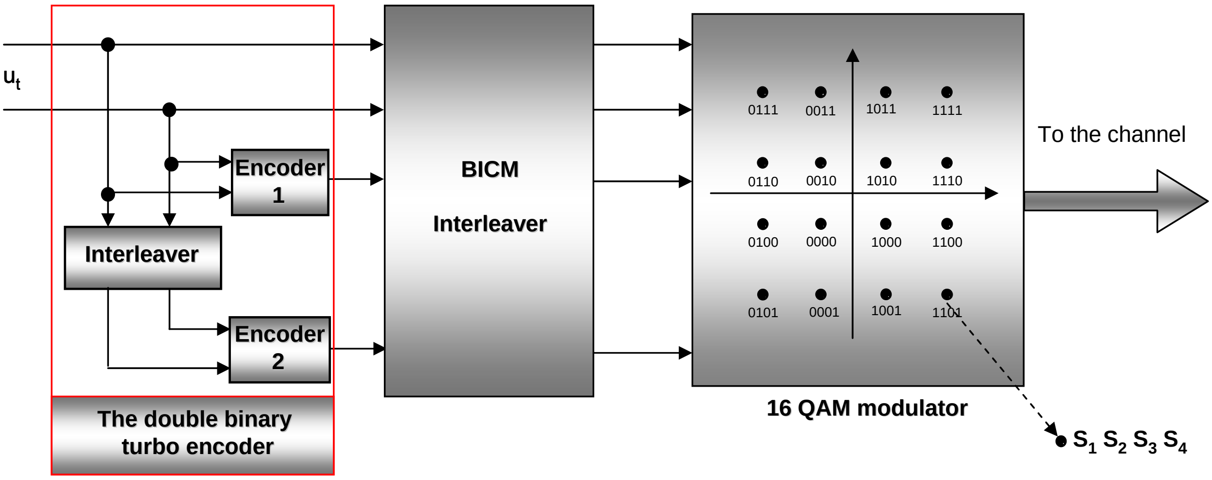

Figure 1.11 — TBICM transmitter with a double binary turbo encoder and a 16-QAM.

In our study of TBICM, we investigate double-binary turbo codes, known to offer advantages in terms of throughput and performance with respect to classical binary turbo codes [41]. From this family of error correcting codes, the double-binary 8-state turbo decoder adopted by the European Telecommunications Standard Institute (ETSI) for the Digital Video Broadcasting Return Channel over Satellite (EN 301 790) (DVB-RCS) standard is used. The interleaver used for non DVB-RCS-based frame sizes follows the Almost Regular Permutation (ARP) model [42]. It represents an arithmetic permutation model fully defined by four parameters (P, Q_1, Q_2, Q_3) [42]. The extension of this turbo code to 16-state component codes is also investigated when low error floors are targeted. Both codes offer good convergence properties mainly due to symbolwise turbo interleaving.

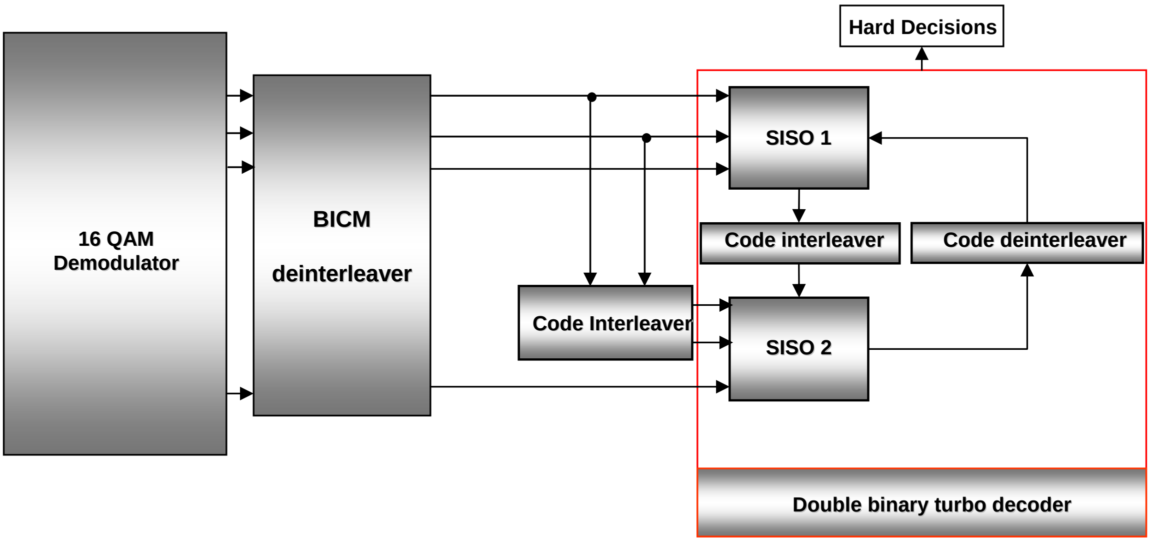

Figure 1.12 — TBICM receiver with a double binary turbo decoder and a 16-QAM.

Concerning the BICM interleaver, the remarks of section 1.3.3 apply here.

As an example, a TBICM scheme with a double-binary turbo decoder and a 16-QAM has been introduced here. Nevertheless, the approach applies for any type of association of a turbo code and a modulation.

Bits-to-symbol allocating techniques and modulator mapping

As presented earlier in the case of BICM-ID, the mapping plays a significant role in error correcting performance. In the case of TBICM, in the absence of iterative demodulation to the demapper, the remarks of section 1.3.3 concerning the mapping still apply. Consequently, Gray mapping provides best performance (this was in particular stated in [38]). With this type of mapping, QAM schemes are reduced to two independent Pulse Amplitude Modulation (PAM) on every component axis represented by the I and Q channels.

Restricted to Gray mapping, PSK and QAM schemes offer different types of bit protection depending on the position of the allocated bit within the transmitted symbol and the order of the modulation. For example, the Gray mapped 16-QAM of Fig. 1.11 offers two levels of bit protection. In fact, bits S_1 and S_3 enjoy lower BER (better protected) than bits S_2 and S_4 due to the position of their respective decision regions.

In [5], the most protected bit positions are allocated to parity bits. In [43], these positions are allocated to systematic bits. The latter allocation method (we chose to call it "systematic") associated with a turbo code outperforms the former (called "redundancy") in the waterfall region due to the fact that systematic bits are used in both component decoders compared to parity bits that are used only in one. Nevertheless, lower error floors are achieved when parity bits are best protected.

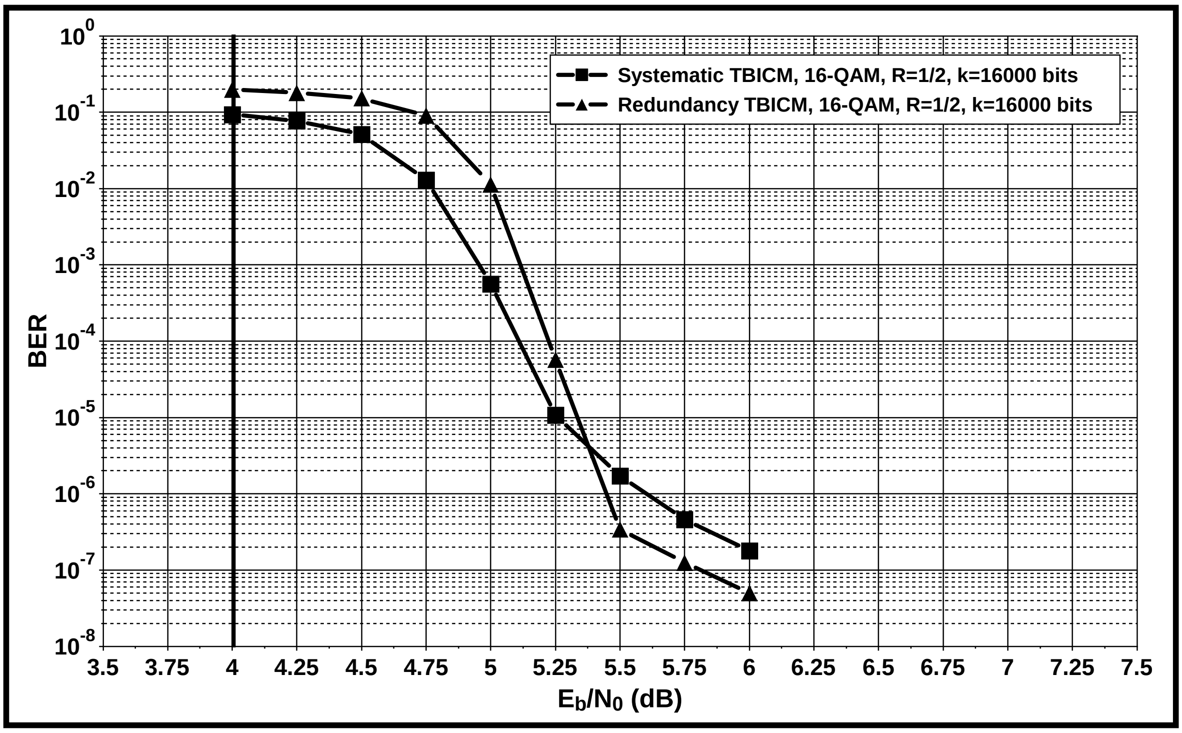

Figure 1.13 — BER comparison between systematic and redundancy bits-to-symbol allocating techniques for 16-QAM TBICM. $R = 1/2$ DVB-RCS code. Gray-mapped 16-QAM transmission of 16,000-information bit frames over Rayleigh fading channels.

Fig. 1.13 offers an insight on the effect of bits-to-symbol allocation on error correcting performance of TBICM. It offers a comparison in terms of BER of the 16-QAM, $R = 1/2$, TBCIM system of fig. 1.11 and fig. 1.12 for the two different types of bit allocation: systematic and redundancy. For comparison purposes, the bold straight line represents the capacity of the Rayleigh fading channel.

These simulation results confirm the fact that systematic-allocated TBICM schemes slightly outperform redundancy-allocated schemes in the waterfall region while they suffer from a higher error floor. Note that a compromise is possible when subsets of systematic and redundancy bits with different ratios are allocated to best protected bit positions. For this type of allocation, BER performance lies between the two extreme cases of fig. 1.13.

Note that the performance difference between the two different allocation methods, systematic and redundancy, diminishes with increasing code rate.

Error correcting performance over Rayleigh fading channel for a wide range of spectral efficiencies

In this section we present simulation results of the DVB-RCS code in a TBICM scenario for various modulation schemes and code rates spanning a large interval of spectral efficiencies from 1.0 bit per channel use (bpcu) to 6.0 bpcu over the Rayleigh fading channel of section 1.1.2 with uniform interleaving. Simulation cases were chosen to illustrate the effect of increasing the order of the modulation and the code rate on error correcting performance. Gaps to capacity are also reported for all cases. These simulation results set the reference performance for the rest of the study. A minimum of 50 erronous frames or 1000 bits in error have been used for every point on the curves

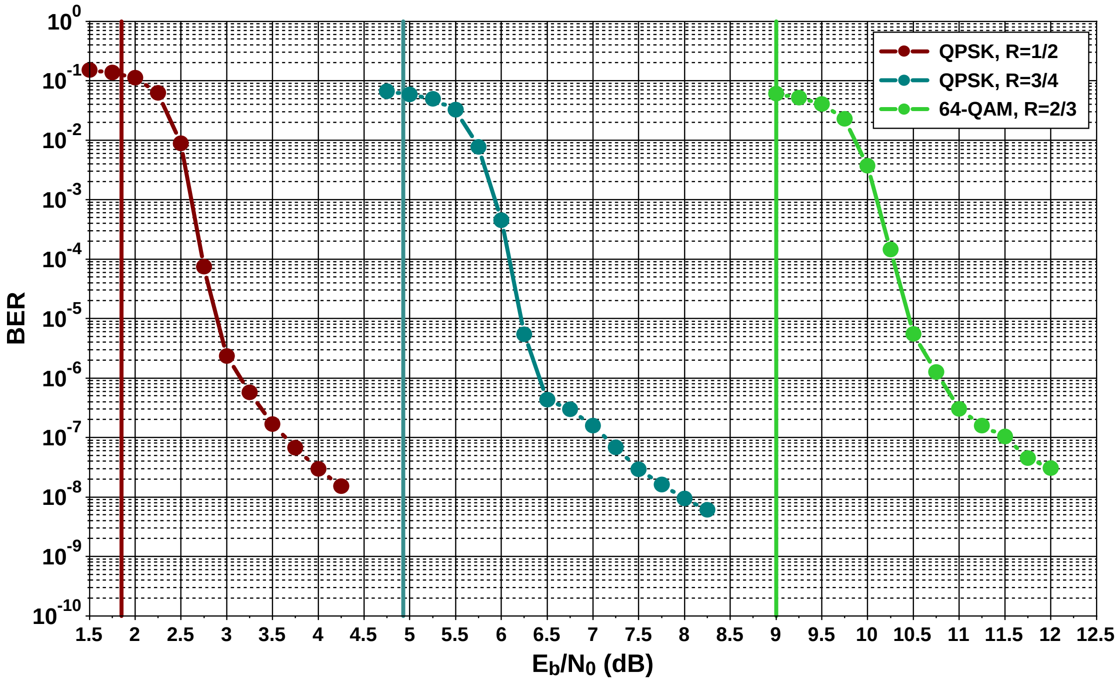

Figure 1.14 — BER performance of three TBICM for the transmission od 16,000-information bit frames over Rayleigh fading channel. DVB-RCS code, QPSK and 64-QAM modulators. Spectral efficiencies of 1.0 bpcu, 1.5 bpcu and 4.0 bpcu. 8 turbo iterations.

In fig. 1.14, fig. 1.15 and fig. 1.16, we have plotted the BER simulation results of DVB-RCS coded TBCIM for the transmission of 16,000-information bit frames. The ARP parameters used for the 16000-bit frames correspond to ($P = 87$, $Q_1 = 8$, $Q_2 = 0$, $Q_3 = 36$). Systematic allocation and 8 turbo iterations have been used. The following schemes were simulated:

- Spectral efficiency of 1.0 bpcu: QPSK, $R = 1/2$
- Spectral efficiency of 1.5 bpcu: QPSK, $R = 3/4$
- Spectral efficiency of 2.0 bpcu: 16-QAM, $R = 1/2$
- Spectral efficiency of 3.0 bpcu:

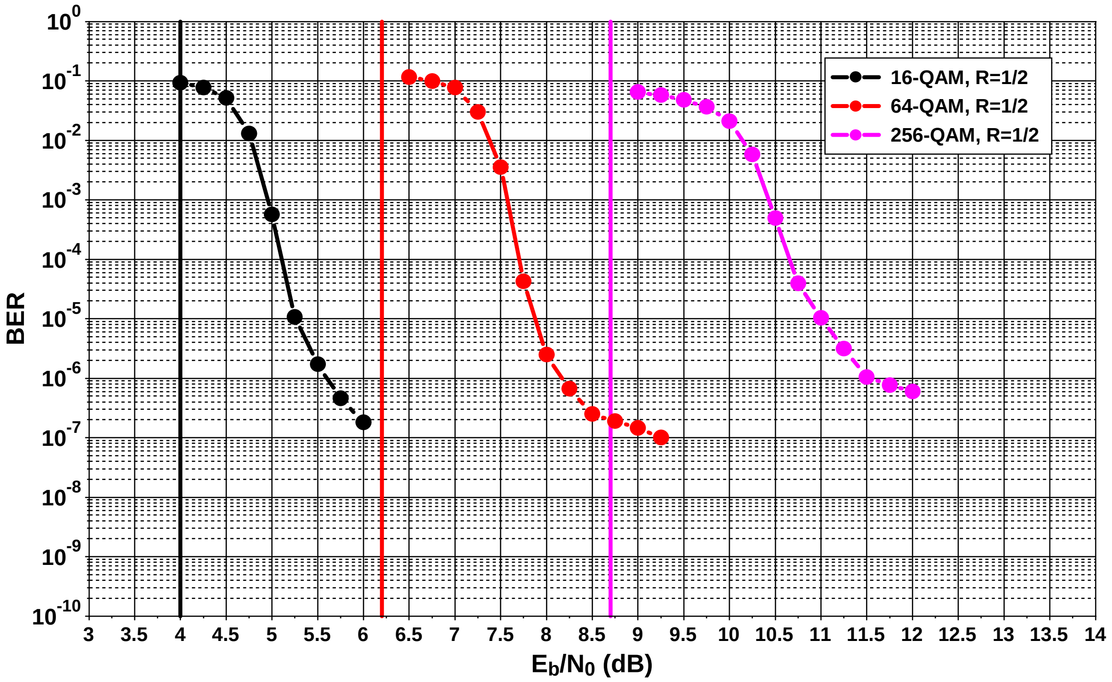

Figure 1.15 — BER performance of three TBICM for the transmission od 16,000-information bit frames over Rayleigh fading channel. DVB-RCS code, 16, 64 and 256-QAM modulators. Spectral efficiencies of 2.0 bpcu, 3.0 bpcu and 4.0 bpcu. 8 turbo iterations.

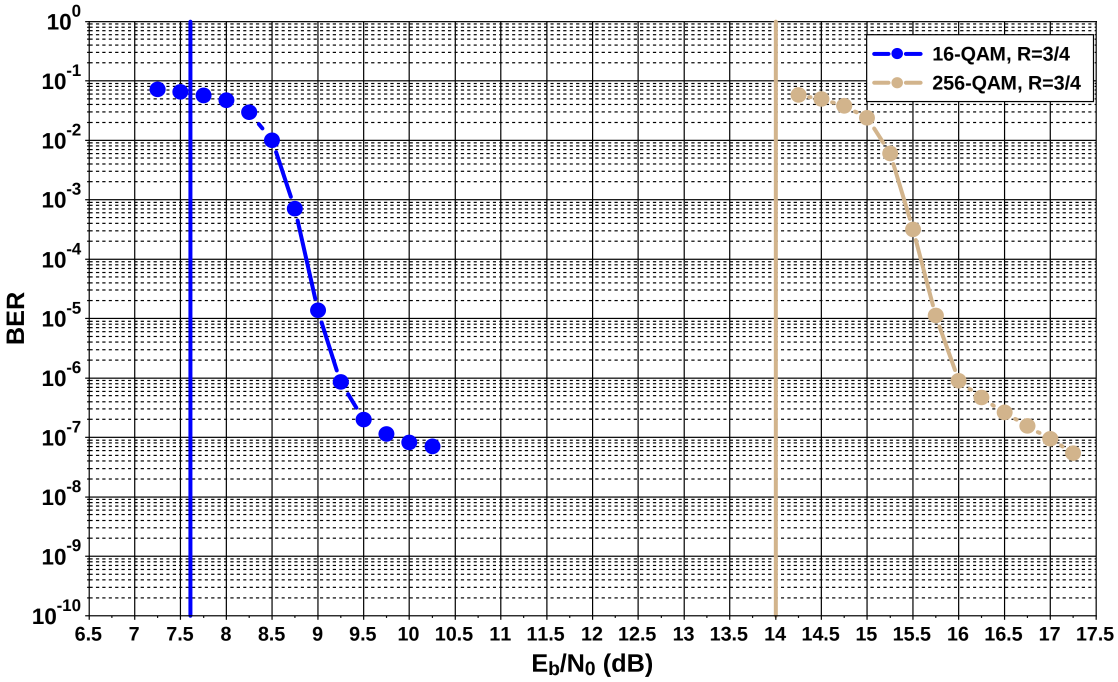

Figure 1.16 — BER performance of three TBICM for the transmission od 16,000-information bit frames over Rayleigh fading channel. DVB-RCS code, 16 and 256-QAM modulators. Spectral efficiencies of 3.0 bpcu and 6.0 bpcu. 8 turbo iterations.

  - 16-QAM, $R = 3/4$
  - 64-QAM, $R = 1/2$
- Spectral efficiency of 4.0 bpcu:
  - 64-QAM, $R = 2/3$
  - 256-QAM, $R = 1/2$
- Spectral efficiency of 6.0 bpcu: 256-QAM, $R = 3/4$

The vertical lines correspond to the channel capacity values.

The following observations deserve to be pointed out:

1. All curves exhibit a change in the slope between 10^{-5} and 10^{-6} of BER predicting an error floor.
2. The gap to capacity is code rate and modulation order dependent. When the order of the modulation increases, the gap to capacity increases if the code rate is kept unchanged. When the code rate increases, the gap to capacity decreases when the modulation order is kept unchanged. However, a limit on this last observation exists. In fact, the error correcting capability of the turbo code diminishes with increasing code rate due to heavy puncturing.
3. For a chosen code rate, gap to capacity increases with the modulation order.

High error floors and wide gaps to capacity even for powerful error correcting codes like turbo codes can be explained by an unsufficient diversity order.

1.3.5.3 Turbo Bit-Interleaved Coded Modulation with Iterative Demodulation TBICM-ID

Inspired by the previous work on BICM-ID with a Convolutional Code (CC) as outer, the authors of [44] have replaced the outer single CC by a more powerful binary turbo code.

On the transmitter side, it is equivalent to replacing the FEC code in fig. 1.6 (a) by the turbo encoder. The interleaver design follows the recommendations of section 1.3.4.1. As for the bits-to-symbol mapping, the recommendations of section 1.3.4.1 are no longer valid. In fact, the introduction of another interleaver corresponding to the turbo code adds an extra randomness level to the mapping. This latter, when optimized for one component code, will certainly not be for the second one. Consequently, without any means of rational optimization, the classical Gray mapping prevails as the mapping type best suited for TBICM-ID. This observation is in coherence with the guidelines of [38] where the Gray mapping was recommended with and without iterative demodulation, when a turbo code was introduced. However, Gray mapping offering negligible iterative gain as mentioned in section 1.3.4, the improvement in error correcting performance of TBICM-ID with respect to TBICM is not expected to be significant.

On the receiver side, the SISO decoder of fig. 1.8 consists of a turbo decoder in the case of TBICM-ID. The decoding process is identical to BICM-ID case with the exception of the presence of two iteration levels: iterations inside the turbo decoder and iterations between the turbo decoder and the demodulator. In [44], a feedback to the demodulator is done after each turbo iteration. The resulting system improves the iterative process convergence. We denote by convergence threshold (covergence in short) what is generally known as the beginning of the 'waterfall region' of a turbo code. It corresponds to the value of the SNR for which the error rate curve starts to exhibit steeper slopes. The extent of the improvement for an 8-PSK TBICM with $R = 2/3$ is around 0.3 dB over Gaussian and Rayleigh flat fading channels and around 0.1 dB for a 16-QAM TBICM with $R = 1/2$. However, the performance results presented in [44] show that TBICM-ID suffers from the same error floor as TBICM.

In order to estimate the potential improvement in convergence when iterative demodulation is applied to TBICM and confirm previous results of [44], we have simulated two 16-QAM TBCIM schemes using the DVB-RCS turbo code and its extension to 16 states, with $R = 3/4$, with iterative demodulation. We have compared the obtained BERs with the ones of a simple TBICM scheme for the transmission of 16,000-information bit frames. BER curves of fig. 1.17 confirm the results of [44] as the curve with iterative demodulation and the DVB-RCS code outperforms by only 0.25 dB at 10^{-6} of BER the curve corresponding to TBICM while exhibiting the same error floor. When the code memory increases the convergence improvement due to iterative demodulation is decreased to less than 0.1 dB.

In conclusion, iterative demodulation slightly improves the iterative convergence of TBICM while exhibiting the same error floor. This meager gain is due to Gray mapping that stops short from improving performance when iterative processing is introduced between the decoder and the demodulator. This slight improvement in convergence diminishes when the code memory is increased.

1.4 Conclusion

In this chapter, we have recalled existing coded modulation schemes and their performance over fading channels. It has been established that maximizing the diversity order represents the dominant criterion for designing powerful coded modulations over fading channels.

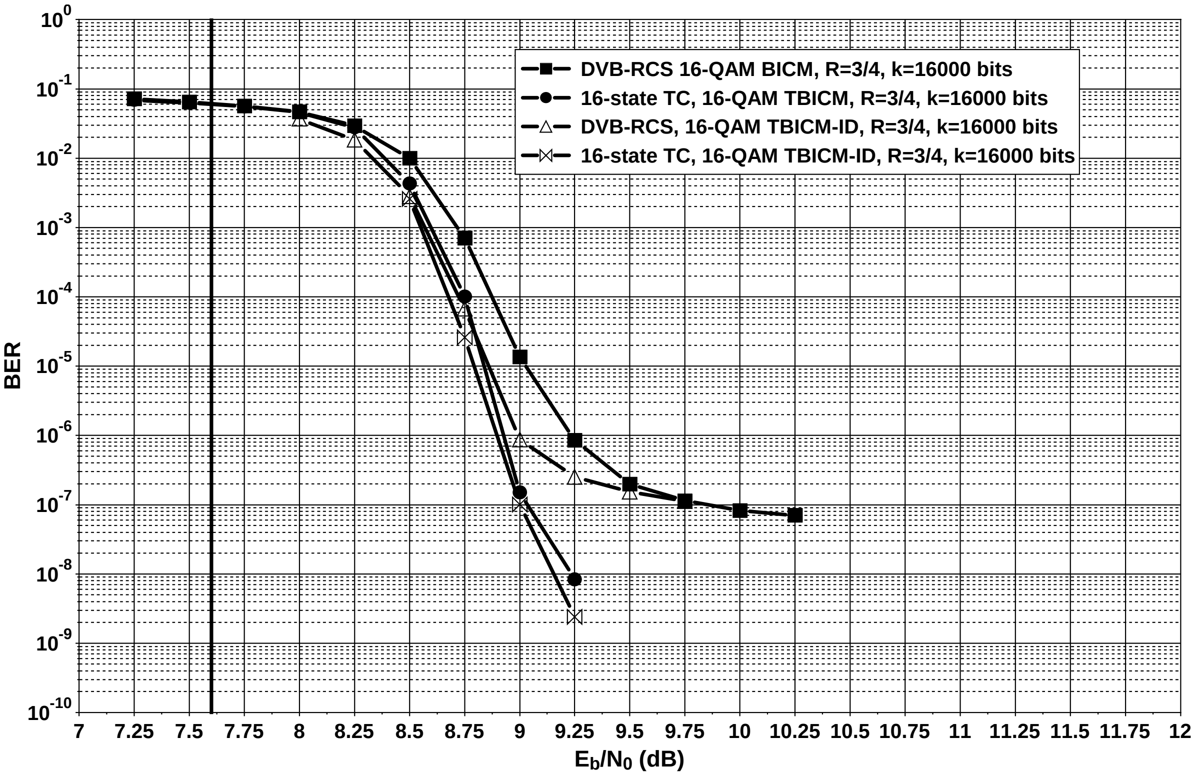

Figure 1.17 — BER comparison of TBICM and TBICM-ID. Systematic allocation. $R = 3/4$ DVB-RCS and 16-state TC. 16-QAM transmission of 16,000-information bit frames. 8 iterations.

By increasing the diversity order, BICM outperforms pre-existing coded modulation schemes. An additional significant improvement of error correcting performance is reached when iterative demodulation is applied to BICM. However, high error floors and wide gaps to capacity are still observed when simple outer codes are used. Consequently, more powerful codes like turbo codes, were investigated. They allow the error correcting performance of BICM schemes to be improved and the gap to capacity to be reduced. For the range of TBICM schemes simulated, we have observed that, for the transmission of 16000-information bit frames this gap varies from 1.0 dB ($R = 1/2$, QPSK modulator) to 2.75 dB ($R = 1/2$ 256-QAM modulator). A large gap to capacity can therefore be observed for high order modulations. The use of iterative demodulation for TBICM schemes only slightly improves the convergence threshold while exhibiting the same error floor.

The increased gap to capacity with increased modulation order can be explained by the fact that at the output of the fading channel, the transmitted constellation signal is subject to the same fading on both component axes. For a M-ary constellation ($M = 2^m$), all the bits carried by a symbol suffer from the same fading. As M increases (and consequently m increases), a greater number of transmitted bits become subject to the same fading coefficient resulting into a lower diversity order that leads to poorer error correcting performance. This decrease in diversity becomes critical for high-order modulation schemes.

In the following chapter we investigate ways of increasing the diversity order of TBICM schemes in the purpose of improving their error correcting performance.

CHAPTER 2

Improving error rates of TBICM schemes over Rayleigh fading channel

DIVERSITY schemes are aimed at improving the performance of transmissions over fading channels. Several families of diversity techniques can be adopted to combat fading: they include for instance frequency diversity in the case of multi-carrier transmission or antenna diversity with Multiple-Input Multiple-Output (MIMO) systems. In our study, the use of these techniques is restricted to the coding and modulation functions, thus limiting the diversity to the time domain.

As mentioned in the previous chapter, the diversity order of BICM schemes is dictated by the minimum Hamming distance of the outer code, thus we start by observing the effect of increasing the code memory on the TBICM performance. Since this basic solution turns out to be unsatisfactory for very high spectral efficiencies, we propose a modification to the transmitter structure in order to double the diversity order of the TBICM and introduce iterative processing to take advantage of this increased diversity.

2.1 Improving error correcting performance by increasing code memory

By considering the TBICM scheme of 1.3.5.2, a straightforward solution to improve the diversity order of the coded modulation involves increasing the component code memory. As the Hamming distance of the code increases with the component code memory ν, TBICM achieves higher orders of diversity for higher values of ν.

Quoting [41] when ν increases from 3 to 4, or equivalently the number of states rises from 8 to 16, a 30 to 50 % improvement in the minimum Hamming distance of double binary turbo codes is observed. In order to estimate the induced improvement in error correcting performance when high order modulations are considered, we have studied the 16-state double binary turbo codes in TBICM scenarios with the systematic allocation.

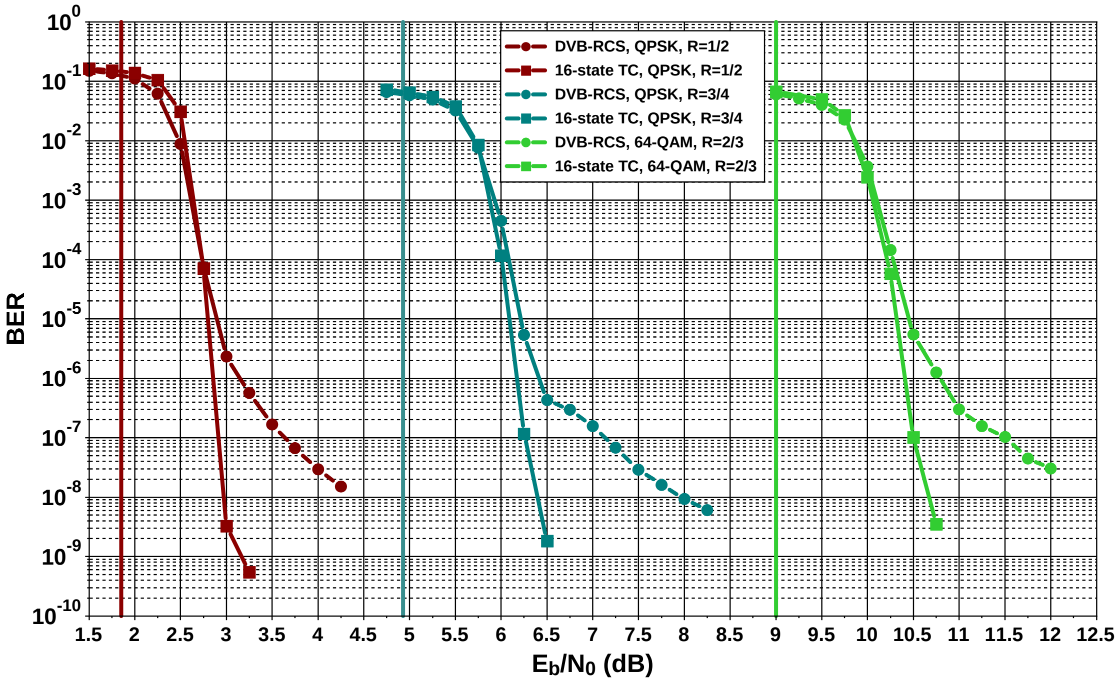

Figure 2.1 — BER performance of three TBICM for the transmission od 16000-information bit frames over Rayleigh fading channel. DVB-RCS and 16-state tubo codes, QPSK and 64-QAM modulators. Spectral efficiencies of 1.0 bpcu, 1.5 bpcu and 4.0 bpcu. 8 turbo iterations.

In fig. 2.1, fig. 2.2 and fig. 2.3, we have plotted the BER simulation results of the DVB-RCS code compared to its extension to 16-state constituent codes in TBCIM schemes for the transmission of 16,000-information bit frames and for spectral efficiencies ranging from 1.0 to 6.0 bpcu. For the 16-state code, the following ARP parameters ($P = 396$, $Q_1 = 6$, $Q_2 = 1$, $Q_3 = 2$) have been used.

The following observations deserve to be mentioned:

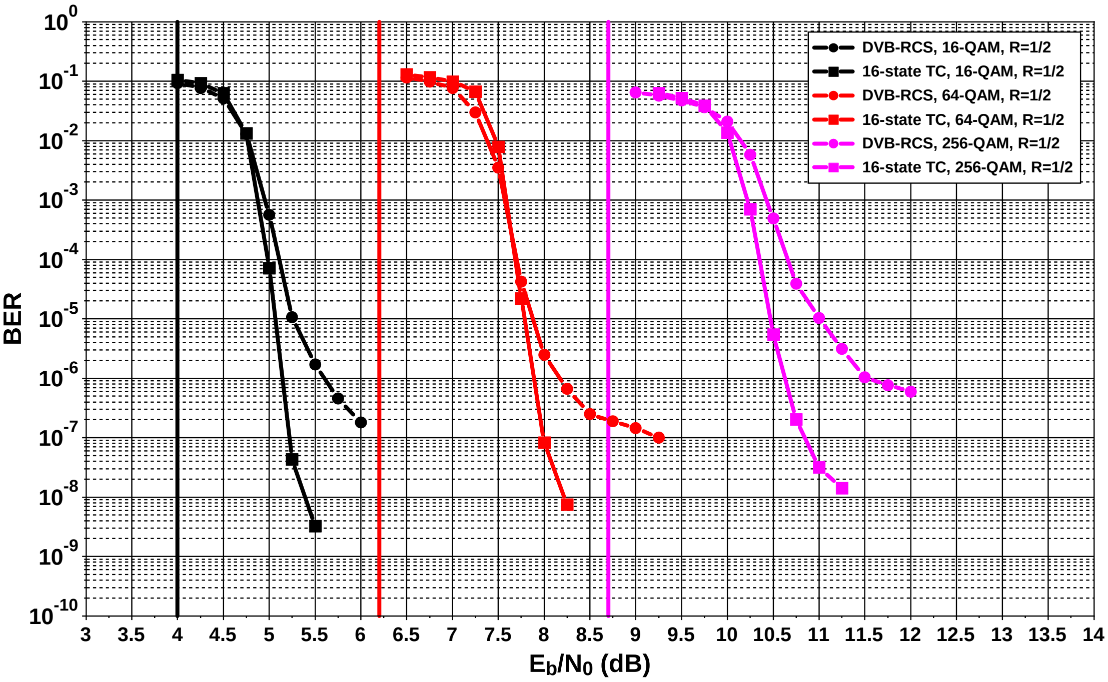

Figure 2.2 — BER performance of three TBICM for the transmission od 16000-information bit frames over Rayleigh fading channel. DVB-RCS and 16-state turbo codes, 16, 64 and 256-QAM modulators. Spectral efficiencies of 2.0 bpcu, 3.0 bpcu and 4.0 bpcu. 8 turbo iterations.

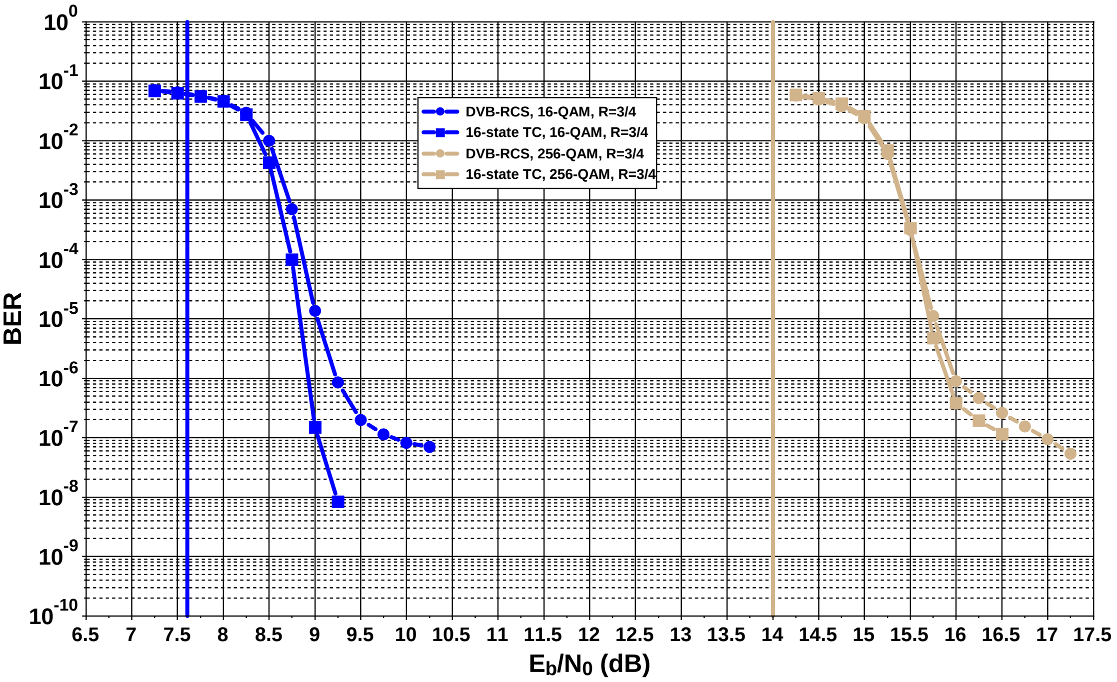

Figure 2.3 — BER performance of three TBICM for the transmission od 16000-information bit frames over Rayleigh fading channel. DVB-RCS and 16-state turbo code, 16 and 256-QAM modulators. Spectral efficiencies of 3.0 bpcu and 6.0 bpcu. 8 turbo iterations.

- Excluding the case of 256-QAM TBICM with $R = 3/4$ (spectral efficiency 6.0 bpcu), the error floor is lowered by at least two orders of magnitude when the 16-state turbo code replaces the 8-state DVB-RCS code. This leads to lower gaps to capacity for low BERs. For the highest efficiency value, the error floor is lowered only by half an order of magnitude. This can be explained by the significant decay of the Hamming distance with increasing code rate even for the 16-state code.

- No convergence threshold penalty has to be paid when increasing the code memory. A slight gain can even be obtained in some cases such as 256-QAM TBICM with $R = 1/2$.

- In order to attain each of the two spectral efficiencies of 3.0 and 4.0 bpcu, two coding and modulation solutions were simulated. The BER results tend to favor the association of a high order modulation scheme and a lower code rate than the other competing case. The selection of a winning coding and modulation scheme could have been be predicted by the computation of the asymptotical gain as proposed in [22].

As a conclusion, despite the additional improvement in error correcting performance introduced by increasing the code memory, when we consider high order modulation schemes coupled with high code rates, the gain in the floor region is limited. Moreover, the increase of the code memory from 3 to 4 leads to doubling the decoding complexity. This is the reason why we have investigated another technique allowing the same decoder complexity to be kept while doubling the diversity order by introducing modifications to the modulator/demodulator couple. This technique is detailed in the following section.

2.2 Doubling the diversity order of TBICM schemes

In this section, we propose a low complexity solution intended to double the diversity order of TBICM schemes. This solution relies on two indispensable parts:

- correlating the in-phase I and quadrature Q components of the transmitted signal

- making these two components fade independently.

We start with a description of the proposed solution through detailing the founding tiers followed by a mathematical justification of doubling the diversity order. Then, we provide a comprehensive description of the proposed system before showing some Monte Carlo simulation results.

2.2.1 Correlating the in-phase and quadrature components

For QAM schemes, as Gray mapping is used for TBICM, the I and Q channels are mapped separatly as two independent PAMs. In the example of fig. 2.4, bits S_1 and S_2 are mapped on the I channel independently of bits S_3 and S_4 which are mapped on the Q channel. All constellation points cannot be uniquely identified in the I channel or the Q channel separately.

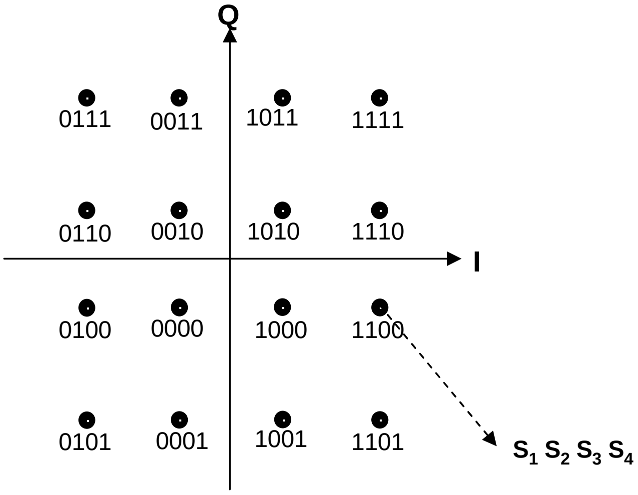

Figure 2.4 — Example of 16-QAM Gray mapping.

In order to circumvent this natural independence and hope for any improvement in the diversity order, we should correlate the I and Q channels of every constellation point. This correlation has as purpose to uniquely identify every constellation point from any component axis.

Several means of correlating I and Q components could be imagined such as precoding or changing the constellation mapping. Since Gray mapping is mandatory due to the use of a turbo code (see section 1.3.5.3), a simple answer to the correlation procedure to be performed involves applying a simple rotation to the constellation as shown in fig. 2.5. This approach is a particular case of the multidimensional modulation schemes designed to optimize diversity order over fading channels and detailed in [45, 46, 47, 48]. The value of the rotation angle is based on a lattice study of the spatial distribution of constellations in a Rayleigh fading environment. It is chosen intentionally to achieve an optimal distribution in terms of spatial separation of the constellation points in signal space. A rotation angle of $\pi/8$ is shown to be optimal in the case of QAMs [48] since it maximizes the minimum Euclidean distance of the constellation in every component axis.

From the complexity point of view, when the rotation is applied, the number of one-dimensional metrics (Euclidean distances) to be computed for LLR estimation regarding the m bits in a symbol is increased from $2^{\frac{m}{2}}$ in the case of usual QAMs to 2^m in the case of

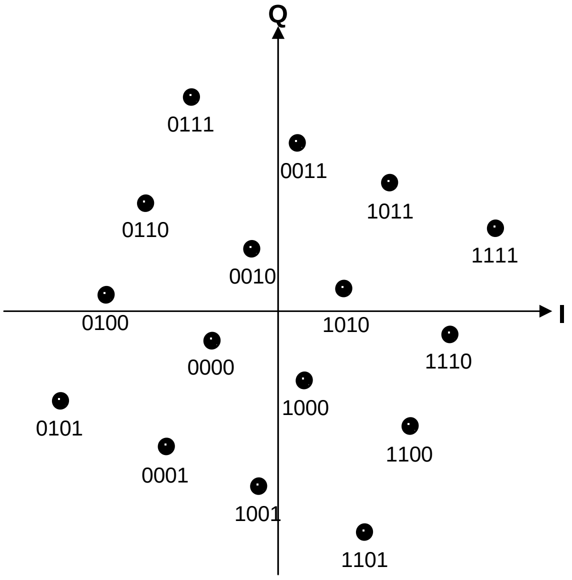

Figure 2.5 — 16-QAM rotated Gray mapper

rotated QAMs. Nevertheless, the metric computation complexity is much lower than the one of the turbo decoder and only represents a small part of the overall receiver complexity.

Note that any rotation of the constellation alters neither the distances between constallation points or the distances to the origin. This means that no modification to the transmit power or bandwidth has to be performed.

2.2.2 Ensuring independent fading for in-phase and quadrature components

When a transmitted constellation point is subject to a fading event, its I and Q coordinates fade identically. When subject to a destructive fading, the information transmitted on I and Q channels suffers from an irreversible loss leading to an erroneous detection of the symbol at the receiver side. If I and Q fade independently, in most cases it is highly unlikely to have both subject to severe fading. Consequently, when combined with the constellation rotation proposed in the previous section, this feature is expected to help the demodulator recover the whole transmitted information.

One way to allow both component axes to fade independently is to introduce coordinate interleaving. This solution known as Signal Space Diversity (SSD) was first proposed as means of increasing diversity for TCM in [49]. The main drawback of coordinate interleaving is the need to quantize and store the modulator signal to be transmitted, operation which requires allocating large amounts of rapid access memory.

Simplified component interleaving can be introduced depending on the fading channel model. In [36], the authors proposed the replacement of I and Q component interleaving by a simple time delay for one of the two component axes over uncorrelated flat Rayleigh fading channels. In fact, since any two modulation symbols of a frame are subject to an independent fading in the case of uncorrelated flat fading, a simple delay of the I component with respect to the Q component of only one symbol period is sufficient for having these two subject to different fading amplitudes. We can imagine extending this concept to other types of widely used fading channels:

- For correlated fading channels [7, 50], the delay should be superior to the correlation length in number of symbol periods.
- For block fading channels [7, 50], a number of different delay values, equal to the size of the faded blocks, should be introduced. Then a suitable switching operation should be performed for the delayed component of the transmitted signal so that successive components in a given faded block are not affected by the same fading event.

I and Q channels being affected by independent Gaussian noise components, the I or Q delay becomes transparent over Gaussian channel. Consequently, the proposed solution offers identical performance to the pragmatic approach over this type of channels and close to the optimum performance attained by a TTCM.

From the implementation point of view, an additional latency consisting of a delay identical to the one introduced at the transmitter is needed in order to match the I and Q channels for accurate detection of the transmitted signal.

2.2.3 Effect on the diversity order of the TBICM scheme

This section is intended to demonstrate that the diversity order of the proposed solution is doubled with respect to a classical TBICM scheme.

When the transmitted signal fades without I/Q component interleaving, the constellation used for detection is equally faded on both axes. When component interleaving (in practice component delay) is introduced, the I and Q channels are subject to independent fading coefficients. Consequently, we can write the discrete time complex received signal y_n at time interval n with respect to the discrete time transmitted signal x_n, the fading amplitude ρ_n, the fading amplitude ρ_{n-d} in time interval $n-d$ and the zero mean double sided discrete time white Gaussian noise process b_n with power spectral density $N_0/2$ as:

$$y_n = \rho_{n-d} x_{n-d}^I + j \rho_n x_n^Q + b_n \tag{2.1}$$

The delay d is chosen in such a way that the fading coefficients ρ_{n-d} and ρ_n are independent. If we dismiss the time index n, we can write:

$$y{=}\rho^I x^I + j\rho^Q x^Q + b \tag{2.2}$$

where ρ^I and ρ^Q represent independent fading amplitudes. Consequently, the diversity order of the uncoded modulation is increased by one additional dimension with respect to the fading. In the light of the modified channel model due to constellation rotation and the introduced Q delay, the detection metric is written as:

$$met(y_n, x_n, \rho_n) = \sum_{i=I,Q} - \left|y_n^i - \rho_n^i x_n^i\right|^2 \tag{2.3}$$

where y_n^I and y_n^Q denote the I and Q components of y_n, x_n^I and x_n^Q denote the I and Q components of x_n. Equ. 2.3 differs from the description of equ. 1.24 in section 1.3.2 by offering different fading amplitudes by component axis ($\rho_n^I \neq \rho_n^Q$). The ML metric (see equ. 1.21) is now expressed as:

$$met(\mathbf{y}, \mathbf{x}, \rho) = \ln P_N(\mathbf{y}|\mathbf{x}, \rho) = \sum_{n=1}^{N} met(y_n, x_n, \rho_n) = \sum_{n=1}^{N} \sum_{i=I,Q} - \left|y_n^i - \rho_n^i x_n^i\right|^2 \tag{2.4}$$

where N is the transmitted sequence length. This equation can be rewritten as:

$$met(\mathbf{y}, \mathbf{x}, \rho) = \ln P_N(\mathbf{y}|\mathbf{x}, \rho) = \sum_{n=1}^{N_{\dim}} met_{\dim}(y_n, x_n, \rho_n) \tag{2.5}$$

where $N_{\dim} = 2N$ and $met_{\dim}(y_n, x_n, \rho_n)$ represents the metric per component I or Q. Consequently, the resulting PEP for the proposed scheme has the same expression as in section 1.3.2:

$$P(\mathbf{v} \to \hat{\mathbf{v}}) \leq \frac{1}{\prod\limits_{n_{\dim} \in \eta_{SSD}} \frac{E_s}{4N_0} \left|v_n - \hat{v}_n\right|^2} \tag{2.6}$$

However, since $N_{\dim} = 2N$, the cardinality $n_{d_{SSD}}$ of η_{SSD}, is doubled with respect to the cardinality n_d of η for a standard BICM scheme. Hence, the proposed scheme doubles the diversity order over Rayleigh faded channel with respect to standard TBICM schemes.

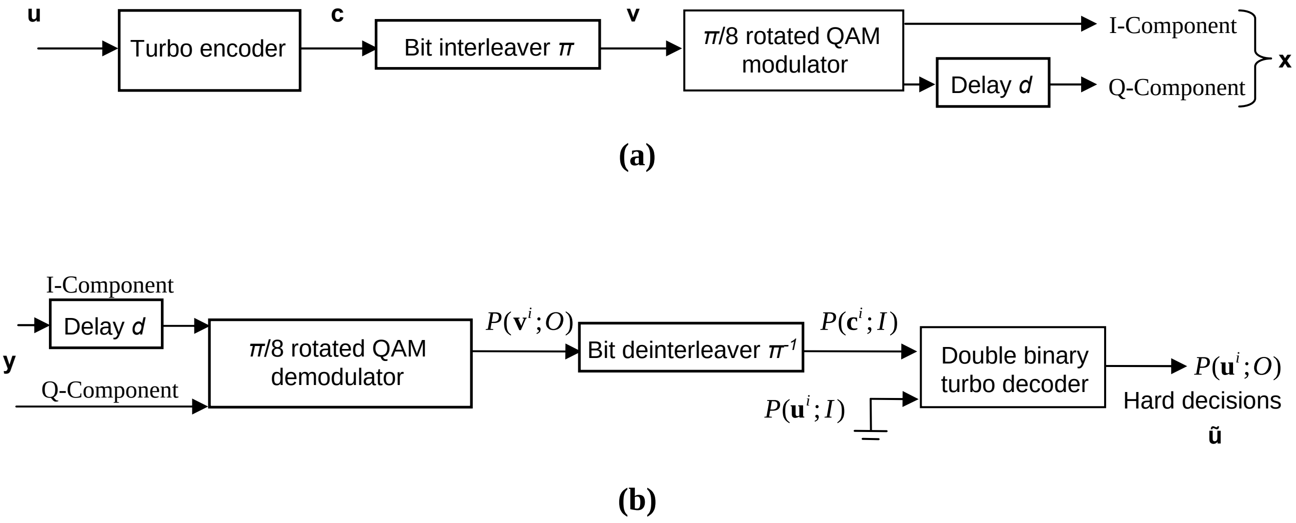

Figure 2.6 — General system decription for the proposed solution. (a) transmitter (b) receiver.

2.2.4 Overall system description of a TBICM-SSD

In this section we provide the transmitter and receiver description of a TBICM-SSD scheme. The system diagram is shown in fig. 2.6.

The transmitter structure (see fig. 2.6 (a)) only differs from the classical TBCIM approach detailed in section 1.3.5.2 in the modulator that has been replaced by a $\pi/8$-rotated modulator. Then the Q component for every transmitted constellation signal is delayed by a delay d being a multiple of the symbol period (instead, the delay could identically be applied to the I component).

At the receiver side (see fig. 2.6 (b)), in order to compute the soft metrics for each modulation symbol, we have to apply a delay with the same value d on the other component, that is I. At signaling time t, the bit probabilities $P(v_{t-d}^i = b|\mathbf{y}; O)$ at the output of the demodulator or demapper can then be obtained via:

$$P(v_{t-d}^i = b|\mathbf{y}; O) = \sum_{x_{t-d} \in \chi} P(x_{t-d}|y_{t-d}) = \sum_{x_{t-d} \in \chi} P(y_{t-d}|x_{t-d}) \cdot P(x_{t-d}) \tag{2.7}$$

where $b = \{0, 1\}$, $i = \{0, .., m-1\}$ and $P(x_{t-d})$ designates the *a priori* probability of transmitting x_{t-d}. Assuming a perfect estimation of the CSI, the soft information at the output of the decoder can be rewritten as:

$$P(v_{t-d}^i = b|\mathbf{y};O) = \sum_{x_{t-d}\in\chi} \frac{1}{\sigma\sqrt{2\pi}} \cdot \exp\left(-\frac{\left|y_{t-d}^I - \rho_{t-d}x_{t-d}^I\right|^2 + \left|y_t^Q - \rho_t x_{t-d}^Q\right|^2}{2\sigma^2} \right) \cdot P(x_{t-d}) \tag{2.8}$$

where σ^2 represents the noise variance and ρ_t is the fading amplitude at signaling time t. $P(x_{t-d})$ is unavailable at the receiver, therefore an equally likely assumption is adopted. After deinterleaving, $P(c_t^i = b|\mathbf{y};O)$ constitutes the input of the SISO decoder. At the output of the decoder, hard decisions are computed.

2.2.5 Performance comparison of TBICM and TBICM-SSD schemes over flat fading channels

We have performed simulations of the TBICM-SSD scheme using the DVB-RCS code with coding rate $R = 1/2$ and a 16-QAM modulator for the transmission of 16,000-information bit frames. Fig. 2.7 compares the resulting BER performance with TBICM.

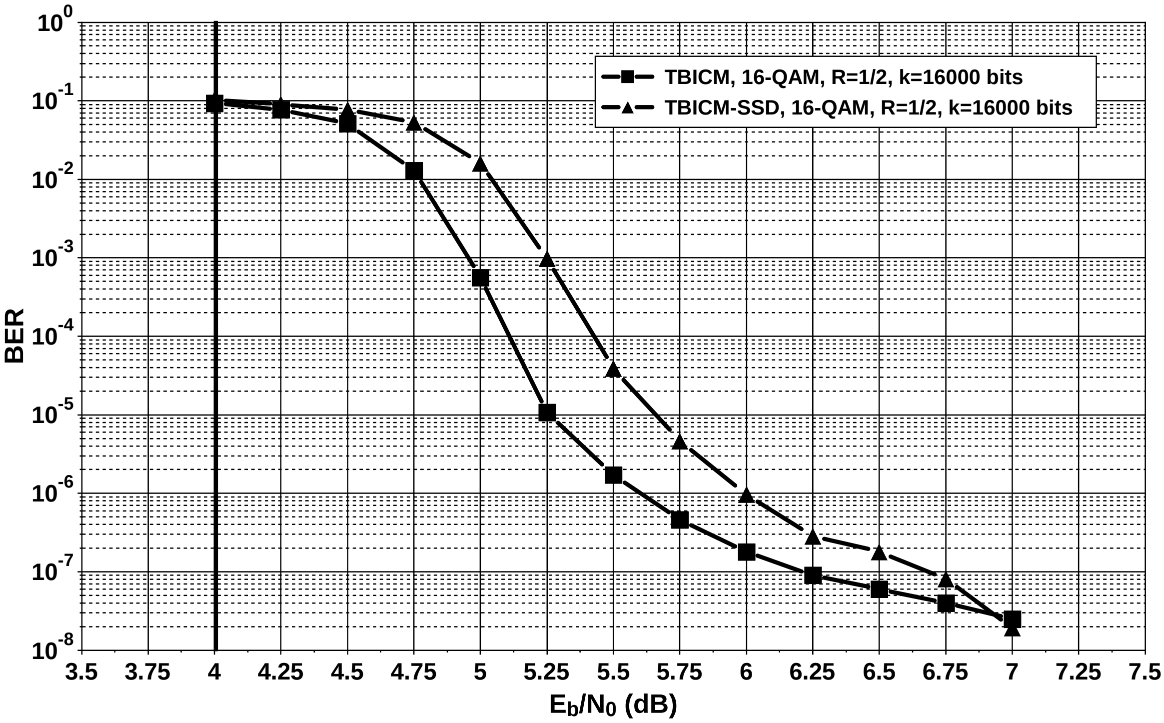

Figure 2.7 — BER comparison of TBICM and TBICM-SSD. $R = 1/2$ DVB-RCS code, 16-QAM for 16000-information bit frames, systematic allocation.

We can observe that TBICM-SSD offers a poorer convergence threshold than TBICM. It looses around 0.3 dB for the simulated scheme and suffers from a change in the slope at an E_b/N_0 value comparable to TBICM.

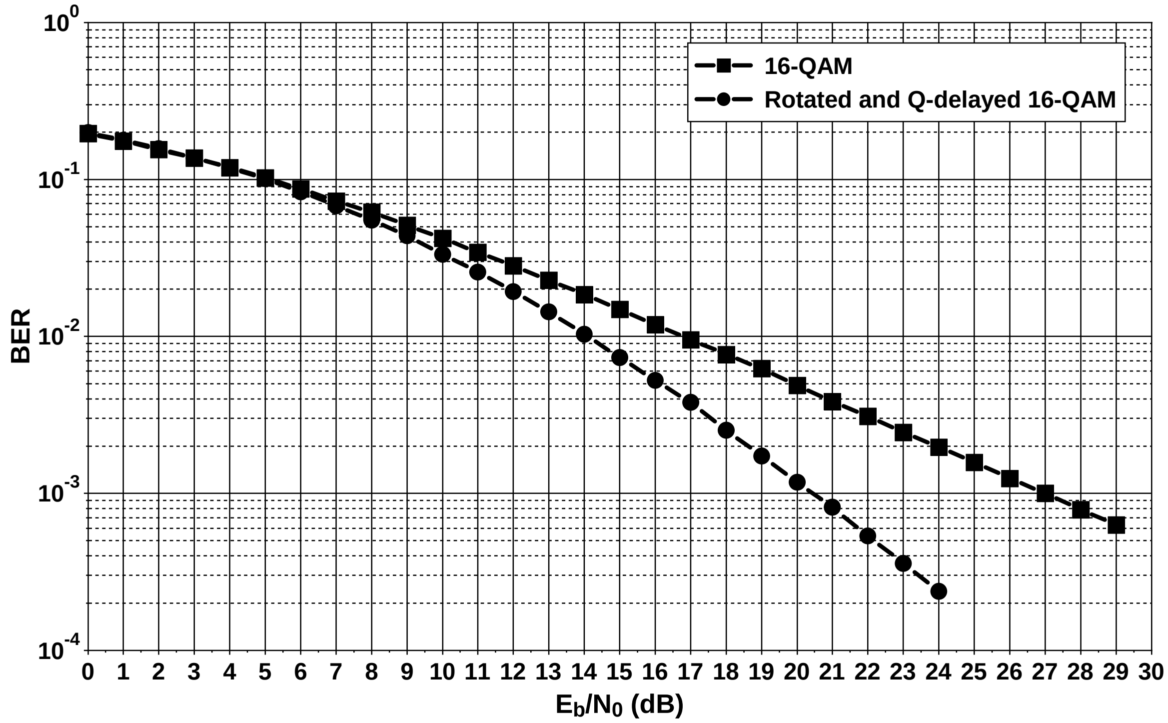

Figure 2.8 — BER comparison of uncoded 16-QAM and rotated and Q-delayed 16-QAM.

In order to understand the underlying reasons for such a degradation, we have plotted in fig. 2.8 the BER of an uncoded standard 16-QAM compared to the Rotated and Q-Delayed 16-Quadrature Amplitude Modulation (RQD-16-QAM). A performance gain of 6.5 dB is observed at 10^{-3} of BER. As both curves do not show the same slope, the performance improvement continues to increase with E_b/N_0. Since these curves constitute the error probability at the input of the decoder, we would expect an improved asymptotical performance of TBICM-SSD with respect to TBICM. This has already been observed in fig. 2.7 where, despite the loss in the convergence, the BER curve of TBICM-SSD crosses the one corresponding to TBICM between 6.75 and 7.00 dB.

If we take a closer look at the uncoded curves between E_b/N_0 values of 0.0 and 5.0 dB (fig. 2.9), we notice that uncoded 16-QAM slightly outperforms RQD-16-QAM for low values of E_b/N_0. A crossing occurs between 3.0 and 4.0 dB where the latter starts to exhibit the best error correcting performance.

Considering the curve plotted in fig. 2.7, we can estimate the convergence threshold of TBICM at $E_b/N_0 \simeq 5$ dB. If we take into account the outer code rate $R = 1/2$ inducing a shift of 3 dB in E_b/N_0, the BER at the input of the decoder is the y-axis coordinate value of the 16-QAM curve corresponding to an approximate value of $E_b/N_0 \simeq 2$ dB. At this value of SNR, the uncoded 16-QAM still outperforms the RQD-16-QAM. Consequently, the TBICM-SSD decoder suffers from a higher average probability of error at its input and

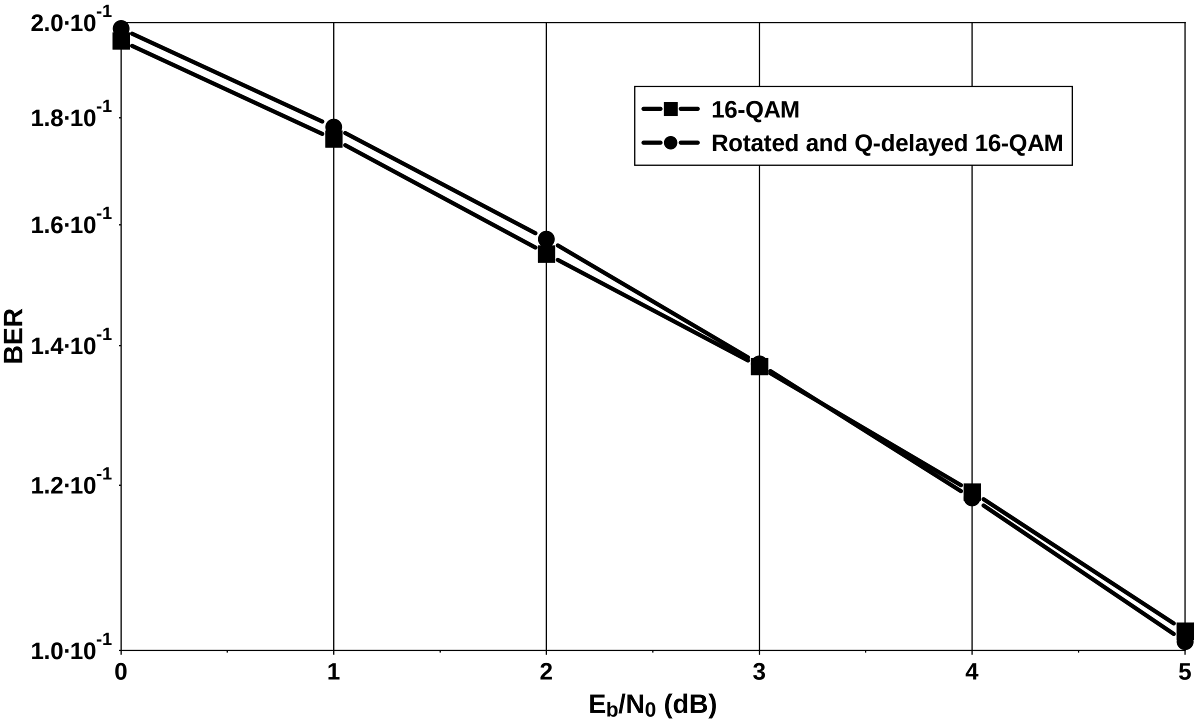

Figure 2.9 — BER comparison of uncoded 16-QAM and rotated and Q-delayed 16-QAM between 0.0 and 5.0 dB

provides a degraded error correcting performance when compared to TBICM. We can expect an improvement in error correcting performance of TBICM-SSD with respect to TBICM for E_b/N_0 values greater than 6.5 $\sim$ 7.0 dB since it corresponds to the crossing values between uncoded RQD-16-QAM and 16-QAM (see fig. 2.7).

The worsened uncoded performance of RQD-16-QAM at low SNR values with respect to classical 16-QAM explains why this technique has never been associated with coding in a practical application. However, in the following section we propose a way of improving the convergence threshold of TBICM-SSD schemes by means of iterative demodulation.

2.3 Improving error correcting performance of TBICM-SSD schemes

As pointed out in the previous section, TBICM-SSD suffers from a worsened convergence threshold while presenting a similar error floor in comparison with TBICM due to the uncoded modulator performance. In this section, we propose an approach to improve convergence threshold of TBICM-SSD while taking advantage of the doubled diversity order to lower error floors.

We start with an analysis of the uncoded modulator by means of tools widely used in the coding field. Then a detailed description of the proposed solution is provided and finally Monte Carlo simulation results validate the good performance of our proposal.

2.3.1 Uncoded modulator analysis

2.3.1.1 EXIT chart analysis

The key to any improvement in performance of the TBICM-SSD scheme resides in the understanding of the RQD-16-QAM modulator/demodulator. EXtrinsic Information Transfer (EXIT) chart [51] is a tool that plots the mutual information at the output of a block as a function of the information at its input. It gives an insight on a potential performance improvement when the mutual information at the output increases with the one at the input in an iterative processing scenario.

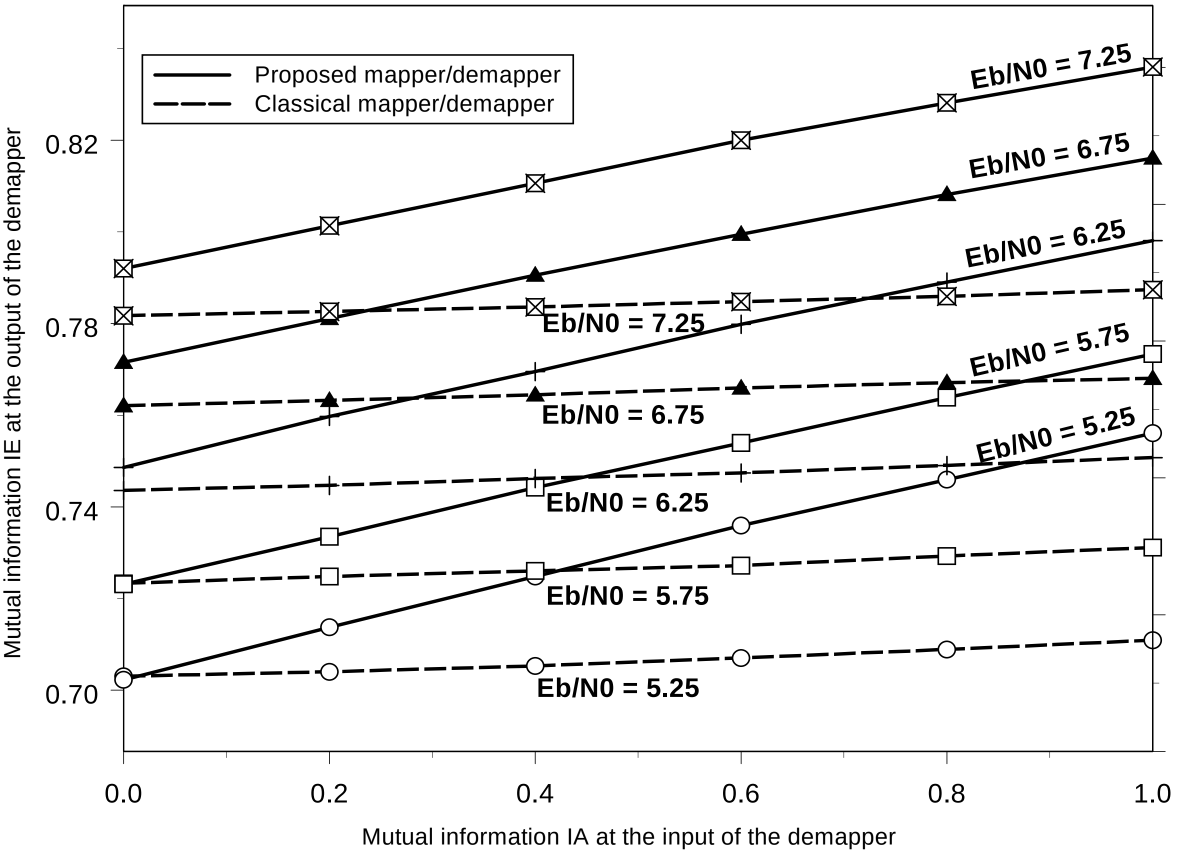

Figure 2.10 — EXIT chart analysis comparison of uncoded Gray mapped 16-QAM and rotated and Q-delayed 16-QAM.

In fig. 2.10, we have compared the EXIT chart of the Gray-mapped 16-QAM to the EXIT chart of the Gray-mapped RQD 16-QAM. The curve corresponding to the standard 16-QAM demodulator, nearly a flat line, predicts almost no improvement in performance with increased information at the input as already observed in the previous chapter. However, the curve corresponding to the proposed modulator/demodulator has a tilted slope with respect to the classical modulation. In other words, as the mutual information at the input IA increases, the mutual information at the output IE increases as well. Consequently, an increase of the mutual information at the output of the RQD 16-QAM demodulator is possible when mutual information at its input increases.

In conclusion to this analysis, we can predict that the RQD-16-QAM should be able to take advantage from iterative processing in order to improve error correcting performance whereas negligeable gain can be obtained with the classical 16-QAM.

One way to consolidate the prediction concerning the proposed modulator involves simulating the demodulator with the assumption of perfect *a priori* information at the input of the demodulator or what is called *genie-aided* demodulator.

2.3.1.2 Uncoded genie-aided performance

The genie-aided performance corresponds to feeding into the demodulator input, perfect *a priori* information, i.e. $P(x_t)$ in equ. 1.36 for the classical demodulator and $P(x_{t-d})$ in equ. 2.8 for the RQD-16-QAM demodulator.

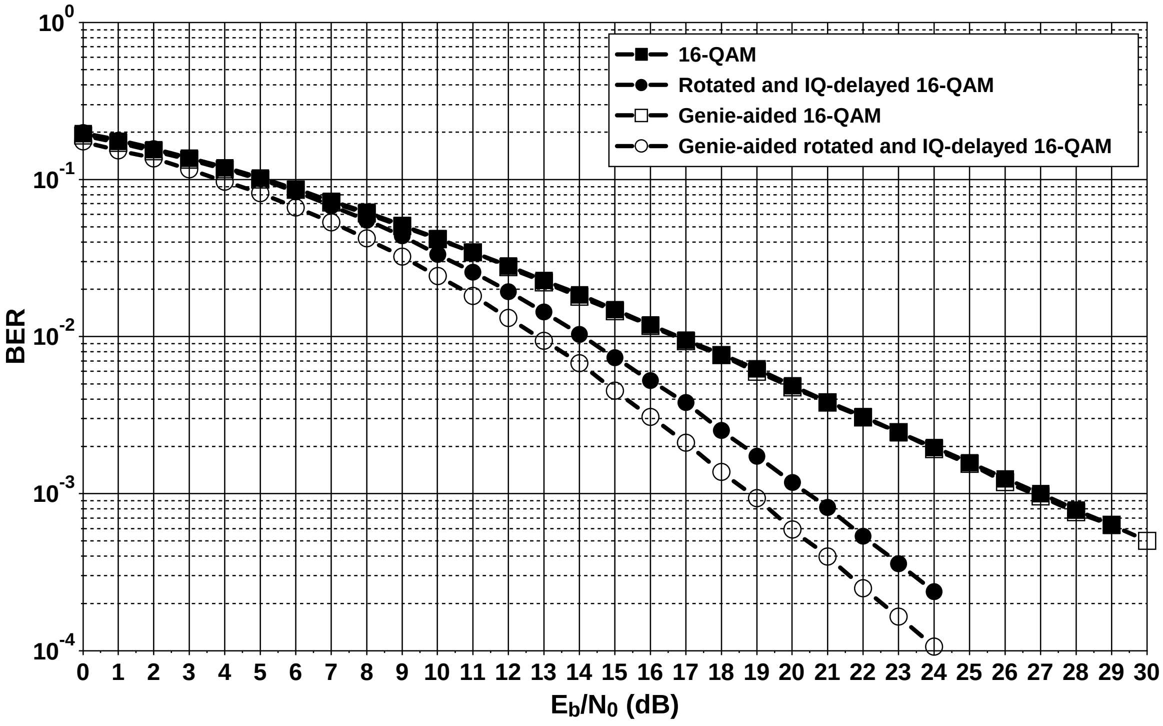

Figure 2.11 — BER comparison at the demodulator output for uncoded 16-QAM and uncoded RQD-16-QAM with and without perfect *a priori* information.

Fig. 2.11 shows the BER at the output of the demodulator for 16-QAM and RQD 16-QAM. Curves corresponding to the genie-aided demodulation have also been added. The following observations can be made:

- The BER curve corresponding to the genie-aided 16-QAM demodulator is quasi-identical to the one corresponding to 16-QAM confirming no improvement in performance with iterative processing.
- Genie-aided RQD 16-QAM demodulation improves the performance of RQD-16-QAM for all values of E_b/N_0. For example, at 10^{-3} of BER, a gap around 1.75 dB in favor of the genie-aided curve can be observed. In the interval of interest for TBICM-SSD, the genie-aided RQD 16-QAM offers the best BER performance of all curves in fig. 2.11 with an improvement around 1 dB.

These results allow us to confirm that, in contrast to classical Gray-mapped 16-QAM where the existence of *a priori* information offers no or negligeable improvement in error correcting performance, RQD 16-QAM with *a priori* information shows improved BER even for low SNR values.

Since TBICM-SSD also doubles the diversity order, one would expect that TBICM-SSD with iterative demodulation improves both convergence threshold and error floors with respect to TBICM.

2.3.2 TBICM-ID-SSD

When the transmission is coded and iterative demodulation is adopted, extrinsic information at the output of the decoder is fedback as *a priori* probabilities to the input of the demodulator or demapper. The BER performance at the output of the demodulator/demapper in the case of iterative demodulation tends to the one of the genie-aided demodulator/demapper as the SNR increases.

2.3.2.1 TBICM-ID-SSD system description

The transmitter structure is identical to the one in fig. 2.6 (a), whereas the receiver introduces iterative demodulation as shown in fig. 2.12.

The feedback of *a priori* information $P(x_t)$ for all transmitted symbols is constructed by combining the soft information related to the coded bits available at the decoder output $P(c_t^i; O)$, transformed to $P(v_t^i; I)$ by the interleaver. Two levels of iterations now exist:

1. iterations inside the turbo decoder
2. iterations from the decoder to the demodulator.

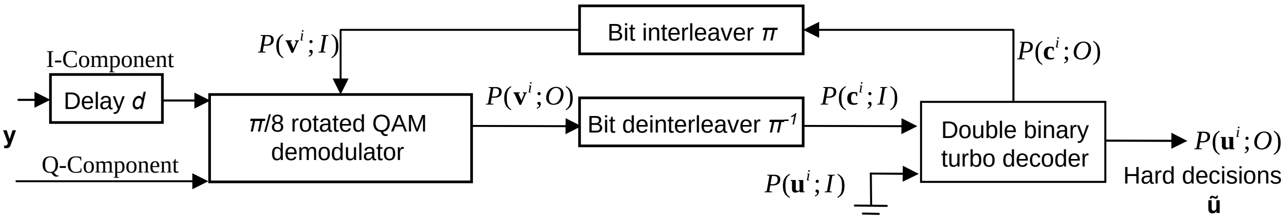

Figure 2.12 — General system decription for the receiver of the proposed solution with iterative demodulation.

In order to determine the number of iterations to be run at each level aiming for the best error correcting performance for TBICM-ID-SSD, we have performed an EXIT chart analysis of the DVB-RCS turbo code, also taking into account iterative demodulation. Due to this analysis, the effect of iterative demodulation on error correcting performance of TBICM-ID-SSD can be clearly emphasized.

2.3.2.2 EXIT chart analysis of the decoder in a TBICM-ID-SSD scheme

Fig. 2.13 presents an EXIT chart analysis of the association of the RQD 16-QAM demapper and the DVB-RCS turbo code with and without iterations to the demapper. The mutual information at the output of each component decoder is a function of the channel SNR and the *a priori* mutual information at the input:

$$IE = T(IA, E_b/N_0) \tag{2.9}$$

The *a priori* information available at the demapper input allows the BER to be improved at its output. The resulting scheme can be seen as a demapper without *a priori* input performing at a different value of E_b/N_0. Having a changing value of E_b/N_0 at the input of the decoder every demapping iteration, the computation of the mutual information IE of equ. 2.9 for the turbo decoder should, as a result, also be performed every demapping iteration. The simulations of fig. 2.13 have been carried out for realistic decoder feedbacks at an E_b/N_0 of 5.25 dB. Mutual information at the output of each component decoder is re-evaluated every demapping iteration. At the first iteration, the computed mutual information represents the one of the proposed demapper without *a priori* information. While in the absence of demapping iterations the receiver does not attain convergence (innermost curves) at 5.25 dB, the area between the two curves widens when feedbacks from the decoder are available and the equivalent receiver attains convergence within a few iterations.

We have observed that the profile of iterations optimizing convergence is the one that applies a demapping iteration for every turbo code iteration. Note that for this profile, after the third demapping iteration, only a slight improvement is predicted from the EXIT chart.

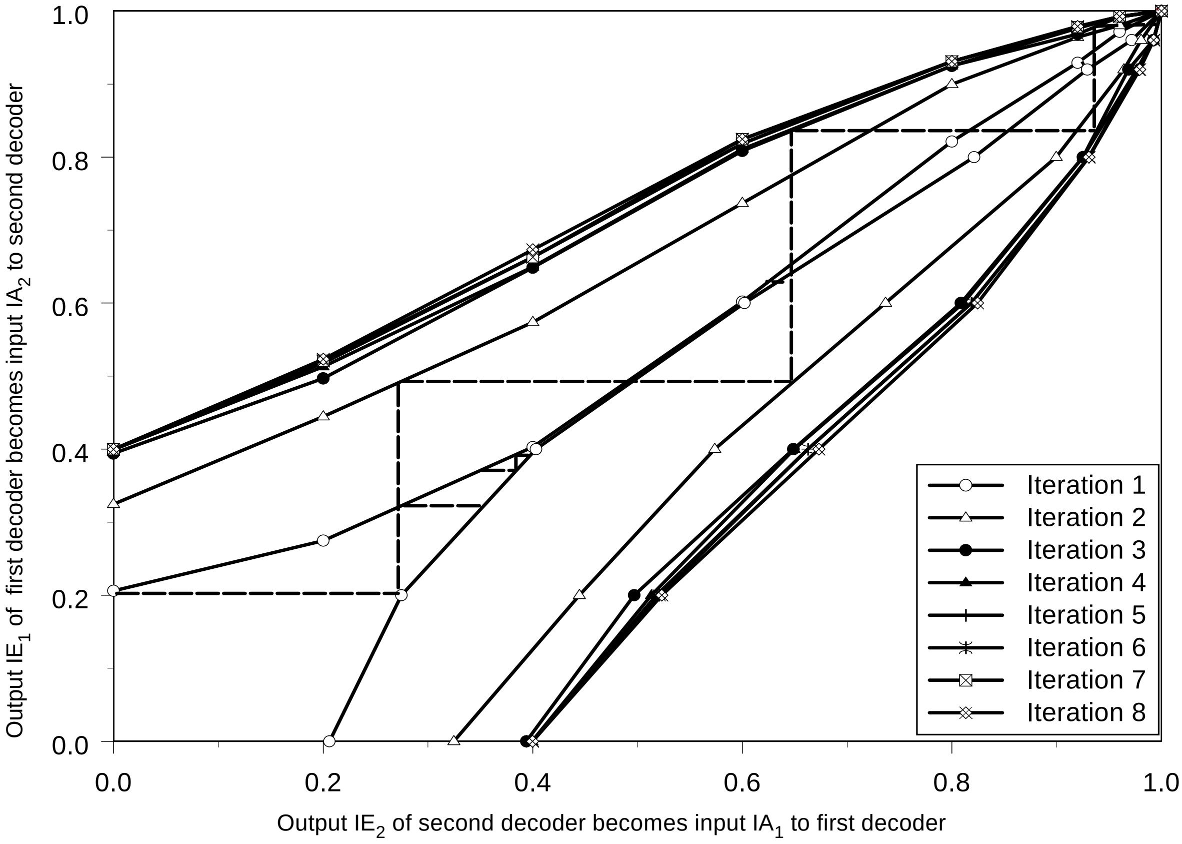

Figure 2.13 — EXIT chart analysis at an SNR of 5.25 dB of the 8-state DVB-RCS decoder for every iteration to the RQD-16-QAM demapper for transmission over Rayleigh flat fading channels.

Fig. 2.14 compares the EXIT chart at 5.25 dB of:

- The classical BICM receiver

- The proposed receiver.

A better iterative convergence is predicted for the proposed system since only four iterations are needed to achieve convergence for TBICM-ID-SSD, whereas five iterations are required for classical TBICM.

Consequently, taking into account the improved uncoded performance of genie-aided RQD-16-QAM and the EXIT chart analysis of fig. 2.14, we can expect an improvement in achievable error rates for TBICM-ID-SSD in terms of both convergence threshold and error floor with respect to TBICM.

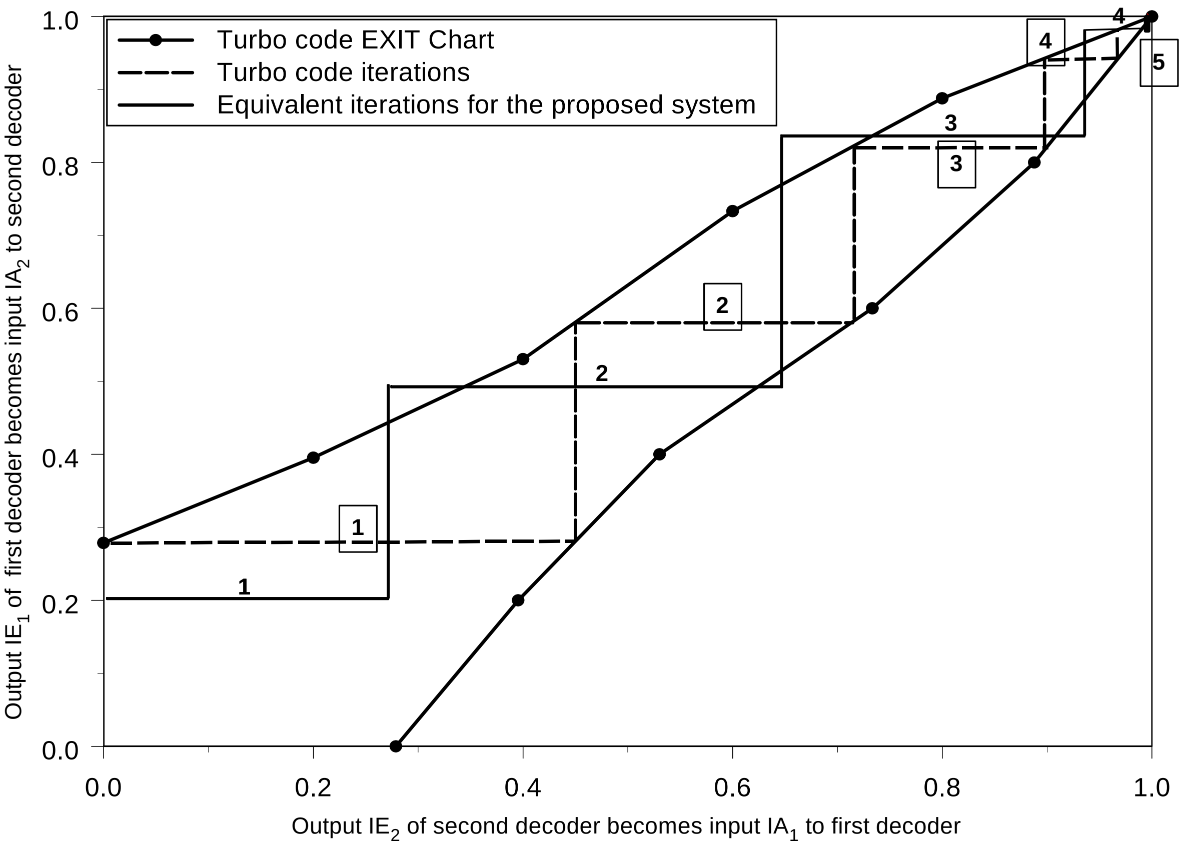

Figure 2.14 — EXIT chart analysis comparison at an SNR of 5.25 dB between 16-QAM TBICM and the equivalent EXIT chart of the 16-QAM TBICM-ID-SSD over Rayleigh flat fading channels.

2.3.3 Expected influence of code rate, frame length and code memory on performance of TBICM-ID-SSD schemes

For a given modulation, the improvement in performance of TBICM-ID-SSD schemes with respect to TBICM schemes is dependent on two main parts:

1. The performance of the uncoded RQD modulation scheme with respect to the classical modulator as well as the extent of the improvement in performance introduced by genie-aided iterative demodulation.
2. The reliability of the feedbacks to the demodulator, as they are constructed from the output of the decoder. It should tend toward the reliability of error free feedbacks with increasing SNR.

The existence of an error correcting improvement for TBICM-ID-SSD with respect to TBICM in the waterfall region can be in a way predicted without the computation of EXIT charts. The prediction relies on using the performance curves of the TBICM scheme under study on one hand and of the uncoded standard and RQD modulations with and without perfect *a priori* information on the other hand.

In order to improve error correction, the RQD demodulator has to outperform the classical one. This obviously depends on the E_b/N_0 value of interest for the turbo decoder in a TBICM context that we call its *operating point*. The minimum operating point to be contemplated is the E_b/N_0 value where the turbo decoder attains its convergence threshold.

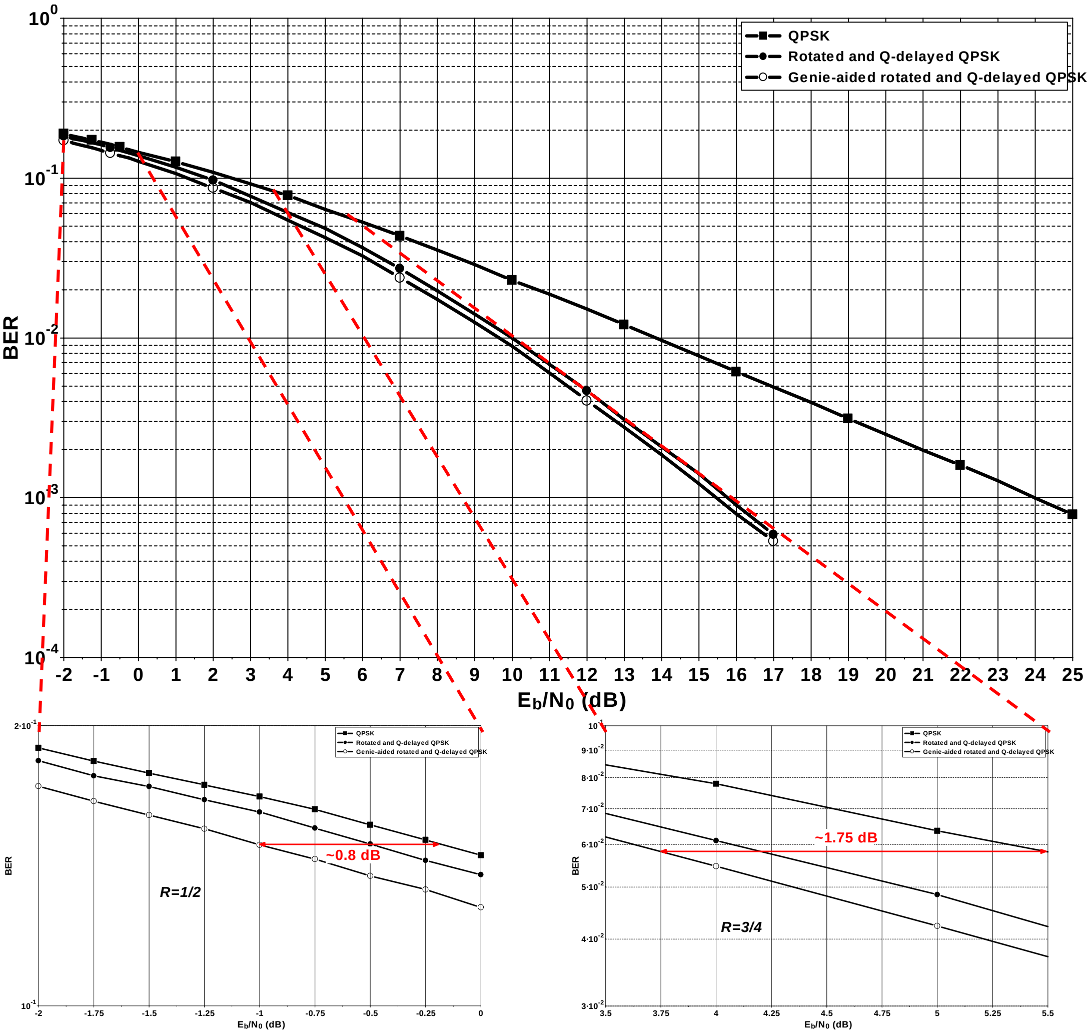

Figure 2.15 — BER comparison over Rayleigh flat fading channel of uncoded QPSK and uncoded RQD QPSK with and without perfect $a-priori$ information. The lower diagrams correspond to a zoom of the performance for a window from -2.0 to 0.0 dB corresponding to the operating point of $R = 1/2$ and from 3.5 to 5.5 dB corresponding to the operating point of $R = 3/4$.

For example, let us study the influence of the code rate on a TBICM-ID-SSD scheme using a QPSK modulation. From fig. 2.1, we can observe that, for $R = 1/2$, the minimum operating point of the turbo decoder corresponds to an E_b/N_0 around 2.0 dB. Taking into account the shift of 3.0 dB due to the code rate, the probability of error at the input of the decoder corresponds to the one at -1.0 dB for the uncoded curve. For a rate $R = 3/4$ turbo code, the minimum operating point is around 5.0 dB. Shifted by 1.3 dB due to the code rate, the probability of error at the output of the demodulator has to be studied for SNRs greater than 3.7 dB.

In fig. 2.15, we have illustrated the BER performance of uncoded QPSK, RQD-QPSK and genie-aided RQD-QPSK over Rayleigh fading channel. The lower diagrams correspond to two zoomed versions of the curves, for a window from -2.0 dB to 0.0 dB corresponding to the area of interest for the rate $R = 1/2$ case, and for a window from 3.5 to 5.5 dB corresponding to the area of interest for $R = 3/4$. As stated in the lower diagrams of fig. 2.15, in these SNR regions, if the feedbacks from the decoder were error free, the potential gain could reach 0.8 dB at the input of the decoder for the former case, whereas it should be around 1.75 dB for the latter case. However, since feedbacks to the demapper are not perfect, these gains will not be attained in practice.

Consequently, we can expect from these curves an improvement in error correcting performance when increasing the code rate. Showing steeper error correcting curve slopes when compared to standard modulation schemes, genie-aided uncoded RQD modulation schemes improve the potentiel gain since the operating point is located at a higher value of E_b/N_0 when the code rate increases.

The same phenomenon should be observed when the length of the transmitted blocks is reduced. The operating point for a given BER is shifted to the right and the potential gain of the TBICM-ID-SSD scheme with respect to a classical BICM scheme is increased.

With regard to the influence of the code memory, it has been shown in [19] that, over fading channels, under the ML decoding hypothesis, the SNR gain due to the increase of the product distance of a coded modulation is inversely proportional to the Hamming distance of the code. Consequenly, in a TBICM-ID-SSD scenario one can expect greater performance gains for lower constraint length codes.

2.4 Monte Carlo simulation results of TBICM-ID-SSD schemes

Monte Carlo simulations have been carried out in order to confirm the analysis results of the previous sections and to observe the effect of signal space diversity combined with iterative demodulation on the asymptotic behaviour of the TBICM scheme. BER simulations for TBICM-ID-SSD have been performed for the modulation schemes, spectral efficiencies, code rates mentioned in section 1.3.5.2 and for two frame sizes: 16,000 and 1,504 bits. The DVB-RCS code and its extension to 16 states constitute the outer turbo codes used.

The simulation of the transmission of long data blocks allow us to directly compare obtained results with the channel capacity, whereas the transmission of short blocks is more representative of actual packet-based transmissions such as in wireless communications.

One simulation has also been performed using the Rician channel model in order to validate the TBICM-ID-SSD principle for this type of channels.

2.4.1 Simulation results for the transmission of long data blocks over flat fading Rayleigh channel

The simulation results for the transmission of 16,000-information bit blocks are plotted in fig. 2.16, fig. 2.17 and fig. 2.18.

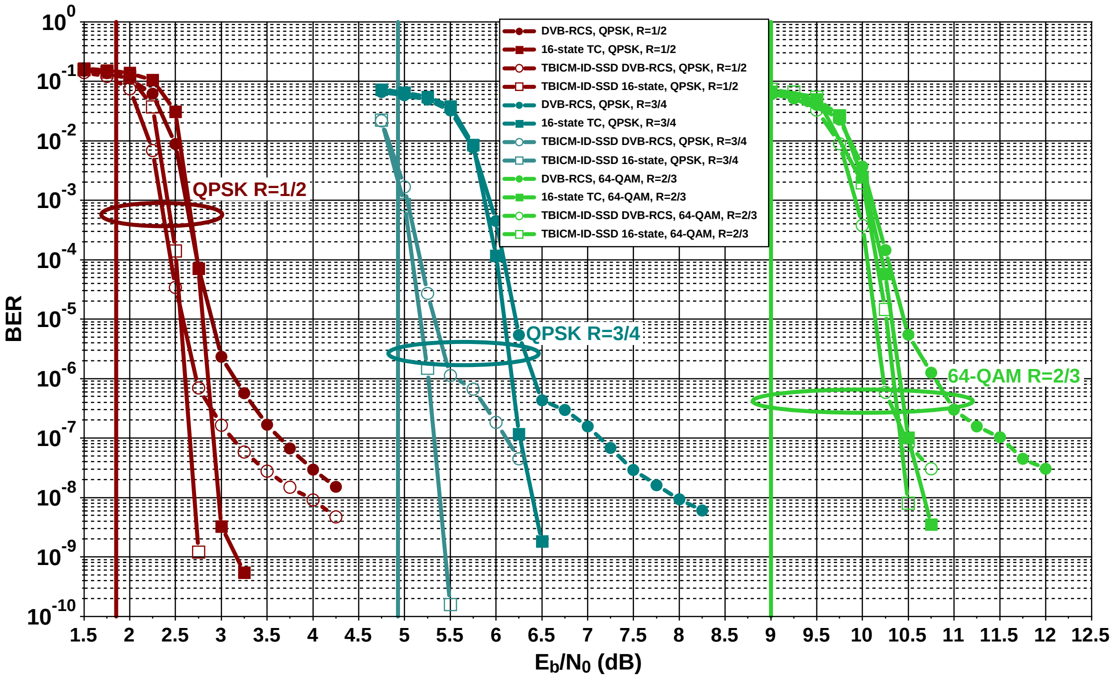

Figure 2.16 — BER performance of DVB-RCS, its extension to 16-state TBICM and TBICM-ID-SSD for 16000 information bit-frames associated with QPSK $R = 1/2$ and $R = 3/4$, 64-QAM $R = 2/3$ over Rayleigh fading channels. Spectral efficiencies of 1.0 bpcu, 1.5 bpcu and 4.0 bpcu.

Selected informative results regarding the gap to capacity, the slope change and the performance difference in convergence and in the floor between TBICM-ID-SSD and TBICM schemes have been summarized in table 2.1 for the DVB-RCS turbo code and in table 2.2 for the 16-state turbo code. The gaps to capacity are displayed for BER values high enough so that the slope change has not occured yet, that is 10^{-5} for the 8-state code and at 10^{-7}

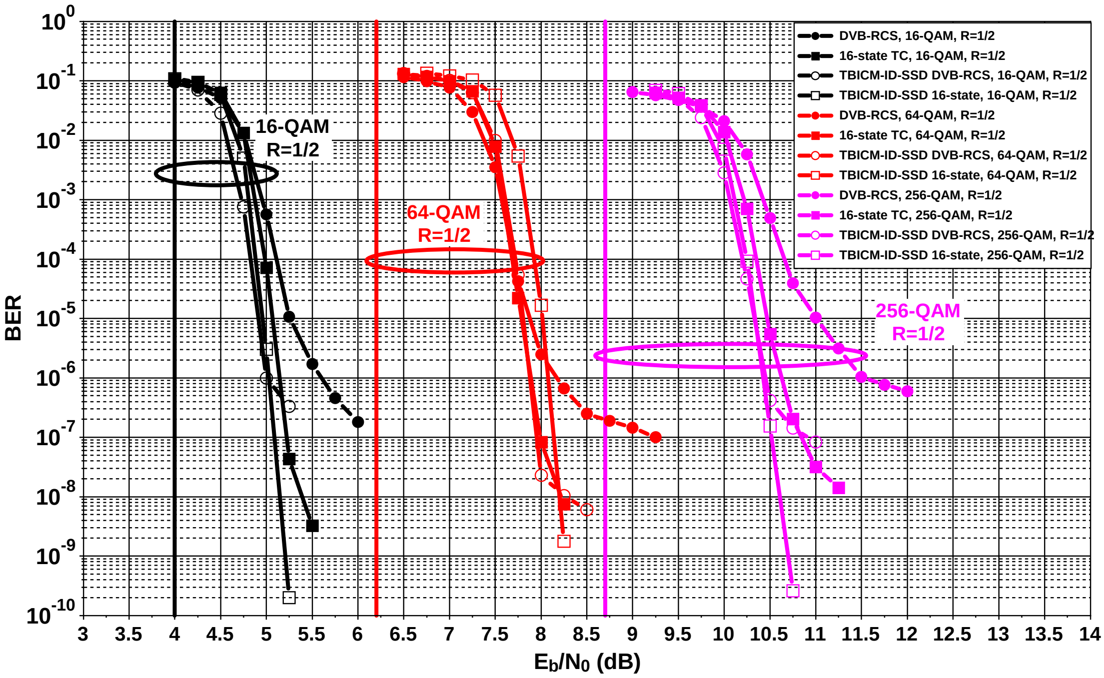

Figure 2.17 — BER performance of DVB-RCS, its extension to 16-state TBICM and TBICM-ID-SSD for 16000 information bit-frames associated with 16-QAM $R = 1/2$, 64-QAM $R = 1/2$ and 256-QAM $R = 1/2$ over Rayleigh fading channels. Spectral efficiencies of 2.0 bpcu, 3.0 bpcu and 4.0 bpcu.

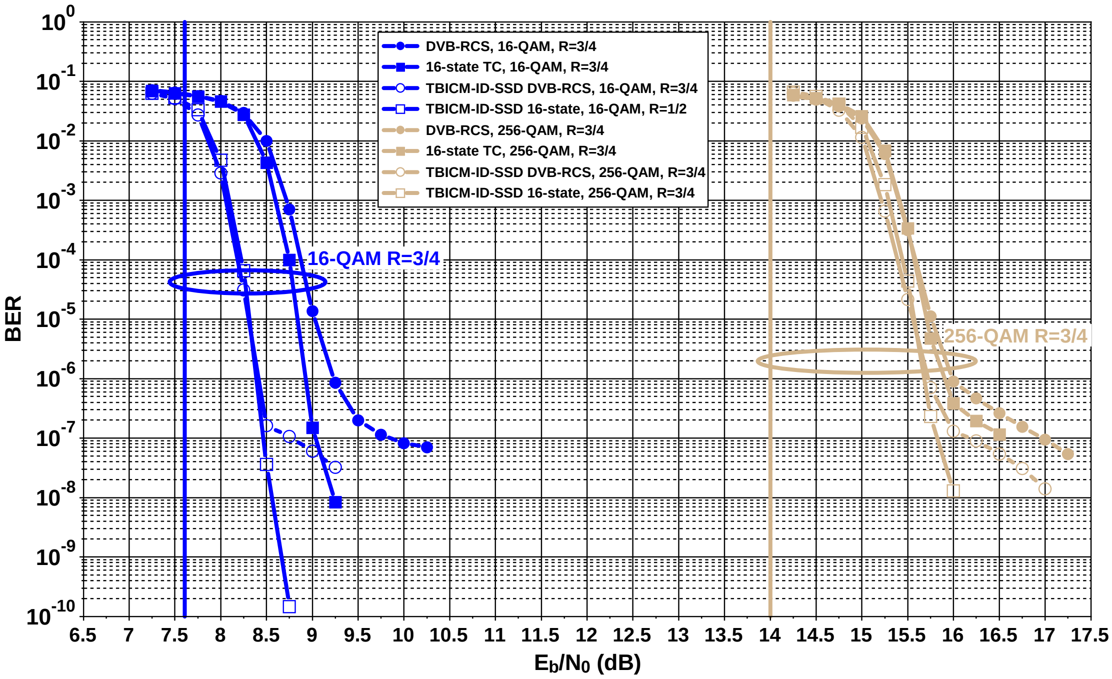

Figure 2.18 — BER performance of DVB-RCS, its extension to 16-state TBICM and TBICM-ID-SSD for 16000 information bit-frames associated with 16-QAM $R = 3/4$, 256-QAM $R = 3/4$ over Rayleigh fading channels. Spectral efficiencies of 3.0 bpcu and 6.0 bpcu.

for the 16-state code. In table 2.2, the relative lowering of the error floor of TBICM-ID-SSD with respect to TBICM is measured in number of orders of magnitude.

TBICM-ID-SSD scheme using the DVB-RCS turbo code				
Modulation and Code rate	Gap to capacity at 10^{-5} of BER	Slope change	Waterfall vs TBICM	Floor vs TBICM
QPSK $R = 1/2$	1.00 dB	$1.0{\cdot}10^{-6}$ of BER	-0.30 dB	-1.0 order(s)
QPSK $R = 3/4$	0.40 dB	$1.0{\cdot}10^{-6}$ of BER	-0.90 dB	-
16-QAM $R = 1/2$	0.90 dB	$1.0{\cdot}10^{-6}$ of BER	-0.30 dB	-1.0 order(s)
16-QAM $R = 3/4$	0.70 dB	$2.0{\cdot}10^{-7}$ of BER	-0.75 dB	-0.5 order(s)
64-QAM $R = 1/2$	1.50 dB	$2.0{\cdot}10^{-8}$ of BER	-	-2.0 order(s)
64-QAM $R = 2/3$	1.10 dB	$1.0{\cdot}10^{-7}$ of BER	-0.25 dB	-1.5 order(s)
256-QAM $R = 1/2$	1.55 dB	$4.0{\cdot}10^{-7}$ of BER	-0.45 dB	-2.0 order(s)
256-QAM $R = 3/4$	1.55 dB	$2.0{\cdot}10^{-7}$ of BER	-0.20 dB	-1.0 order(s)

Table 2.1 — Gap to capacity, slope change, waterfall and floor difference for DVB-RCS coded TBICM-ID-SSD with respect to TBICM.

For the 16-state code, no change in the slope was observed for the TBICM-ID-SSD scheme in all treated cases except 256-QAM, $R = 3/4$ where a slight change in the slope is detected at 10^{-7} of BER. Consequently, in table 2.2, instead of reporting the change in the slope as in the case of the DVB-RCS code, we have opted for mentioning the lowest attained simulated point of the curve without any slope change. In the case of 16-state coded TBICM, only a slight change in the BER slope is observed for all cases except the case of 256-QAM, $R = 3/4$. This was reported in the last line of table 2.2.

TBICM-ID-SSD scheme using a double-binary 16-state turbo code				
Modulation and Code rate	Gap to capacity at 10^{-7} of BER	Slope change lower than	Waterfall vs TBICM	TBICM slight slope change at
QPSK $R = 1/2$	0.75 dB	$1.0{\cdot}10^{-9}$ of BER	-0.30 dB	$3.0{\cdot}10^{-9}$ of BER
QPSK $R = 3/4$	0.40 dB	$2.0{\cdot}10^{-10}$ of BER	-0.90 dB	$3.0{\cdot}10^{-8}$ of BER
16-QAM $R = 1/2$	1.00 dB	$2.0{\cdot}10^{-10}$ of BER	-0.10 dB	$4.0{\cdot}10^{-8}$ of BER
16-QAM $R = 3/4$	0.80 dB	$1.5{\cdot}10^{-10}$ of BER	-0.55 dB	$4.0{\cdot}10^{-8}$ of BER
64-QAM $R = 1/2$	2.00 dB	$2.0{\cdot}10^{-9}$ of BER	+0.17 dB	$6.0{\cdot}10^{-8}$ of BER
64-QAM $R = 2/3$	1.40 dB	$7.0{\cdot}10^{-9}$ of BER	-	$4.0{\cdot}10^{-8}$ of BER
256-QAM $R = 1/2$	1.80 dB	$3.0{\cdot}10^{-10}$ of BER	-0.10 dB	$1.0{\cdot}10^{-7}$ of BER
256-QAM $R = 3/4$	1.80 dB	$1.0{\cdot}10^{-7}$ of BER	-0.20 dB	$3.0{\cdot}10^{-7}$ of BER

Table 2.2 — Gap to capacity, slope change, waterfall and floor difference for 16-state turbo coded TBICM-ID-SSD with respect to TBICM.

From table 2.1 we can mention the following:

- At 10^{-5} of BER, the gap to capacity varies from 0.40 to 1.55 dB for the DVB-RCS coded TBICM-ID-SSD schemes studied, whereas it lies between 1.0 to 2.3 dB in the case of standard TBICM schemes.
- When the code rate increases, the gap to capacity decreases except for the case of 256-QAM, where the observed gap for $R = 3/4$ is the same as for $R = 1/2$.
- In most cases, the gap to capacity increases with the modulation order.
- The performance improvement in the waterfall region with respect to TBICM depends on the code rate and the modulation order. It ranges from no improvement (64-QAM $R = 1/2$ case) to 0.9 dB (QPSK $R = 3/4$). As predicted in section 2.3.3, we can observe an increasing gap between TBICM and TBICM-ID-SSD curves when the code rate increases for a given modulation.
- The improvements in the waterfall and in the floor regions with respect to TBICM vary in the opposite direction. When large threshold gaps are observed (QPSK, $R = 3/4$ case for example), small improvement or no improvement at all in the floor region is attained. On the contrary, when no or negligeable improvement in the threshold is seen (64-QAM, $R = 1/2$ case for example), the error floor is significantly lowered (by at least 2 orders of magnitude in the cases simulated).
- For all treated cases, the DVB-RCS coded TBICM-ID-SSD schemes guarantee error floors lower than 10^{-6} of BER. This upper limit resides at 10^{-5} of BER for TBICM.

When low error floors are targeted, a double-binary 16-state turbo code is introduced. In this case, we can make the following remarks on the summarized results of table 2.2:

- At 10^{-7} of BER, the gap to capacity varies from 0.40 to 2.00 dB for the 16-state turbo coded TBICM-ID-SSD schemes simulated whereas it lies between 1.1 to 2.5 dB in the case of standard TBICM schemes. As expected, in most cases, the gain of TBICM-ID-SSD with respect to BICM is lower with the 16-state turbo code than with the DVB-RCS code.
- The observations regarding the influence of code rate and modulation order on the gap to capacity made in the case of DVB-RCS coded TBICM-ID-SSD schemes still apply when a 16-state double-binary turbo code is used.
- In the waterfall region, a case where TBICM outperforms TBICM-ID-SSD has been detected. It corresponds to the 64-QAM modulator with $R = 1/2$, where the degradation in

waterfall performance reaches 0.17 dB. This could have be predicted from a comparison of the uncoded performance of 64-QAM with respect to RQD-64-QAM, as detailed in section 2.3.3. For the remaining cases, TBICM-ID-SSD schemes display a similar convergence behavior (64-QAM, $R = 2/3$ case) or an improvement up to 0.9 dB (QPSK, $R = 3/4$ case).

- When comparing the third column of table 2.2 with the last column, we can observe that TBICM-ID-SSD significantly lowers the error floor with respect to TBICM. Excluding the 256-QAM, $R = 3/4$ case the BER curves show no change in the slope until the lowest simulated point. For the excluded case, despite the change in the slope, the error floor is improved with respect to TBICM.
- Even if we were unable to simulate enough data sequences to show error floors, we expect that the comment concerning the compromise between the improvement in convergence threshold and the one in the floor observed in the case of the DVB-RCS coded TBICM-ID-SSD schemes still holds for the 16-state turbo coded TBICM-ID-SSD schemes.

Note that, for a chosen modulation scheme, the improvement in error correcting performance of TBICM-ID-SSD with respect to TBICM increases with the code rate R for both code types used. This is an interesting result knowing that convolutional turbo codes suffer from an important degradation in performance when increasing the code rate due to heavy puncturing.

To conclude these remarks on the BER performance of TBICM-ID-SSD schemes, it is worth pointing out that QPSK modulation coupled with high rate turbo codes constitutes the best case scenario. In fact, since the proposed solution is limited to doubling the diversity order, the modulation scheme with the highest diversity order per transmitted bit is QPSK. In this case, the TBICM-ID-SSD scheme with $R = 3/4$ approaches capacity by 0.5 dB at a BER as low as 10^{-9} for only 16,000-information bit frames. On the contrary, the 256-QAM case with $R = 3/4$ represents the worst case scenario where doubling the diversity order reveals to be unsufficient in order to avoid a change in the BER curve slope around 10^{-7} of BER, even when a 16-state turbo code is used. If spectral efficiencies of this magnitude (6.0 bpcu) and error floors lower than 10^{-7} are targeted over fading channels, more powerful error correcting codes than the ones considered here or ways of increasing further the diversity order should be investigated.

2.4.2 Comparison with TBICM-ID schemes

In order to identify the effect of the increased diversity order apart from the iterative demodulation process, we have compared the performance of a TBICM-ID-SSD scheme with a standard TBICM with Iterative Demodulation (TBICM-ID) scheme. This comparison is fairer in the sense that the underlying systems are quite similar in complexity point of view (except for the number of metrics to be computed).

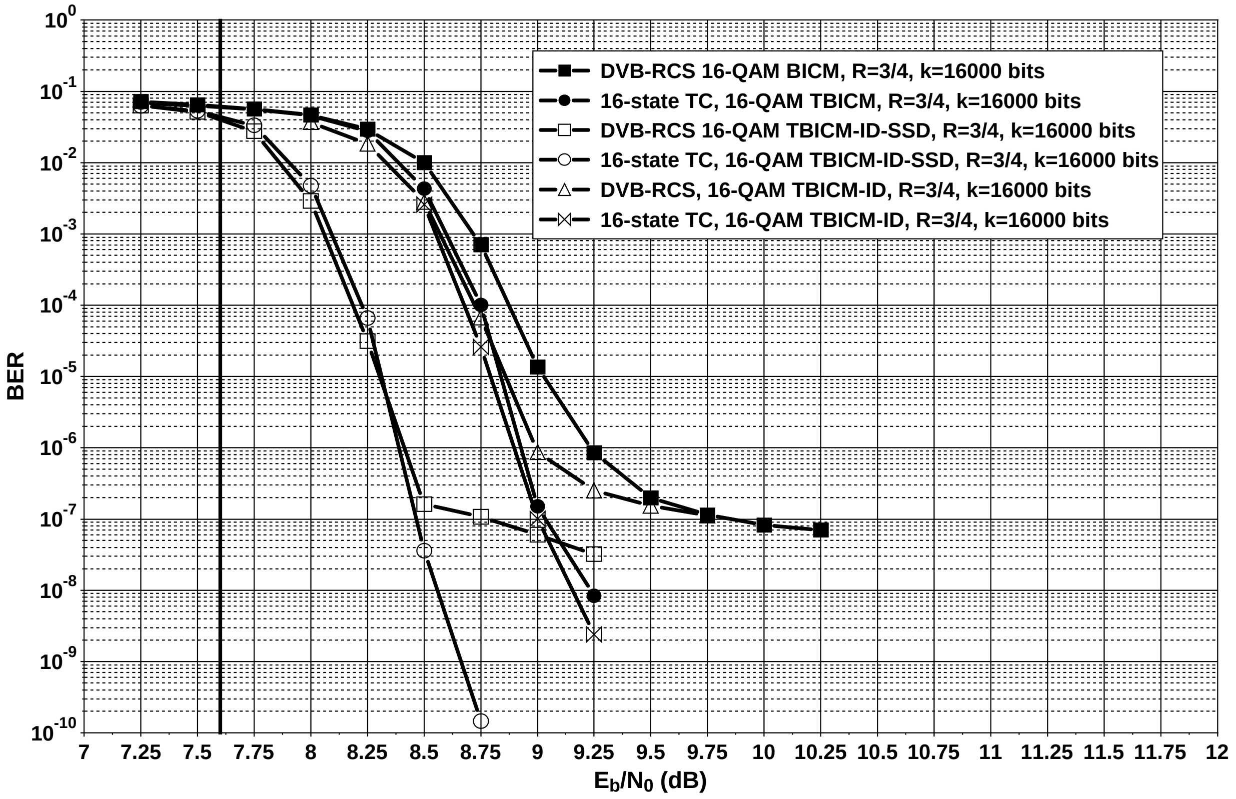

Figure 2.19 — BER comparison of TBICM, TBICM-ID and TBICM-SSD. Systematic, $R = 3/4$ DVB-RCS and 16-state TC, 16-QAM for 16000 information bit-frames.

In fig. 2.19 we have plotted the simulation results of TBICM, TBICM-ID and TBICM-ID-SSD schemes for the DVB-RCS turbo code as well as its extension to 16 states for the transmission of 16,000-information bit frames, using 16-QAM and coding rate $R = 3/4$.

As already mentioned in the previous chapter (section 1.3.5.3), the DVB-RCS code in a TBICM-ID scenario slightly improves the waterfall performance of the TBICM. As for the 16-state turbo code, the gain is much smaller.

Nevertheless, for the two different turbo codes under study, we can confirm that the increased diversity order introduced by the proposed solution is the dominant factor in improving the performance in the waterfall region. Concerning the error floor, since the TBICM-ID scheme suffers from the same floor as the TBICM scheme, the gain in asymptotical performance is entirely due to the diversity increase.

2.4.3 Simulation results for the transmission of shorter data blocks over flat fading Rayleigh channel

Reducing the frame size results in delayed convergence for turbo coded systems. This section investigates the effect of reducing the frame size on the TBICM-ID-SSD performance with respect to TBICM. FER simulations were then undertaken for MPEG frames (1,504 information bits) for the same spectral efficiencies, modulation schemes and turbo codes as simulated in the previous section. Results are plotted in fig. 2.20, fig. 2.21 and fig. 2.22.

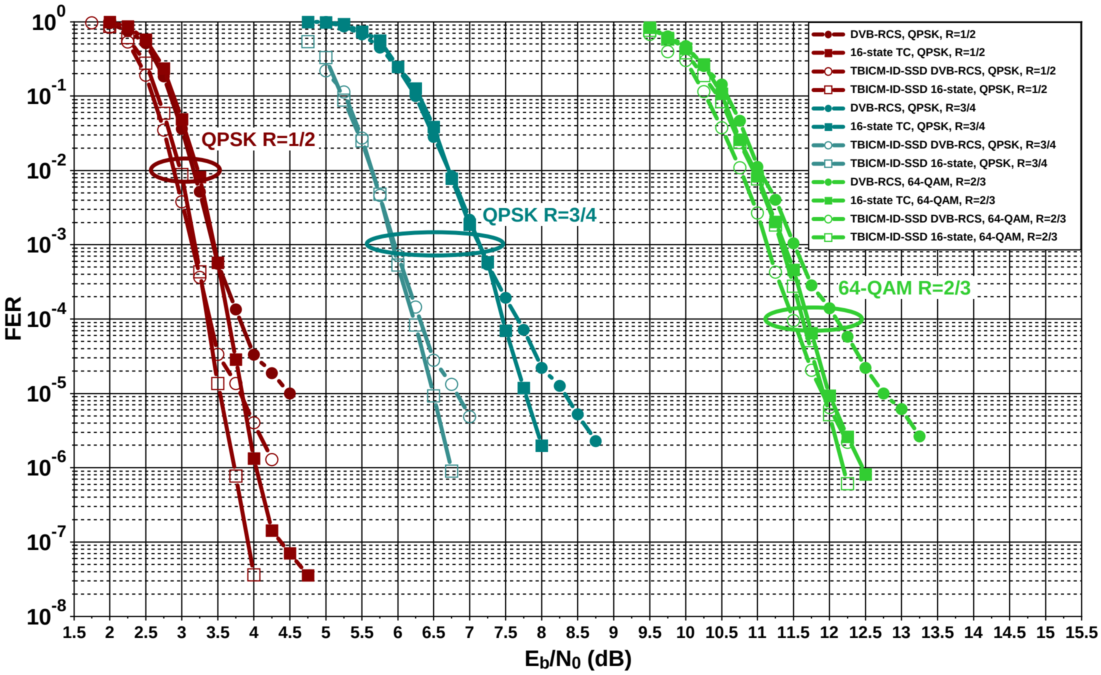

Figure 2.20 — FER performance of DVB-RCS, its extension to 16-state TBICM and TBICM-ID-SSD for MPEG frames of 1504-information bit frames associated with QPSK $R = 1/2$ and $R = 3/4$, 64-QAM $R = 2/3$ over Rayleigh fading channels. Spectral efficiencies of 1.0 bpcu, 1.5 bpcu and 4.0 bpcu.

The main observations concerning the simulation results are summarized in table 2.3 for the DVB-RCS turbo code and in table 2.4 for the 16-state turbo code. Most of the comments regarding the long block transmission still apply for the MPEG frames.

Table 2.3 includes the FER values where a change in the slope has been observed, the waterfall improvement with respect to TBICM as well as the relative gain to TBICM in the error floor region measured in number of orders of magnitude.

For the 16-state turbo code, since no change in the slope was detected for the TBICM-ID-SSD scheme in all simulated cases, table 2.4 displays the FER values for the last simulated point. The remaining two columns report on one side the difference in waterfall performance with respect to TBICM and on the other side the FER value corresponding to a change in

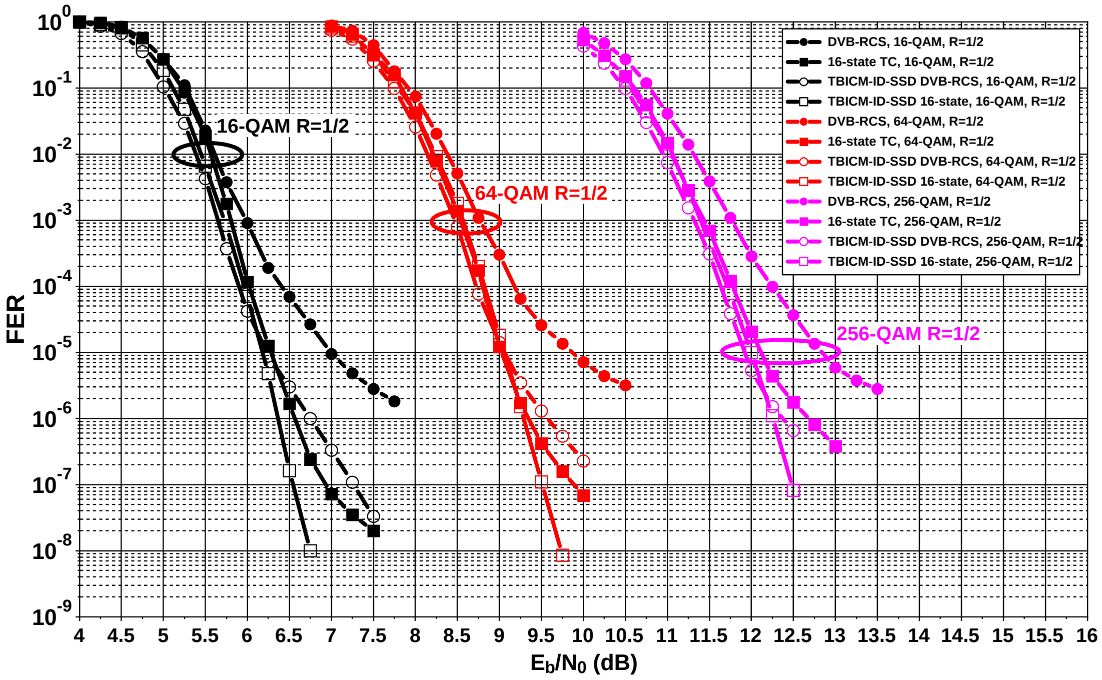

Figure 2.21 — BER performance of DVB-RCS, its extension to 16-state TBICM and TBICM-ID-SSD for MPEG frames of 1504-information bit frames associated with 16-QAM $R = 1/2$, 64-QAM $R = 1/2$ and 256-QAM $R = 1/2$ over Rayleigh fading channels. Spectral efficiencies of 2.0 bpcu, 3.0 bpcu and 4.0 bpcu.

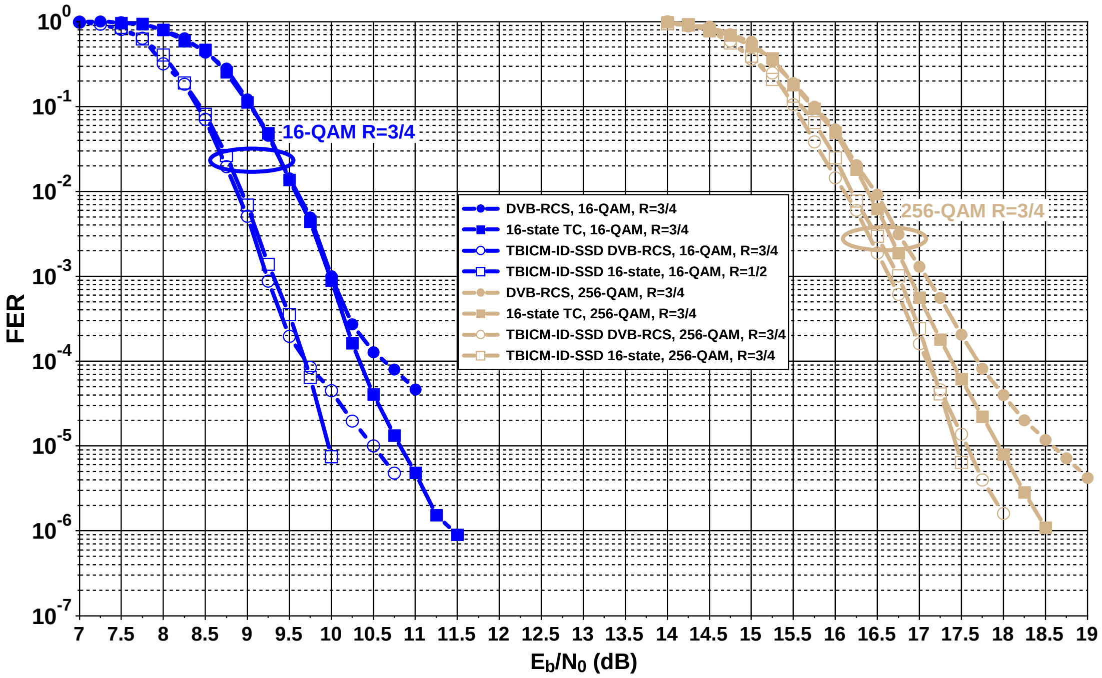

Figure 2.22 — BER performance of DVB-RCS, its extension to 16-state TBICM and TBICM-ID-SSD for MPEG frames of 1504-information bit frames associated with 16-QAM $R = 3/4$, 256-QAM $R = 3/4$ over Rayleigh fading channels. Spectral efficiencies of 3.0 bpcu and 6.0 bpcu.

TBICM-ID-SSD scheme using the DVB-RCS turbo code (short blocks)			
Modulation and Code rate	Slope change	Waterfall vs TBICM	Difference at slope change Vs TBICM
QPSK $R = 1/2$	$3.0{\cdot}10^{-5}$ of FER	-0.25 dB	-1.00 order(s)
QPSK $R = 3/4$	$3.0{\cdot}10^{-5}$ of FER	-1.20 dB	-0.75 order(s)
16-QAM $R = 1/2$	$8.0{\cdot}10^{-6}$ of FER	-0.30 dB	-1.75 order(s)
16-QAM $R = 3/4$	$2.0{\cdot}10^{-4}$ of FER	-0.75 dB	-
64-QAM $R = 1/2$	$1.0{\cdot}10^{-5}$ of FER	-0.20 dB	-1.00 order(s)
64-QAM $R = 2/3$	$1.0{\cdot}10^{-5}$ of FER	-0.30 dB	-1.25 order(s)
256-QAM $R = 1/2$	$5.0{\cdot}10^{-6}$ of FER	-0.40 dB	-2.00 order(s)
256-QAM $R = 3/4$	$3.0{\cdot}10^{-6}$ of FER	-0.40 dB	-2.00 order(s)

Table 2.3 — Gap to capacity, slope change, waterfall and floor difference for DVB-RCS coded TBICM-ID-SSD with respect to TBICM for the transmission of short blocks.

TBICM-ID-SSD scheme using a double-binary 16-state turbo code (short blocks)			
Modulation and Code rate	Slope change lower than	Waterfall vs TBICM	TBICM slope change at
QPSK $R = 1/2$	$3.0{\cdot}10^{-8}$ of FER	-0.30 dB	$1.5{\cdot}10^{-7}$ of FER
QPSK $R = 3/4$	$9.0{\cdot}10^{-7}$ of FER	-1.20 dB	$2.0{\cdot}10^{-6}$ of FER
16-QAM $R = 1/2$	$1.0{\cdot}10^{-8}$ of FER	-0.10 dB	$2.3{\cdot}10^{-7}$ of FER
16-QAM $R = 3/4$	$7.0{\cdot}10^{-6}$ of FER	-0.75 dB	$2.0{\cdot}10^{-6}$ of FER
64-QAM $R = 1/2$	$8.0{\cdot}10^{-9}$ of FER	-	$2.0{\cdot}10^{-6}$ of FER
64-QAM $R = 2/3$	$6.0{\cdot}10^{-7}$ of FER	-	$8.0{\cdot}10^{-6}$ of FER
256-QAM $R = 1/2$	$8.0{\cdot}10^{-8}$ of FER	-	$4.0{\cdot}10^{-6}$ of FER
256-QAM $R = 3/4$	$6.0{\cdot}10^{-6}$ of FER	-0.10 dB	$1.0{\cdot}10^{-6}$ of FER

Table 2.4 — Gap to capacity, slope change, waterfall and floor difference for 16-state turbo coded TBICM-ID-SSD with respect to TBICM for the transmission of short blocks.

the slope of the TBICM scheme. Note that for the two cases of the QPSK and 256-QAM modulations with code rate $R = 3/4$, the TBICM scheme did not exhibit a change in the slope for the lowest simulated points. Consequently we have opted for reporting the FER values for the lowest simulated points.

As in the long frame case, one can observe that the improvement in the waterfall region is generally lower with the 16-state turbo code than with the DVB-RCS code. In return, the error floor lowering exceeds in some cases 2 orders of magnitude. Note that in the 64-QAM $R = 1/2$ case, there is no longer any degradation of the TBICM-ID-SSD with respect to TBICM in the waterfall region.

With a reasoning based on the one in section 2.3.3, we can say that for short frame sizes the curves related to the TBICM schemes in the waterfall region have less steep slopes than in the case of the transmission of long blocks. Consequently, the operating region of interest in terms of E_b/N_0 values for the uncoded modulation curves becomes wider, thus increasing the potential improvement in performance for the RQD-demodulator with respect to the classical one. Therefore, the slope difference between the TBICM-ID-SSD and TBICM schemes is greater for short frames than for long frames and the improvement of TBICM-ID-SSD with respect to TBICM grows larger with E_b/N_0 than in the long frame transmission case.

It is also worthwhile mentioning that in several cases corresponding to high modulation orders and/or coding rates, the TBICM-ID-SSD scheme based on the DVB-RCS code performs better than the standard TBICM scheme using the 16-state turbo code both in the waterfall and in the floor regions, with an implementation complexity of the receiver that is around half the complexity of the classical TBICM receiver.

For all modulation schemes, FER lower than 10^{-5} are attained without any change in the slope. In some cases, like QPSK, 16-QAM and 64-QAM modulations with $R = 1/2$, FER values equal to 10^{-8} have been reached.

In brief, TBICM-ID-SSD performs better with short frames than with long frames, since the potential relative gain of TBICM-ID-SSD schemes with respect to TBICM increases when the frame size decreases.

2.4.4 Performance of TBICM-ID-SSD schemes over Rician fading channels

When a Line Of Sight (LOS) exists between the transmitter and the receiver, the fading is modeled by a Rician distribution [7, 50] as expressed in section 1.1.2. The ratio of the LOS path with respect to the mean local power K becomes an important parameter. The Rician distribution model can be used to describe both the Gaussian channel when $K = \infty$, and the Rayleigh fading channel when $K = 0$.

Since TBICM-ID-SSD shows the same error correcting performance as TBICM over Gaussian channel and improves it over Rayleigh fading channel, we expect to obtain an improvement in error correcting performance over Rician fading channel to an extent reflecting a halfway behavior between these extreme cases.

BER Monte Carlo simulations were undertaken for the 16-QAM, $R = 3/4$, DVB-RCS coded TBICM-ID-SSD and TBICM for the transmission of 16,000-information bit frames. Simulation results corresponding to a typical indoor environment with a value of $K = 0.25$ ($K_{dB} = 6.0$ dB) are plotted in fig. 2.23.

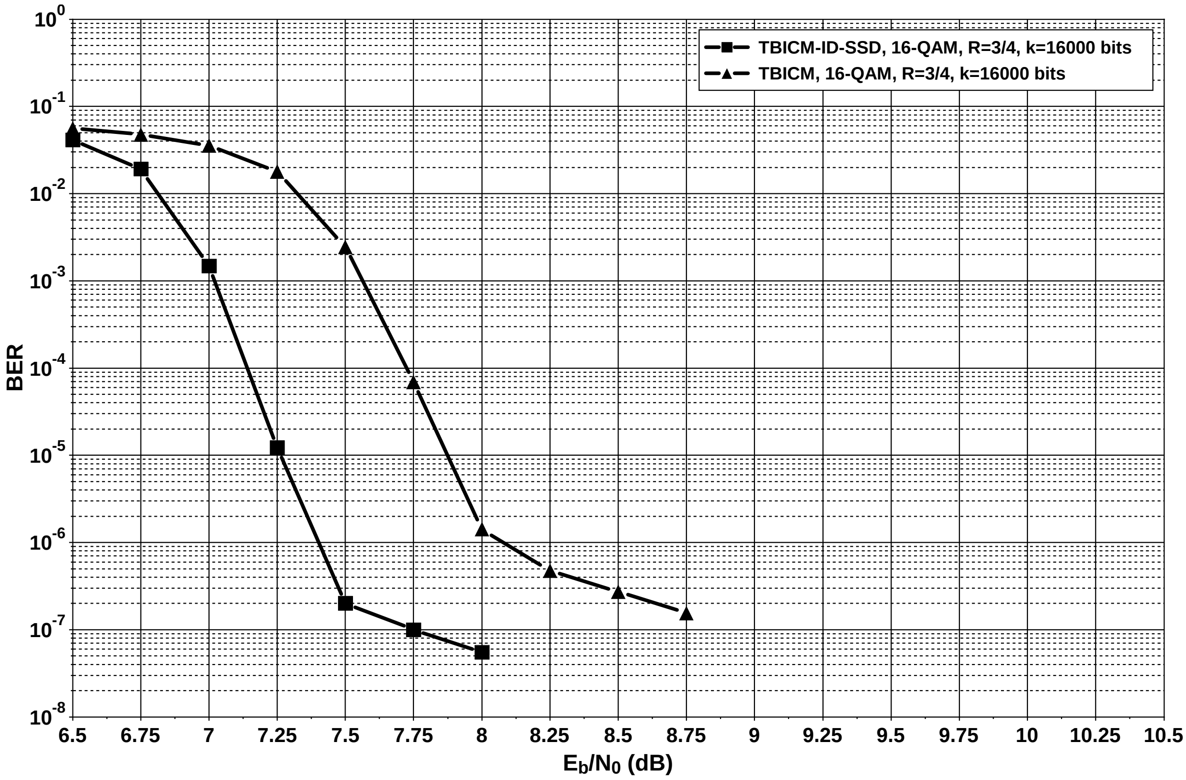

Figure 2.23 — BER comparison of TBICM and TBICM-SSD. Systematic, $R = 3/4$ DVB-RCS code, 16-QAM for 16000 information bit-frames over Rician fading channels with $K = 6$ dB.

If we compare these results with those obtained over Rayleigh fading channel in fig. 2.18, we can observe that the improvement in error correcting performance of TBICM-ID-SSD with respect to TBICM is practically at the same level for both fading channel types: around 0.75 dB in convergence and an error floor lowered by one order of magnitude.

In conclusion, TBICM-ID-SSD seems to offer similar levels of improvement of error correcting performance over Rician channel as over Rayleigh channel. These levels should be lower though as we tend toward a Gaussian channel.

2.5 Conclusion

In this chapter, we have provided solutions intended for improving existing coding solutions for high order modulations over fading channels. Previous works have proven that the diversity order plays the leading role in error correcting performance. We have revisited existing contributions for doubling the diversity order. They involve the introduction of simple modifications to the modulator and the demodulator. We have investigated the impact of its association with powerful error correcting codes like turbo codes in a BICM scenario. After a thorough investigation of the proposed contribution, we have seen that the use of an additional iterative process at the receiver side enables us to fully take advantage of the proposed diversity increase method. In fact, in most treated cases, we have observed by means of Monte Carlo simulations that an improvement in error correcting performance of turbo coded high order modulations is achieved in both waterfall and floor regions. This comes at the price of a small increment in complexity.

We have proven by means of EXIT charts and uncoded error rate curves that this improvement increases with the code rate somehow compensating the weakness of convolutional turbo codes.

We would like to mention that our solution has been adopted as a mean of improving performance in the context of the forthcoming DVB-T2 standard. Work perspectives include deriving bounding techniques for the proposed contribution in addition to extending it to a broader family of codes and to realistic fading channel models elaborated in the context of the DVB-T2 and DVB-H2 standards.

Part II

Coded continuous phase modulation schemes for satellite transmissions

The work presented in this second part of the manuscript has been carried out within the framework of the Study of enhanced digital transmission techniques for Broadband Satellite Digital Transmissions (BSDT) project, funded by the European Space Agency. The obtained results are the fruit of a joint work with Dr. Alexandre Graell i Amat.

The BSDT project aims at designing advanced modem solutions for the triple play service provided via a satellite link. In telecommunications, triple play service is a marketing term for the provisioning of two broadband services, high-speed internet access and television, and one narrowband service, telephone, over a single broadband connection.

Technical solutions for satellite triple play services already exist. They involve Digital Video Broadcasting, Satellite, Second Generation (EN 302 307) (DVB-S2) systems [52] intended mainly for TV broadcast; they include as well DVB-RCS systems [53] offering interactive services like internet access, Wide Area Networking (WAN), telemedicine, video conferencing and Voice over Internet Protocol (VoIP). Other alternatives to interactive DVB-based systems exist such as the latest ESA two-way satellite system SATMODE [54]. It allows the connection of consumer TVs individually, both ways with their interactive TV content providers, with other consumers and with other infrastructures (Global System for Mobile communications (GSM) and internet) in real time. This two-way connectivity enables several new services to the viewer, like betting, chatting, MMS, e-mail, gaming, interactive advertising, personal data consultation/banking and statistics gathering ...

Nevertheless, the increasing needs in bandwidth for next generation services like interactive High Definition TV (HDTV), very high speed secure internet services or reliable video conferencing have pushed system designers toward the study of technical solutions better suited for the transmission channel. Two unquestionable qualifiers describe the satellite transmission channel in the context of BSDT: non-linear and band-limited. These characteristics logically lead into the investigation of improved spectral and power efficient modulation schemes.

In the context of coherent linear digital phase modulation techniques such as M-PSK or M-APSK schemes adopted in the DVB-S2 and DVB-RCS standards, the carrier phase exhibits abrupt changes at the start of every symbol. This causes a discontinuity that requires an important percentage of the power to occur outside of the intended frequency band (high fractional out-of-band power), leading to a limited spectral efficiency. This discontinuity can be avoided by adopting a Continuous Phase Modulation (CPM). It represents a method for phase modulation distinguished by a continuous carrier phase with respect to other digital phase-modulation techniques. Furthermore, CPM is typically implemented as a constant-envelope waveform, consequently the transmitted carrier power is constant. This feature makes CPM appealing when the transmitter amplifier is not perfectly linear. Therefore, CPM offers undeniable advantages consisting of high spectral efficiency thanks to the phase continuity and excellent power efficiency due to the partly constant-envelope waveform. These advantages make this type of modulation particularly interesting for band-limited systems employing non-linear power amplifiers as in the case of satellite communication systems.

Despite an enthusiastic interest by the international research community for CPM, it has so far been applied to only a limited number of applications. Among these, the Gaussian Minimum Shift Keying (GMSK) has been used in the GSM of most of the 2^{nd} generation cell phones worldwide, in the Wireless Local Area Network (WLAN) IEEE 802.11 standard using Frequency-Hopping Spread Spectrum (FHSS) and in Bluetooth. More spectral/energy efficient CPM schemes, which however imply a higher level of demodulation/decoding complexity, have not yet found their way to any commercial application. This is mostly due to the lack of maturity of digital signal processing chips at the time of the most intense research effort.

Recently, thanks to a new flourishing interest of literature on the topic of reduced complexity receivers for CPM together with the tremendous increase of processing power in consumer-grade equipments, a renewed interest in high spectral/energy efficient CPM modulated systems saw the light. The BSDT project follows this line of thought. In the context of this project, we have performed a study of high spectral/energy efficient coded CPM schemes designed in order to provide the error correcting performance required in next generation broadband satellite communications and that for a wide range of spectral efficiencies.

This part of the manuscript is divided into three chapters:

In chapter three, we start by a detailed description of the CPM followed by definitions concerning power, spectral efficiency, Euclidean distance and CPM error events.

Chapter four includes an in-depth study of coded CPM systems adapted for a broadband satellite link. In fact, coded CPM can be treated as a serial concatenation of an outer error correcting code and an inner code: the CPM itself. A wide choice of outer codes is available, from simple convolutional codes up to higher complexity turbo-like codes and block codes. The important number of CPM parameters and the presence of several possible outer code solutions have driven us to elaborate criteria for the selection of the set of parameters resulting into error correcting performance satisfying the BSDT project constraints.

We conclude in chapter five by presenting the results of the selection providing the parameters of a coded CPM system covering a wide range of spectral efficiencies. The obtained system offers the best compromise in terms of error correction and complexity.

CHAPTER 3

Continuous Phase Modulation

THIS chapter provides the technical background necessary for a successful in-depth study of CPM modulated systems.

It starts by a mathematical description of a CPM signal showing that the modulator can be derived into a linear time invariant continuous trellis encoder coupled with a memoryless mapper. The corresponding demodulator/detector has to incorporate a decoding structure based on the Viterbi or the BCJR algorithm for a successful maximum likelihood detection of the received signals.

It continues by describing the families of CPM pulse shapes that are covered in our study. In addition, definitions of the spectral efficiency, the theoretical limits, the Euclidean distance and the CPM error events are provided and will proove to be of great usefulness in designing coded CPM systems with good error correcting performance.

3.1 The CPM general description

The CPM is a phase modulation with a constant envelope. The description presented in this scope is compliant with [55].

The CPM transmitted signal can be expressed as:

$$s(t,\alpha) = \sqrt{\frac{2E}{T}}\cos(2\pi f_0 t + \varphi(t,\alpha) + \varphi_0) \tag{3.1}$$

where E is the symbol energy, T is the symbol time, f_0 is the carrier frequency, and φ_0 is an arbitrary constant phase shift which, without loss of generality, can be set to zero in the case of a coherent receiver. α is a sequence of uncorrelated data information symbols to be transmitted, all equiprobable and each taking one of the values:

$$\alpha_i = \pm 1, \pm 3, ..., \pm(M-1); \qquad i = 0, \pm 1, \pm 2, ... \tag{3.2}$$

The information carrying phase $\varphi(t,\alpha)$ can be written as:

$$\varphi(t,\alpha) = 2\pi h \int\limits_{-\infty}^{t} \sum_{i=-\infty}^{\infty} \alpha_i g(\tau - iT)d\tau; \qquad -\infty < t < \infty \tag{3.3}$$

The variable h is referred to as the *modulation index*. The amplitude of the baseband pulse $g(t)$ is chosen to give the maximum phase change $\alpha_i h\pi$ radians over each symbol interval when all the data symbols in the sequence α take the same value α_i.

To obtain a causal CPM system, frequency pulse $g(t)$ is chosen to satisfy:

$$\begin{cases} g(t) = 0; & t < 0 \text{ or } t > LT \\ g(t) \neq 0; & 0 \leq t \leq LT \end{cases} \tag{3.4}$$

where the pulse length L is measured in symbol intervals T. Defining the baseband phase response as:

$$q(t) = \int\limits_{-\infty}^{t} g(\tau)d\tau \tag{3.5}$$

$q(t)$ should be chosen to verify:

$$\begin{cases} q(t) = 0; & t < 0 \\ q(t) \neq 0; & 0 \leq t \leq LT \\ q(t) = 1/2; & t > LT \end{cases} \tag{3.6}$$

The CPM phase signal can be written as:

$$\varphi(t,\alpha) = 2\pi h \sum_{i=-\infty}^{\infty} \alpha_i q(t-iT); \qquad -\infty < t < \infty \tag{3.7}$$

Taking into account equ. 3.6 and the fact that finite frames of size N are transmitted, the phase signal up to symbol n can be rewritten as:

$$\varphi(t,\alpha_n) = \theta_n + \theta(t,\alpha_n) = \left(\pi h \sum_{i=0}^{n-L} \alpha_i\right) \mathrm{mod}(2\pi) + 2\pi h \sum_{i=n-L+1}^{n} \alpha_i q(t-iT) \tag{3.8}$$

θ_n can be seen as the phase state at time $n-L$ and $\theta(t,\alpha_n)$ as the phase function from time period $n-L$ up to time period n. In other words, we can say that for any symbol interval n, the phase $\varphi(t,\alpha_n)$ is uniquely defined by the current data symbol α_n, the correlative state vector $(\alpha_{n-1},\alpha_{n-2},...,\alpha_{n-L+1})$ and the phase state θ_n at symbol $n-L$.

In practice, rational modulation indexes are used such that:

$$h = \frac{k}{p} \tag{3.9}$$

where k and p are relatively prime positive integers. The values of θ_n are limited to $\left\{0, \frac{2\pi}{p}, ..., \frac{(p-1)}{p}2\pi\right\}$ and the CPM can be seen as a time variant trellis based modulation having a phase state defined by the vector $\partial_n = (\theta_n, \alpha_{n-1}, \alpha_{n-2}, ..., \alpha_{n-L+1})$. The current possible symbol values α_n can then be seen as trellis transitions.

Due to the presence of memory, a trellis based decoder is needed in order to detect CPM signals. It uses the trellis description of CPM signals having pM^{L-1} states each defined by a variant in the vector ∂_n. For a transmission over a Gaussian channel, the received complex signal at time t is:

$$r(t) = s(t,\boldsymbol{\alpha}) + n(t) \tag{3.10}$$

where $n(t)$ is a complex additive white Gaussian noise. We will denote by $\tilde{o}$ the estimated received version of variable o. The ML receiver maximizes :

$$\ln\left[P(r(t);\tilde{\alpha})\right] \simeq -\int_{-\infty}^{\infty} \left[r(t) - s(t,\tilde{\alpha})\right]^2 dt \tag{3.11}$$

which is equivalent to maximize the intercorrelation between the transmitted and received signals:

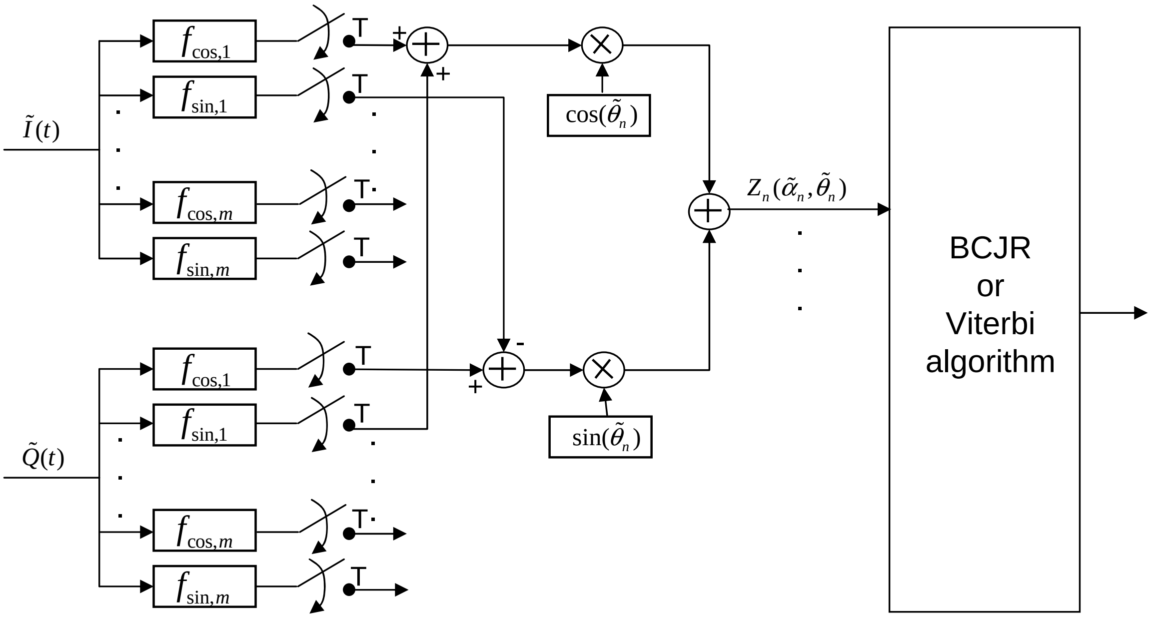

Figure 3.1 — The CPM receiver

$$J(\tilde{\alpha}) = \int_{-\infty}^{\infty} r(t)s(t,\tilde{\alpha})dt \tag{3.12}$$

The computation of $J(\tilde{\alpha})$ can be done recursively:

$$J_n(\tilde{\alpha}) = \int_{-\infty}^{(n+1)T} r(t)s(t,\tilde{\alpha})dt \tag{3.13}$$

with

$$J_n(\tilde{\alpha}) = J_{n-1}(\tilde{\alpha}) + Z_n(\tilde{\alpha}) \tag{3.14}$$

and

$$Z_n(\tilde{\alpha}) = \int_{nT}^{(n+1)T} r(t)\cos\left[w_0 t + \varphi(t,\tilde{\alpha})\right] dt \tag{3.15}$$

The metric $Z_n(\tilde{\alpha})$ represents the correlation between the received signal over the n^{th} symbol interval and an estimated signal from the receiver. This correlation is downsampled keeping a sample every $t = (n+1)T$. A metric for every different M^L input data sequences and p possible θ_n values constitute sufficient statistics. The resulting metric after downsampling becomes:

$$Z_n(\tilde{\alpha}_n, \tilde{\theta}_n) = \int\limits_{nT}^{(n+1)T} r(t) \cos\left[w_0 t + \theta(t, \tilde{\alpha}_n) + \tilde{\theta}_n\right] dt \tag{3.16}$$

Metrics $Z_n(\tilde{\alpha}_n, \tilde{\theta}_n)$ are fed into the decoder which applies the Viterbi algorithm in order to find the sequence maximizing the log-likelihood function up to the n^{th} symbol interval. When the CPM detector has to be embedded into an iterative receiver, a SISO detection algorithm has to be implemented. Classically, it consists of the Bahl, Cocke, Jelinek and Raviv (BCJR) algorithm [56]. The resulting receiver structure is presented in fig. 3.1.

In fact by using the basic quadrature detector, the received components are:

$$\begin{aligned} \tilde{I}(t) &= \sqrt{\frac{2E}{T}} I(t) + n_I(t) \\ \tilde{Q}(t) &= \sqrt{\frac{2E}{T}} Q(t) + n_Q(t) \end{aligned} \tag{3.17}$$

where $I(t)$ and $Q(t)$ designate the in-phase and quadrature components of the transmitted signal. $n_I(t)$ and $n_Q(t)$ represent the complex Gaussian noise with a double-sided power spectral density of $N_0/2$. Assuming a perfect coherent detection, metrics $Z_n(\tilde{\alpha}_n, \tilde{\theta}_n)$ can be written as:

$$\begin{aligned} Z_n(\tilde{\alpha}_n, \tilde{\theta}_n) = {} & \cos\tilde{\theta}_n \int\limits_{nT}^{(n+1)T} \tilde{I}(t) \cos\left[\theta(t, \tilde{\alpha}_n)\right] dt + \cos\tilde{\theta}_n \int\limits_{nT}^{(n+1)T} \tilde{Q}(t) \sin\left[\theta(t, \tilde{\alpha}_n)\right] dt \\ & + \sin\tilde{\theta}_n \int\limits_{nT}^{(n+1)T} \tilde{Q}(t) \cos\left[\theta(t, \tilde{\alpha}_n)\right] dt - \sin\tilde{\theta}_n \int\limits_{nT}^{(n+1)T} \tilde{I}(t) \sin\left[\theta(t, \tilde{\alpha}_n)\right] dt \end{aligned} \tag{3.18}$$

The pM^L metrics are then calculated by $4M^L$ filtering operations (the integral terms in equ. 3.18) of the received signal using $m = 2M^L$ different baseband filters with impulse responses:

$$f_{\cos}(t, \tilde{\alpha}_n) = \begin{cases} \cos(2\pi h \sum_{j=-L+1}^{0} \tilde{\alpha}_j q((1-j)T - t)); & 0 \leq t \ \leq T \\ 0; \qquad t < 0 \quad \text{or} \quad t > T \end{cases}$$

and

$$f_{\sin}(t, \tilde{\alpha}_n) = \begin{cases} \sin(2\pi h \sum_{j=-L+1}^{0} \tilde{\alpha}_j q((1-j)T - t)); & 0 \leq t \ \leq T \\ 0; \qquad t < 0 \quad \text{or} \quad t > T \end{cases} \tag{3.19}$$

Rimoldi in [57] was able to decompose CPM modulator into a time invariant linear continuous trellis encoder part and a memoryless mapper. This decomposition will be detailed in the following section.

3.2 The Rimoldi decomposition of CPM

The description of the decomposition of CPM into a linear time invariant continuous trellis encoder and a memoryless mapper presented in fig. 3.2 is compliant with the description in [57]. It offers two main advantages:

- It allows the CPM "encoding" operation to be studied independently of the signal mapping. This suggests an alternative realization of the CPM. Now, it consists of a Continuous Phase Encoder (CPE) and a Memoryless Mapper (MM). The former presents the advantages of being time invariant and linear over ring algebraic structures. As a consequence, it can be studied with the same techniques as those used for convolutional codes.
- It isolates the MM. Consequently, the cascade of the MM, the waveform channel (white additive Gaussian noise) and the demodulator that operates over one symbol time interval can be seen as a classical discrete memoryless channel (see fig. 3.2).

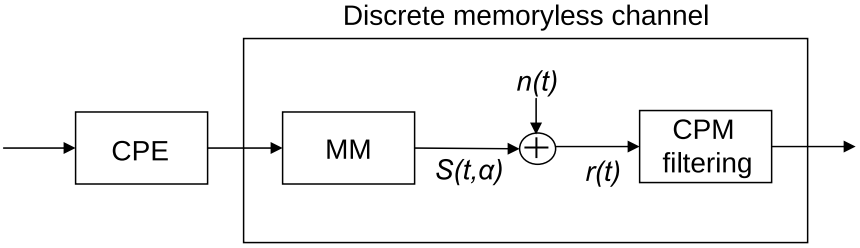

Figure 3.2 — The CPE and the discrete memoryless channel representation of CPM

Rimoldi proved that by taking a particular phase path in the time varying trellis as a reference phase, and expressing all the remaining phase paths with respect to it, the phase trellis is time invariant. A "modified" phase path is called *tilted phase* [58] and obtained by:

$$\psi(t, \alpha) = \varphi(t, \alpha) + \pi h(M-1)\frac{t}{T} \tag{3.20}$$

where $\varphi(t, \alpha)$ is the traditional phase. In addition to the tilted phase, Rimoldi introduces the "modified" data sequence as follows:

$$U_i = \frac{(\alpha_i + (M-1))}{2} \tag{3.21}$$

where $U_i \in \{0, 1, ..., M-1\}$. The symbols of the modified data sequence simply become M-ary digits.

After some mathematical operations, the tilted phase in the time interval n $(t = \tau + nT)$ can be written as:

$$\psi(\tau + nT) = \left[\underbrace{2\pi h \left[\left(\sum_{i=0}^{n-L} U_i \right) \mathrm{mod}(P) \right]}_{\text{data only dependent term } \theta_n} + \underbrace{4\pi h \sum_{i=0}^{L-1} U_{n-i} q(\tau + iT)}_{\text{data and pulse dependent}} + \underbrace{W(\tau)}_{\text{data independent}} \right] \mathrm{mod}(2\pi) \tag{3.22}$$

$$\tag{3.23}$$

where $0 \leq \tau < T$ and

$$W(\tau) = \pi h(M-1)\frac{\tau}{T} - 2\pi h(M-1)\sum_{i=0}^{L-1} q(\tau + iT) + \pi h(M-1)(L-1) \tag{3.24}$$

is a data independent term (absence of U_i terms). $W(\tau)$ can be omitted for error rate simulation purposes. In fact, the tilted phase is a linear function of the input sequence whose "modified" alphabet contains the zero symbol element. Therefore, when the input sequence is the zero sequence, all data-dependent terms vanish. There remains only data independent term $W(\tau)$. If the derivative of $W(\tau)$ depends on τ, the transmitted signal frequency is subject to a periodic data-independent variation that wastes bandwidth. Therefore, the choice of the frequency (respectively phase) pulse should ensure that the derivative of $W(\tau)$ is a constant term. Pulses considered in this study, addressed in section 3.3 are designed to respect this constraint.

The data only dependent term in equ. 3.22 represents the phase state θ_n and the recursive output of the CPE (see fig. 3.3). The data and pulse dependent term represents the input of the MM.

The transmitted carrier based signal over the n^{th} interval $(t = \tau + nT)$ is then defined by:

$$s_c(\tau + nT) = \mathrm{Re}\left[s(\tau + nT) \exp(j\left[2\pi f_1(\tau + nT)\right]) \right] \tag{3.25}$$

where

$$s(\tau + nT) = \sqrt{\frac{2E}{T}}\exp(j\psi(\tau + nT)) \tag{3.26}$$

is the baseband signal and

$$f_1 = f_0 - \frac{h(M-1)}{2T} \tag{3.27}$$

is the tilted carrier frequency.

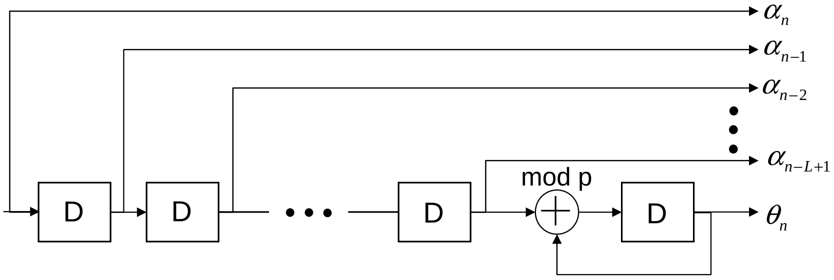

Figure 3.3 — The continuous phase encoder CPE

As for the receiver, the detection method presented in the previous section still applies, operating on the resulting time invariant trellis of the Rimoldi decomposition.

3.3 CPM schemes under consideration

Our study of CPM signals in the framework of project BSDT is limited to two subclasses of partial response ($L > 1$) CPM:

- Raised Cosine (RC) family of frequency pulses with the following expression:

$$g(t) = \begin{cases} \dfrac{1}{2LT}\left(1 - \cos\left[\dfrac{2\pi t}{LT}\right]\right); & 0 \leq t \leq LT \\ 0 & \text{otherwise} \end{cases} \tag{3.28}$$

$g(t)$ is a raised cosine over L symbol intervals leading to the following phase pulse response:

$$q(t) = \begin{cases} 0\ ; & t < 0 \\ \dfrac{1}{2}\left(\dfrac{t}{LT} - \dfrac{1}{2\pi}\sin\left[\dfrac{2\pi t}{LT}\right]\right); & 0 \leq t \leq LT \\ 1/2\ ; & t > LT \end{cases} \tag{3.29}$$

The subclass under study is then obtained by varying M, L and the modulation index h. It is denoted by (B for binary or Q for quaternary or O for octal alphabet)-LRC.

- Spectrally Raised Cosine frequency (SRC) pulses, in other words, the Fourier transform of the frequency pulse $g(t)$ is raised cosine shaped:

$$G(f) = F\{g(t)\} = \begin{cases} \dfrac{LT}{4}\left(1+\cos\left[\dfrac{\pi Lt}{2\beta}\,|f| - \dfrac{1-\beta}{LT}\right]\right); & \dfrac{1-\beta}{LT} < |f| \leq \dfrac{1+\beta}{LT} \\ 0 & \text{otherwise} \end{cases} \tag{3.30}$$

The resulting frequency pulse is :

$$g(t) = \frac{1}{LT}\frac{\sin\left(\dfrac{2\pi t}{LT}\right)}{\dfrac{2\pi t}{LT}}\frac{\cos\left(\beta\dfrac{2\pi t}{LT}\right)}{1-\left(\dfrac{4\beta}{LT}t\right)^2} \tag{3.31}$$

where $0 \leq \beta \leq 1$ is the roll-off factor. In order to compute the phase response, equ. 3.5 should be applied. This integration is quite cumbersome for any value of β. For some particular values of the roll-off factor, simplifications are possible and an analytical expression can be obtained. For instance, when $\beta = 1$, the phase response becomes:

$$q(t) = \begin{cases} q_1\left(\dfrac{LT}{2}\right) - q_1\left(\dfrac{LT}{2} - t\right); & 0 \leq t \leq \dfrac{LT}{2} \\ q_1\left(\dfrac{LT}{2}\right) + q_1\left(t - \dfrac{LT}{2}\right); & 0 \leq t \leq \dfrac{LT}{2} \\ 1/2\ ; & t > LT \end{cases} \tag{3.32}$$

where

$$q_1(t) = \frac{1}{8\pi}\left[2S\left(\frac{4\pi t}{LT}\right) + S\left(\pi\frac{4t-LT}{LT}\right) + S\left(\pi\frac{4t+LT}{LT}\right)\right] \tag{3.33}$$

and

$$S(x) = \int_0^x \frac{\sin t}{t}dt \tag{3.34}$$

is the sinus integral of x. The resulting subclass of CPM is denoted by (B or Q or O)$-L$SRC.

3.4 Computation of the spectral efficiency of CPM

As nowadays telecommunication applications require high rates, spectral efficiency defined as the actual transfer rate of a transmission system represents an important parameter.

In order to assess the spectral efficiency of a CPM, we first need to compute its Power Spectral Density (PSD). Several methods exist: we can mention the periodogram method described in [59]. This method first computes the Fourier transform of several observation windows of the signal at hand. Then it proceeds to an averaging of the obtained transform values. This is a rather cumbersome operation: in order to achieve an accurate estimation, averaging on a large number of windows is needed. A semi-analytical method for PSD estimation based on the autocorrelation of CPM signals is proposed in [55]. It requires a lower number of resources when compared to the periodogram method. Consequently, it has been used in our study.

The PSD of a CPM signal is then given by [55]:

$$S(f) = 2\,\mathrm{Re}\left\{ \int_0^{LT} R(\tau)\exp(-j2\pi f\tau)d\tau + \frac{\exp(-j2\pi fLT)}{1 - C_\alpha \exp(-j2\pi fT)} \int_0^{T} R(\tau + LT)\exp(-j2\pi f\tau)d\tau \right\} \tag{3.35}$$

where the autocorrelation function $R(\tau)$ is calculated over the interval $[0, (L+1)T]$ using the following equation:

$$\begin{aligned} R(\tau) &= R(\tau' + m_t T) && (3.36)\\ &= \frac{1}{T}\int_0^{T} \prod_{i=1-L}^{m_t+1} \left\{ \sum_{k=-(M-1)\text{ for } k \text{ odd}}^{M-1} P_k \exp\Big(j2\pi hk\Big[q(t+\tau' - (i-m_t)T) - q(t-iT)\Big]\Big) \right\} dt \end{aligned}$$

with $m_t = \left\lfloor \frac{\tau}{T} \right\rfloor$ where $\lfloor \epsilon \rfloor$ represents the integer part of ϵ. The probability $P_k = 1/M$ for equiprobable symbol sources. The decay constant (independent of τ) C_α in equ. 3.35 is computed by:

$$C_\alpha = \sum_{k=-(M-1)\text{ for } k \text{ odd}}^{M-1} P_k \exp(j2\pi hkq(LT)) \tag{3.37}$$

Fig. 3.4 shows the PSD of four CPM signals as a function of the normalized frequency fT where f denotes the frequency. The following CPM schemes were investigated: Minimum Shift Keying (MSK), Q2RC $h = 1/4$, O3RC $h = 1/7$, Q3SRC $h = 1/7$.

The total power of the transmitted signal can be computed using the PSD by:

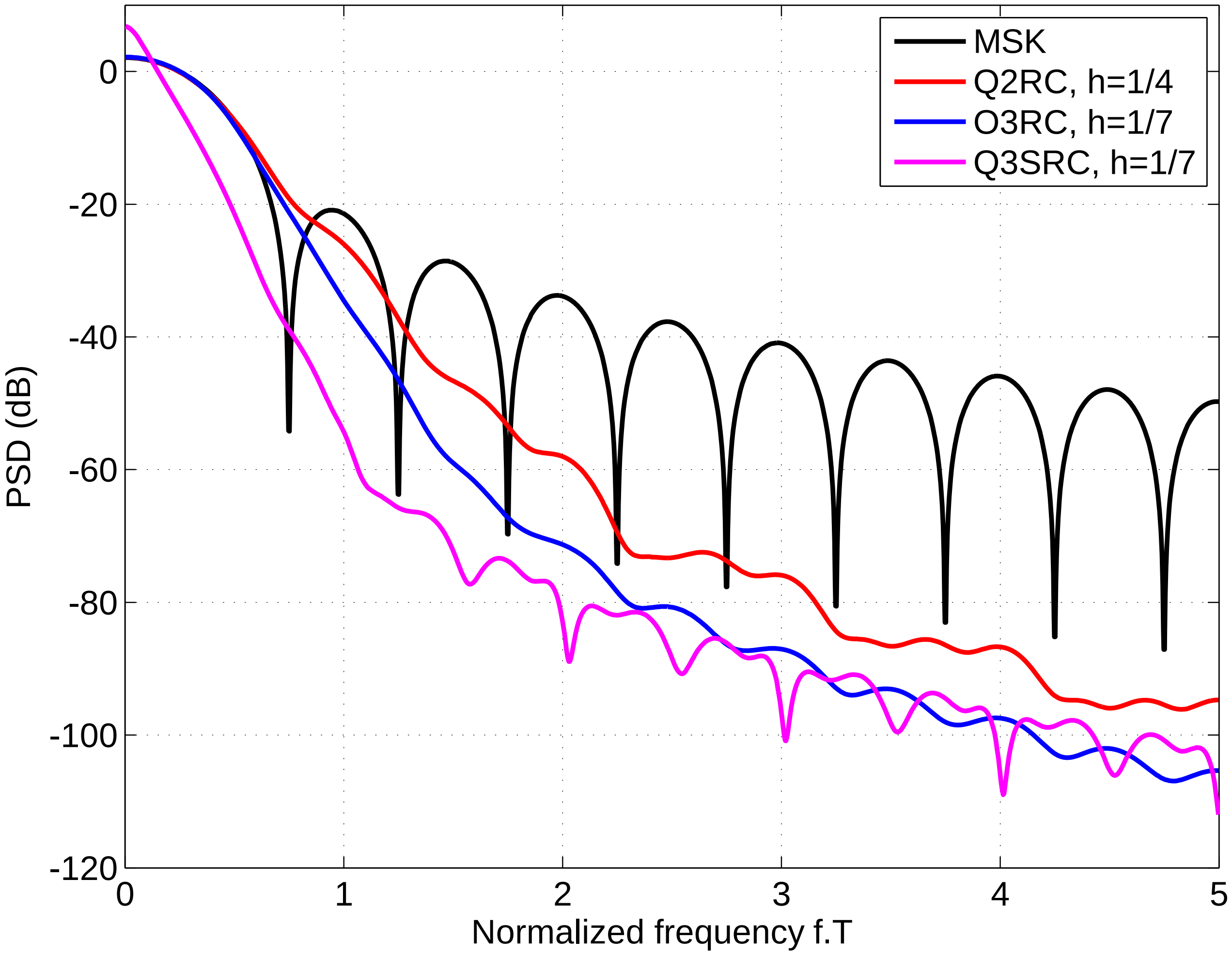

Figure 3.4 — Power spectral density as a function of the normalized frequency of four different CPM schemes

$$Pow_t = \int_{-\infty}^{+\infty} S(f)df \tag{3.38}$$

When the available bandwidth is limited, only the power within this defined bandwidth is of interest:

$$Pow_B = \int_{-BT/2}^{+BT/2} S(f)df \tag{3.39}$$

The fractional Out of Band Power (OBP), generally expressed in dB, is defined as the amount of power outside the defined bandwidth and is given by:

$$P_{OBP}(in\ dB) = 10\log_{10}\left(1 - \frac{Pow_B}{Pow_t}\right) \tag{3.40}$$

The signal bandwidth is then defined as X-dB bandwidth with:

$$\text{X dB bandwidth} = B\,|_{P_{OBP}=-X\;dB} \tag{3.41}$$

In our study, we have adopted the bandwidth measurement proposed in [55] as the 99% in-band power, equivalent to the 20 dB bandwidth of equ. 3.41.

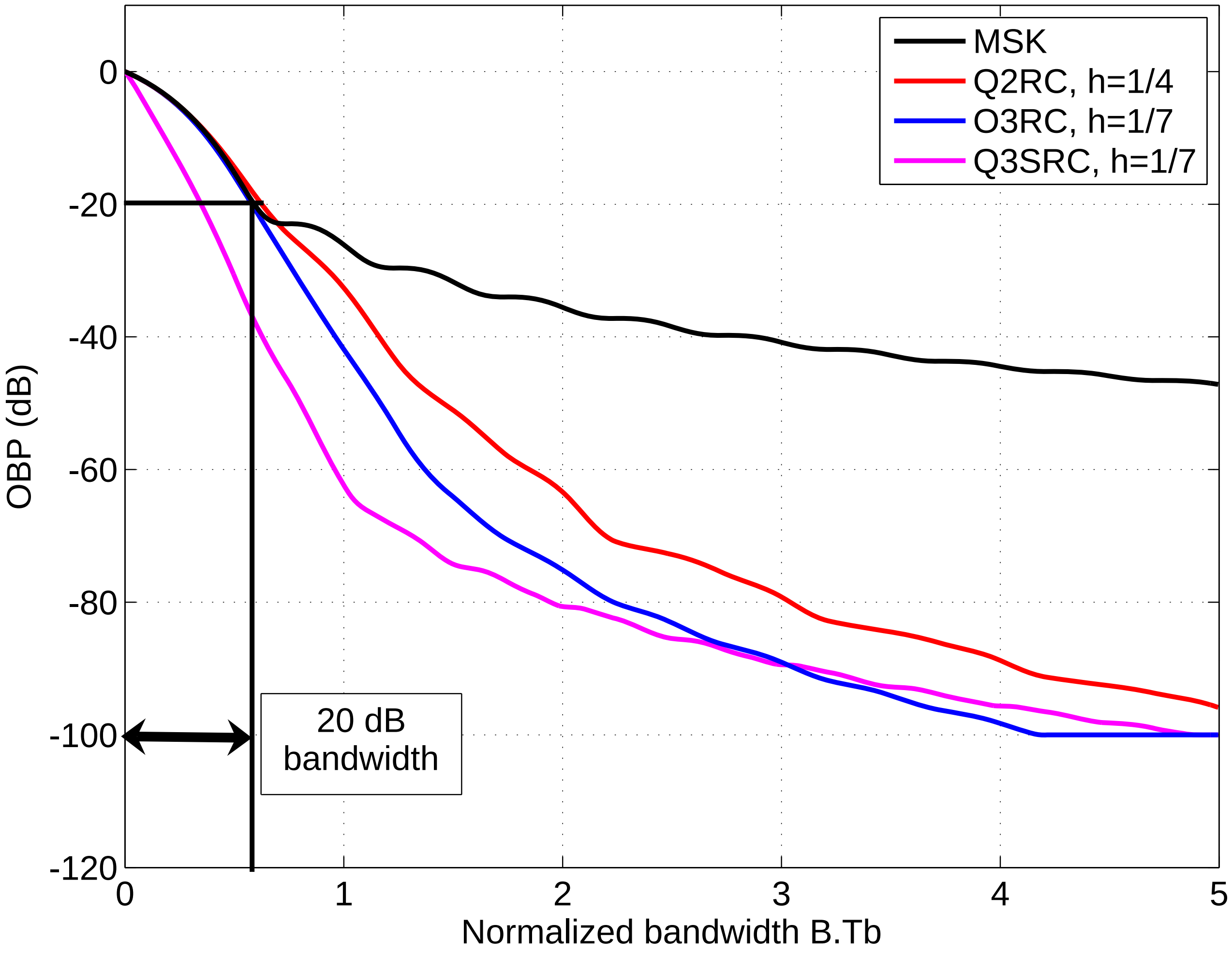

Figure 3.5 — Out of band power as a function of the normalized bandwidth of CPM schemes of fig. 2.4

Fig. 3.5 shows the OBP of four different CPM schemes as a function of the bandwidth normalized to the CPM symbol rate: MSK, Q2RC $h = 1/4$, O3RC $h = 1/7$, Q3SRC $h = 1/7$. Note that the Q3SRC CPM occupies less 99% bandwidth than the other CPM schemes as indicated in fig. 3.5.

Since the Symmetric Information Rate (SIR) (a capacity equivalent, details and description in the following section) is upper bounded by $\log_2 M$, the Spectral Efficiency (SE) of a coded CPM with outer code rate R can be upper bounded by:

$$SE = \frac{SIR}{B \cdot T} \leq R \cdot \frac{\log_2 M}{B \cdot T} = \frac{R}{B \cdot \dfrac{T}{\log_2 M}} = \frac{R}{B \cdot T_b} \qquad \text{in bps/Hz} \tag{3.42}$$

Where $1/T_b$ denotes the normalized bitrate. This bound is tight at high SNR. It will be used as means of SE computation in our study.

3.5 Capacity and information rate of CPM schemes

The capacity of a channel is given by the maximum of the mutual information between the input and output of the channel, where the maximization is with respect to the input distribution. It offers an insight into the maximum spectral efficiency achievable with a reliable transmission.

The classical capacity computation of AWGN channels by Shannon [2] does not directly apply for CPM mainly because of the modulator memory. Nevertheless, methods of capacity computation for channels with memory exist [60] and could be applied in this case. These methods rely on defining the channel as a finite state machine with a deterministic number of states. In fact, considering CPM as a finite state machine represents a direct application of the Rimoldi decomposition of CPM signals as described in the previous section. Other bottlenecks exist though:

- No analytical expression of the channel entropy rate for signals with memory is known to date, even for the simplest hidden Markov processes.
- In Independent Discrete Memoryless Channels (IDMC) with binary inputs, it was shown that the choice of codeword letters equiprobably and independently constitutes a valid assumption [10]. In the case of CPM signals (channel with memory), capacity computation involves optimizing the distribution of the symbol sequences at the input of the modulator. In this case, no theoretically proven hypothesis on the choice of the distribution of symbol exists. In fact, it is not clear if the individual α_i should be selected independently, and for non binary $M-$ary alphabets, should be selected equiprobably.

Due to all of these difficulties, the SIR is evaluated instead of the channel capacity. It predicts the limit on the bandwidth efficiency of error free transmission, assuming an equiprobable and uniform distribution of the modulation symbols.

In fact, studies of IDMCs [10] have shown that information rate often places little difference between the uniform and the optimal non-uniform distribution. Assuming that this still applies in the case of CPM signals, independent equiprobable symbol sequences are used for SIR computation.

As for the channel entropy evaluation problem, a measurement could be done via simulation relying on the Shannon-McMillan-Breimann algorithm [60]. It ensures the convergence with a probability of 1.0 of:

$$H(Y_I) \simeq -\frac{1}{N^s} \log[f(Y_I^{N^s})] \tag{3.43}$$

where $Y_I^{N^s}$ is a finite state machine representation of the signal at the channel output corresponding to the modulator input frame. $f(Y_I^{N^s})$ is the probability density function of the N^s-symbol channel output Y_I observed in simulation and $H(Y_I)$ is the entropy rate of Y_I.

In other words, if we generate a sequence of realizations of $Y_I^{N^s}$, and compute the right hand side of equ. 3.43, it will converge to the entropy rate of Y_I with a probability of 1. The computation of the probability density function $f(Y_I^{N^s})$ is quite complicated. The authors of [61] proposed a method for the computation of $f(Y_I^{N^s})$ based on the BCJR algorithm. They went further to apply it for CPM signals where they provided SIR results for some schemes. We have adopted the proposed approach in [61] for SIR computation in our study.

In fig 3.6[1], the results of SIR computation for quaternary CPM schemes with different values of L and h can be seen. Notice that between 0.5 and 1.6 bps/Hz many quaternary schemes offer almost identical SIRs. These systems are then indistinguishable from the SIR point of view. Fig 3.7[1] shows octal CPM SIR for different parameters. In this case, the systems between 1.0 and 2.5 bps/Hz are the ones with comparable SIRs.

The SIR computation assumes infinite codeword length. For finite codeword length N^s, Shannon derived a lower bound on the probability of codeword error over the AWGN channel in [2] known as the sphere-packing bound. In his setting, each code symbol takes real values, and all the codewords are distributed over the N^s-dimensional sphere. The additional SNR required in dB (compared with the computed SIR) for the system to operate at symbol rate T with information block size N^s and probability of codeword error P_{cod} could be computed by [14]:

$$\Delta \left(\frac{E_b}{N_0}\right)_{dB} \geq \sqrt{\frac{SE}{2N^s}\left(\frac{40}{\ln 10}\right)\left(\frac{2^{SE}+1}{2^{SE}-1}\right)(P_{cod}^{-1})_{dB}} \tag{3.44}$$

where SE is the spectral efficiency in bps/Hz. Although this penalty term is originally derived for the AWGN channel without any modulation constraint, it still gives us a simple and insightful estimation on the practical limit of the modulation constrained AWGN channel. Adding the expression in equ. 3.44 to the SIR value, we can compute a bound on the

---

[1] Capacity figures are courtesy of Daniel Delaruelle from NEWTEC company

required SNR for a coded system to operate at a specific code rate, given the codeword length, and the probability of codeword error. This estimate is defined as the Penalized Symmetric Information Rate (PSIR) in [61] of the modulation constrained AWGN channel. The accuracy of the PSIR depends on the modulation constraints. Intuitively, the modulation scheme which could distribute the codewords uniformly over the N^s-dimensional sphere should have performance close to the PSIR. Otherwise, additional gap to the SIR is expected.

3.6 CPM error events and normalized squared Euclidean distance

3.6.1 CPM error events

Since we are interested in the error correcting capability of CPM, it is useful to clearly define CPM error events. Errors of a CPM differ from the ones of a linear modulation by the fact that they should satisfy particular conditions due to the CPM memory and to the non-linearity of CPM pulses.

And since the CPE is a convolutional code over rings, an error event starts when the detected path through the trellis leaves the one given by the transmitter. It ends when the two paths remerge into the same ending state. Since CPM does not satisfy the Uniform Error Property (UEP) [24], the zero state cannot be assumed as a reference. Consequently, to study CPM error events, we have to consider all possible pairs of detected and transmitted paths. To that end, it is convenient to use the so-called difference symbol sequence instead. It is defined as:

$$\tilde{\mathbf{V}} = \{\tilde{V}_{n-L+1}, ..., \tilde{V}_{n-1}\} \quad \text{where} \quad \tilde{V}_i = U_i - \tilde{U}_i \quad \text{and} \quad n-L+1 \leq i \leq n-1 \tag{3.45}$$

U_i and $\tilde{U}_i$ denote the transmitted symbol and the received symbol at time i respectively. $\tilde{\mathbf{V}}$ represents the difference correlative state vector (see section 3.1).

$\tilde{V}_i$ is in the range $\{-M+1, ..., M-1\}$. Thus, expressed in a difference symbol sequence reasoning, an error event begins when a difference sequence leaves the all-zero path, and finishes when its path merges with the all zeros path for the first time. From [62] the condition for a non zero difference symbol sequence to form a CPM error event is:

$$\sum_i \tilde{V}_i \operatorname{mod}.P = 0 \tag{3.46}$$

Compound error events could also appear in CPM. They can be seen as two successive error events where the second starts immediatly after the end of the first one. We will denote

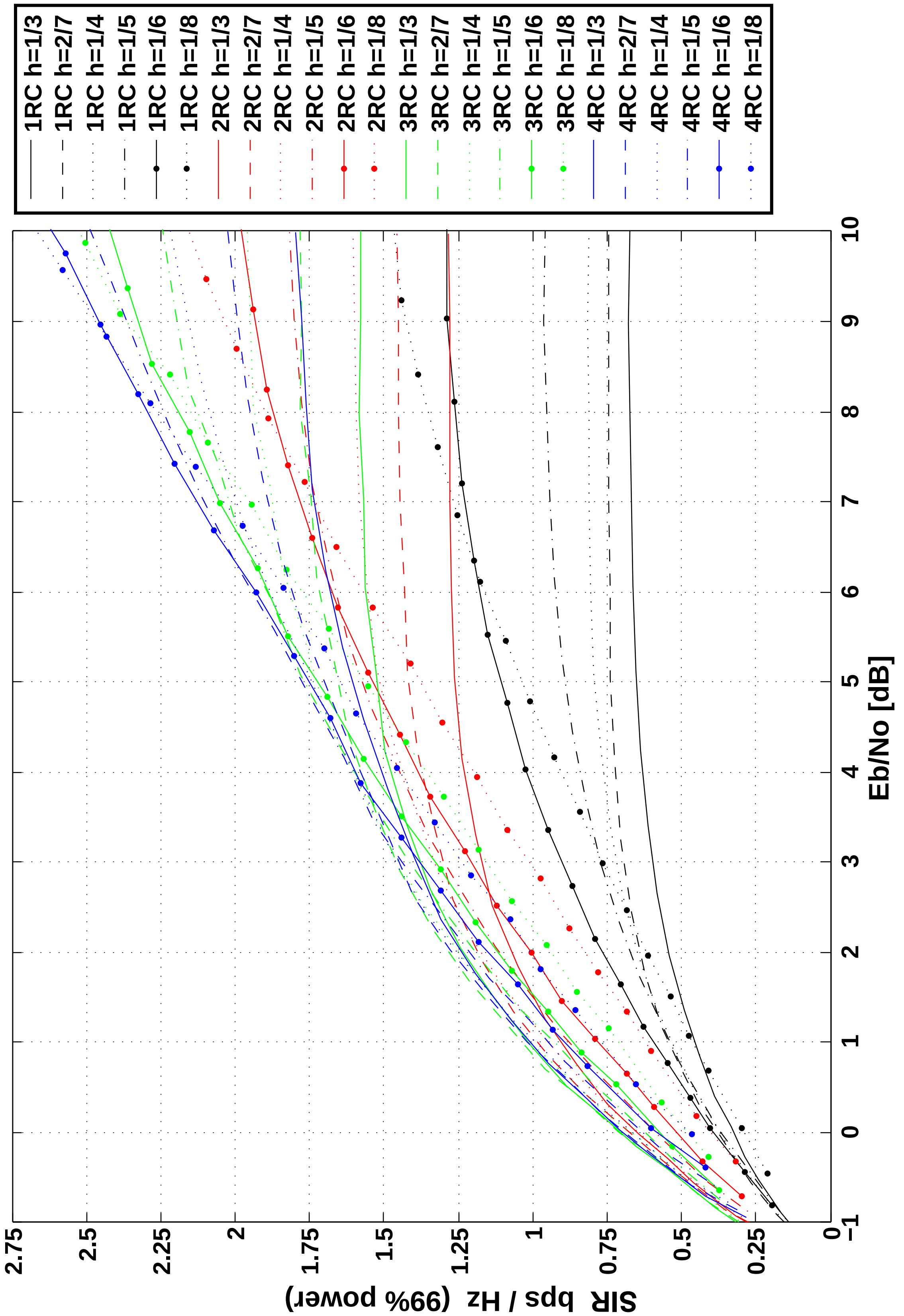

Figure 3.6 — SIR of quaternary alphabet LRC schemes

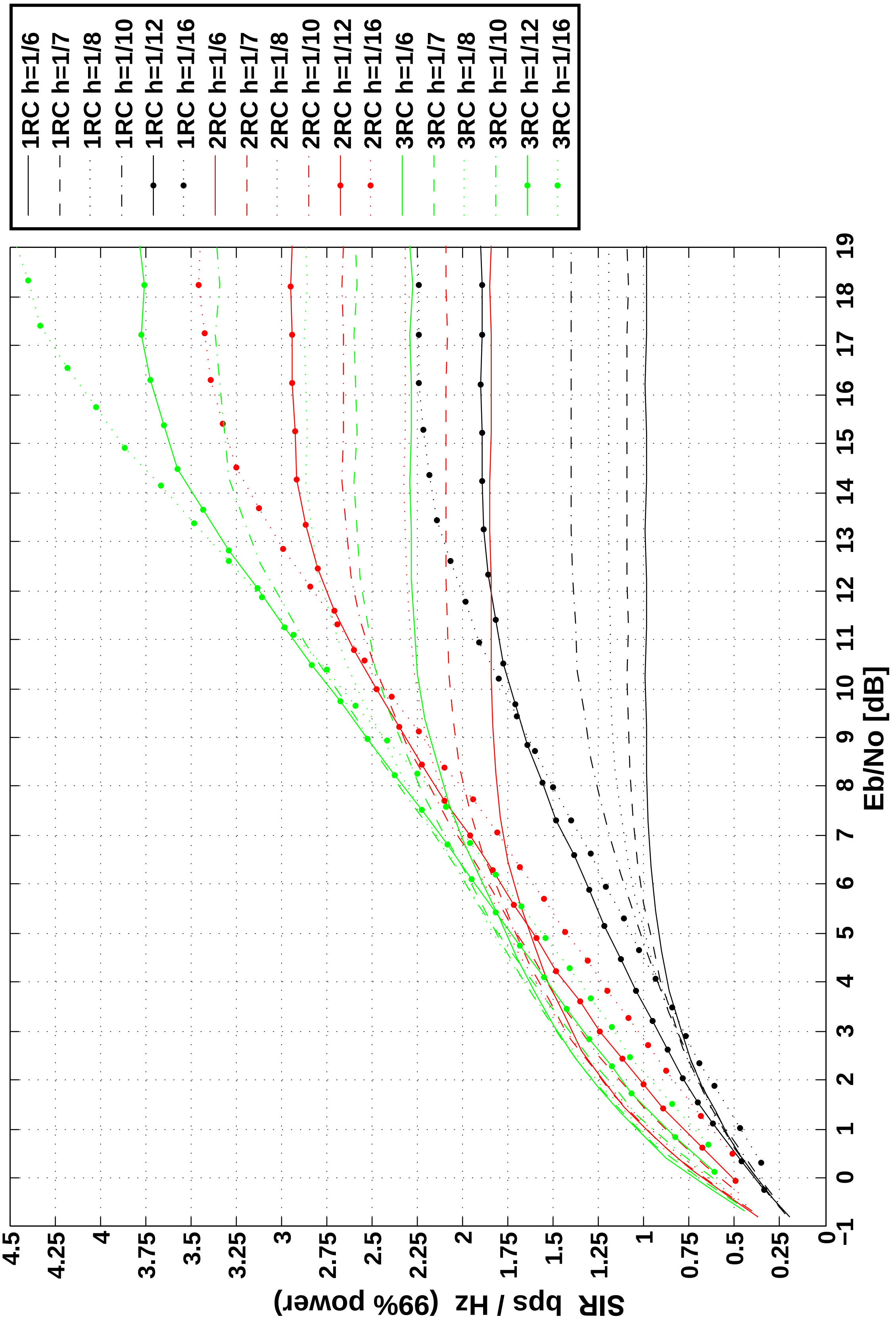

Figure 3.7 — SIR of octal alphabet LRC schemes

by *effective difference sequence*, a sequence at the input of the CPM satisfying equation 3.46. An effective difference as well as any of its permuted versions induces an error event.

3.6.2 Normalized squared Euclidean distance of CPM

The Normalized Squared Euclidean Distance (NSED) between two $M-$ary CPM sequences Seq_1 and Seq_2 of length N_e is defined as [63]:

$$\begin{aligned} d_{NSED}(Seq_1, Seq_2) &= \log_2 M \int_0^{N_eT} \left\| s(t, Seq_1) - s(t, Seq_2) \right\|^2 dt \\ &= \log_2 M \left(N_e - \frac{1}{T} \sum_{i=0}^{N_e-1} \int_{iT}^{(i+1)T} \cos \left[2\pi h W_i + 4\pi h \sum_{j=i-L+1}^{i} \tilde{V}_j q(t - jT) \right] dt \right) \end{aligned} \tag{3.47}$$

where $\tilde{V}_j = U_{j,Seq_1} - U_{j,Seq_2}$ is the difference symbol and $W_i = \left(\sum_{n=0}^{i-L} \tilde{V}_j \right) \mod p$.

The minimum value of NSED for a particular value of N_e offers an insight on the error correcting capability of uncoded CPM schemes for sequences of N_e symbols.

3.7 Conclusion

In this chapter we have provided a detailed mathematical definition of the CPM modulator and the corresponding demodulator. An alternative description is possible via the Rimoldi decompostion of CPM into a linear time invariant trellis encoder and a memoryless mapper. It allows the study of CPM signals via pre-existing tools of the coding and modulation fields.

The provided material will proove to be of great importance in the following chapters where CPM is studied in a coded iterative scenario. In fact, coding tools can take advantage of the CPM trellis structure in order to provide iterative convergence threshold estimation in addition to error floor prediction, facilitating the design of coded CPM systems.

CHAPTER

4

Study of coded continuous phase modulation schemes for satellite transmissions

THIS chapter is intended to describe the design of coded CPM systems that satisfy constraints imposed in the context of the BSDT project. It is true that coding solutions for CPM systems have already found their way into literature. Logically, we have first proceeded to an in-depth review of previous works that provided the necessary technical background allowing us to propose innovative solutions. Some of these have proven to be particularly appealing for the broadband satellite link application targeted in our study.

Crippled by the great amount of design parameters to be taken into consideration for the design of a coded CPM system (pulse type, modulation order, modulation index, code type, code rate), we have adopted a two-step methodology. The first step is intended for the choice of CPM parameters based on iterative process waterfall performance. It is followed by a second step planned to satisfy code design constraints in terms of error floors.

This chapter is organized as follows:

We start by defining the design constraints (spectral efficiency, target error rates, code rate flexibility, CPM parameters). Then, we detail the steps needed for the choice of CPM parameters based on a capacity comparison and on the waterfall performance of the coded system. We proceed afterwards to the investigation of several outer code solutions for CPM. It includes the interleaving type (bit or symbol), the mapping type (Gray, natural) and the code type (convolutional codes, block codes, parallel turbo codes, serial turbo codes, Flexicodes). It uses extrinsic information transfer charts for estimating convergence thresholds and bounding techniques for predicting error floors. Monte Carlo error rate simulations are then performed.

4.1 General description of a coded CPM

When the Rimoldi decomposition is used, coded CPM can be seen as a Serial Concatenation of Codes (SCC), having a FEC code as an outer code and the CPE as an inner code. The general description of Serially Concatenated Continuous Phase Modulation (SCCPM) is presented in fig 4.1.

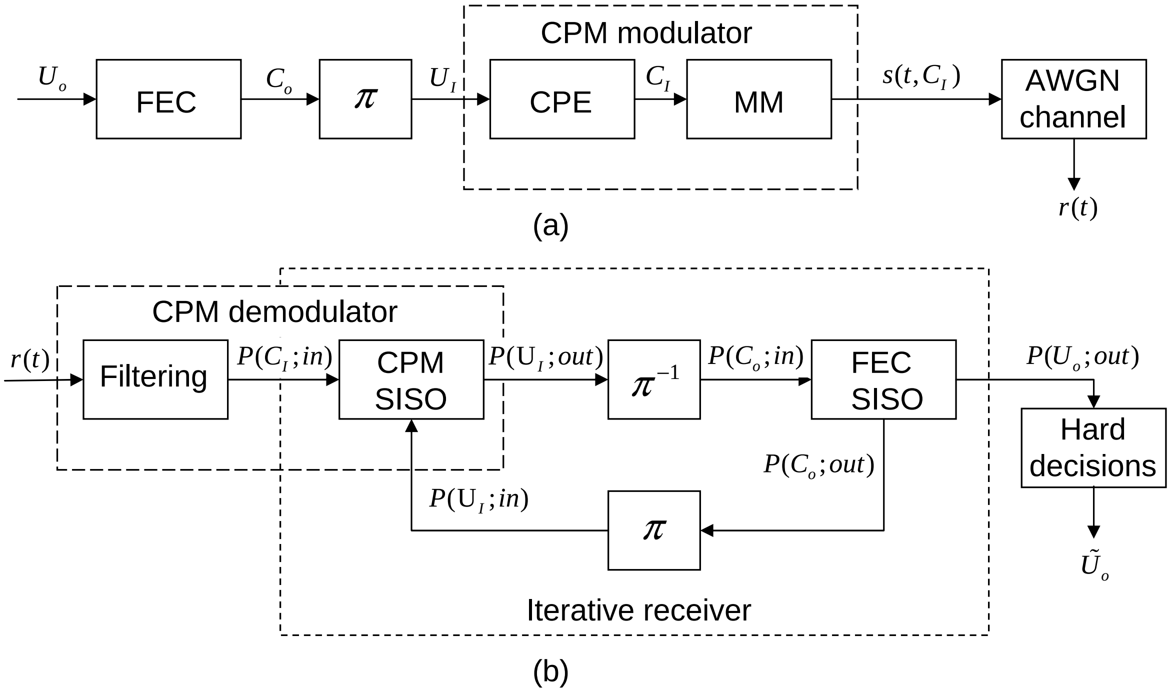

Figure 4.1 — Coded CPM seen as a classical SCC (a) Transmitter and AWGN channel (b) Receiver.

The outer code has rate $R = k_{out}/n_{out}$. For convenience n_{out} is an integer chosen as a multiple of $n_{CPM} = \log_2 M$. Since the information data is binary, and since the CPM works with $M-$ary symbols, a mapper should be introduced into the chain (not represented in fig. 4.1). Depending on the location of the mapper in the transmission chain, bitwise or symbolwise interleaving separates the outer and the inner code.

At the receiver side, iterative decoding can be carried out provided that the FEC and the CPE decoders call for SISO algorithms. Extrinsic soft information [15] is exchanged between the SISO modules until iterative process convergence is attained. Then hard decisions are computed at the output of the outer decoder.

4.2 Study objectives and parameters

4.2.1 Error correcting performance of SCCPM

Error correcting performance of iteratively decoded concatenated codes relies on two tiers:

- the convergence threshold of the iterative process that predicts the position of the waterfall region
- the error floor performance of the concatenated scheme.

In order to propose SCCPM schemes offering error correcting performance satisfying target convergence threshold and error floor criteria, we have tried to introduce study guidelines inspired by the ones proposed for SCC. For a target spectral efficiency, recent studies on SCC have shown that the best error correcting performance is attained when the inner code is punctured [64]. In the case of SCCPM, puncturing the inner encoder is not conceivable. The CPM modulator plays at the same time the role of inner encoder and signal mapper. In fact, the CPE is uniquely defined by the CPM parameters. As a consequence, the choice of a particular CPM scheme (the order M, the modulation index h, the pulse length L and the pulse type) dictates the maximum achievable spectral efficiency and goes even further to impose the inner encoder and its transfer function. This leads to outer code design restrictions. In fact, in order to achieve the best concatenated performance in terms of error rates, the outer and inner codes in a serial concatenation should be carefully "matched".

4.2.2 Study scenario

At this early stage of the study, we propose to start by defining the code design objectives. They are dictated by the target application consisting of a return link for satellite communications. The design parameters for such an application are:

- Frame sizes around one and two Asynchronous Transfer Mode (ATM) cells ($\sim$ 500 and 1000 bits).
- Spectral efficiencies ranging from 0.75 bps/Hz to 2.5 bps/Hz.
- AWGN channel.

We can then define the objectives in terms of target error correcting performance by:

- For convergence threshold: the best possible convergence threshold when target error floor is met.

- For error floor: below 10^{-6} of average Frame Error Rate (FER).

To meet these requirements, it is useful to enumerate the possible degrees of freedom available for a suitable design of a SCCPM. When a target spectral efficiency and a pulse type are chosen, they include :

- The CPM set of parameters (M, L, h) dictating channel capacity, the inner encoder transfer function and the outer code rate R.
- The choice of the mapping and interleaving types.
- The design of the outer code matching best the transfer function of the CPM dictated inner encoder. The FEC should also satisfy the target code design objectives in terms of convergence threshold and error floor taking into account the chosen mapping and interleaving types.

Having in mind these design requirements and possible degrees of freedom, design oriented questions arise:

- What criteria could be applied to choose the best CPM scheme achieving a particular spectral efficiency (especially that some are undistinguishable from the SIR point of view)? This is equivalent to finding a search criteria that leads to the best CPM set of parameters acting as inner code.
- What could be considered as a suitable interleaver and mapping types for our chosen set of CPM parameters?
- How can we propose an outer code best matched to the previously enumerated restrictions and satisfying the target code design objectives?

In the following sections, we try to answer these questions appropriety.

4.3 The choice of CPM parameters

4.3.1 Introduction

We started our selection procedure of CPM parameters by a capacity comparison. This is a classical approach for linear modulation schemes, where in general best systems are those achieving higher spectral efficiencies for a given signal to noise ratio.

Due to its direct influence on system complexity, the alphabet size M of the CPM, being a power of 2, should be kept reasonably low. This study investigates only quaternary and octal alphabet sizes.

For different ranges of spectral efficiencies (from 0.5 and 1.6 bps/Hz for QLRC schemes and 1.0 to 2.5 bps/Hz for OLRC schemes) several CPM schemes are undistinguishable from the SIR point of view. Consequently two questions arise:

- Can we establish a systematic criterion to choose CPM parameters upon other than SIR?
- Is the actual gap to SIR independent of the CPM parameters? If not, other alternative CPM schemes may be competitive in the range of interest even though they show poorer SIR.

We would like to acknowledge the work in [65] presenting some power and bandwidth efficient CPM systems with respect to uncoded MSK. This study has shown that by modifying the different CPM parameters large gains in power and bandwidth with respect to MSK become attainable. Based on these conclusions, we tried to propose methodologies for the choice of CPM parameters.

In a first stage of the study, we have kept the values of the alphabet size M and the pulse length L unchanged. In that case, a target spectral efficiency can be attained by several modulation index and code rate (h, R) pairs. Then, increasing h dictates a higher code rate R but the CPM system becomes less sensitive to noise. In this case one could wonder whether the decreasing sensitivity to noise compensates for the rate loss.

We know from [55] that increasing L offers higher spectral efficiencies. Another aspect of the study involves the analysis of error correcting performance of CPM schemes with different values of L achieving the same spectral efficiency in order to observe whether L plays a role in the error rate performance in this case.

4.3.2 Methodology based on convergence property of SCCPM

Having as a design objective the best possible convergence threshold of the SCCPM, a design methodology should be proposed due to the multitude of CPM parameters affecting spectral efficiency and error correcting performance. The EXIT chart analysis [51, 66] represents a rather efficient tool to compare and select component codes in a SCC. In the SCCPM case, it allows us to compare several SCCPM schemes with different set of parameters in terms of convergence threshold. As a consequence, for a target spectral efficiency, a subgroup of CPM set of parameters with best achieved convergence threshold can be constructed via EXIT chart analysis. This subgroup represents a preselection based on waterfall performance of CPM parameters.

EXIT chart analysis is based on the plotting of an extrinsic information transfer chart between two components of a concatenated scheme. As in SCCPM the CPE and the outer code represent the two components; in order to study the effect of changing one, the other component needs to be kept unchanged. Consequently, for a fair preselection of CPM parameters based on convergence behavior, we need to choose an outer code and keep it unchanged for all of the performed EXIT analyses. The hierarchy of the CPM parameters based on waterfall performance is kept if the outer code is changed.

4.3.3 Convergence study and illustration example

We have performed EXIT chart analyses over a large number of CPM parameters for particular values of spectral efficiencies ranging from 0.75 bps/Hz to 2.5 bps/Hz. Q2RC, Q3RC, O2RC, O3RC, Q2SRC, Q3SRC families of CPM for multiple values of h were investigated. For every treated spectral efficiency, a subgroup of CPM parameters has been preselected based on its superior waterfall performance with respect to the rest. The outer code chosen for the analysis is the $(1, 35/23)$ 16-state RSC. We are going to illustrate the steps to be followed in a study example.

4.3.3.1 Illustration example

As a study example, we compared the EXIT charts of two CPM systems having an almost identical SIR and attaining the same spectral efficiency for two different ranges of spectral efficiencies:

- SE range: 1.2-1.4 bps/Hz, Q3RC CPM

  Case 1: Spectral efficiency 1.2 bps/Hz : $(h = 2/7, R = 2/3)$ and $(h = 1/4, R = 3/5)$.

  Case 2: Spectral efficiency 1.4 bps/Hz : $(h = 1/4, R = 7/10)$ and $(h = 1/5, R = 3/5)$.

- SE range: 1.7-2.5 bps/Hz, O3RC CPM:

  Case 3: Spectral efficiency 1.7 bps/Hz : $(h = 1/8, R = 3/5)$ and $(h = 1/10, R = 1/2)$.

  Case 4: Spectral efficiency 2.5 bps/Hz : $(h = 1/8, R = 7/8)$ and $(h = 1/10, R = 3/4)$.

If we denote by TSE the Target Spectral Efficiency, when two sets of CPM parameters (M_1, L_1, h_1) and (M_2, L_2, h_2) are compared, the difference in their bandwidth occupation can be compensated by adjusting the outer code rates (R_1, R_2). This operation is based on equ. 3.42 (identical symbol periods are assumed for both cases):

$$TSE = R_1 \cdot \frac{\log_2 M_1}{B_1} = R_2 \cdot \frac{\log_2 M_2}{B_2} \tag{4.1}$$

The same procedure can be applied for the comparison of several CPM schemes attaining a particular TSE. Equ. 4.1 allows us to compute the code rates dictated by the sets of parameters to be compared. Once the rates computed, we can proceed to an EXIT chart analysis to compute the convergence threshold of the iterative process.

EXIT chart analysis

Let $I_I(CC)$ and $I_o(CC)$ denote the prior and the extrinsic Mutual Information (MI) for the FEC code. In a similar way, $I_I(CPM)$ and $I_o(CPM)$ denote the prior and extrinsic MI for the CPM. $I_o(CC)$ and $I_o(CPM)$ can be obtained via separate Monte Carlo simulation of the two constituent codes for different values of $\mathrm{E}_b/\mathrm{N}_0$. We have:

$$I_o(CC) = T_{CC}(I_I(CC)) \text{ and } I_o(CPM) = T_{CPM}(I_I(CPM), E_b/N_0) \tag{4.2}$$

where $T_{CC}()$ and $T_{CPM}()$ denote the EXIT functions of the CC and the CPM respectively. Assuming infinite length interleavers, the convergence threshold can be predicted by plotting the EXIT curves for the CC and the CPM in the same diagram. When the process converges, an opening appears between the two curves. The threshold is the lowest value of E_b/N_0 resulting into a process convergence.

Since the CPM is non-linear, the transmission of the all-zero codeword could not be assumed for EXIT chart analysis. In [67], the author presents a method that extends EXIT chart analysis by means of simulation to non-linear schemes. This method was applied for all CPM EXIT charts performed in this study.

Fig 4.2 provides the result of the EXIT chart analysis of case 1 corresponding to SC-CPM with TSE equal to 1.2 bps/Hz. A tunnel between the curve of $I_o(CPM)$ with higher modulation index $h = 2/7$ and the $I_o(CC)$ with $R = 0.67$ opens at 3.8 dB predicting the convergence threshold for infinite block length. In the case of the CPM with $h = 1/4$ and an outer code rate of 0.6, the predicted convergence threshold is debased by 0.4 dB. From the iterative convergence point of view we can say that the pair $(h = 2/7, R = 0.67)$ outperforms the pair $(h = 1/4, R = 0.60)$.

Fig 4.3 shows that the observation from the previous EXIT chart still applies for a TSE of 1.4bps/Hz: the system with higher modulation index and a higher code rate $(h = 1/4, R = 0.70)$ converges 1 dB earlier than the one with $(h = 1/5, R = 0.60)$.

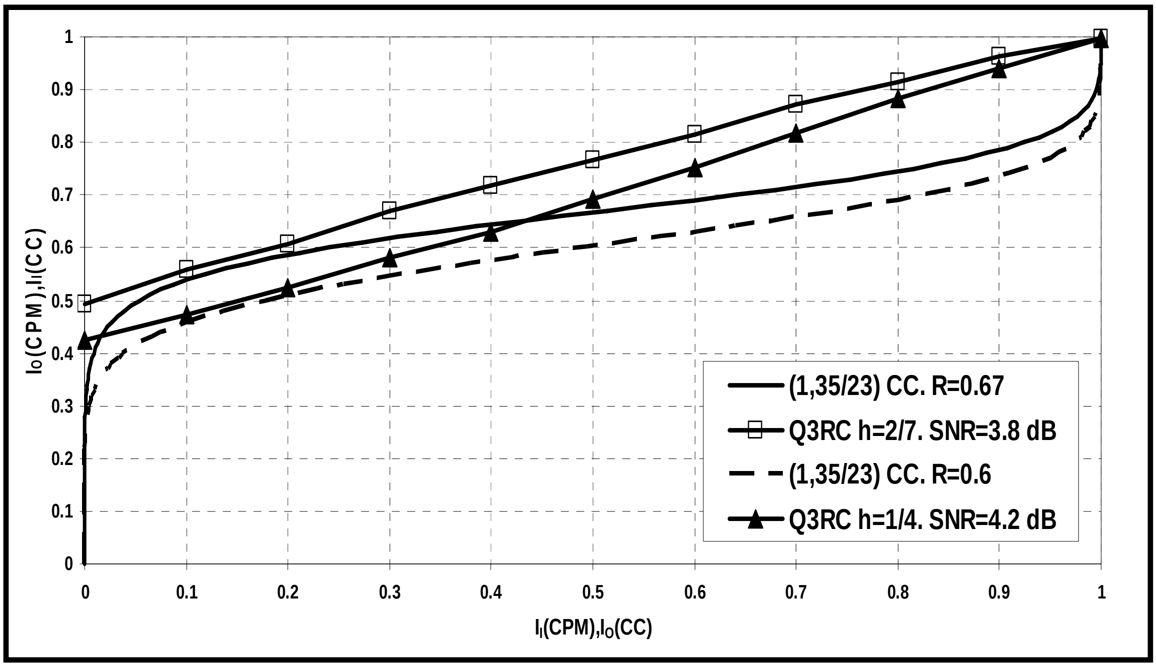

Figure 4.2 — EXIT chart analysis of two coded CPM schemes having a spectral efficiency of 1.2 bps/Hz

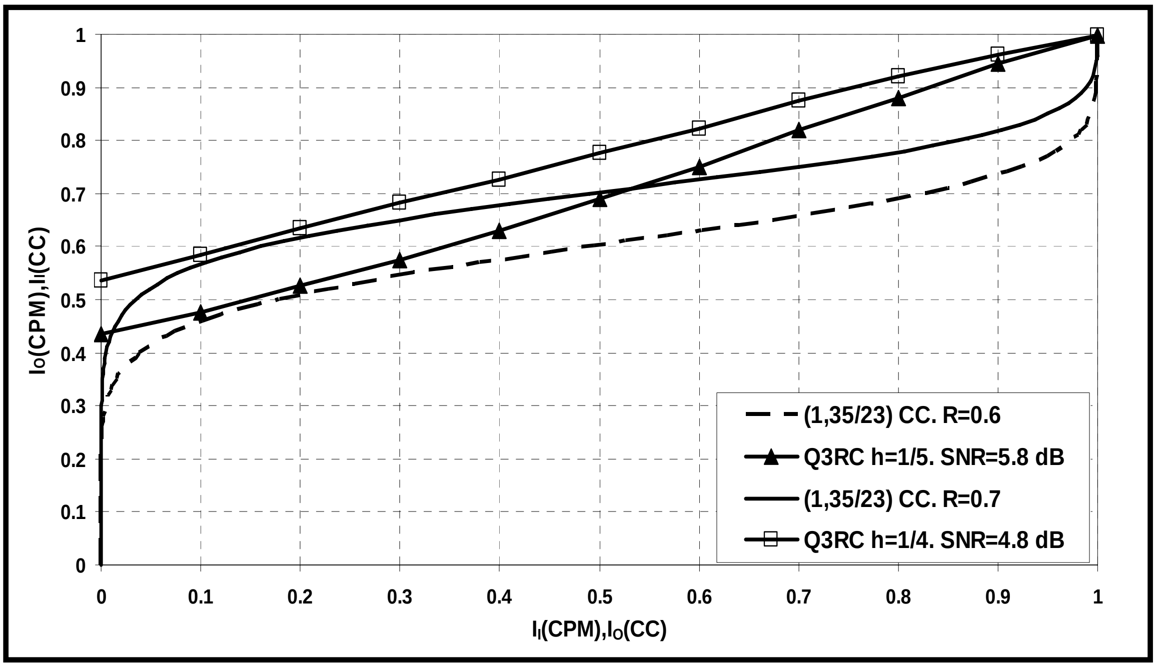

Figure 4.3 — EXIT chart analysis of two coded CPM schemes having a spectral efficiency of 1.4 bps/Hz

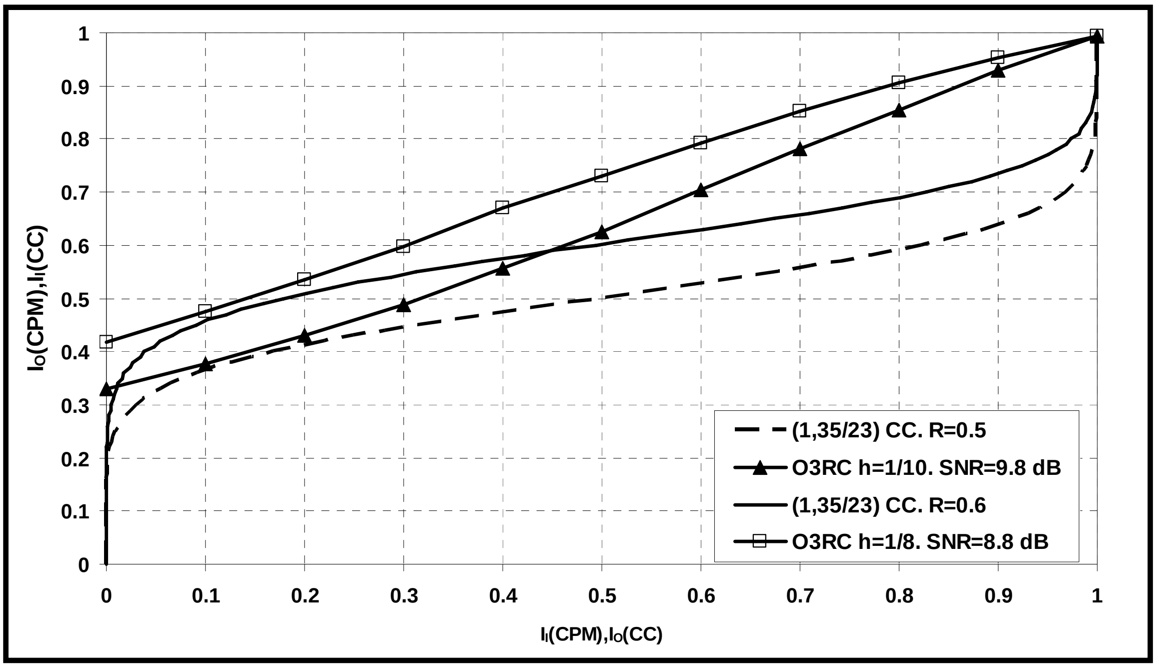

Figure 4.4 — EXIT chart analysis of two coded CPM schemes having a spectral efficiency of 1.7 bps/Hz

Confirming the tendency, the CPM systems in fig 4.4 and fig. 4.5 for TSE of 1.7 bps/Hz and 2.5 bps/Hz also show that the scheme with higher h and higher R enjoys the earlier convergence thresholds by 1.0 and 0.7 dB respectively.

Results

We have summarized threshold estimation results from the computed EXIT charts for the studied spectral efficiencies in table 4.1. Gaps to respective SIR computed as mentioned in section 3.5 are also included in the table.

From table 4.1 we can conclude the following:

1. For a predefined TSE, a higher modulation index associated to a higher outer code rate not only compensates for the rate loss with respect to their lower counterparts, but even presents an earlier convergence threshold with a gap ranging from 0.4 dB to 1.0 dB.

2. For a given set of CPM parameters (M, L, h, pulse type), the gap to SIR decreases when the TSE increases, that is when the rate R of the outer code increases. This could be explained by two arguments:

   - On one hand, the CPM set of parameters uniquely defines the capacity curve.

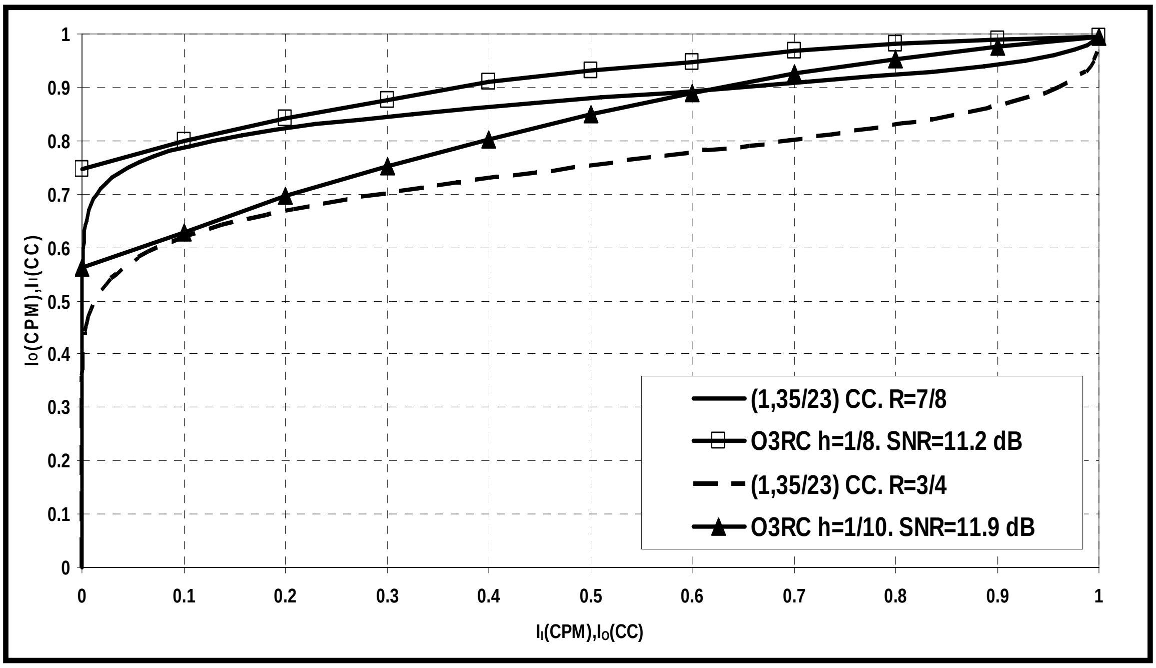

Figure 4.5 — EXIT chart analysis of two coded CPM schemes having a spectral efficiency of 2.5 bps/Hz

Spectral efficiency	CPM system	Convergence threshold	Gap to SIR
1.2 bps/Hz	Q3RC $h = 2/7, R = 2/3$	3.8 dB	2.1 dB
	Q3RC $h = 1/4, R = 3/5$	4.2 dB	2.4 dB
1.4 bps/Hz	Q3RC $h = 1/4, R = 7/10$	4.8 dB	2.2 dB
	Q3RC $h = 1/5, R = 3/5$	5.8 dB	3.2 dB
1.7 bps/Hz	O3RC $h = 1/8, R = 3/5$	8.8 dB	4.5 dB
	O3RC $h = 1/10, R = 1/2$	9.8 dB	5.5 dB
2.5 bps/Hz	O3RC $h = 1/8, R = 7/8$	11.2 dB	1.7 dB
	O3RC $h = 1/10, R = 3/4$	11.9 dB	2.0 dB

Table 4.1 — Convergence thresholds and gaps to SIR of eight different coded CPM schemes attaining four different spectral efficiencies

- On the other hand, this same set of parameters defines the CPE acting as an inner code in the SCCPM as well. Consequently, it plays an unavoidable active role in concatenated error rate performance. As noticed earlier, when increasing h and the outer code rate, an operation equivalent to having an operating point closer to the maximum attainable spectral efficiency in the capacity curve, the SCCPM offers an earlier convergence threshold. This is in contrast with results obtained with linear modulations where gap to capacity increases with the code rate.

Nevertheless, a practical limit on code rate exists. In fact for very high code rates (> 0.9) and for the used frame sizes in practice (around 1000 bits), it could be difficult to find efficient error correcting codes in terms of error floors with reasonable complexity suitable to SCCPM.

4.3.4 Conclusion: design guidelines for the selection of CPM parameters

The results of the previous EXIT chart analysis allow us to provide answers to the questions asked at the beginning of this section and propose some design guidelines for a preselection of CPM parameters in a SCCPM attaining a target spectral efficiency. We can assert that:

- The choice of the modulation index h should not only be based on SIR considerations in a SCCPM scenario. We have seen from the performed comparisons that SCCPM systems with poorer SIR could actually outperform, in terms of error correction, systems with better SIR.
- From the error correction capability point of view, two main aspects should be investigated: convergence thresholds and error floors.
    1. We first propose a preselection of CPM parameters based on the study of convergence thresholds. This study involves comparing several CPM schemes in terms of convergence thresholds by means of EXIT chart analysis when the outer code is kept unchanged. From a large number of performed comparisons (not only the ones of the previous section), we have noticed that for a target spectral efficiency, a good choice would be the CPM scheme with highest possible modulation index achieving this efficiency. This will result into the highest code rate. When respecting this design guideline, SCCPM not only compensates the rate loss, it even offers earlier convergence thresholds. Nevertheless, a limit exists. The outer code should still offer acceptable error correcting performance for the resulting rate. In general, rates exceeding 0.9 are to be avoided.
    2. After the preselection, the final choice of a winner CPM scheme for a target spectral efficiency is based on error floor considerations. These considerations are laid down

by the code design objectives. While it is true that the best preselected set of parameters offers best waterfall performance, it is still questionable if the floor is low enough to satisfy the code design objectives. This constitutes the underlying reason behind the necessity to address error floor issues in the FEC choice part of the study. Nevertheless the procedure should be accomplished in close cooperation with the choice of the CPM set of parameters. In fact, if even for the most efficient proposed outer code, the target floor requirements are not met, a compromise is unavoidable. It consists of choosing the closest set of CPM parameters in terms of waterfall performance that attain the target floor requirements for the proposed outer FEC. The investigation into error floor performance is described in section 4.5.

4.4 Study of the effect of CPM precoding on coded systems

Inspired by the use of precoders to improve the exchanged mutual information between the transmitter and the receiver over non linear channels such as magnetic recording channels [68], we have opted for the study of precoding for coded CPM systems. Any change in the exchanged mutual information should have a direct influence on the transfer function of the CPM modifying its EXIT chart. The modified EXIT chart could predict either an earlier convergence threshold (opening of the tunnel between the EXIT of the CPM and the outer code at a smaller value of E_b/N_0) or a lower error floor (empirically, the distance separating the two EXIT chart curves at a prior mutual information close to 1 is wider when precoding is applied).

Taking into consideration the Rimoldi decomposition of CPM where the CPE operates over an algebraic ring, an intuitive approach can be to conceive precoders over the same algebraic ring. Consequently, the resulting structure consists of a convolutional rate one encoder over rings Z_M inserted at the input of the CPE as shown in fig 4.6. It can be seen as a symbol scrambler decoded by the classical BCJR algorithm. Since the additions and multiplications in the CPE and the precoder are performed over the same algebraic ring, we were able to derive an "equivalent" CPE incorporating these two components. Fig. 4.7 shows the structure of one investigated precoder with a Q2RC as well as the corresponding equivalent CPE. The idea behind the derivation of an equivalent CPE is reducing the complexity of the precoded modulator/demodulator. In fact, in some particular cases, the equivalent model had the same number of trellis states as the original CPE. As a consequence, using the equivalent model avoids an additional implementation of the BCJR algorithm (one for decoding the CPE and another for the precoder). In some cases though, due to the irreversibility of algebraic rings, an increase in the number of trellis states of the equivalent CPE with respect to the

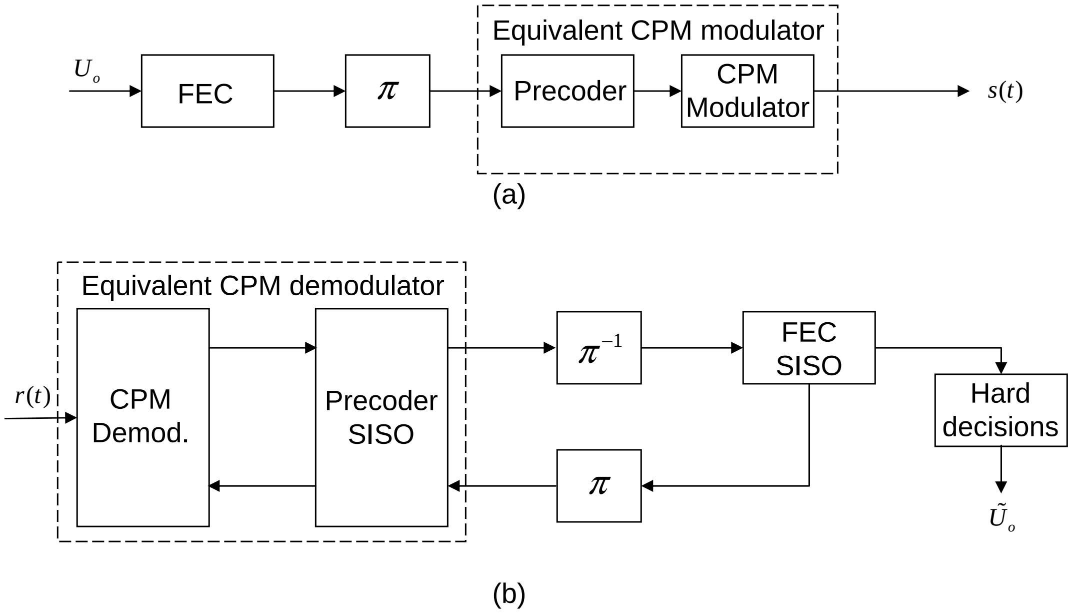

Figure 4.6 — Insertion of a precoder in the coded CPM scheme (a) Transmitter (b) receiver.

classical CPE is unavoidable. Nevertheless, even in this case, the total number of states is still lower for the equivalent CPE.

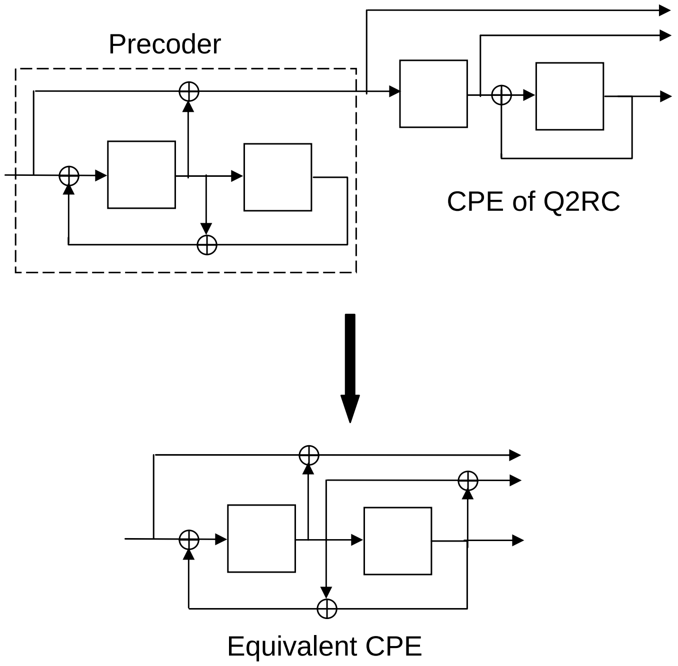

Figure 4.7 — A convolutional precoder over rings example and the corresponding equivalent CPE

The presence of a feedback recursion in the structure of the CPE imposes two strong design constraints:

- The design of a precoder for SCCPM has for objective increasing the minimum distance [24] of the CPE. In order to do so, it has to shift the pre-existing recursion (summation over the parameter p) of the CPE to the left.
- The choice of the CPM parameters has to respect $M = p$. The alphabet size of the CPM has to be the same as the denominator of the modulation index. This transforms the CPE into a classical convolutional code over rings where the mathematical operations over the code structure are all modulo $M = p$. As a consequence, satisfying the first constraint becomes possible.

Despite that the last constraint restricts considerably the search space for efficient CPM parameters, an exhaustive search for precoders was performed for quaternary 2 and 3RC schemes.

For every tested precoder, an EXIT chart analysis was carried out. The obtained results showed that in every tested case, precoding worsens convergence threshold. EXIT chart analysis of the precoded structure in fig. 4.7, having a Q2RC, $h = 1/4$ as CPM scheme and a $(1, 35/23)$ $R = 1/2$ CC as outer code, is presented in fig. 4.8. We can observe that the convergence threshold of the non-precoded CPM (dashed curve) is predicted at an E_b/N_0 of 2.2 dB. For this same value of E_b/N_0, the EXIT chart of the precoded system (straight line curves) crosses the EXIT chart curve of the outer code and the iterative receiver fails to converge. Convergence is possible starting from an E_b/N_0 of 2.9 dB. The estimated waterfall shift is around 0.7 dB. Nevertheless, we would expect a rather important improvement in the error floor performance.

EXIT chart analysis of yet another precoded case with an octal 3RC, $h = 1/10$ CPM and a (1,5/7) $R = 5/6$ outer code is shown in 4.9. Similarly to the previous analysis, if we take a look at the EXIT analysis of fig 4.9 we can clearly see that the precoded CPM curve crosses the outer code curve resulting into late convergence. But when the extrinsic information at the input gets higher than 0.2, the precoded system presents a wider tunnel (tunnel between the precoded system and the outer code EXIT charts) which incinuates a lower floor. At 13.2 dB, the precoded system still doesn't attain convergence whereas the non precoded system converges at 12.4 dB.

For all tested precoders, we observed a worsening of the convergence threshold for precoded compared to the non-precoded CPM. This threshold shift varies from 0.7 to 1 dB as a function of the CPM parameters, the outer code and its parameters and obviously the chosen precoder. Precoding would have remained a viable option when very low error floors were an objective if it was not for the constraints it imposes on the choice of CPM parameters.

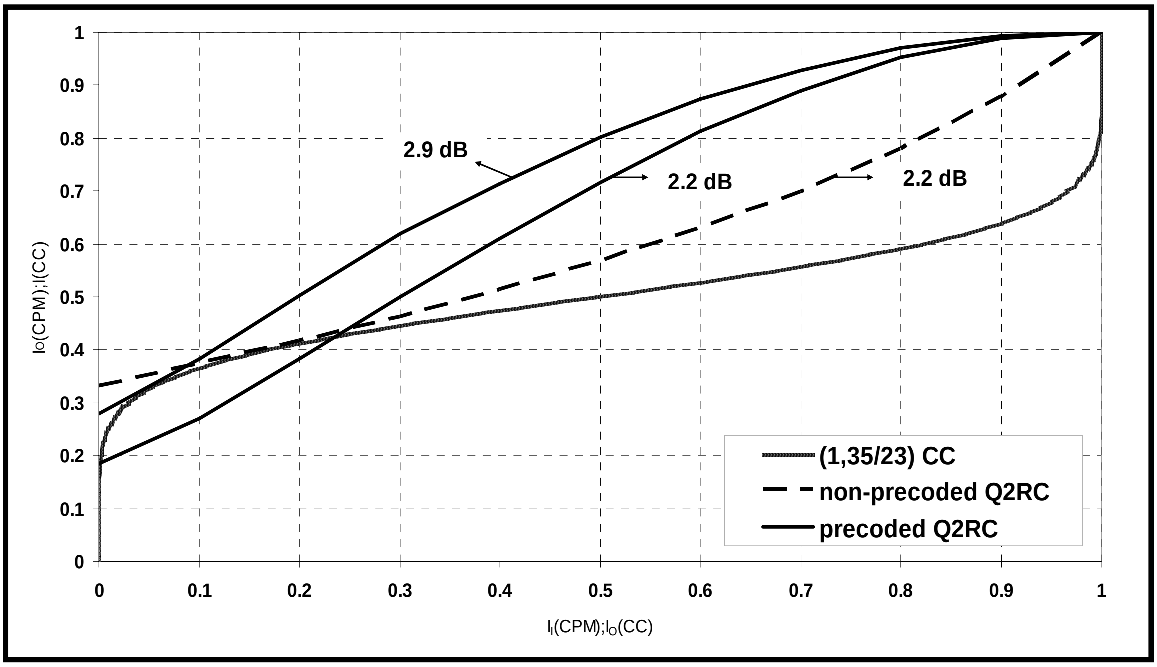

Figure 4.8 — EXIT chart comparison of precoded and non-precoded Q2RC $h = 1/4$ schemes having the (1,35/23) $R = 1/2$ CC as outer code

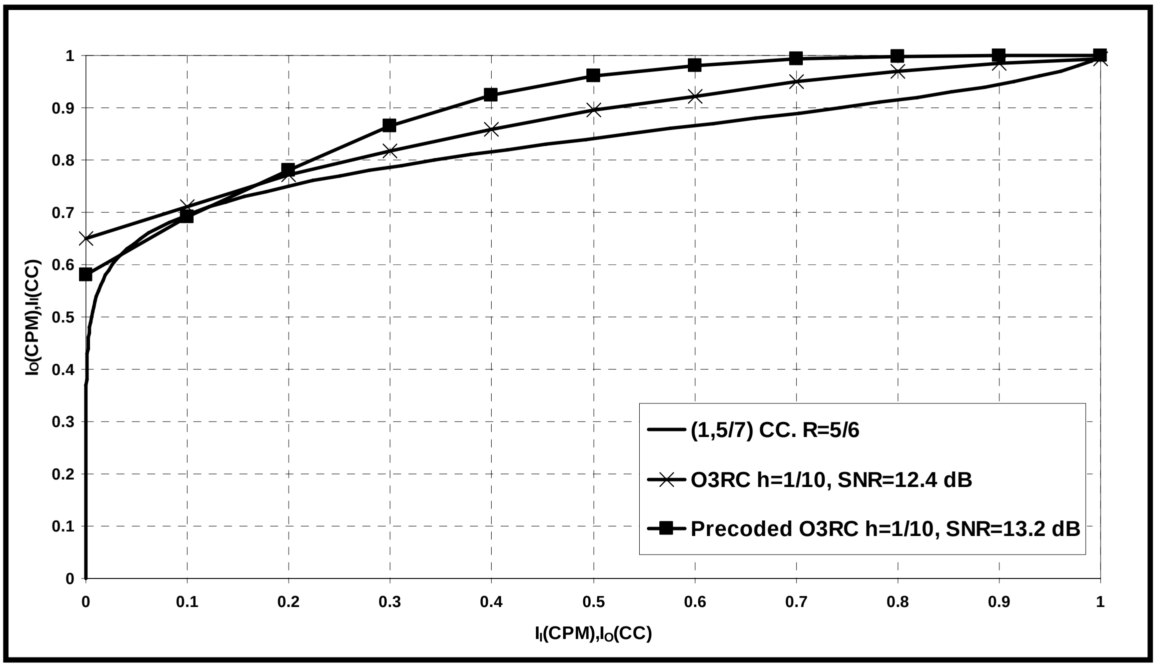

Figure 4.9 — EXIT chart comparison of precoded and non-precoded octal 3RC $h = 1/10$ schemes having the (1,5/7) $R = 5/6$ CC as outer code

Due to all of the mentioned limitations, and due to the worsened convergence threshold, we conclude that precoded CPM systems do not represent good candidates when error rate performance is the sole design criteria.

4.5 Outer FEC selection for SCCPM

4.5.1 Review of the previous work on coded CPM systems

A considerable work has already been done on coded CPM systems where concatenation with different outer codes has been investigated. These studies can be divided into three different types:

- Type 1: Studies of coded MSK (1REC) [69, 70, 71]. In almost all cases though, it represents work that cannot be extrapolated to higher order CPM schemes with higher complexities and spectral efficiencies.

- Type 2: Studies of several SCCPM schemes having different CPM parameters with an unvaried outer code solution [63, 72, 73, 74, 62, 75]. They were undertaken basically in order to achieve a deeper understanding of SCCPM. In some cases, comparisons were performed. But since MSK was taken as a reference, these comparisons were useful to investigate SCCPM behavior compared to the simplest one, MSK. In fact, since the achieved spectral efficiencies were not the same as the design parameters of section 4.2.2, the conclusions of these comparisons were not directly applicable to our study. Nevertheless, they offered an insight into the effect of CPM parameters on the achievable spectral efficiency, the bandwidth occupation and the error correcting capability of SCCPM.

- Type 3: Studies of a particular CPM scheme concatenated with a particular outer code [76, 77]. In some cases [77], the set of CPM parameters was carefully chosen in order to offer an interesting error correcting capability for the chosen outer code solution. The proposed schemes lack flexiblity as the error correcting performance of the proposed solution is dependent on the carefully chosen CPM parameters and outer code. In other cases [76], the choice of CPM parameters was undertaken randomly. The goal of this type of studies is to give guidelines on the design of the outer code. No insight into the choice of CPM parameters was given.

  For type 3-like solutions, the set of CPM parameters was not chosen to be the same as in previous studies. Consequently the proposed different outer code solutions were not comparable with pre-existing SCCPM structures.

None of the results of previous studies turned out to be directly applicable for our target application. The main goal of our study was then to fill in the existing gap in the literature concerning the study of SCCPM solutions achieving a range of spectral efficiencies with the best error correcting performance in convergence and in the floor.

Since section 4.3 proposes a methodology to choose CPM parameters based on waterfall performance, we now need to propose outer FEC code allowing SCCPM to satisfy performance criteria in terms of error floors with the least possible degradation of the convergence thresholds. We start by providing suitable conditions for direct and fair comparisons of outer FEC solutions inspired by the ones already proposed in literature.

4.5.2 Description of the SCCPM solutions covered in our study

Inspired by the investigation into the previously proposed outer code solutions for CPM, we propose a deep study of three main configuration types. The transmitters for the proposed configurations, representing the different associations of outer codes and CPM schemes, are presented in fig 4.10. They enjoy several structural differences going from the interleaver type, the outer code type to the mapper position and type. The corresponding receiver configurations are shown in fig. 4.11.

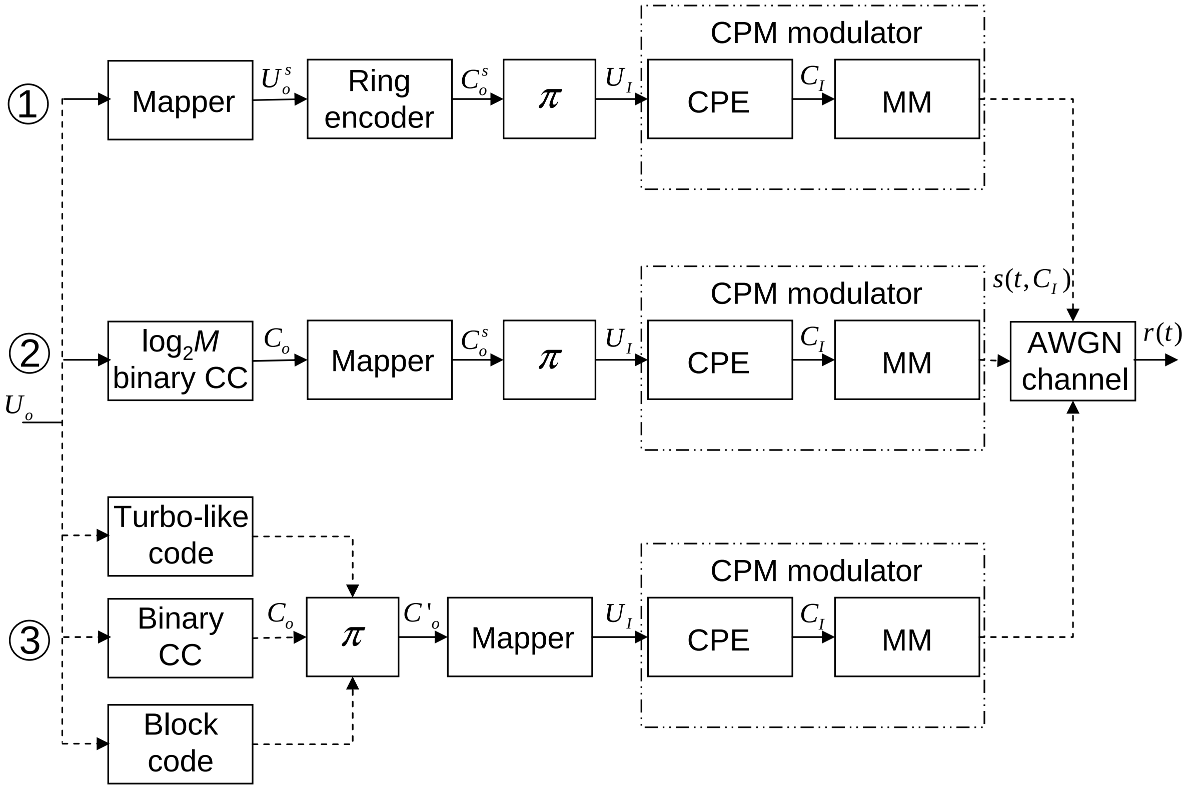

Figure 4.10 — Studied cases of coded CPM transmitter seen as a classical SCC

1. First configuration: Configuration (1) in fig. 4.10, corresponds to the proposition of the authors of [73, 62, 75] where outer convolutional codes over rings [78, 79] and symbol interleaving were adopted. When compared to previous works where bit interleaving was introduced, it has been shown in [73, 62, 75] that solutions based on the structure of the first configuration offer earlier convergence thresholds. In some cases a significant gain in waterfall performance of several tenths of dB (up to 0.8 dB) was observed. Consequently, this type of coding solution seemed to be well suited for satisfying code design requirements of section 4.2 where best convergence thresholds represent an objective. Nevertheless, the design of efficient symbol-based codes for SCCPM in terms of error correction is not an easy task as detailed in [73, 62, 75]. Notice that the $M-$ary mapper is located at the start of the transmitter chain of blocks, therefore, as a direct consequence, all the following blocks work on $M-$ary symbols starting from the ring encoder up to the CPM.

   At the transmitter side (configuration (1) in fig. 4.10), the information data bits vector U_o is mapped to symbol vector U_o^s which is then encoded by the outer convolutional ring encoder working on an alphabet matched to the $M-$ary order of the CPM encoder. The resulting codeword C_o^s is symbol-interleaved via permutation π to U_I which constitutes the input of the CPM modulator. The signal at the output of the CPM modulator $s(t, C_I)$ is transmitted over a classical AWGN channel.

   At the receiver side (configuration (1) in fig. 4.11), the signal $r(t)$ goes first through a phase of filtering as previously described in section 3.1. Note that the filtering operation is performed only once for every received frame. The filtered signal is then subject to an iterative decoding process via a SISO module working on the trellis of the CPE. Probabilities $P(U_I; out)$ at the output of the CPE SISO are deinterleaved to $P(C_o^s; in)$ via π^{-1}. A second SISO module working on the trellis of the outer code over rings is then initiated. This module provides extrinsic information $P(C_o^s; out)$ related to the coded symbols. This soft information is interleaved via the permutation function π to $P(U_I; in)$ used as *a priori* probabilities in the CPE SISO after the each iteration. When operating at a suitable SNR, this latter attains convergence within a small number of iterations. Thereafter, the symbol-based information probabilities $P(U_o^s; out)$ at the output of the outer code SISO are marginalised to provide estimations $P(U_o; out)$ of the input information bits that allow the hard decisions to be computed.

2. Second configuration: Configuration (2) in fig. 4.10 is one of our propositions for outer code solutions. It is motivated by the good convergence properties of symbol-based schemes. We propose to replace the outer convolutional ring encoder of configuration (1) by a rate 1/2 systematic $\log_2 M$-binary Convolutional Code ($\log_2 M$-CC) [80, 81]. This type of CC encodes in one step $\log_2 M$ bits available at its input. With this type

of solution, we expect to offer error correcting capability comparable to the first configuration. Nevertheless, this type of CC offers higher flexibility than codes over rings in the sense that a switch to convolutionally coded third configuration of fig. 4.10 is easily conceivable. Also, as a key difference with respect to the codes in [73, 62, 75] we propose puncturing at symbol level to adapt the code rate to system requirements. A method for designing competitive $\log_2 M$-CC for SCCPM is presented in the next section.

At the transmitter side (configuration (2) in fig. 4.10), the information vector U_o is first encoded through the $\log_2 M$ convolutional encoder. Coded bits C_o are mapped to symbols C_o^s and interleaved to constitute the input symbols of the CPM modulator U_I.

At the receiver side, (configuration (2) in fig. 4.11) the CPM demodulator and the interleaving type being unchanged, the same steps as in the first configuration are reproduced. Nevertheless, at the output of the deinterleaver, the extrinsic symbol-based soft information $P(C_o^s; in)$ is, in this case, marginalised to bit probabilities $P(C_o; in)$ used as input to the $\log_2 M$ CC SISO. The extrinsic soft bitwise information $P(C_o; out)$ at the output of the CC is combined to symbol probabilities $P(C_o^s; out)$ which, after interleaving, forms the input *a priori* information to the CPE SISO.

3. Third configuration: Configuration (3) in fig. 4.10 calls for a bit-based interleaving approach. Under this assumption, three types of outer codes were studied:

   (a) Binary recursive systematic convolutional codes: this structure is (almost) identical to the one investigated in [63] and [72], with the difference that we used systematic codes, while [63] and [72] consider the use of non-systematic codes. Nevertheless, from the performance point of view, the two structures are equivalent.

   (b) Turbo-like outer codes: this includes Parallel Concatenated Convolutional Codes (PCCC) [15], Serially Concatenated Convolutional Codes (SCCC) [64] and Flexi-like codes [82]. This represents one of our propositions if error floor requirement is not attained with simpler outer codes.

   (c) Block codes: extended Bose, Ray-Chaudhuri, Hocquenghem (eBCH) codes were under consideration in our study. They constitute one of our propositions when high Hamming distances are needed for high code rates.

This configuration differs from the previous two mainly by the type of interleaving. Bitwise interleaving is adopted. The mapper is therefore pushed to the input of the CPM.

At the transmitter side (configuration (3) in fig. 4.10), the information vector U_o is encoded via one of the three considered encoders (turbo-like, convolutional, block). The mapper transforms the interleaved version C'_o of the coded bits C_o to the symbolwise input U_I of the CPM.

In this case, only the CPM modulator/demodulator is identical to the previous configurations. At the output of the demodulator block (configuration (3) in fig. 4.11), symbol-based extrinsic information $P(U_I; out)$ is marginalised to bitwise soft information $P(C'_o; in)$. This latter is then deinterleaved to $P(C_o; in)$ constituting the input of the outer SISO decoder. This decoder should obviously correspond to the chosen encoder. At the output of the decoder, bitwise extrinsic information $P(C_o; out)$ is interleaved to $P(C'_o; out)$. Symbolwise extrinsic *a priori* probabilities $P(U_I; in)$ are then generated after the bits to symbols conversion.

4.5.3 Design methodology and tools for SCCPM outer FEC selection

4.5.3.1 Design methodology

In order to study the available configurations in terms of error correction, tools for code design should be introduced. Again, they involve two aspects:

- Convergence threshold estimation. It could be performed via:
    1. Monte Carlo simulation.
    2. EXIT chart analysis. In contrast with EXIT charts of section 4.3 where the outer code was kept unchanged varying the CPM parameters, EXIT charts proposed in this scope hold a CPM set of parameters and varies the outer code. This will give us a clear insight into the outer code choice based on waterfall performance.
- Error floor estimation. There exists mainly two ways of predicting the probability of error asymptotically:
    1. By Monte Carlo simulation.
    2. By deriving analytical expressions in the purpose of providing accurate bounds on the asymptotic error rates.

Having a target FER of 10^{-6}, identifying error floors by simulation is a time consuming operation. It couldn't be used as a time efficient tool for the selection of the outer codes when a large number of cases are to be treated. It could be used though for the final validation of the chosen outer code solution. Instead, bounding techniques represent a suitable efficient alternative for the choice of the outer code solution. They offer upper bounds on the probability of errors.

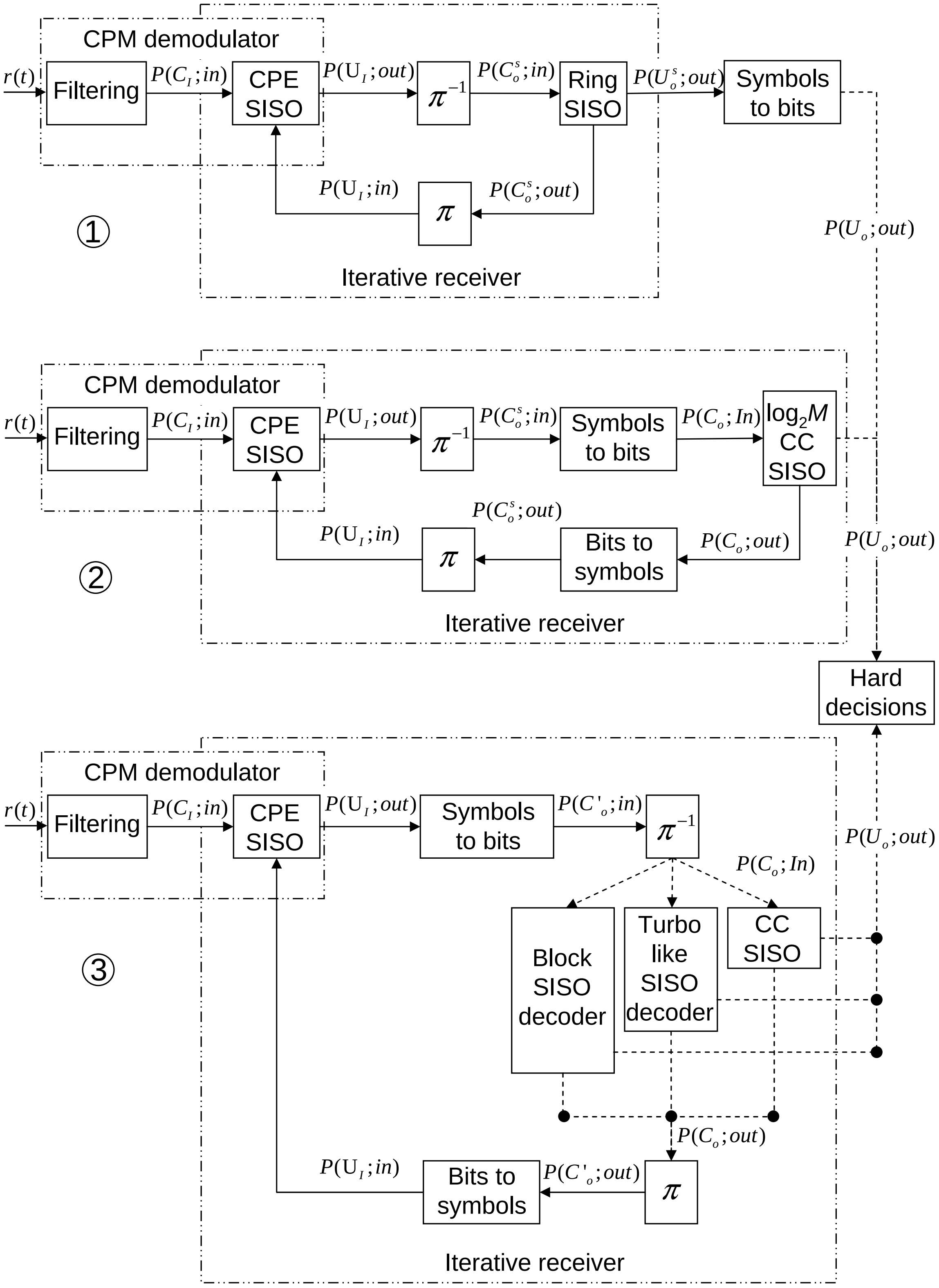

Figure 4.11 — Structure of the iterative coded CPM receiver for the three configurations of fig. 3.10

In the study of the three SCCPM configurations, an SCCPM scheme consisting of the third configuration with an outer CC concatenated with a Q2RC, $h = 1/4$ is chosen as a reference. The hierarchy of the outer code solutions in terms of convergence threshold and error floor should be preserved when concatenated with other sets of CPM parameters. In some cases though, additional CPM schemes were also investigated in order to validate results on a wider range of parameters.

4.5.3.2 Bound derivation for bit-interleaved systems:

Bounding techniques provide time saving error floor prediction tools. In our study, we derived an upper bound on the word error probability greatly inspired by the work in [24, 28, 83] and [63, 72]. They are based on the union bound technique.

Any derivation of the union bound [24] for concatenated codes with Maximum Likelihood Sequence Detection (MLSD) implies the study of concatenated error events. For trellis based decoders, an error event starts when the detected path through the trellis leaves the one given by the transmitter. It ends when the two paths remerge into the same ending state. A compound error event represents an error event where several remerging to and diverging from a state occur in the trellis steps corresponding to the sequence of length N. For the study of error events in the case of linear codes, the all-zero sequence can be taken as a reference. A concatenated error event represents an error event for all component codes in a concatenated structure. For parallel concatenated codes, a concatenated error event is a nonzero input sequence generating an error event for the first constituent code and for the second after interleaving. In a serial concatenation scenario, concatenated error events are nonzero input sequences causing an error event in the outer code with an output Hamming weight d_H. These sequences of weight d_H should then induce an inner error event having an output Hamming weight of d_{H_o}. Input sequences resulting into the lowest value of d_{H_o} dominate the asymptotical performance.

In the case of SCCPM, as the inner is a modulator with memory, input sequences with the greatest impact on asymptotical performance are the ones with an outer code weight d_H and length N_s in symbols causing an error event for the CPE corresponding to the minimum NSED for this length (see section 3.6.1). In addition, since CPM does not respect the UEP where all the transmitted bits are equally protected, we cannot restrict our study to a comparison to the all-zero sequence. In fact, the NSED could be different for an effective difference sequence (see section 3.6.1) and any of its possible permutations.

As concatenated codes are separated by an interleaver, this latter plays a role in bounding the averaged probability of errors. We have adopted the same interleaver function as for the derivation of the bounds for SCC [24, 28, 83]. It is the so-called *uniform interleaver* defined as the probabilistic device that maps a sequence at its input to all of its possible permutations equiprobably. Fig 4.12 illustrates the uniform interleaving and the non UEP compliance for the NSED of CPM sequences with respect to any of their permutations.

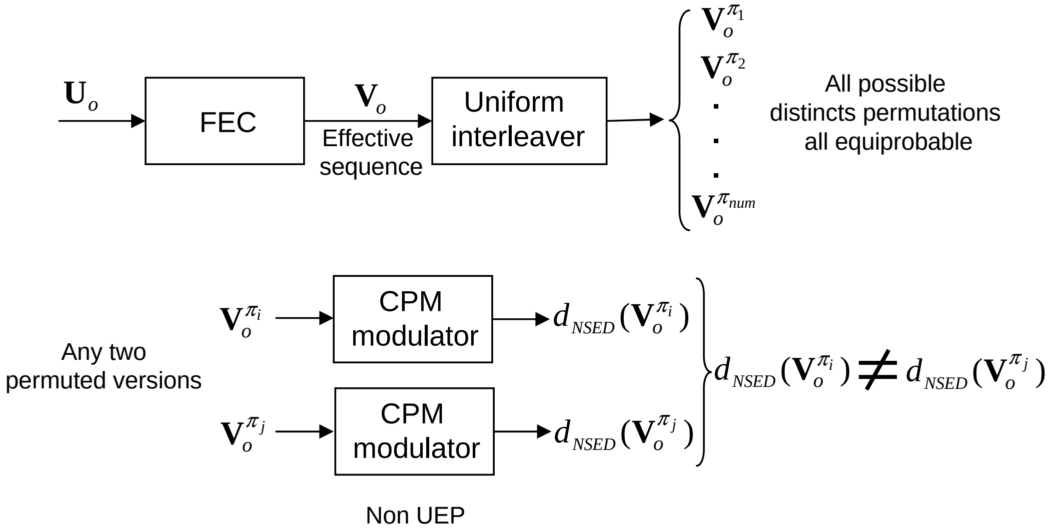

Figure 4.12 — Uniform interleaver and CPM UEP illustration example

The union bound on the frame error probability over AWGN channels with double-sided spectral density $\frac{N_0}{2}$ and MLSD with bit interleaving for a serial concatenation of codes is expressed as [24, 28, 83]:

$$P_w \leq \frac{1}{2} \sum_{d_{NSED}} B_{d_{NSED}} \exp\left(-\frac{d_{NSED} R E_b}{2N_0}\right) \tag{4.3}$$

where

$$B_{d_{NSED}} = \sum_{d_H} \frac{A_{d_H}^{out} \cdot \overline{A}_{d_H, d_{NSED}}^{in}}{\binom{N}{d_H}} \tag{4.4}$$

is the word error multiplicity for error events with NSED d_{NSED}. $A_{d_H}^{out}$ and $\overline{A}_{d_H,d_{NSED}}^{in}$ represent the weight spectra of the outer code and the CPM respectively. In other words, the Output Weight Enumerating Function (OWEF) $A_{d_H}^{out}$ is the number of length-N concatenated outer code error events with Hamming distance d_H. $\overline{A}_{d_H,d_{NSED}}^{in}$ represents the Input-Output Weight Enumerating Function (IOWEF) with an input weight of d_H corresponding to an outer NSED d_{NSED}, averaged with respect to the number of transmitted codewords they correspond to. The denominator counts the number of distinct permutations that the uniform interleaver can produce from an output weight codeword d_H provided by the outer encoder. The derived bound depends on the bit labeling of the CPM symbols (natural binary, Gray, etc...) if $M \geq 4$.

Compound events made up of single error events having a minimum NSED d_{NSED} for the length N_s are considered. Every compound error event gives a particular contribution to the bound where:

$$B_{d_{NSED}} \approx \frac{A^{out}_{d_{H\min}} \cdot \overline{A}^{in}_{d_{H\min},d_{NSED}}}{\begin{pmatrix} N \\ d_{H\min} \end{pmatrix}} \tag{4.5}$$

The computation of $\overline{A}^{in}_{d_{H\min},d_{NSED}}$being cumbersome, an approximation is proposed in [63, 72]. It consists of the following argument: A compound event consisting of n_{in} single inner code error events in a block of size N can be obtained in $\begin{pmatrix} N \\ n_{in} \end{pmatrix}$ ways. Since the computation of $\overline{A}^{in}_{d_{H\min},d_{NSED}}$ is performed on a truncated trellis, compound error events could be truncated resulting into an underestimate of their corresponding multiplicities. However, if N is large compared to n_{in} and the length of these events, the impact of truncating the trellis can be neglected. If we use the approximation $\binom{N}{n_{in}} < \frac{N^{n_{in}}}{n_{in}!}$, equ. 4.5 leads to an overestimate of $B_{d_{NSED}}$ as follows:

$$B_{d_{NSED}} \approx A^{out}_{d_{H\min}} \frac{d_{H\min}!}{n_{in}!} N^{n_{in}-d_{H\min}} \tag{4.6}$$

where $A^{out}_{d_{H\min}}$ could be computed in a similar way as in [24, 28, 83].

$B_{d_{NSED}}$ computed following equ. 4.6, the NSED computed following equ. 3.47, the probability of word error P_w could now be estimated following equ. 4.3.

Fig. 4.13 shows the result of union bound computation for several bit-interleaved coded CPM schemes. For comparison purposes, the simulated FER curves have also been added. The outer code is the (1,5/7) 4-state CC. It has been punctured to $R = 0.8$ when concatenated with Q3RC, $h = 1/3$ and Q2RC, $h = 1/4$ and to $R = 0.7$ when concatenated with Q3RC, $h = 2/7$. From Fig. 4.13, we can observe that the derived bounds represent an accurate estimation of the error floor.

The conclusions of fig. 4.13 on the tightness of the bounds still apply for fig. 4.14 where a $(1, 35/23)$ 16-state outer CC replaces the 4-state CC.

Taking into account the tightness of the union bound asymptotically, we can confirm that this coding design tool constitutes an efficient and time saving way of predicting error rate curve slope change for bit-interleaved SCCPM schemes.

4.5.3.3 Bound derivation for symbol-interleaved systems

Switching to symbol interleaving enduces small modifications in the computation of bounds on the probability of frame error derived in section 4.5.3.2 for bit-interleaved SCCPM. This

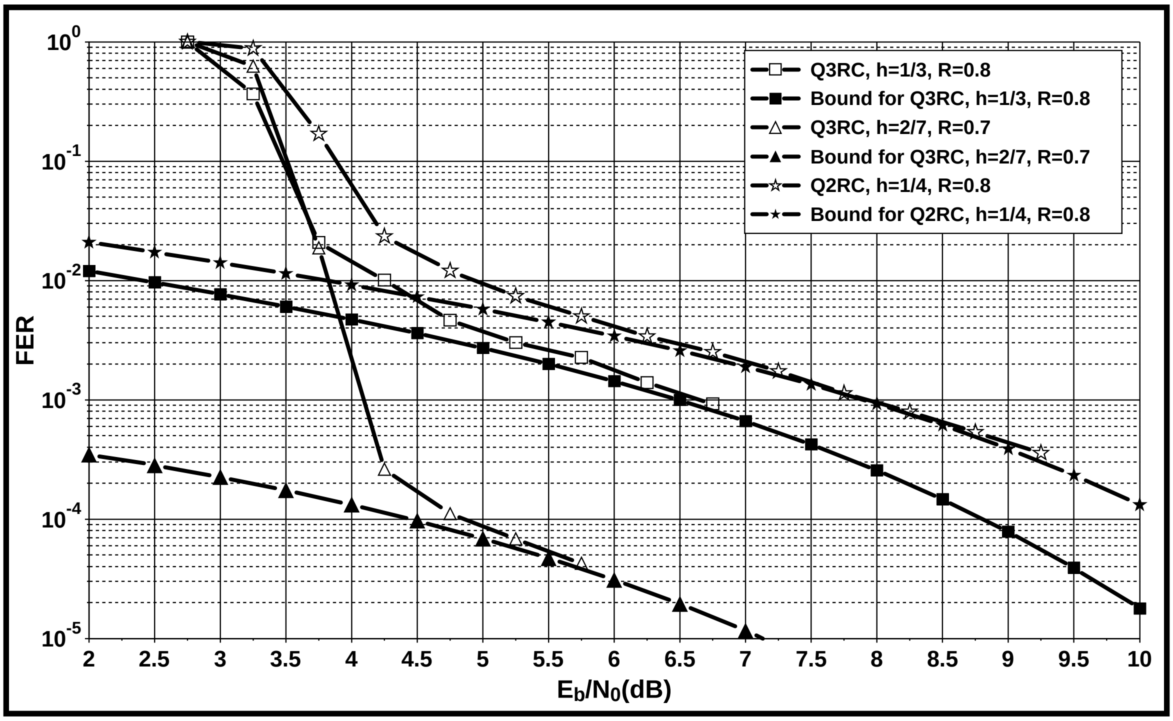

Figure 4.13 — Bound validation example for several (1,5/7) CC coded CPM schemes and code rates

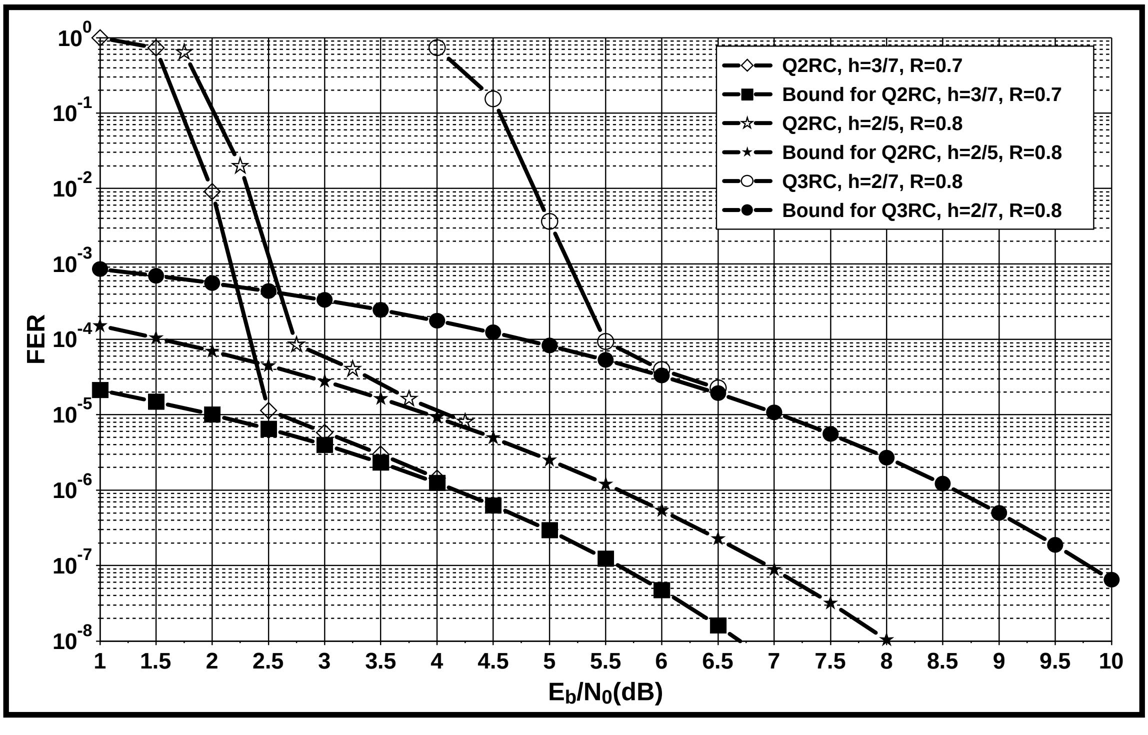

Figure 4.14 — Bound validation example for several (1,35/23) CC coded CPM schemes and code rates

section follows at first the derivation and terminology in [73], thenafter, it differs in some key parameter computation. The union bound on the frame error probability for symbol-interleaved serial concatenation of codes over AWGN channels with double-sided spectral density $\frac{N_0}{2}$ under MLSD is identical to the bit-interleaved case and can be written as:

$$P_w \leq \frac{1}{2} \sum_{d_{NSED}} B_{d_{NSED}} \exp\left(-\frac{d_{NSED} R E_b}{2N_0}\right) \tag{4.7}$$

Nevertheless, in the case of symbol interleaving $B_{d_{NSED}}$ becomes [73, 62, 75]:

$$B_{d_{NSED}} = \sum_{\tilde{l}} \frac{A^{out}_{\tilde{l}} \cdot \overline{A}^{in}_{\tilde{l},d_{NSED}}}{\binom{N_s}{l_{-M+1}, l_{-M+2}, ..., l_{M-2}, l_{M-1}}} \tag{4.8}$$

where the addition over $\tilde{l}$ represents an addition over the set of distincts vectors enumerating the number of non-zero difference symbols l_i corresponding to return to zero symbol sequences in the trellis of the outer code. For example, for quaternary CPM and the following difference sequence $\{-3, -1, -1, 0, 0, 1, 2\}$ the corresponding vector $\tilde{l}$ is equal to {num. of $(-3) = l_{-3}$, num. of $(-2) = l_{-2}$, num. of $(-1) = l_{-1}$, num. of $(1) = l_1$, num. of $(2) = l_2$, num. of $(3) = l_3\} = \{1, 0, 2, 1, 1, 0\}$. The evaluation of equ. 4.8 is a complex task. In [73, 62, 75] a truncated bound was proposed, based on the use of the difference state graph to compute the spectrum of the outer code and the CPM. Despite lowering the complexity of the task at hand, this approach remains computationally demanding, especially for long constraint length codes and CPM with a large number of trellis states. Therefore, in [73, 62, 75] the computation was limited to few dominant terms.

Here, we propose a slightly different computation of equ. 4.8 exploiting the linearity of the outer code. The resulting computation becomes simpler allowing to keep yet a higher number of terms in the weight spectrum. We recall that symbol based codes proposed in our study consisting of codes over rings and $\log_2 M-$binary CC are linear codes. Therefore, despite the concatenation with inner CPM, we can still assume that the uniform error probability holds for the outer code, and the transmission of the all-zero codeword can still be considered to compute the OWEF of the convolutional encoder. In this case the symbol alphabet at the output of the convolutional code corresponds to $\{0, 1, ..., M-1\}$. Sequences causing an outer code error are identified as well as their enumerating function with respect to the all-zero sequence $\bar{l}$ ($\bar{l} = \{$num. of (1), num. of (2), num. of (3)$\}$). These sequences could be easily mapped into difference sequences when a symbol to symbol subtraction with respect to the all-zero symbol sequence is performed. Note that the cardinality of the outer code error sequences is the same for symbol and difference symbol sequences ($\left|\bar{l}\right| = \left|\tilde{l}\right|$).

The resulting alphabet is then extended to $\{-M+1, -M+2, ..., M-2, M-1\}$. The corresponding enumerating function becomes then $\tilde{l}$ and the OWEF $A^{out}_{\tilde{l}}$ can be easily obtained using standard WEF computation methods for binary codes with the slight difference that the procedure is performed at difference symbol level. Finally, the totality of $A^{out}_{\tilde{l}}$ coefficients can be simply obtained by considering all possible difference symbol combinations $\tilde{l}$.

Note that only difference symbol combinations that lead to an error event for the CPM known as effective symbol sequences satisfying equ. 3.46 of section 3.6.1 need to be considered. Consequently, we define $A^{out}_{\tilde{l}_{eff}}$ as the effective WEF of the outer code and replace $A^{out}_{\tilde{l}}$ in equ. 4.8 by this term.

The computation of $A^{out}_{\tilde{l}_{eff}}$ is followed by the computation of the IOWEF $\overline{A}^{in}_{\tilde{l},d_{NSED}}$ of the CPM. For every effective sequence $\tilde{l}_{eff}$ identified in $A^{out}_{\tilde{l}_{eff}}$, the corresponding $\overline{A}^{in}_{\tilde{l},d_{NSED}}$ should be computed.

We can summarize the steps to be followed in order to compute the bound on the frame error probability of symbol-interleaved SCCPM as follows:

1. Compute $A^{out}_{\tilde{l}}$ using standard WEF computations for linear codes. To reduce complexity, the computation of $A^{out}_{\tilde{l}}$ can be truncated to a maximum number of non-zero symbols $\left|\tilde{l}\right|_{\max}$. Typically, $\left|\tilde{l}\right|_{\max} = 6$ or 7 is sufficient.
2. Identify vector sequences known as $\tilde{l}_{eff}$ corresponding to non-zero enumerating sequences $\tilde{l}$ leading to effective difference sequences in CPM. This is followed by the derivation of the effective WEF $A^{out}_{\tilde{l}_{eff}}$.
3. Process all possible difference symbol permutations corresponding to every $\tilde{l}_{eff}$ enumerating vector over a sequence with a truncated length N_s^{trunc}.
4. For every permuted sequence corresponding to a vector $\tilde{l}_{eff}$, compute the corresponding Euclidean distance of the CPM and its multiplicity $\overline{A}^{in}_{\tilde{l},d_{NSED}}$.
5. Substitute the computed terms in equ. 4.8 and then in equ. 4.7.

Note that the accurate evaluation of $\overline{A}^{in}_{\tilde{l},d_{NSED}}$ requires considering all possible difference sequence permutations over the frame length in symbols N_s, corresponding to the totality of vectors $\tilde{l}_{eff}$ of the outer code spectrum. This task is unfeasible for large values of $\tilde{l}_{eff}$ and N_s. In order to simplify this step while keeping dominant terms in the computation of the bound, the length of $\tilde{l}_{eff}$ vectors is limited to values around 6 or 7 (as in step 1.) and the permutations are performed over a truncated length $N_s^{trunc} < N_s$. In practice, $N_s^{trunc} = 10$ to 12 can be assumed.

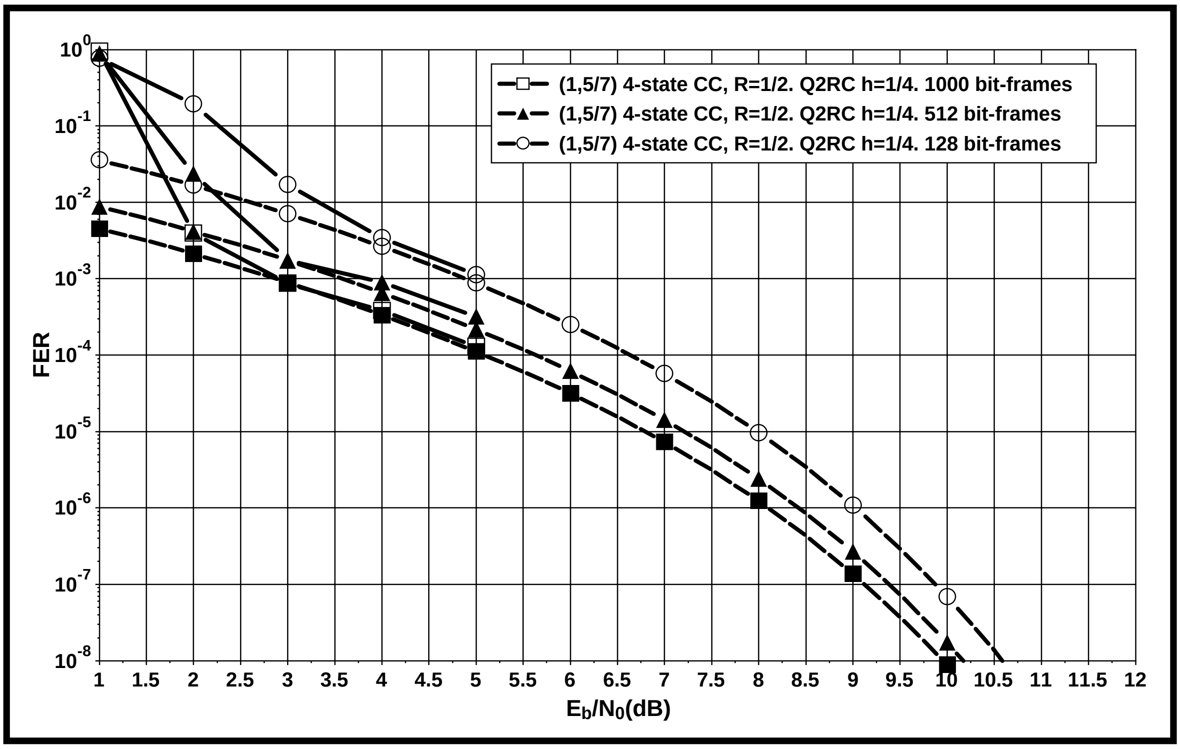

Figure 4.15 — Bound validation example for $R = 1/2$ symbol-interleaved (1,5/7) CC coded Q2RC $h = 1/4$ for the transmission of 128-, 512- and 1000-bit frames

Fig. 4.15 demonstrates the accuracy of the frame error rate bound for symbol-interleaved $(1, 5/7)$ $R = 1/2$ coded Q2RC $h = 1/4$ for the transmission of 128-, 512- and 1000-bit frames.

FER curves of Fig. 4.16 represent yet another evidence of the accuracy of the symbol-interleaved bounds on the probability of frame error as they confirm the tightness of these analytical bounds for the following SCCPM systems:

- $R = 1/2$ symbol-interleaved (1,5/7) CC coded Q2RC $h = 1/4$ and $h = 2/5$ for the transmission of 1000- and 512-bit frames respectively.
- $R = 4/5$ symbol-interleaved $(1,(1 + D)/(1 + D + D^2))$ CC over ring Z_4 with Q3RC $h = 2/7$ for the transmission of 1272-bit frames.

4.5.4 Symbol-interleaved SCCPM

4.5.4.1 Introduction

Targeting the best convergence threshold for a given SE, we actually started our study of SCCPM by investigating symbol-based interleaving, since in previously treated studies of concatenated codes (e. g. [41]) symbol-based systems have been shown to offer earlier convergence when compared to their bit-based counterparts.

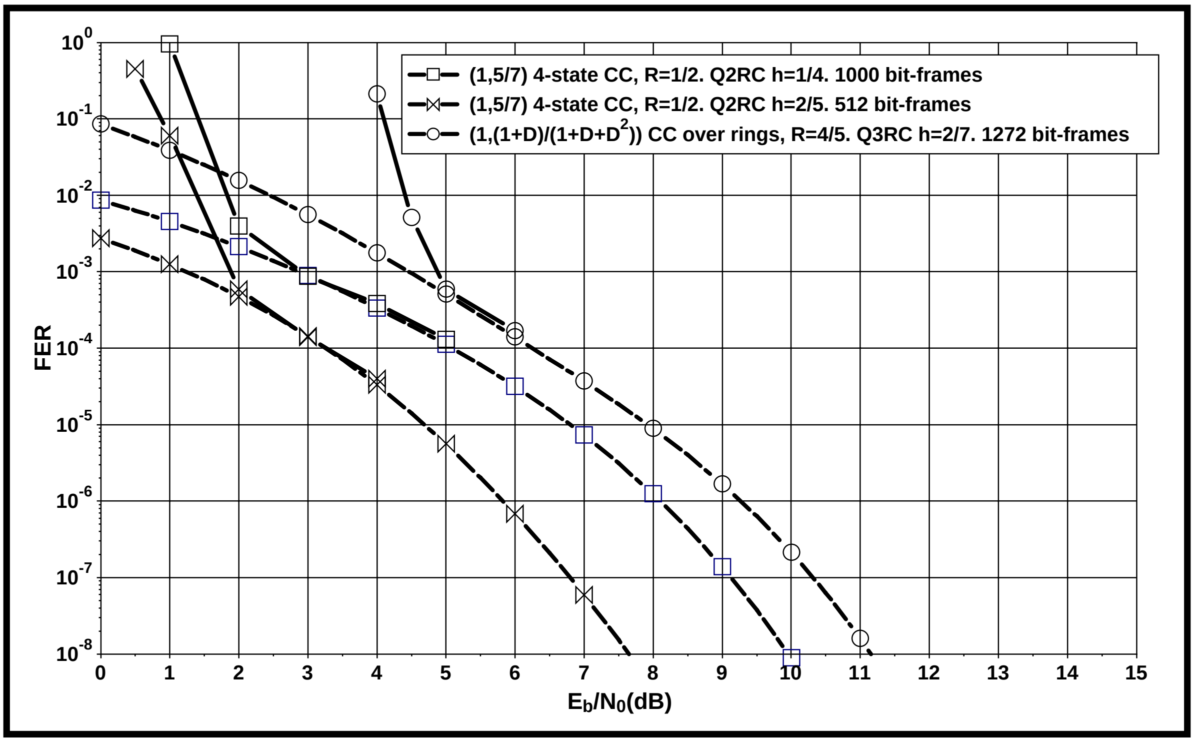

Figure 4.16 — Bound validation example for two types of symbol-interleaved SCCPM: $R = 1/2$ (1,5/7) CC coded Q2RC with $h = 1/4$ and $h = 2/5$ for the transmission of 1000- and 512-bit frames respectively and $R = 4/5$ $(1, (1+D)/(1+D+D^2))$ CC over ring Z_4 with Q3RC $h = 2/7$ for the transmission of 1272-bit frames.

4.5.4.2 Signal mapping

In the case of symbol-interleaved SCCPM, the mapping type does not affect FER error correcting performance. In fact as the mapping is performed before the interleaver, it does not have any influence on the FER performance. BER curve could be slightly modified, but since the probability of bit error is symmetric for 1s and 0s we would not expect the difference to be noticeable.

4.5.4.3 Symbol-interleaved SCCPM with codes over rings

The authors of [73, 62, 75] have compared symbol-based to bit-based interleaving techniques for SCCPM. For the symbol-based systems, they have studied binary codes as well as codes over algebraic rings. The SCCPM structure under investigation is described by configuration (1) of section 4.5.2. The motivation for going from the usual GF(2) to integer rings is to explore the existing natural relation between M-ary CPM and codes over integer rings. They call for the same algebra concerning addition and multiplication operations by labelling the signal points of M-ary phase modulation by the ring elements $0, 1, \cdots, M-1$.

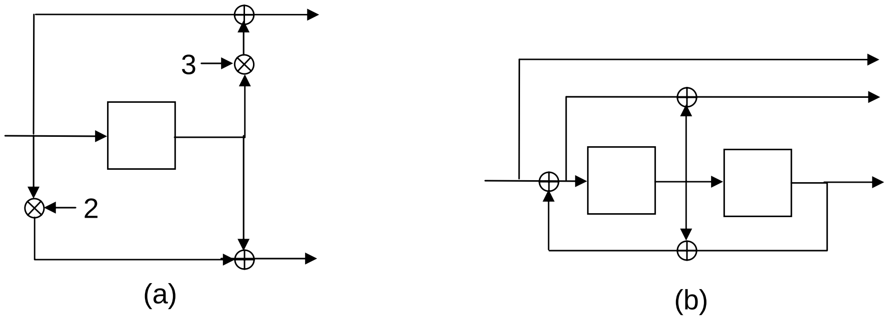

Figure 4.17 — Codes over ring Z_4 for Q2RC SCCPM (a) 4-state code. (b) 16-state code. Symbol $\oplus$ stands for the modulo 4 addition.

The conclusions of the study point out that the design of symbol-based codes adapted to the CPM is essential when symbol interleaving is adopted. The design procedure should follow specific guidelines taking into account CPM error events and effective difference symbol distance (see section 3.6.1). Best proposed 4- and 16-state codes over ring Z_4 in the error floor region for Q2RC by the authors of [73, 62, 75] are presented in fig. 4.17. These codes over rings designed for symbol interleaving show earlier convergence thresholds than classical binary codes with bit interleaving and comparable complexity.

The study in [73, 62, 75] of symbol-interleaved codes over rings is complete in the sense that both aspects (convergence threshold and error floor) of the corresponding SCCPM were treated. The obtained results in [73, 62, 75] can easily be extrapolated to be used in our study. We had only to check by means of Monte Carlo simulations and bounding techniques if the proposed codes over rings satisfy the SCCPM requirements of our study in terms of convergence threshold and error floor.

4.5.4.4 Symbol-interleaved SCCPM with $\log_2 M-$binary convolutional codes

A possible alternative to the codes over rings could be the $\log_2 M-$binary code. This code structure is symbol-based as it encodes $\log_2 M$ bits in one symbol period. The SCCPM structure under investigation is configuration (2) in fig. 4.10. The generator polynomial of the $\log_2 M-$binary code should satisfy the design constraints of the symbol based SCCPM. Consequently, a search for competitive $\log_2 M$-binary codes for SCCPM has been performed. This search has been performed considering the code structure presented in [80] and reported in fig 4.18.

Fig. 4.18 describes a convolutional code with n inputs U_i and w outputs R_j. The alphabet of the inputs and outputs is a variable and it can span all integers (generally a power of 2). h_{ij} and z_{ij} are elements of connection matrices. h_{ij} values define the recursivity of the code as well as the input matrix connections. z_{ij} values define the ouput polynomials for parity

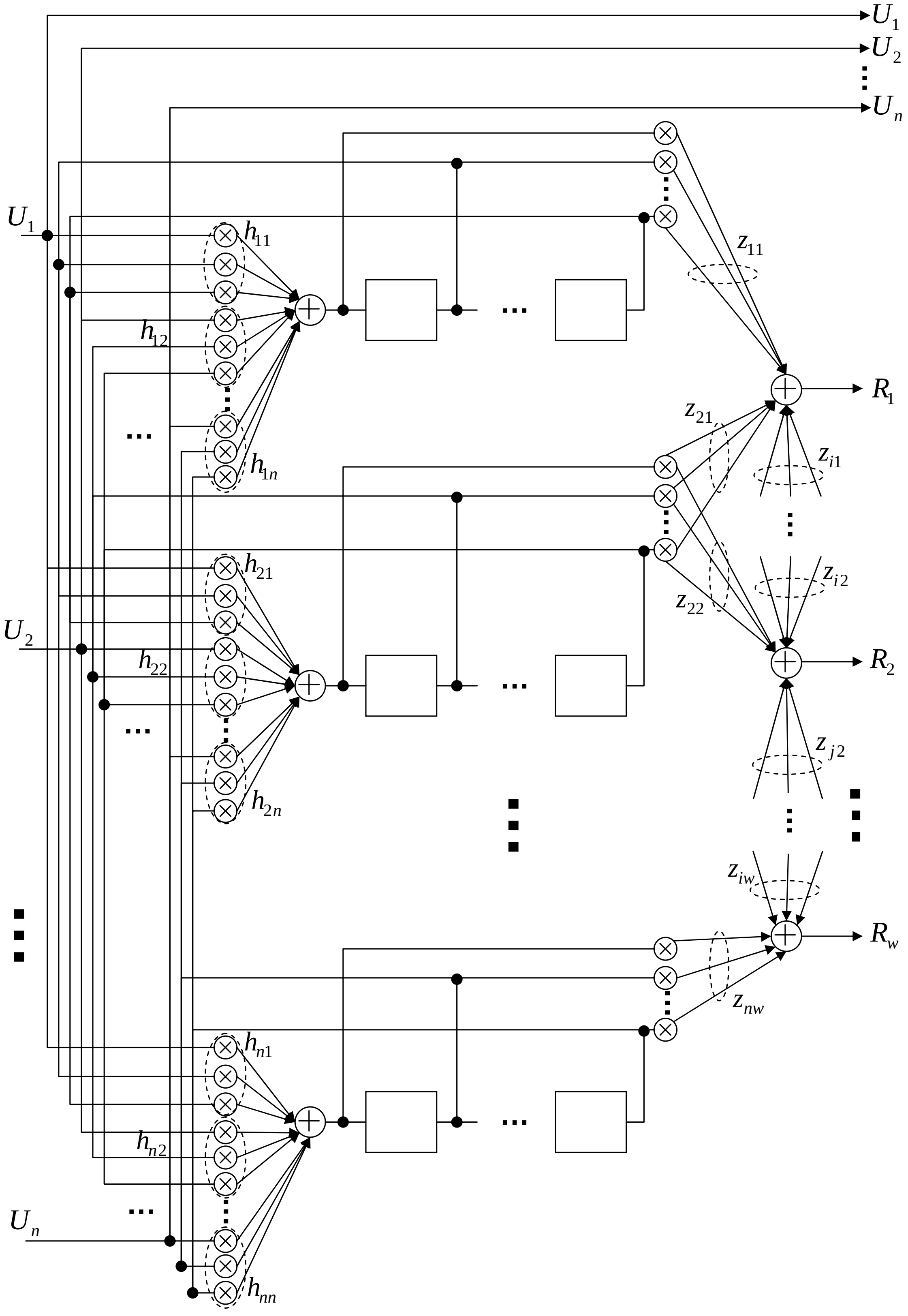

Figure 4.18 — Generalized code structure used for the search for symbol based codes

outputs.

Code optimization:

The outer code and its puncturing should be selected to minimize the error floor. The dominant term in the error floor is the one associated with the highest exponent $\alpha_{M,\max}$ of the interleaver size, defined as [73, 62, 75]:

$$\alpha_{M,\max} = \max\left\{ n_{in} + n_{out} - \left|\tilde{l}\right|_{\min}^{eff} - 1 \right\} \tag{4.9}$$

where $\left|\tilde{l}\right|_{\min}^{eff}$ denotes the number of non-zero symbols of the CPM effective sequence. n_{in} and n_{out} denote the number of inner and outer error events in symbols, respectively. In [73, 62, 75] the minimization of $\alpha_{M,\max}$ is proposed to list all codes achieving the highest interleaving gain. Then union bounds are computed to select the best code in terms of error floor. Unfortunately, this criterion links the selection of the outer code to the CPM (note that $\left|\tilde{l}\right|_{\min}^{eff}$ depends on both the outer code and the CPM). In other words, changing the CPM may lead to another outer code choice. However, one would be primarily interested in designing a good outer code independently of the CPM. Therefore, a different optimization criterion is proposed here. From (equ. 4.9) it arises that the interleaver gain increases with $\left|\tilde{l}\right|_{\min}^{eff}$. Moreover, one would expect that maximizing $\left|\tilde{l}\right|_{\min}$ leads to the maximization of $\left|\tilde{l}\right|_{\min}^{eff}$, and hopefully to the maximization of $\alpha_{M,\max}$. Since $\left|\tilde{l}\right|_{\min}$ depends only on the outer code, it is a more appealing parameter for code optimization. Now, maximizing $\left|\tilde{l}\right|_{\min}$ is equivalent to maximizing $\left|\bar{l}\right|_{\min}$ (actually, $\left|\tilde{l}\right|_{\min} = \left|\bar{l}\right|_{\min}$). Therefore, we can assume the maximization of $\left|\bar{l}\right|_{\min}$, and more generally the optimization of the symbol distance spectrum $A_{\tilde{l}}^{out}$ of the outer code, as the key design criterion, independently of the inner CPM. $A_{\tilde{l}}^{out}$ can be easily evaluated by using standard WEF computations for linear codes.

An exhaustive search for rate $\frac{2}{4}$, 4-state and 16-state double-binary codes was performed to optimize $A_{\tilde{l}}^{out}$, as previously described. We are going to illustrate our search procedure by an example.

Search example:

In this example, we have launched a search to find codes suited for Q2RC $h = 1/4$ as it was chosen as a reference in section 4.5.3.1. This implies $n = 2$, $w = 2$ in the code structure of fig. 4.18. The code to be found is a rate $\frac{2}{4}$ binary code that can be seen as a rate $\frac{1}{2}$ quaternary code if a mapping is applied at the output of the corresponding encoder.

In the case of a 4-state outer code, an effective distance of 4 and a maximum interleaver gain of $\alpha_{M,\max} = -2$ was found for both, the best double binary code in the error floor region resulting from our search and the best code over rings reported by the authors of [73, 62, 75] (see fig. 4.17).

When the number of code states is increased to 16, the highest interleaver gain of the codes over rings reported in [73, 62, 75] for Q2RC is -3. It is the code presented in fig. 4.17. It was proposed as an alternative to the 4-state code when lower floors are needed.

16-state $\log_2 M$ CC	h_{ij} matrix		z_{ij} matrix		d_{symb}
	U_1	U_2	R_1	R_2	
Code # 1	$h_{11} = 111$ $h_{21} = 000$	$h_{12} = 011$ $h_{22} = 101$	$z_{11} = 111$ $z_{21} = 000$	$z_{12} = 010$ $z_{22} = 111$	6
	U_1	U_2	R_1	R_2	
Code # 2	$h_{11} = 111$ $h_{21} = 000$	$h_{12} = 011$ $h_{22} = 110$	$z_{11} = 001$ $z_{21} = 101$	$z_{12} = 010$ $z_{22} = 101$	6
	U_1	U_2	R_1	R_2	
Code # 3	$h_{11} = 111$ $h_{21} = 000$	$h_{12} = 011$ $h_{22} = 110$	$z_{11} = 101$ $z_{21} = 011$	$z_{12} = 001$ $z_{22} = 101$	6

Table 4.2 — Table of first three best 16-state double binary codes in terms of symbol distance. The classification takes their respective multiplicities into account.

Table 4.2 enumerates the best three 16-state double binary codes ($\log_2 M = 2$) found, in terms of symbol distance.They are enumerated in increasing multiplicity [24] order. Code number 1 enjoys a minimum effective difference distance of 6 and an interleaver gain of -3. It should offer the best error correcting performance asymptotically with SCCPM of all double binary symbol-interleaved codes. It is expected to outperform the 16-state code over ring proposed in [73, 62, 75] when associated with the same inner CPM since it offers improved multiplicity.

4.5.4.5 Frame error rate Monte Carlo simulation results

FER Monte Carlo simulations were undertaken in order to:

- check the results of the search procedure.
- verify if the proposed codes (over rings and double binary) can satisfy the code design requirements.

We have simulated:

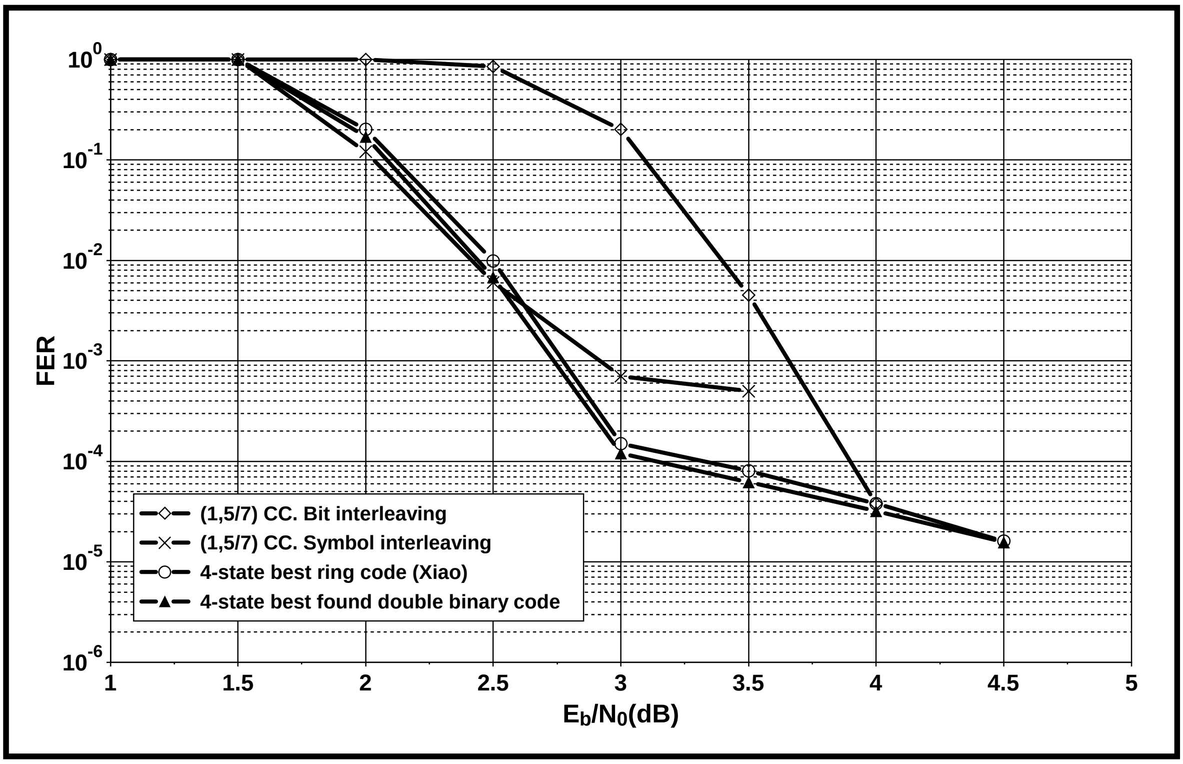

Figure 4.19 — FER comparison of $R = 1/2$ 4-state codes with a Q2RC $h = 1/4$ CPM

- 4-state codes: the code over ring Z_4 of section 4.5.4.3, the best found double binary code, and the symbol and bit interleaved classical $(1, 5/7)$ binary code. Results are presented in fig. 4.19.

- 16-state codes: the code over ring Z_4 of section 4.5.4.3, the double binary code number 1 of table 4.2 and the symbol and bit-interleaved classical $(1, 35/23)$ binary code. Results are shown in fig. 4.20.

For all simulated codes, 10 iterations to the CPM were performed for the transmission of 500-bit frames with a code rate of 1/2 and uniform symbol and bit interleaving.

From simulation results of fig. 4.19 we can observe that:

- The best code over ring enjoys a lower floor when compared to the classical $(1, 5/7)$ 4-state code.

- The symbol-based double binary 4-state code shows quasi-identical error correcting performance as the best 4-state code over rings.

- Symbol-interleaved SCCPM enjoys earlier waterfall performance than bit interleaved SCCPM. The gap is estimated to 0.8 dB for 4-state codes.

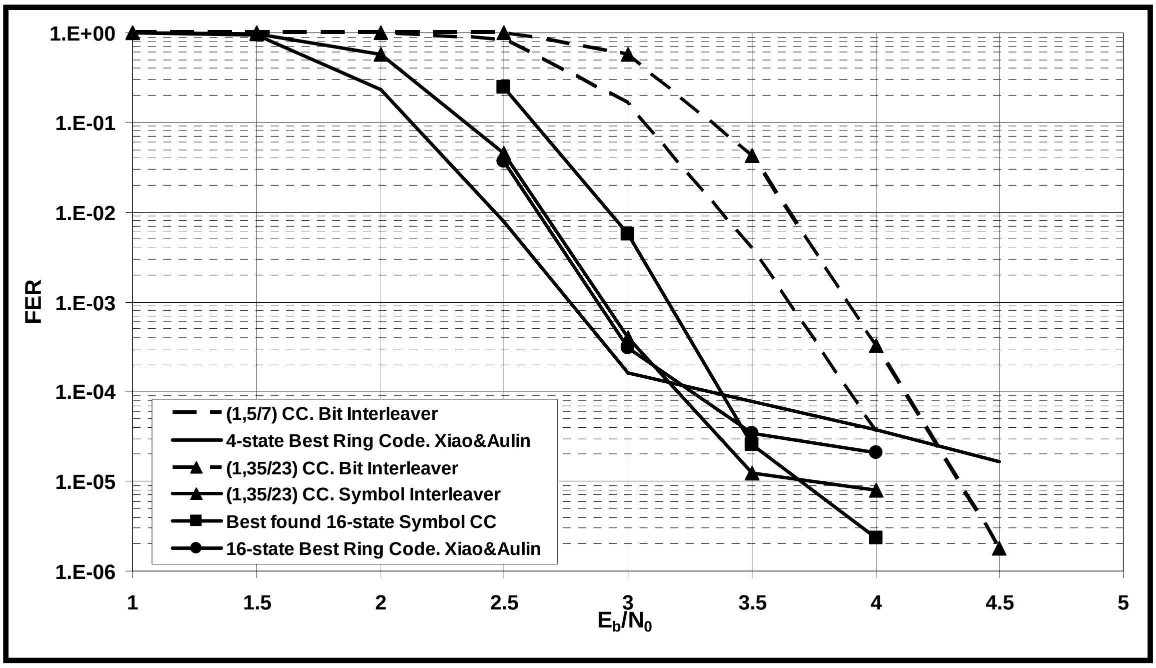

Figure 4.20 — FER comparison of $R = 1/2$ codes with a Q2RC $h = 1/4$ CPM

- Bit-interleaved SCCPM shows lower error floors when compared to symbol interleaved SCCPM.

When the number of code states is increased to 16 (fig. 4.20), we can say that:

- 16-state symbol CC suffers from a loss in convergence with respect to 4-state CC. It is around 0.2 dB for the $(1, 35/23)$ binary CC and the code over ring. Around 0.45 dB separates the best 4-state code and the best 16-state double binary code.

- The symbol-based double binary code shows the lowest error floor of all simulated symbol-based codes. This improved asymptotical performance confirms the code search results. The floor is around one order of magnitude lower than the one for the code over rings.

- A gap of 0.2 dB separates the 4 state $(1, 5/7)$ code from the 16-state $(1, 35/23)$ code with bit interleaving.

- A gap of 0.5 dB separates the best 16-state double binary code from the bit-interleaved $(1, 5/7)$ code at 10^{-4} of FER. An even larger gap to the $(1, 35/23)$ exists.

Taking into account that the corresponding SIR resides at an E_b/N_0 of 1.4 dB, it is worth mentioning that even for a quite small frame size we are able to be within 2.0 dB (symbol-based) from the SIR at 10^{-4} of FER. Nevertheless, despite the search for best codes, a floor at 10^{-4} of FER is unavoidable for 4-state symbol based codes even without puncturing. Consequently, this type of codes cannot satisfy target floors of 10^{-6} of FER.

On the contrary, simulations of fig. 4.20 show that the proposed best double binary $R = 1/2$ 16-state code is able to achieve the target error floor. Nevertheless, it is questionable if it will still be the case after puncturing.

In order to apply suitable symbol puncturing patterns, we had to run a new search. We have used the best found symbol-based code and performed a trellis search for puncturing patterns that lead to the highest effective distance and interleaver gain for the target code rate:

- For $R = 4/5$, a puncturing periodicity of 8 symbols and the following pattern: 11X11X1X where 1 denotes a kept position and X a punctured one and the symbols are ordered in the form SR...SR. where S denotes a systematic symbol and R denotes a redundancy symbol.
- For $R = 2/3$, a puncturing periodicity of 6 symbols and the following pattern: 111X1X.

FER simulations have been undertaken for the double binary code number 1 of table 4.2 for $R = 2/3$ and $R = 4/5$ and have been compared to the bit interleaved $(1, 5/7)$ CC for $R = 2/3$, and to the bit-interleaved $(1, 35/23)$ CC for $R = 4/5$. Results for $R = 2/3$ are presented in fig. 4.21.

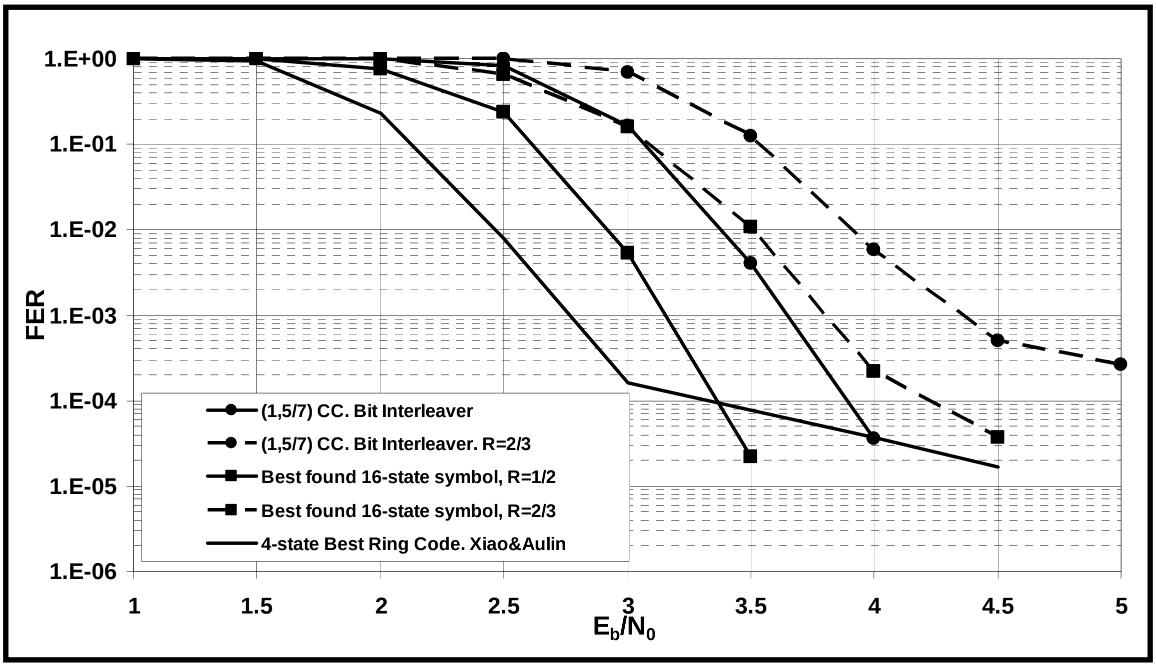

Figure 4.21 — FER comparison of $R = 1/2$ and $R = 2/3$ CC with a Q2RC $h = 1/4$ CPM

The simulations for $R = 2/3$ show a presence of an error floor for the 16-state best symbol-interleaved code at 2.10^{-4} of FER and for the $(1, 5/7)$ CC at 5.10^{-4} of FER. Here, the 16-state symbol code offers a floor comparable to the one of a 4-state bit-interleaved code. Hence, the two simulated codes do not satisfy error floor requirements for $R = 2/3$.

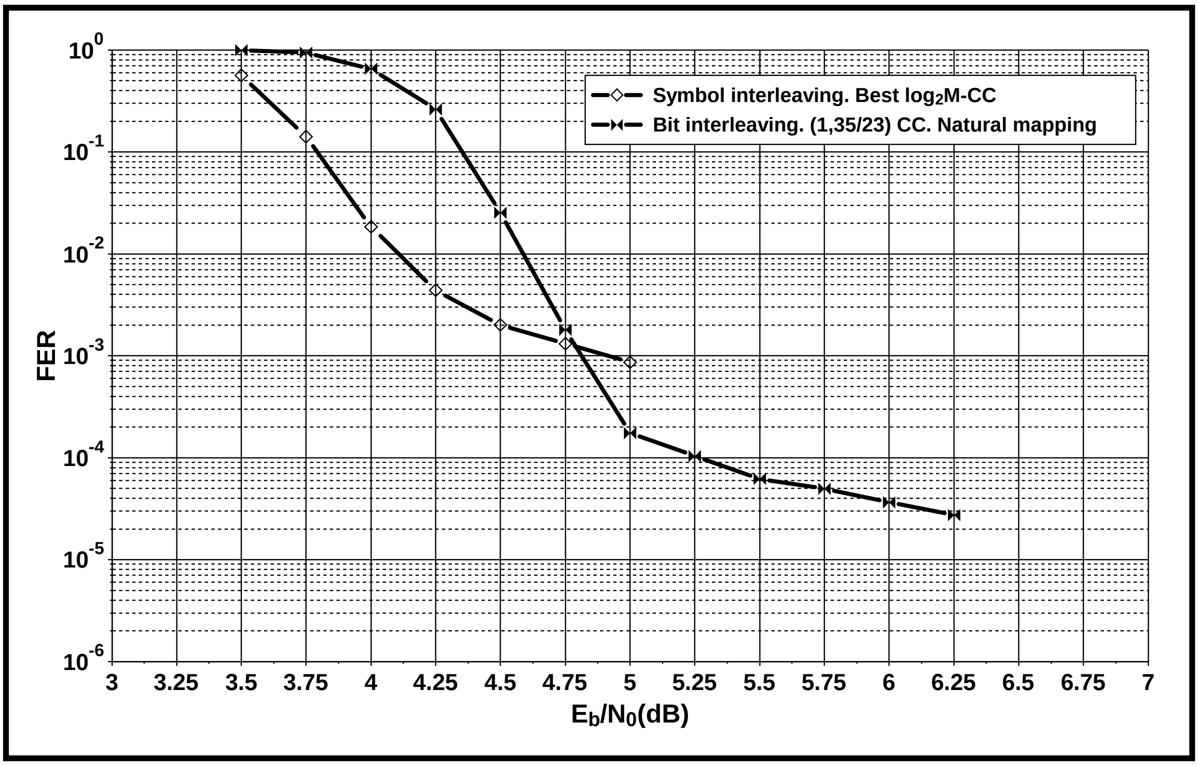

Figure 4.22 — FER comparison of bit and symbol-interleaved Q2RC $h = 1/4$. For symbol interleaving the best symbol-based code is used. For bit interleaving, the 16-state (1,23/35) code is used for natural mapping. Code rate is $R = 4/5$

The high sensitivity of error floor performance to the increase of the code rate for symbol-interleaved codes becomes obvious for $R = 4/5$. In fact, results of fig. 4.22 show an error floor for the double binary CC around 10^{-3} of FER whereas it is at 2.10^{-4} for the bit-interleaved $(1, 35/23)$ CC. Notice that the gap between the convergence thresholds is reduced to 0.5 dB when the code rate is increased to 0.8.

Conclusions:

We can conclude this section by stressing on the following observations:

1. Symbol-based SCCPM offers the earliest iterative convergence thresholds.
2. Best found 4 and 16-state double binary codes for Q2RC $h = 1/4$ do not satisfy code design requirement for the target error floors. The error correcting behaviour of SCCPM becomes alarming when the code rate increases.

3. When the code rate increases, the gap between the waterfall of the symbol and bit-interleaved SCCPM decreases.

Consequently, powerful symbol-interleaved codes should be investigated. They could include higher constraint length $\log_2 M$-CC or concatenated codes such as turbo codes.

4.5.4.6 Symbol-interleaved SCCPM with turbo codes

Introduction

After the breakthrough of turbo codes and iterative decoding techniques, turbo-like codes became the building stone of many studies of coded systems. Offering quasi-optimum performance when associated with linear modulations over Gaussian channels, it seemed then natural to study the association of turbo-like codes with non-linear modulations and more precisely CPM.

Previous work

Previous work on double binary turbo coded CPM with symbol interleaving has already been done in literature. The approach in [77] is obtained from configuration (2) of fig. 4.10 by replacing the simple outer CC by a double binary turbo code and by setting the permutation function π to the identity function. The solution in [77] is designed to group the systematic outer code symbol and its corresponding redundancy together into one CPM symbol. The resulting transmitter represents then a sort of Trellis-Coded Continuous Phase Modulation (TCCPM). As we know from previous works on trellis-coded modulations, this type of schemes offers best performance in terms of error rates over Gaussian channels. Only symbol based double binary turbo coded O2RC systems were investigated in [77].

Study of symbol-based SCCPM with turbo codes

We have started by comparing the proposed solution of [77] to the previously proposed solutions of [63, 72] where bit interleaving and an outer CC were adopted. The approach of [77] reveals to be interesting from the error correcting point of view. It shows waterfall performance comparable to the best achievable previously presented approaches and lower error floors.

The superior error correcting performance results from the fact that the O2RC scheme is tailored to the outer code in order to achieve a TCCPM-like structure. We can think of yet another possible SCCPM scheme offering a TCM-like structure consisting of a quaternary CPM with an outer binary turbo code with a code rate of $R = 1/2$. However, this type of solution looses its interesting error correcting capability and the trellis coded modulation property when any of the following parameters is changed:

- the code rate
- the alphabet size of the CPM.

In fact simulations were undertaken using the well known double binary DVB-RCS [53] code associated with different CPM sets of parameters. When a TCCPM structure was respected, the resulting system offered interesting error correcting performance, rather close to the SIR (within 1 dB at 10^{-5} of BER for the transmission of 2000-bit frames). When this structure type was not respected (changing either the rate or the alphabet size of the CPM), the system offered late convergence thresholds (2 to 2.5 dB) away from the SIR. Symbol puncturings and the division of the code rate between two constituents are to be blamed in this case.

TCCPM structure being very restricting from the design point of view, the design of turbo codes with symbol interleaving for SCCPM was abandoned.

4.5.4.7 Conclusions on symbol-based SCCPM

We have tested different codes with symbol-based SCCPM ranging from convolutional codes over rings and $\log_2 M-$binary CC to turbo codes. For all tested SCCPM structures with symbol interleaving, the solutions did not offer a satisfactory answer to the code design requirements of our study. The cases where the outer code was a standalone CC suffered from an alarming error floor. The cases where the outer code was a turbo code did not present acceptable convergence thresholds.

We can conclude the symbol based SCCPM study by asserting that structures based on this type of solution do not satisfy the code design requirements of our study with a reasonable complexity. This research axis has been abandoned.

4.5.5 Bit-interleaved SCCPM

4.5.5.1 Introduction

Since bit-based SCCPMs offer higher spread and higher diversity order than their symbol counterparts, we have opted for the study of this type of SCCPM schemes. In fact, if we consider equ. 4.6 when symbol interleaving is adopted, N represents the sequence length in number of symbols. For quaternary CPM for example it represents half the total number of bits in the frame. Consequently, as the decay of the probability of error is dependent on the power of the frame size, bit-interleaved SCCPM having a larger value of N should outperform in terms of error correction symbol-interleaved SCCPM. Moreover, the symbol interleaver working on half the frame size of the bit interleaver, it can logically offer half the spreading properties when compared to the latter.

The approach adopted in our study is inspired by the work in [63] and [72]. The authors have studied the concatenation of some CPM systems and an outer convolutional code with bit interleaving. The considered CPM schemes enjoy low complexity but do not achieve high spectral efficiencies. In fact, a comparison to MSK in terms of bandwidth occupation, error rate performance and complexity was one of the motivations of the study. The work in [63, 72] has provided a deep first comprehension of concatenated iterative CPM schemes and has the merit of starting a renewed wave SCCPM studies. Nevertheless, as it had different goals from our study, the reported results are not directly applicable in our case.

Other outer codes but a CC have already been investigated with SCCPM:

- Irregular Repeat Accumulate (IRA) codes [84] in [74]. The degree profile of IRA codes represents a main design parameter as it defines the transfer chart of the code. When encapsulated in a SCCPM structure, the degree profile can be chosen in a way that matches best the CPM from the EXIT charts point of view. This type of codes is simple to decode. The price to pay is high error rate floors (around 10^{-5} of BER for unpunctured codes and 2000-bit frames). We can also mention a high implementation latency as the number of iterations necessary to achieve convergence is quite high (around 100 iterations).

- Low Density Parity Check (LDPC) codes in [76]. The authors study the design of an outer LDPC code for a serial concatenation with CPM and propose ways of parity-check matrix optimization. On one side, the main interest of this study lies in its propositions on LDPC design methods for CPM. On the other side, the authors prechoose the CPM set of parameters that is kept unchanged for the study. We can also point out that no comparison with pre-existing coding techniques for CPM is shown. In fact, if compared with solutions presented in [63, 72], the proposed best LDPC schemes for CPM show a gap of 2.0 dB in waterfall performance.

As far as we know about previous work on bit-interleaved SCCPM, no direct and complete comparison between different families of codes and between different set of CPM parameters yielding the best SCCPM structure attaining a target spectral efficiency has been done yet. The main goal of our study is then to fill in the existing gap in the literature concerning the real world implementation of bit-interleaved SCCPM solutions.

4.5.5.2 Signal mapping

In the case of bit-interleaved SCCPM, the mapping type represents one of the parameters that act on the error correction capability. It has been mentioned in [63, 72] that CPM systems suffer from weight one error events. For this type of errors, the decoder could diverge at a particular state from the transmitted sequence without merging back until the end of the frame. These are undesirable events causing quite high error floors and should be avoided. The authors of [63, 72] proposed to modify the mapping type as a solution. In fact weight one error events are modulation index dependent:

- For $M = 2$, weight one error events appear for integer values of the modulation index.
- For $M = 4$ with natural binary mapping, only $h = K/2$ modulation indices suffer from this type of errors. On the other hand, with Gray mapping we get the condition $h = K/3$.
- For $M = 8$ with natural binary mapping, we have $h = K/4$. With Gray mapping, $h = K/3$, $h = K/5$ or $h = K/7$ all are necessary and sufficient conditions.

Since the values of p leading to weight one error events are different for the 2 types of mapping when $M \leq 8$, it is always possible for a given modulation index to avoid input weight one error events by selecting the mapping.

From FER simulations, we observed that Gray mapping offers earlier convergence than natural mapping when weight one error events are avoided. It seems that this result has not been reported in any previous work. Further EXIT chart analysis allowed us to confirm this behavior.

Fig 4.23 shows that for any value of the mutual information I_{in} at the input of the Q2RC $h = 1/4$ scheme, the corresponding mutual information at the output I_{out} is greater or at worse equal for the Gray mapped CPM when compared to the natural binary mapped one. Both are expected to have comparable floors as the gap between the two curves of fig 4.23 closes when the exchanged extrinsic information at the input increases approaching 1.

For quaternary CPM schemes, natural binary or Gray mapping constitute the only available options. For the octal schemes however, even if additional mapping types are possible, we chose to restrict ourselves to these two mapping types.

4.5.5.3 Bit-interleaved SCCPM with convolutional codes

In this section we investigate the SCCPM scheme of the configuration (3) of fig. 4.10 with an outer CC. The investigation starts by studying the effect of the mapping on the error correcting performance of this type of coded CPM. It continues to identify the effect of the

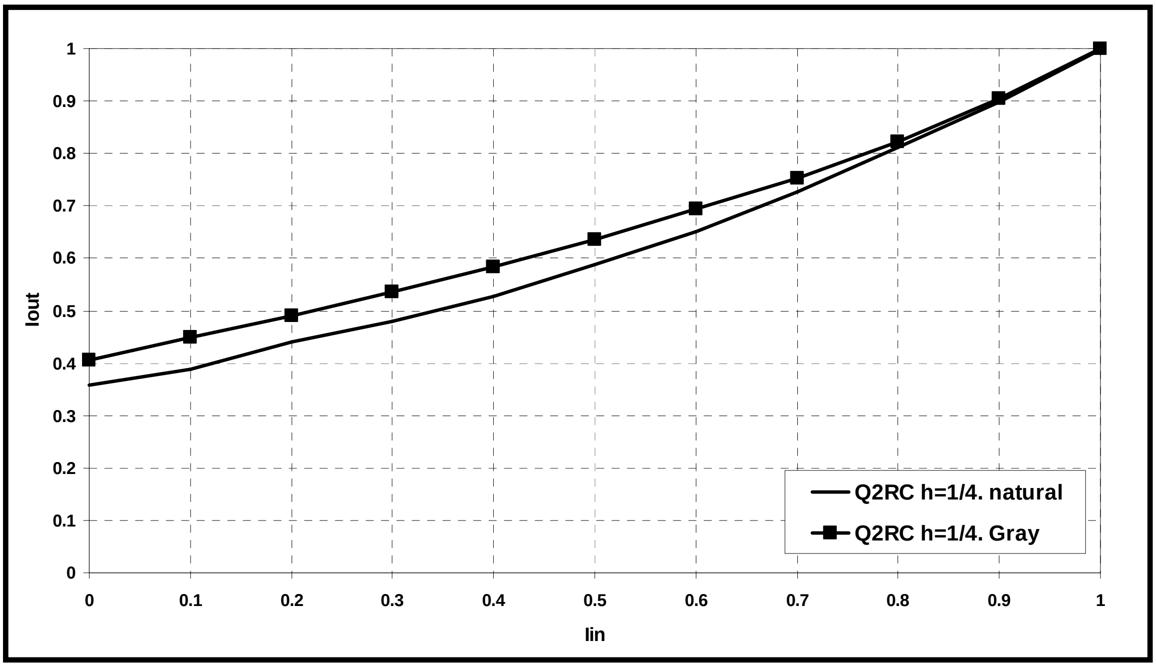

Figure 4.23 — EXIT comparison of natural and Gray mappings for Q2RC $h = 1/4$

constraint length of the outer CC on the convergence threshold and the error floor of bit interleaved SCCPM. The study then proceeds to evaluate the effect of puncturing on the performance. It ends by drawing some conclusions.

Mapping choice validation example

In order to validate our rationale concerning the mapping choice, FER simulations have been carried out for the concatenation of the outer 16-state $(1, 35/23)$ rate $1/2$ code with our reference CPM scheme (Q2RC $h = 1/4$). Results are plotted in fig 4.24.

We can see from fig. 4.24 that bit-interleaved Q2RC $h = 1/4$ converges 0.6 dB earlier when Gray mapping is used. On the other hand, it is still 0.4 dB away from symbol interleaving with the same outer code. But when higher rates are to be used, knowing that symbol puncturing leads to higher losses in convergence when compared to bit puncturing for the same rate, the Gray mapped system adopting bit interleaving could offer the best compromise in terms of error correcting performance both in convergence and floor regions.

Fig. 4.25 preserves the same SCCPM scheme as in fig. 4.23 but the outer code is punctured to a higher code rate of 0.8. The correposnding puncturing has a periodicity of 8 bits with the pattern 111X1X1X in the SRSRSRSR format (S= systematic bit and R= redundancy bit). For the symbol-interleaved system, the best 16-state double binary CC in the floor region is used with the best found puncturing pattern for the simulated rate (see section 4.5.4.5). For bit-interleaved systems, the outer $(1, 35/23)$ CC is used.

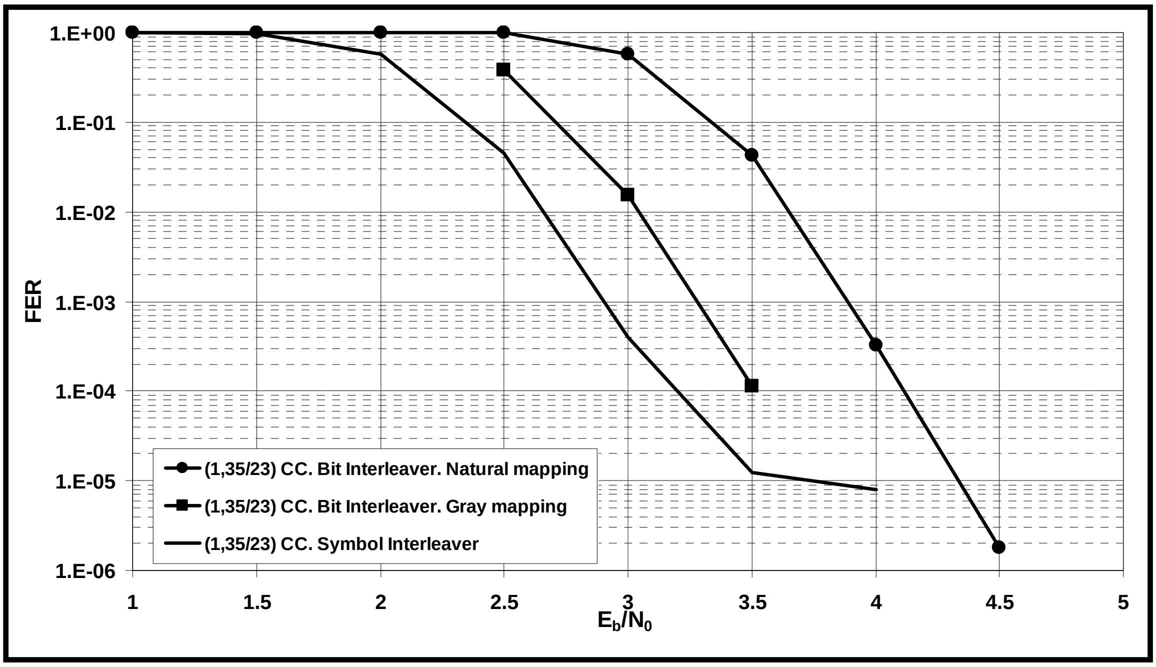

Figure 4.24 — FER comparison of Gray and natural mapping for bit-interleaved Q2RC $h = 1/4$ with the outer 16-state $R = 1/2$ (1,23/35) code for the transmission of 500-bit frames. Symbol-interleaved SCCPM was introduced for comparison purpose.

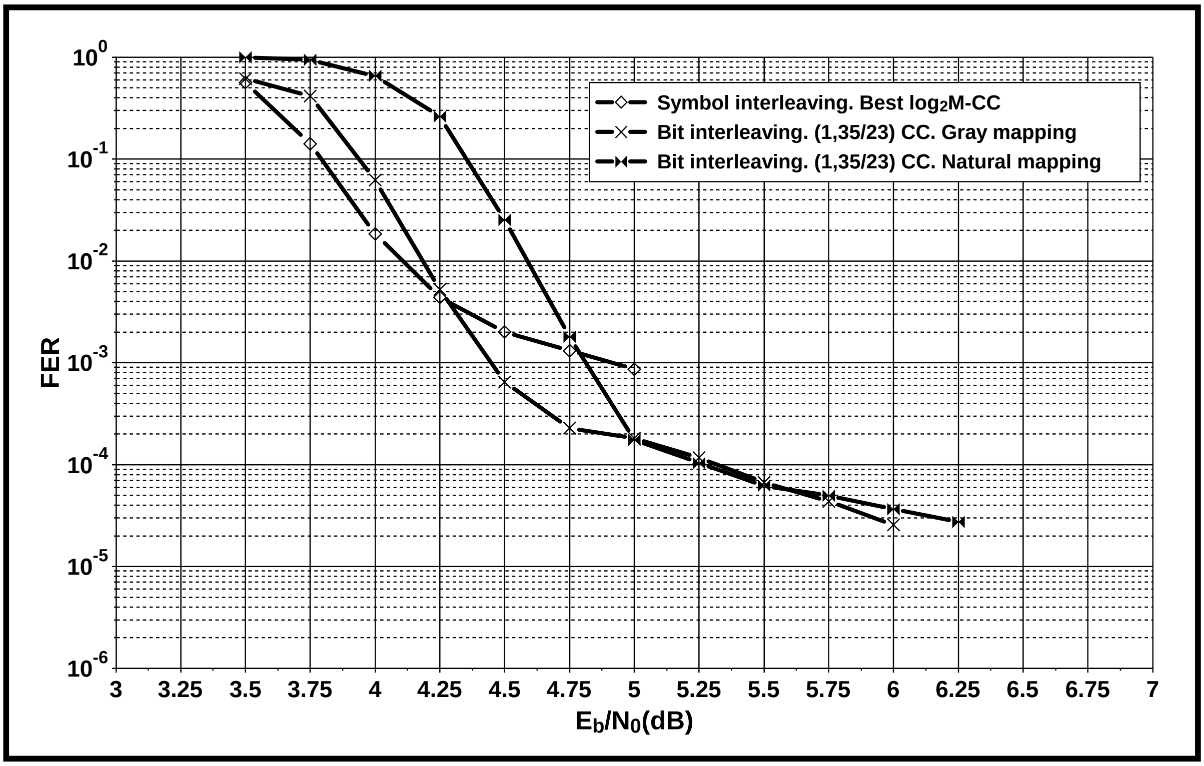

Figure 4.25 — FER comparison of Gray and natural mapping for bit-interleaved Q2RC $h = 1/4$ with the outer 16-state $R = 0.8$ (1,23/35) code for the transmission of 1272-bit frames. Symbol-interleaved SCCPM was introduced for bit-symbol comparison purposes

The symbol-interleaved SCCPM of fig. 4.25 shows unacceptable floor for our study. This was expected as the outer code is punctured to a high rate of 0.8. Having an interleaver working on 2-bit symbols, the spread of the interleaver is divided by a factor of 2. The gap separating the bit interleaved systems from the symbol-interleaved ones decreases when the code rate increases. In fact, the Gray mapped bit-interleaved SCCPM looses only 0.1 dB in convergence when compared to the symbol-interleaved SCCPM. It shows a lower error floor by two orders of magnitude: 0.4 dB separates natural from Gray mapping at the convergence threshold. They show quasi-identical floors. This result was predicted by the EXIT chart analysis of fig. 4.23.

Fig. 4.25 also shows that even with bit-interleaving, the SCCPM with a 16-state outer CC is not able to satisfy the 10^{-6} target error floor. Showing a minimum Hamming distance of 3 for a code rate of 0.8, this code suffers floors at 10^{-4} of FER for the Q2RC $h = 1/4$ CPM. Higher floors were also detected when concatenated with different sets of CPM parameters.

A trivial way to circumvent the floor problem involves increasing the number of memory cells of the convolutional code.

Effect of the code memory on the convergence threshold of SCCPM

Increasing the code memory leads to lower error floors but we expect a performance penalty for the convergence threshold. In the case of SCCPM, this penalty can be easily estimated by an EXIT chart analysis of different outer codes when the CPM set of parameters is kept unchanged.

Table 4.3 summarizes the convergence thresholds for the 4-state $(1, 5/7)$, the 8-state $(1, 13/15)$, the 16-state $(1, 35/23)$ and the 32-state $(1, 75/53)$ convolutional codes concatenated with our reference CPM scheme Q2RC, $h = 1/4$.

Convolutional code	4-state $(1, 5/7)$	8-state $(1, 13/15)$	16-state $(1, 35/23)$	32-state $(1, 75/53)$	64-state $(1, 171/133)$
Convergence threshold	1.8 dB	2.1 dB	2.2 dB	2.4 dB	2.6 dB
Gap to 4-state threshold	-	0.3 dB	0.4 dB	0.6 dB	0.8 dB

Table 4.3 — Convergence thresholds for 4, 8, 16, 32 and 64-state convolutional codes concatenated with a Q2RC $h = 1/4$ CPM

The values of the threshold gap provided in table 4.3 is CPM scheme dependent. In fact if we replace the Q2RC $h = 1/4$ by a Q3RC $h = 2/7$, the threshold gap values can be slightly different as shown in fig. 4.27 and table 4.4.

In the case of Q3RC $h = 2/7$ SCCPM, the threshold gaps seem slightly higher when compared to the Q2RC $h = 1/4$ case.

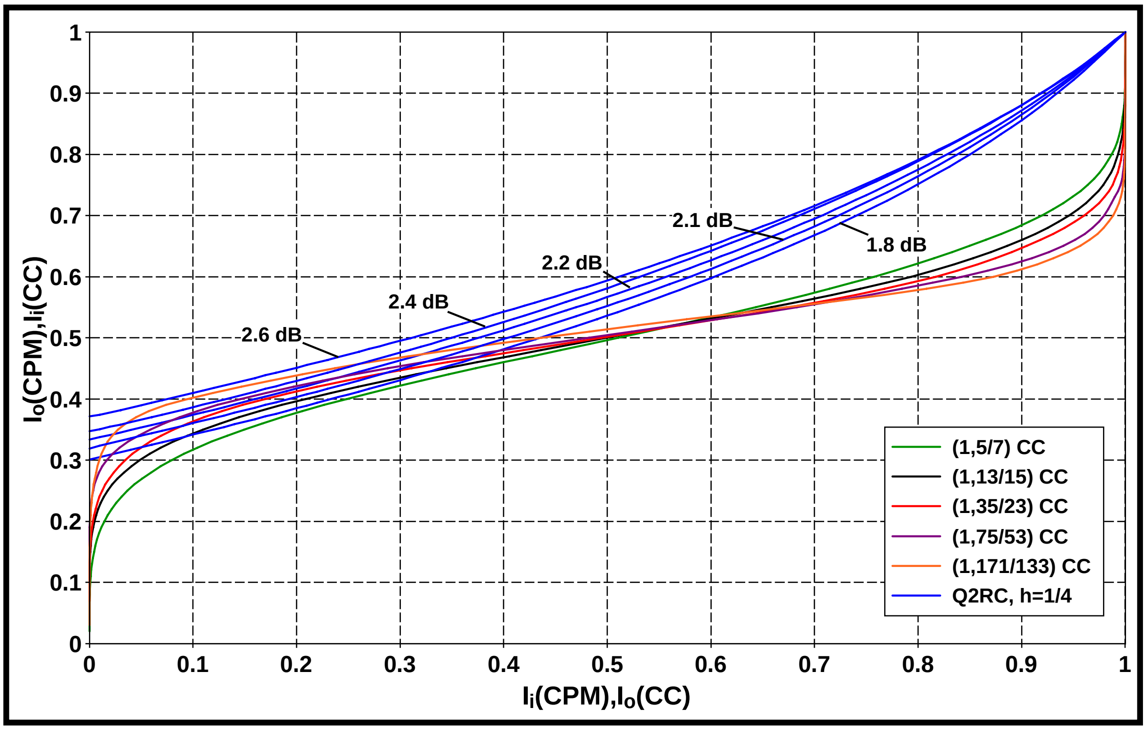

Figure 4.26 — EXIT chart comparison for $R = 1/2$ of (1,5/7), (1,13/15), (1,35/23), (1,75/53) and (1,171/133) outer CC codes concatenated with Gray mapped Q2RC $h = 1/4$

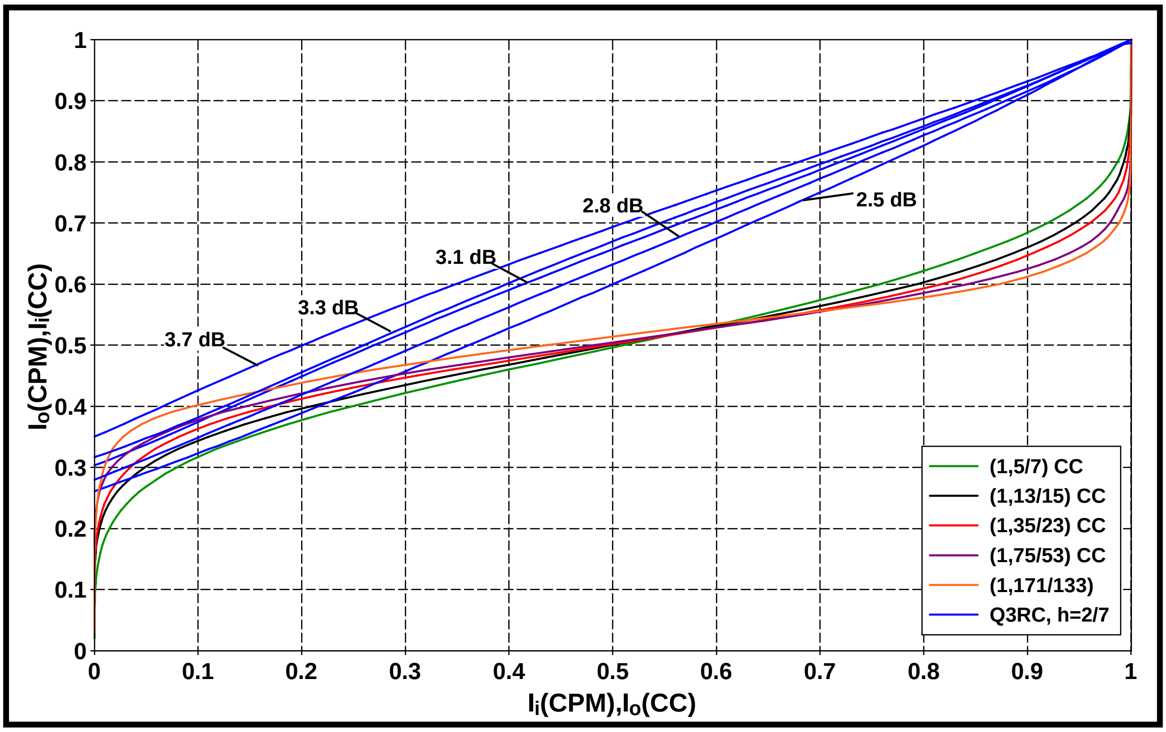

Figure 4.27 — EXIT chart comparison for $R = 1/2$ of (1,5/7), (1,13/15), (1,35/23), (1,75/53) and (1,171/133) outer CC codes concatenated with Gray mapped Q3RC $h = 2/7$ CPM

Convolutional code	4-state $(1, 5/7)$	8-state $(1, 13/15)$	16-state $(1, 35/23)$	32-state $(1, 75/53)$	64-state $(1, 171/133)$
Convergence threshold	2.5 dB	2.8 dB	3.1 dB	3.3 dB	3.7 dB
Gap to 4-state threshold	-	0.3 dB	0.6 dB	0.8 dB	1.2 dB

Table 4.4 — Convergence thresholds for 4, 8, 16, 32 and 64-state convolutional codes concatenated with a Q3RC $h = 2/7$ CPM

From EXIT chart analysis, we can assert that a loss in convergence threshold is unavoidable when the code memory of the outer CC increases. This degradation of error correcting performance can reach non-negligeable levels. A gap around 0.5 dB commonly separates the threshold of a 4-state CC from the threshold of a 16-state CC. It gets even wider when the number of code memory cells increases.

Effect of the code memory on the error floor of SCCPM

The natural effect of incrementing the code memory is to offer superior asymptotical performance. The error floor is lowered and the slope of the FER curve gets steeper. These consequences could be explained through the computation of the interleaver gain and bounds on the asymptotical error rate.

The interleaver gain for bit-interleaved SCCPM can be expressed as follows [24, 28, 83]:

$$\alpha_{M,\max} = -\left\lfloor \frac{d_{H\min} + 1}{2} \right\rfloor \tag{4.10}$$

where $d_{H\min}$ represents the minimum Hamming distance of the outer CC code and $\lfloor O \rfloor$ is the integer part of the variable O. As $d_{H\min}$ increases with the code memory, the interleaver gain decreases, leading to lower error floors for SCCPM.

Convolutional code	4-state $(1, 5/7)$	8-state $(1, 13/15)$	16-state $(1, 35/23)$	32-state $(1, 75/53)$	64-state $(1, 171/133)$
$d_{H\min}$	5	6	7	8	10
$\alpha_{M,\max}$	-3	-3	-4	-4	-5

Table 4.5 — Minimum Hamming distances of 4, 8, 16, 32 and 64-state convolutional codes and the corresponding interleaver gains

Table 4.5 shows the minimum Hamming distances and their corresponding interleaver gains of commonly used CC for $R = 1/2$. Notice that the $\alpha_{M,\max}$ decreases only when the number of states is an even power of 2 due to the integer part of equ. 4.10. Even if the interleaver gain is kept unchanged for (odd power of 2)-state CC, a slight asymptotical improvement is expected. In fact the bound on the probability of word error depends as well on the minimum Hamming distance and its multiplicity [28, 83].

In order to quantify the effect of the code memory on error floors, we have computed the FER bounds described in section 4.5.3.2 for the 4, 8, 16 and 32-state codes of table 4.5 where the inner CPM is kept unchanged (Q2RC, $h = 1/4$) and plotted results for 1272 bit-frames in fig. 4.28..

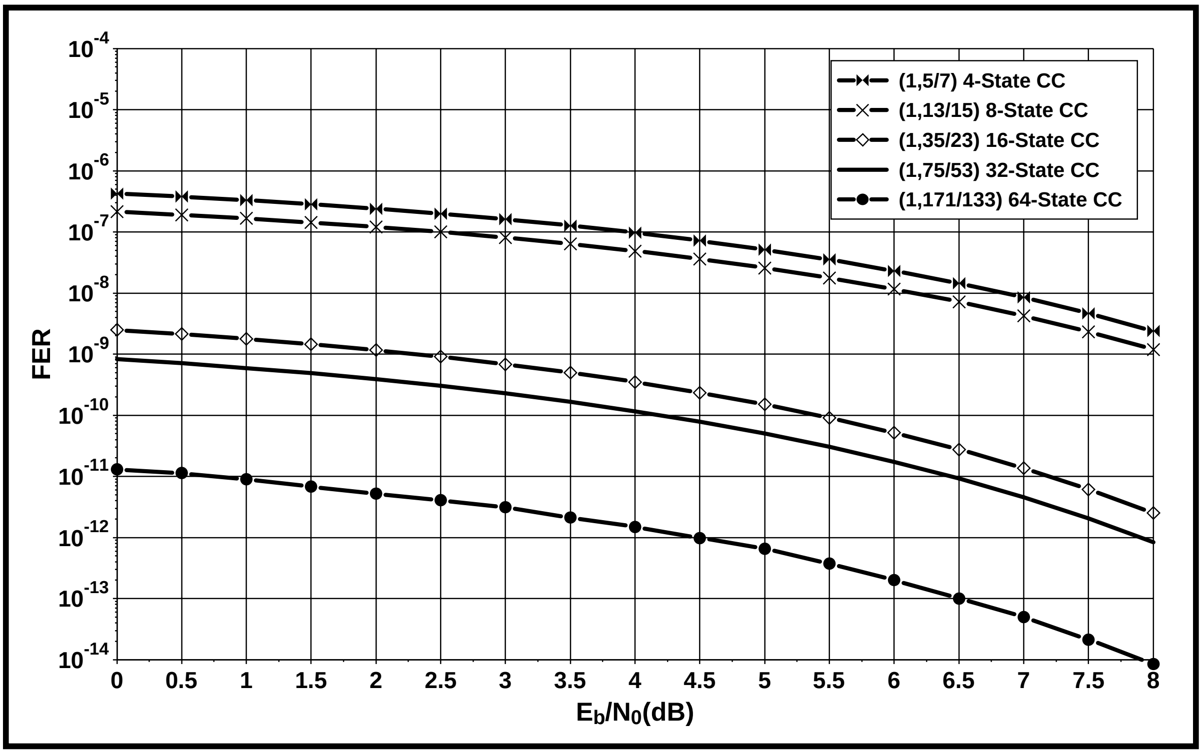

Figure 4.28 — Bounds on the frame error rate of $R = 1/2$ CC with increasing code memory and for an inner Q2RC $h = 1/4$ CPM

From the bound curves of fig. 4.28, we can enumerate the following observations:

- Only a slight improvement in the floor is observed when we replace the 4-state by the 8-state CC as the interleaver gain is the same. The same observation applies in the case where the 32-state replaces the 16-state CC.

- The error floor of a Q2RC CPM is lowered by 2 orders of magnitude when the 16-state code is introduced instead of the 4-state CC. Identical gap exists between the floor of a 16-state coded Q2RC and the one of a 64-state coded Q2RC.

- All codes satisfy the error floor requirement of 10^{-6} of FER for $R = 1/2$ Q2RC $h = 1/4$ CPM.

From the design guidelines of section 4.3.4, we are interested in working at high code rates as SCCPM offers earlier convergence thresholds for a target spectral efficiency. Consequently, we have to evaluate the effect of puncturing on the asymptotical performance of bit-interleaved SCCPM with an outer CC.

Effect of puncturing on the error floor of SCCPM

The natural effect of puncturing a CC is to decrease its minimum Hamming distance. Therefore, lower interleaver gains are attained resulting into higher error floors. We will start evaluating the effect of puncturing by computing the Hamming distance and interleaver gain for the codes of table 4.5 for code rates ranging from 1/2 to 4/5. The obtained results are summarized in table 4.6.

Convolutional code	4-state $(1, 5/7)$	8-state $(1, 13/15)$	16-state $(1, 35/23)$	32-state $(1, 75/53)$	64-state $(1, 171/133)$
$d_{H\,\text{min}}$ for $R = 1/2$	5	6	7	8	10
$\alpha_{M,\text{max}}$ for $R = 1/2$	-3	-3	-4	-4	-5
$d_{H\,\text{min}}$ for $R = 3/5$	4	4	5	6	7
$\alpha_{M,\text{max}}$ for $R = 3/5$	-2	-2	-3	-3	-4
$d_{H\,\text{min}}$ for $R = 7/10$	3	4	4	5	5
$\alpha_{M,\text{max}}$ for $R = 7/10$	-2	-2	-2	-3	-3
$d_{H\,\text{min}}$ for $R = 4/5$	2	3	3	4	4
$\alpha_{M,\text{max}}$ for $R = 4/5$	-1	-2	-2	-2	-2

Table 4.6 — Minimum Hamming distances of 4, 8, 16, 32, 64-state convolutional codes and the corresponding interleaver gains for rates ranging from $R = 0.5$ to $R = 0.8$

From Table 4.6, we can see that even for the 64-state code, the interleaver gain decreases dramatically from $\alpha_{M,\text{max}} = -5$ at rate 1/2 to $\alpha_{M,\text{max}} = -2$ at rate 4/5. As it represents the CC with the best behavior in the error floor region investigated in our bit-interleaved SCCPM study, bounds for the $(1, 171/133)$ CC are computed to give an insight into the lower limit of the error floor to be expected with this type of solution.

Fig. 4.29 presents the bounds on word error probability of the 64-state CC of table 4.6 for rates ranging from 1/2 to 4/5 concatenated with a Q2RC $h = 1/4$ inner CPM. Results point out that if rates higher than 0.7 are needed, even the best CC in the error floor region does not achieve the target of 10^{-6} of FER for our application. This is explained by the low value of the interleaver gain ($\alpha_{M,\text{max}} = -2$) for this code rate. Taking into consideration that the interleaver gain is independent of the CPM parameters, we would expect unacceptable error floors even for the 64-state CC for high code rates.

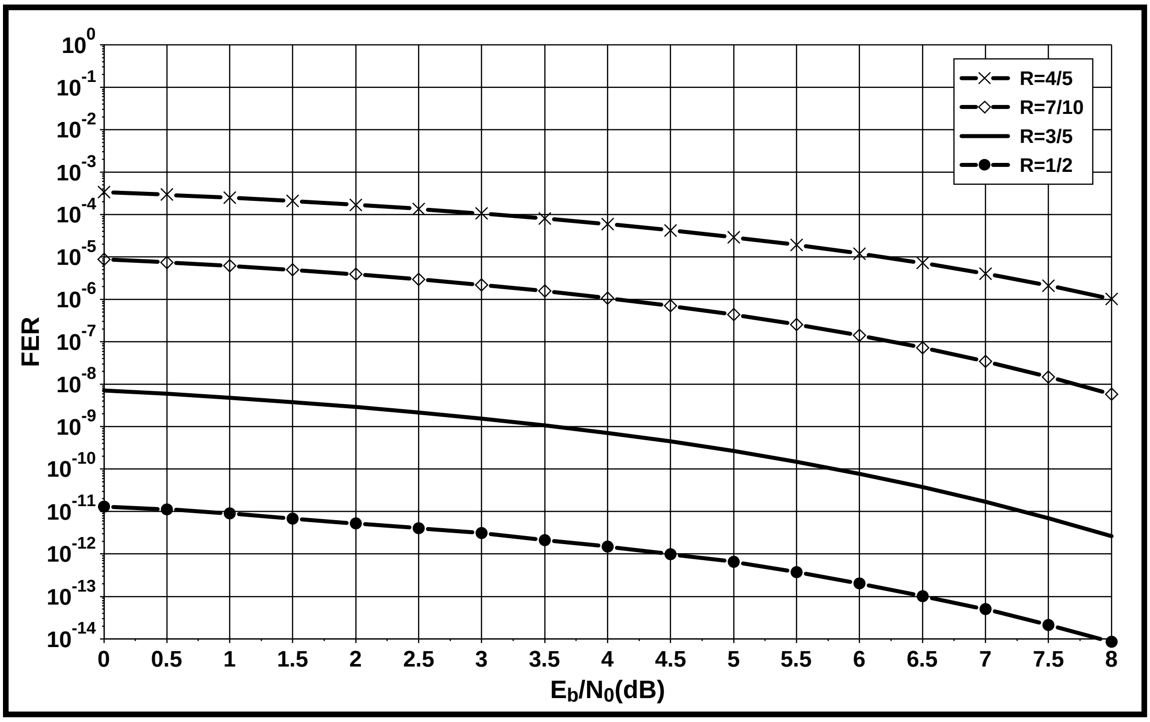

Figure 4.29 — Bound on the FER for rates ranging from $R = 1/2$ to $R = 4/5$ for the (1,177/133) 64-state CC and an inner Q2RC $h = 1/4$ CPM

Conclusion

From the results of the EXIT analyses and simulations undertaken in this section we can underscore the following observations:

- The gap between the waterfall of the symbol SCCPM and the Gray mapped bit SCCPM decreases when the code rate increases. It varies from 0.3 to 0.1 dB for rates ranging from 0.7 to 0.9.

- Gray mapped SCCPM outperforms natural binary mapped SCCPM in convergence threshold provided that weight one error events are avoided. This conclusion was verified by EXIT chart and simulation results.

- Gray mapped SCCPM shows comparable floors to natural binary mapped SCCPM, considerably lower than symbol-interleaved systems when high rates are used.

- Even for Gray mapped SCCPM, the 64-state outer CC is not able to satisfy target error floors. Showing an interleaver gain of -2 for a code rate of 0.8, this code suffered floors at 10^{-4} of FER for the Q2RC $h = 1/4$ CPM. Higher floors were also detected when concatenated with different sets of CPM parameters.

Taking into account these observations, we can conclude this section by confirming that bit-interleaved Gray mapped SCCPM can satisfy target error floor when concatenated with high minimum Hamming distance codes. Nevertheless, these codes resulting into high interleaver gain should be carefully chosen in order to offer competitive convergence thresholds. Since best SCCPM schemes in waterfall performance correspond to outer code solutions with high rates (see section 4.3.4), outer codes offering high Hamming distances for high code rates should be investigated.

Aiming at outer code solutions with greater error correcting capability when the code rate increases, turbo-like codes seem to be good candidates. A turbo and Flexi-like structures are investigated in the following sections.

4.5.5.4 Bit-interleaved SCCPM with turbo-like outer codes

Turbo-like codes are known to offer higher Hamming distances when compared to standalone CC. Since the performance of bit-interleaved SCCPM is greatly degraded when single outer CC are used with high code rates, a natural replacement could be turbo-like codes. The resulting SCCPM scheme is configuration (3) of section 4.5.2 with turbo-like code as outer. In contrast with the symbol-based turbo-like solution, flexiblity of the alphabet size and the code rate is possible for bit-interleaved turbo coded SCCPM.

As pointed out in section 4.5.5.2 and verified in the example of section 4.5.5.3, Gray mapping should be adopted with bit-interleaved SCCPM as it offers an improvement of the convergence threshold with no impact on the error floor performance.

The introduction of turbo-like outer codes could have some drawbacks though, having two elementary codes, the concatenation with the CPE results into a three-fold equivalent code for the SCCPM. As far as convolutional codes are concerned, it was shown in [83] that an increase in the dimension of the concatenation tends to improve the asymptotic performance of the code at the expense of a loss in convergence. In fact, since every component code has a code rate $R \leq 1$, the overall outer code rate is divided between two modules (as the CPE constitutes a rate-1 encoder) consisting of the elementary CC components of the turbo-like outer code. This induces a threshold penalty.

In order to verify if the hypothesis in [83] about three-fold concatenations still applies in the case of a SCCPM, we simulated the FER performance of turbo coded SCCPM with two different families of codes:

- A PCCC: It consists of the DVB-RCS code (known to be one of the best turbo codes in the waterfall performance region).

- An SCCC: The serial code in [85] that has been retained in the project funded by the European Space Agency, entitled Modem for High Order Modulation Schemes (MHOMS) [86], aimed at the design of a high-rate reconfigurable satellite digital modem prototype. It is a low complexity code achieving good error floor performance at the price of a small loss in the iterative convergence process.

FER simulations were conducted for the SCCPM system taken as reference for two outer code rates: 0.5 and 0.8.

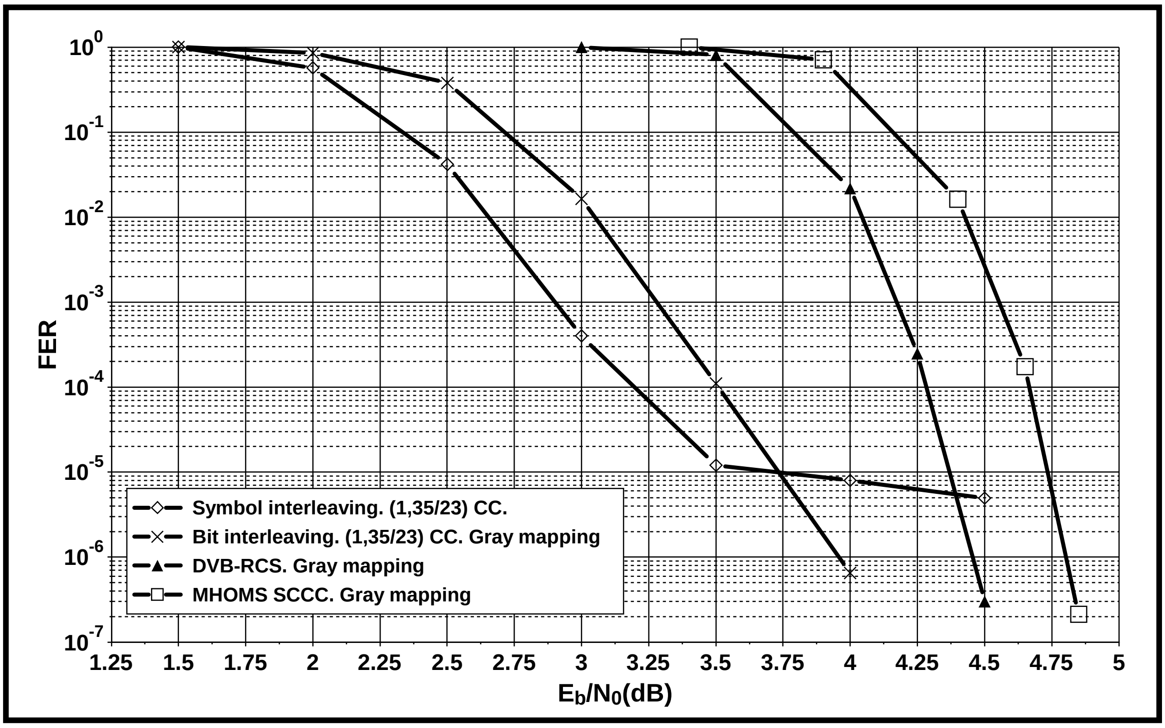

Figure 4.30 — FER Simulation of $R = 0.5$ Q2RC $h = 1/4$ SCCPM with three different outer codes: the single bit and symbol inteleaved 16-state (1,35/23) CC, the MHOMS serial turbo code and the DVB-RCS parallel turbo code

Fig. 4.30 shows FER simulation results for the MHOMS SCCC turbo code and the DVB-RCS PCCC with $R = 0.5$ and 1272-bit frames. 10 iterative decoding and demodulation steps are performed whereas only one turbo iteration is carried out for every iteration to the CPM SISO. The error correcting performance is compared with the one of the symbol and bit-interleaved $(1, 35/23)$ CC. This figure presents around 1.0 dB gap at the beginning of the waterfall region between the bit-interleaved convolutionally coded and the DVB-RCS coded SCCPM. An additional gap of 0.3 dB exists between the PCCC and the SCCC coded SCCPM in the favour of the former. It is worth mentioning that the FER curves of the simulated two families of turbo coded SCCPM offer a steeper slope when compared to the CC coded SCCPM. This indicates a larger interleaver gain for the turbo-like codes and predicts a crossing between the FER curves at lower values of frame error probabilities. In fact the gap between the CC coded curves and turbo coded curves decreases with decreasing probability of error.

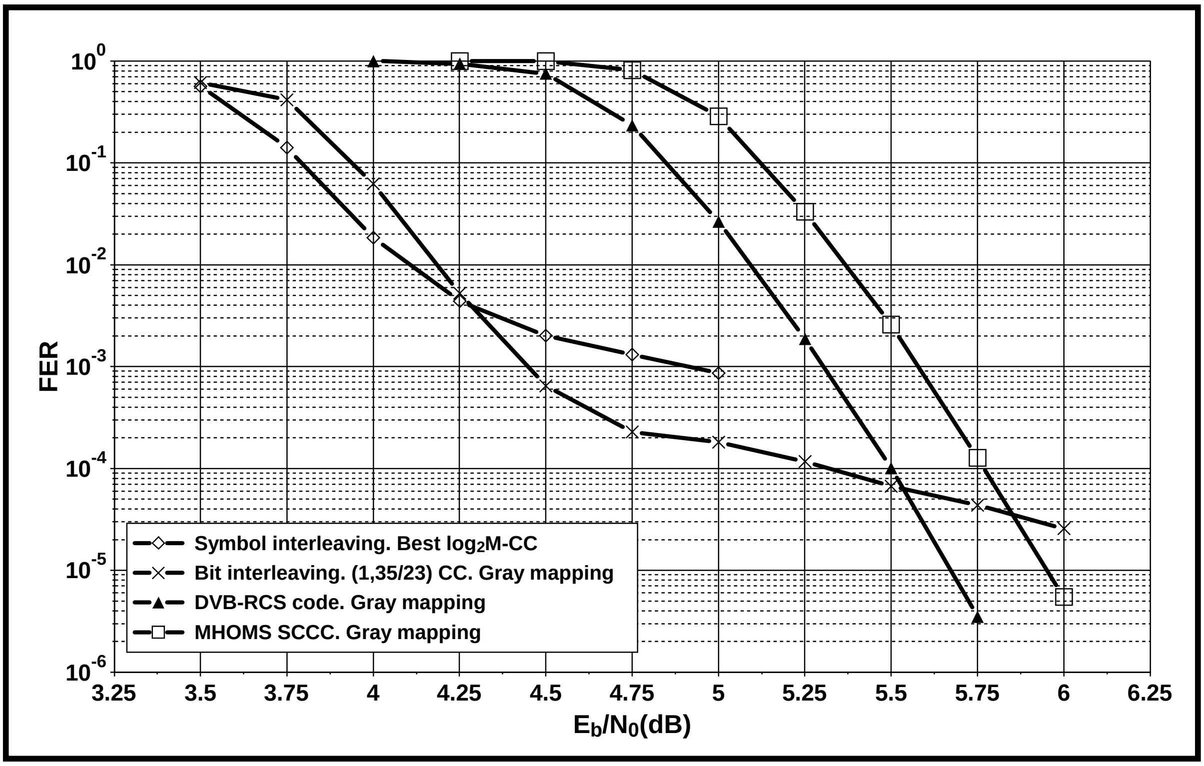

Figure 4.31 — FER Simulation of $R = 0.8$ Q2RC $h = 1/4$ SCCPM with four different outer codes: the single bit-interleaved 16-state (1,35/23) CC, the best symbol-interleaved DB code, the MHOMS serial turbo code and the DVB-RCS parallel turbo code

Fig. 4.31 shows simulation results for the same type of codes as in fig. 4.30 for a code rateequal to 0.8. As presented in section 4.5.5.3, the CC is penalized by the heavy puncturing and suffers from a diminishing Hamming distance at $R = 0.8$ resulting into a floor at 10^{-4} of FER. The serial and parallel turbo codes are able to achieve FER as low as 10^{-5} with no change in the slope. They should be able to satisfy the target error floor constraint. Once more, turbo coded SCCPM being a three-fold concatenation suffers from a large loss in convergence comparable to the one of fig. 4.30 of around 1.0 dB. The gap between the PCCC and the SCCC coded CPM is also comparable to the $R = 0.5$ case with a value close to 0.3 dB.

To conclude, simulation results confirm the previous observations regarding the error correcting behaviour of three-fold concatenation schemes where higher Hamming distances were attained at the price of a loss in convergence thresholds. Consequently, other SCCPM structures offering high Hamming distances for higher code rates should be investigated, for example flexi-like SCCPM.

4.5.5.5 Bit-interleaved Flexi-like SCCPM structure

Flexicodes [82] enjoy interesting performance in the error floor at the price of a small loss in convergence especially for very high code rates. They were developped by TrellisWare technologies in 2003. They represent a class of Turbo-Like Codes (TLC) technically called Systematic with Serially Concatenated Parity (S-SCP) codes. This new TLC is a systematic code with parity bits generated using a serial concatenation of an outer code, an interleaver and an inner recursive parity generator as in [82]. The key feature of this code is that the inner parity generator outputs fewer bits than it takes in. It allows the code rate to be adjusted easily by adjusting this ratio.

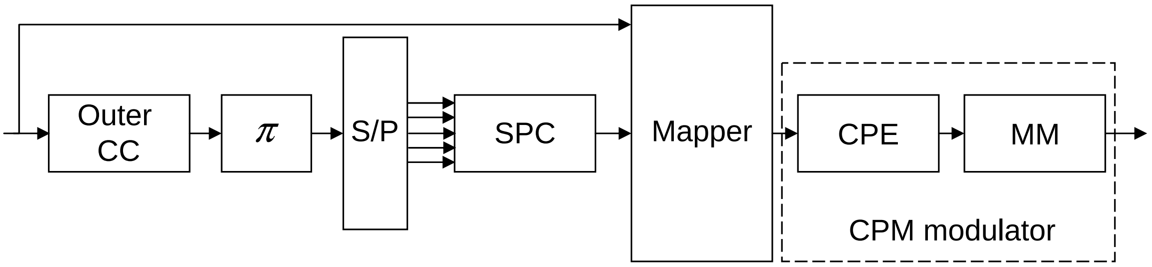

Figure 4.32 — Structure of the flexi-like SCCPM transmitter

Motivated by the unavoidable introduction of high code rates for our SCCPM, and taking into account the serial concatenation aspect of a flexicode structure, we tried to introduce design modifications in order to adapt this code type to SCCPM. The result is a flexi-like structure having an outer convolutional code, a Single Parity Check SPC code acting as a puncturer replacement and a CPE as a rate-1 inner code. The transmitter corresponding to our flexi-like structure is presented in fig.4.32. It operates as follows:

The systematic information bits are sent to the mapper and the outer code. All outer CC encoded bits (systematic and parity) are interleaved by π and then sent to the Serial to Parallel (S/P) converter. For every $m_{S/P}$ bits at its input, the SPC provides one output bit. It plays a similar role to puncturing. The resulting code rate is a function of $m_{S/P}$ following:

$$R = \frac{m_{S/P}}{m_{S/P} + 2} \tag{4.11}$$

Systematic bits added to the bits at the output of the SPC are mapped to M-ary symbols. These are then forwarded to the CPM modulator.

The advantage of a flexi-like structure resides in the SPC. In fact, instead of keeping 1 bit out of $m_{S/P}$ as for a classical SCCC puncturing, the SPC combines $m_{S/P}$ bits together to provide 1 bit. Since it is iteratively decoded, the information on combined bits would be available after the first iteration and these bits can be recovered.

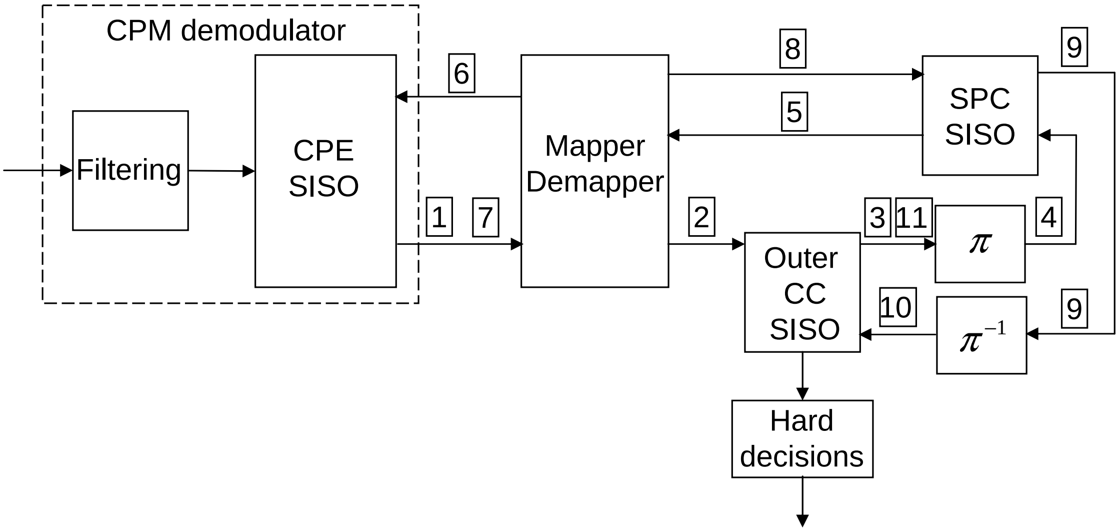

Figure 4.33 — Structure of the flexi-like SCCPM receiver

A block diagram of the flexi-like SCCPM receiver is presented in fig. 4.33. The soft information on systematic bits at the output of the demapper is passed to the CC. The soft information on coded bits (systematic and parity) is passed to the SPC. The systematic nature of the flexi-like structure means that the decoding process must always start by the outer code [82]. A timing schedule showing steps (from 1 to 11) undertaken by the receiver is presented in fig. 4.33. The extrinsic information at the ouput of the outer CC SISO is interleaved and sent to the SPC. This latter could be decoded by a classical SISO as presented in [82]. Extrinsic bit information is then combined to symbolwise soft information passed to the CPE SISO. Starting from the second iteration through the demapper, the iterative receiver changes its scheduling and goes through the SPC SISO. Extrinsic information is afterwards deinterleaved and passed to the outer code, thus completing a receiver iteration. After a few iterations, hard decisions on information bits are provided at the output of the CC.

The proposed flexi-like structure represent a turbo-like code. It is a three-fold concatenation of an outer CC, an SPC and an inner CPE. In compliance to the conclusions of section 4.5.5.4, flexi-like SCCPM as a member of three-fold concatenation schemes is expected to offer lower floors at the expense of convergence threshold loss with respect to single outer code solutions. FER simulations in fig. 4.34 and fig. 4.35 have been performed using 1272-bit frames and 10 iterations in order to to verify if this expectation still holds for our proposed structure when adopting two different code rates of $R = 0.5$ and $R = 0.8$ respectively.

FER simulation results for the proposed flexi-like structure compared to the bit and symbol-interleaved single 16-state $(1, 35/23)$ CC are plotted in fig. 4.34. They show that a small gap of around 0.3 dB exists between the single CC and the flexi-like structure at

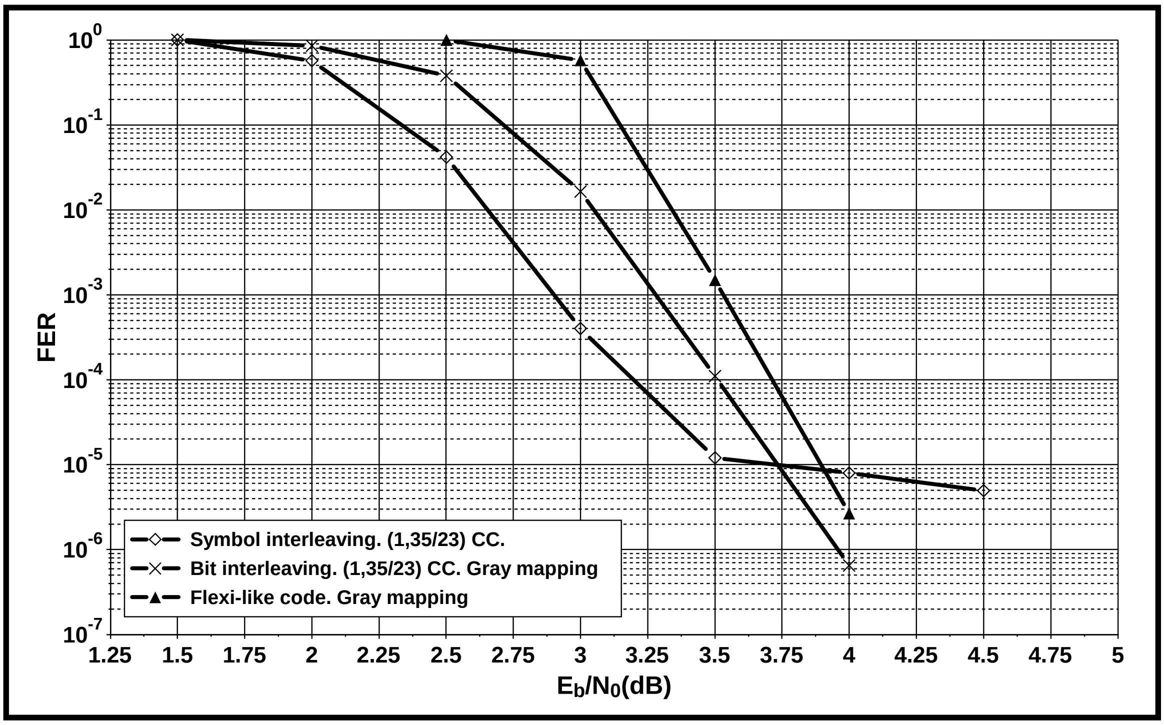

Figure 4.34 — FER Simulation of $R = 0.5$ Q2RC $h = 1/4$ SCCPM with two outer codes: bit- and symbol-interleaved single (1,35/23) 16-state CC and the proposed flexi-like structure

the start of the waterfall region. This gap decreases with decreasing probability of error. It becomes around 0.15 dB at 10^{-5} of FER. This implies that the flexi-like structure enjoys higher interleaver gain for $R = 0.5$ while satisfying the error floor constraint of 10^{-6} of FER.

The same type of comparison is performed for $R = 0.8$ and codes of fig. 4.34 where the symbol-interleaved code is the best $\log_2 M$-binary code of section 4.5.4.4. Results are plotted in fig. 4.35. Once again the flexi-like structure satisfies the error floor constraint. Nevertheless, a considerable loss in the convergence threshold when compared to single outer bit-interleaved CC represents the price to pay. It varies between 1.0 and 1.25 dB.

The proposed flexi-like SCCPM does satisfy the error floor constraint for medium code rates ($R = 0.5$) with a convenient threshold penalty of only around 0.25 dB. When the code rate increases though, this penalty increases to reach an unacceptable value of around 1.25 dB. Consequently, the proposed flexi-like structure does not represent a suitable candidate for our SCCPM study.

Requiring high code rates with good Hamming distances for the lowest possible threshold penalties while avoiding three-fold concatenation schemes, powerful single outer codes should be investigated. Thus, extended BCH codes have then been considered.

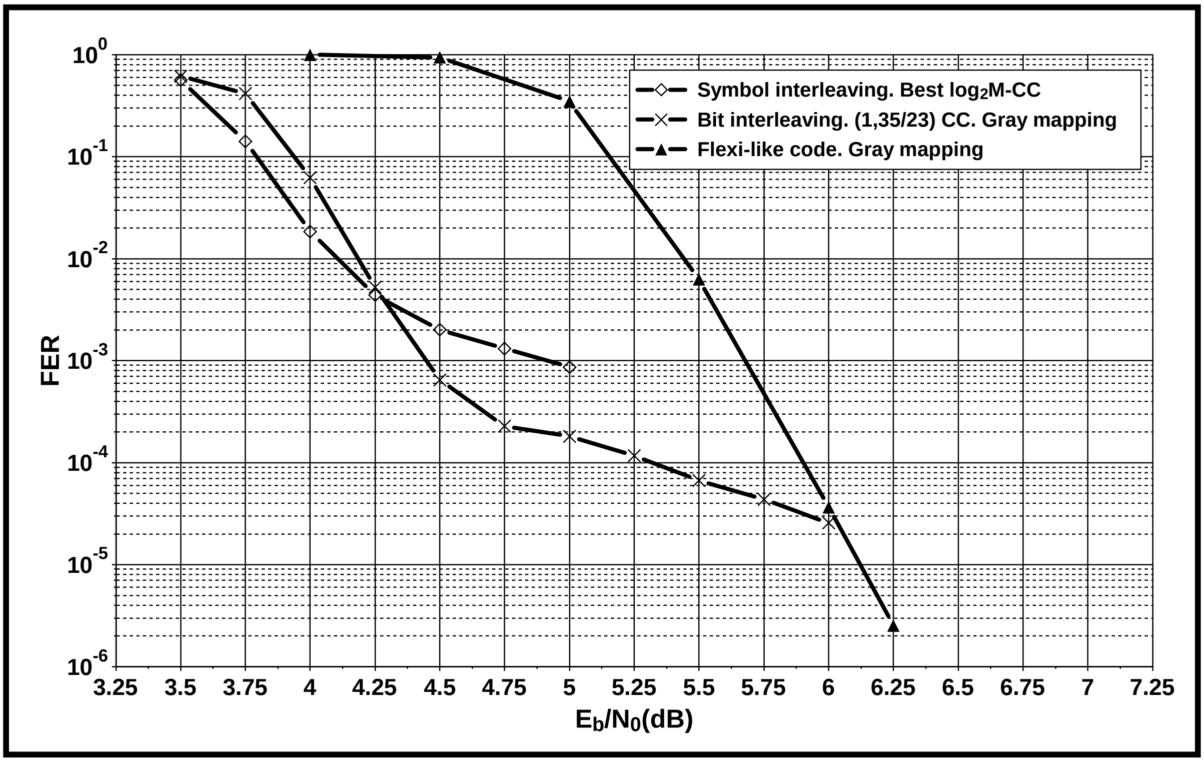

Figure 4.35 — FER Simulation of $R = 0.8$ Q2RC $h = 1/4$ SCCPM with three outer codes: bit-interleaved single (1,35/23) 16-state CC, symbol-interleaved best single DB code and the proposed flexi-like structure

4.5.5.6 Bit-interleaved SCCPM with extended BCH codes

The introduction of extended BCH codes is motivated by the error correcting performance of the serial concatenation of eBCH outer code and inner accumulator [87]. In fact, the CPM can be regarded as the accumulator of the serially concatenated structure. In addition, eBCH codes represent excellent codes for high-rates as they offer larger minimum Hamming distances than CC.

The proposed SCCPM structure is configuration (3) of section 4.5.2 with eBCH codes as outer. Bit interleaving and Gray mapping are adopted.

eBCH codes: description and effect on SCCPM error floor

A family of (k_{out}, n_{out}) eBCH [88] having a correction capability of 2 bits is used. The code is referred to as extended BCH since a parity bit is appended to the primary BCH codeword. It offers a relatively interesting compromise between error performance (in terms of Hamming distance) and SISO complexity. In some cases where the information frame length is not a multiple of k_{out}, some dummy bits were inserted. The use of dummy bits enduces a small rate loss.

In order to study this family of codes, we chose the $(64, 51)$ code as outer code in the concatenated SCCPM structure. It offers a Hamming distance of 6 for a code rate of $R = 0.8$. Consequently, an interleaver gain $\alpha_{M,\max} = -3$ is achieved leading to lower error floors of SCCPM when compared to the CC coded SCCPM. Code rate flexibility is achieved by shortening the eBCH code. Note that by applying shortening the multiplicity of the error events increases, but d_{min} does not change, hence the interleaver gain is preserved.

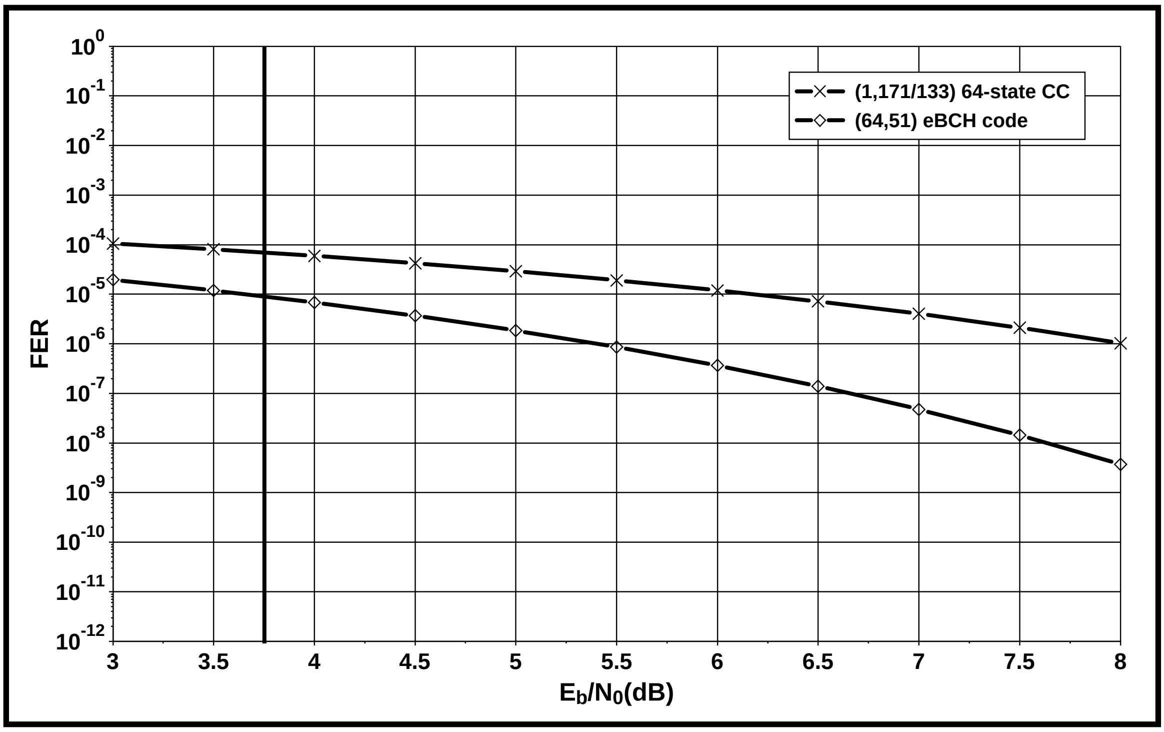

Figure 4.36 — Union bounds on FER for $R = 0.8$ (64,51) eBCH code compared to the 64-state (1,171/133) CC and Q2RC $h = 1/4$ CPM

Fig. 4.36 shows the FER union bounds for the 64-state (1,171/133) CC and the eBCH (64,51) code for $R = 0.8$. The vertical line reports an estimate of the convergence threshold for the Q2RC SCCPM via EXIT chart analysis. If we consider the bound at 1.0 to 1.5 dB from the threshold, we can see that the eBCH code suffers from a floor around one order of magnitude lower than the 64-state CC at around 4.10^{-6} of FER. Taking into account the fact that we have adopted uniform interleaving, floors lower than 10^{-6} of FER could be achieved if high spread interleavers are introduced.

eBCH codes: effect on SCCPM convergence threshold

In order to estimate the effect of the introduction of eBCH codes on the convergence threshold of SCCPM, we have to perform a comparison of the EXIT chart analysis of the CC on one hand and the one corresponding to the eBCH code on the other.

Fig. 4.37 plots the EXIT chart analysis for $R = 0.8$ of three codes: the 16-state (1,35/23) CC, the 64-state (1,171/133) CC and the (64,51) eBCH code. It shows that the convergence

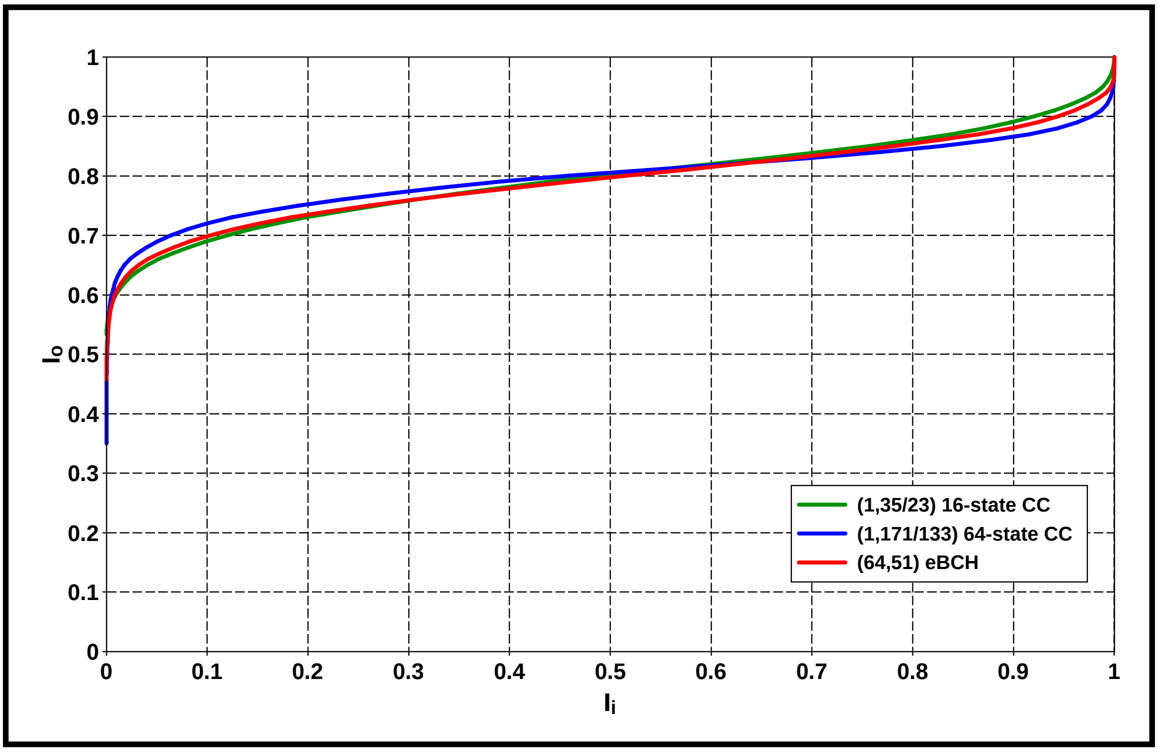

Figure 4.37 — EXIT chart comparison for $R = 0.8$ of 3 codes: the 16-state (1,35/23) CC, the 64-state (1,171/133) CC and the (64,51) eBCH code.

threshold of the eBCH code is comparable to the one of the 16-state CC as for the values of the mutual information at the input I_i ranging from 0.2 to 0.3, the EXIT curve of the (1,35/23) and the (64,51) are almost identical. Notice that the 64-state CC should suffer from a threshold penalty as it presents in the previously selected range of I_i (0.2 to 0.3) higher values of the mutual information at the output I_o.

FER simulations of eBCH coded SCCPM

In order to check the behaviour of eBCH coded SCCPM in the waterfall and in the error floor regions, we have performed FER simulations for the CPM scheme taken as reference. Due to the rather significant complexity of the MAP decoder, a low complexity Chase-Pyndiah decoder [89] has been implemented. This algorithm is quasi-optimum for short correction capability eBCH codes (correction of 1 or 2 errors for every BCH matrix). Note that the complexity of the (64, 51) eBCH code, while decoded using the Chase-Pyndiah algorithm, is rather low, comparable to an 16-state CC Max-Log-MAP decoder in terms of number of logic gates.

A comparison of FER simulation results of four outer code solutions for $R = 0.8$ are plotted in fig. 4.38:

- The best symbol-based 16-state $\log_2 M-$CC coded CPM for 10 and 30 iterations,

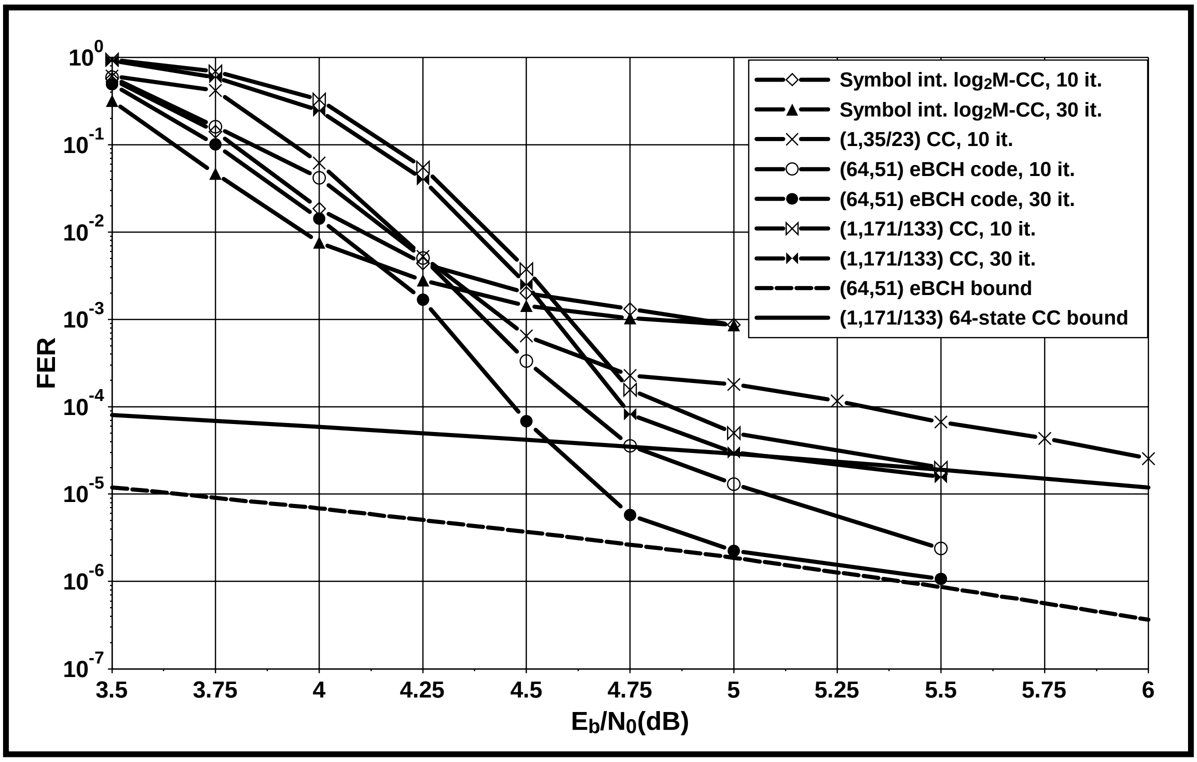

Figure 4.38 — FER simulation results for $R = 0.8$ of 4 codes: the best 16-state symbol-interleaved code, the 16-state (1,35/23) CC, the 64-state (1,171/133) CC and the (64,51) eBCH code.

- The bit-interleaved SCCPM with the 16-state (1,35/23) CC for 10 iterations,
- The bit-interleaved SCCPM with the 64-state (1,171/133) CC for 10 and 30 iterations,
- The bit-interleaved SCCPM with the (64,51) eBCH code for 10 and 30 iterations.

The upper bounds on the word error probability corresponding to the eBCH code and the 64-state CC have also been added. Let us stress on some observations:

- A non-negligeable gain in error correcting performance can be achieved when increasing from 10 to 30 the number of iterations for the eBCH code. This gain is undeniably smaller in the case of the 64-state CC.
- The 64-state (1,171/133) CC suffers from an error floor for frame error rates lower than 10^{-4}. Nevertheless it is around one order of magnitude lower than the 16-state (1,35/23) CC.
- The (64,51) eBCH code suffers from an error floor for frame error rates lower than 5.10^{-6}. Its is more than one order of magnitude lower than the 64-state CC.

- The eBCH code offers a convergence threshold comparable to the 16-state code for 10 iterations. It is 0.4 dB earlier than the 64-state CC. An additional gain of 0.1 dB could be achieved if the number of iterations is raised to 30 for eBCH code.

It is worth mentioning that the increase in number of iterations is of a relatively low cost in terms of complexity for our SCCPM system as eBCH codes offer a reliable stopping criterion. This effective criterion could be introduced leading into a low average number of iterations for the eBCH coded SCCPM.

In conclusion, bit-interleaved eBCH coded SCCPM represents a viable FEC solution in order to satisfy the code design requirements in terms of convergence threshold and error floor. It offers convergence thresholds comparable to the solutions offering best waterfall performance, and attains FER in the 10^{-6} decade without changes in the slope. Note that observed error floors can be lowered further if high spread interleavers are introduced.

4.6 Conclusion

We conclude by a comparison of the error correcting performance of investigated SCCPM schemes in this chapter. It is intended for selecting a winning SCCPM solution that satisfies the code design requirements in terms of error correction at a reasonable complexity.

In order to offer a fair comparison, the same simulation conditions were adopted to obtain the FER results of fig. 4.39. Simulated outer code solutions correspond to the ones investigated in section 4.5.3 with an outer code rate of $R = 0.8$. They have been associated with a Q2RC $h = 1/4$ CPM.

Observing curves of fig. 4.39, we can see that:

- Symbol-based solutions suffer from alarming floors higher than 10^{-3} of FER.
- The bit-interleaved SCCPM with the 64-state CC is not able to satisfy targeted error floors while suffering from a threshold penalty of 0.4 dB when compared to symbol based SCCPM solutions.
- Only eBCH and turbo-like codes allow floors around 10^{-6} of FER or below to be attained.
- Turbo-like codes, serial, parallel as well as the Flexi-like structure suffer from an important convergence penalty exceeding 1.0 dB when compared to the SCCPM scheme offering the best waterfall performance.
- The eBCH coded SCCPM solution offers waterfall performance comparable to the symbol based SCCPM while attaining floors around 10^{-6} of FER.

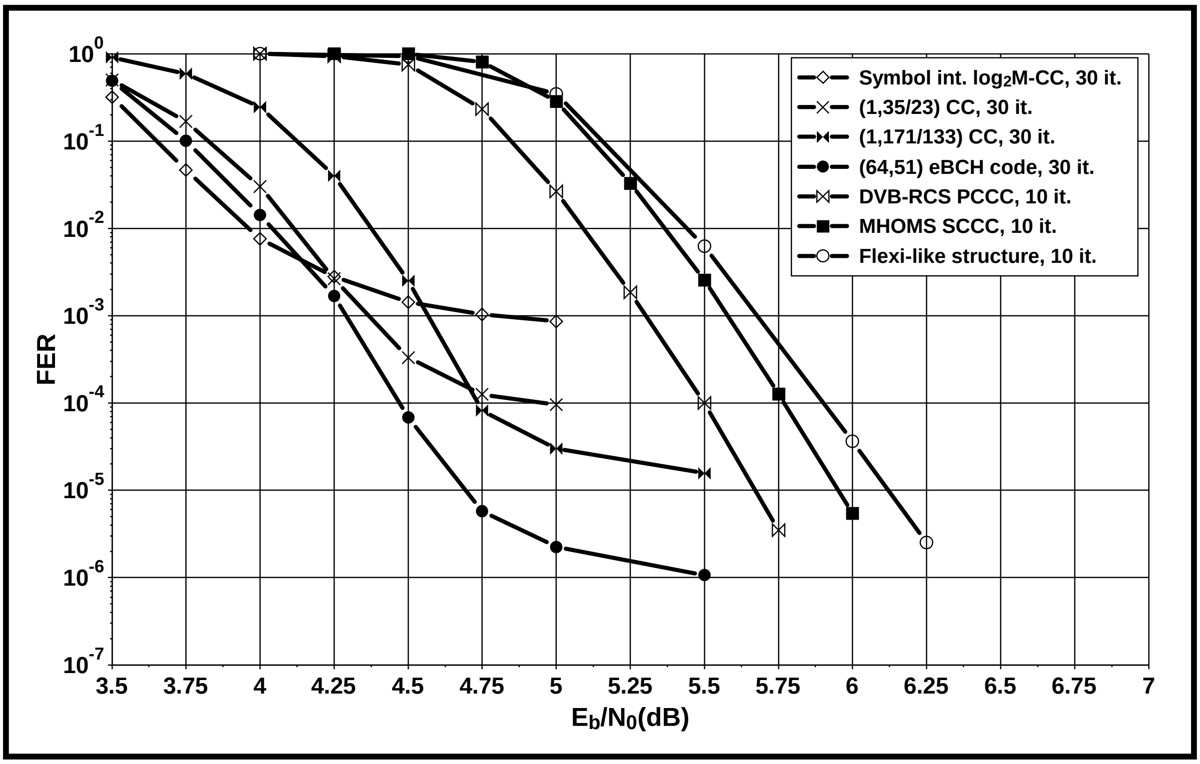

Figure 4.39 — FER simulation results corresponding to the $R = 0.8$ Q2RC h=1/4 concatenated with the seven outer code solutions: the best 16-state symbol-interleaved code, the 16-state (1,35/23) CC, the 64-state (1,171/133) CC, the (64,51) eBCH code, the DVB-RCS PCCC, the MHOMS SCCC and the Flexi-like structure.

Unreported in this chapter, additional FER simulations with different sets of CPM parameters than Q2RC $h = 1/4$ have been performed. They have allowed us to validate the results summarized in fig. 4.39 on a broader scale.

We can conclude by saying that turbo-like codes suffer from a large waterfall region penalty as gaps reaching 2.5 dB with respect to SCCPM schemes with simple outer codes have been observed. Consequently turbo-like codes are to be ruled out as competitive outer code solutions when waterfall performance is of interest. Instead, eBCH codes provide the best compromise in both convergence and floor when compared to studied outer code solutions.

In the end, SCCPM with outer eBCH codes represents the winning solution since it provides the error correcting performance that is best suited for our system constraints. Nevertheless, for comparison purposes, single outer code solutions studied in this context have also been simulated in the rest of our study.

CHAPTER

5

Final selection of the SCCPM parameters for 0.75 to 2.25 bps/Hz spectral efficiencies

THIS chapter is intended to provide the results of the selection procedure for CPM parameters spanning spectral efficiencies ranging from 0.75 to 2.25 bps/Hz. Then, by means of FER simulation results, we proceed to the validation of the outer code solution proposed in the previous chapter.

We start by a swift recall of the steps to be followed in order to design coded CPM systems optimizing the convergence thresholds while satisfying error floor constraints. Afterwards, we detail the approach for one case of spectral efficiency corresponding to 1.5 bps/Hz. We conclude by presenting FER simulation results for the two extreme spectral efficiencies of 0.75 bps/Hz and 2.25 bps/Hz and two different frame sizes.

5.1 Steps for selecting CPM parameters and code rate

Taking into account the guidelines of section 4.3.4 and section 4.6, the steps that have been followed to select a winning SCCPM scheme and code rate for a target spectral efficiency can be summarized as follows:

1. Preselect a group of CPM set of parameters representing the candidates for the study. In fact, as the spectral efficiency is CPM dependent, there exists TSE values unachievable with code rates $R \leq 1$. In addition, as bit-interleaved SCCPM represents the adopted solution, weight-one error events described in section 4.5.5.2 are to be avoided.
2. Compute the outer code rates for the preselected group of parameters attaining the TSE using equ. 4.1.
3. Perform an EXIT chart analysis for every set of CPM parameters taking a particular outer code as reference as proposed in section 4.3.
4. Repeat step 3. until identifying the convergence threshold for every set of CPM parameters in the preselected group.
5. Select the best set of CPM parameters in terms of convergence threshold.
6. Compute the bound on the frame error probability described in section 4.5.3.2 using the selected set of CPM parameters. The computation is performed over a range of E_b/N_0 of several dBs, starting from the convergence threshold value. At 1.5 to 2.0 dB from the threshold value, if the computed bound offers a probability of frame error of 10^{-6} of FER or close, the set of parameters is retained as a CPM solution for this TSE. If not, repeat step 6. with the second best set of parameters in terms of convergence thresholds.
7. Perform FER simulations as a last step in order to verify the performance of winning SCCPM scheme.

In the next section, we proceed to a brief recall of the CPM and code parameters involved in the SCCPM scheme selection.

5.2 Set of CPM parameters and code rates used for the search process

The steps proposed in section 5.1 were undertaken for every value of the spectral efficiency for the following quaternary and octal CPM schemes : Q2RC, Q2SRC, Q3RC, Q3SRC and

O2RC. The values of the modulation index h were chosen to keep the overall CPM complexity reasonable : typically with a denominator lower than 8 for Q3RC and Q3SRC schemes, lower than 10 for Q2RC and Q2SRC schemes and lower than 15 for O2RC schemes. Gray mapping has been considered in all cases as it offers improved convergence threshold when compared to natural mapping (see section 4.5.5.2).

We recall that for Gray-mapped bit-interleaved SCCPM, weight-one error events are encountered for quaternary schemes where the modulation index h satisfies $h = K/3$. For octal CPM, the condition becomes $h = K/3$, $h = K/5$ or $h = K/7$. Consequently, the convergence thresholds were not computed for SCCPM having these values of the modulation index.

The EXIT chart analysis was performed using the 64-state $(1, 171/133)$ CC as outer code. The choice of this outer code taken as a reference, instead of an eBCH code, is motivated by the following reasons:

- Aiming for an accurate estimate of the threshold, a large number of samples in the EXIT chart curve for the outer code and the CPM should be computed. In practice, 100 computation points have been used. Unfortunately the EXIT chart computation for eBCH codes implies the use of a true BCJR decoder. For example, for the $(64, 51)$ eBCH code, the trellis profile has a maximum of $8,192$ states. Consequently, the search for the best set of CPM parameters taking an eBCH code as outer is a very time consuming operation.
- As already mentioned in section 4.3, if the outer code is kept unchanged during the study, the hierarchy between the convergence thresholds obtained with a given set of parameters is kept when the code is changed.
- Taking into account the collapse of the error correcting performance of CCs when extensive puncturing is performed, only codes with rates lower than 0.9 were investigated. For code rates approaching $R = 0.9$ a CC offering reasonable Hamming distances is required. Therefore, a 64-state CC has been adopted for the EXIT analysis.

In order to validate our approach, the procedure is detailed for a spectral efficiency of 1.5 bps/Hz.

5.3 Example of CPM parameters and code rate selection for a target spectral efficiency of 1.5 bps/Hz

In this section, the approach proposed in section 5.1 is detailed for a TSE of 1.5 bps/Hz. We first start by tabulating the CPM set of parameters to be considered. In table 5.1, we present the CPM set of parameters of the Q2RC family that have been considered, their corresponding code rate in order to achieve a TSE of 1.5 bps/Hz and the computed threshold.

Tables 5.1 to 5.5 show the CPM sets of parameters considered for the Q2RC, Q3RC, Q2SRC, Q3SRC and O2RC families, the corresponding code rates required to achieve a TSE of 1.5 bps/Hz and the computed convergence threshold (only for coding rates lower than 0.9). The lines in the tables marked with W1 EE indicate CPM parameters suffering from weight-one error events.

Set number	M	L	Spectral efficiency	Code rate	h	Threshold
1	4	2	1.5 bps/Hz	0.937	1/4	-
2	4	2	1.5 bps/Hz	0.824	1/5	5.6 dB
3	4	2	1.5 bps/Hz	0.748	1/6	6.1 dB
4	4	2	1.5 bps/Hz	0.688	1/7	7.3 dB
5	4	2	1.5 bps/Hz	0.639	1/8	8.1 dB
6	4	2	1.5 bps/Hz	0.597	1/9	9.2 dB
7	4	2	1.5 bps/Hz	0.567	1/10	9.9 dB

Table 5.1 — Convergence thresholds obtained via EXIT chart analysis for Q2RC schemes with modulation index values ranging from $h = 1/4$ to $h = 1/10$ and attaining a TSE of 1.5 bps/Hz

Set number	M	L	Spectral efficiency	Code rate	h	Threshold
1	4	3	1.5 bps/Hz	1.100	2/5	-
2	4	3	1.5 bps/Hz	0.839	2/7	4.7 dB
3	4	3	1.5 bps/Hz	0.761	1/4	4.8 dB
4	4	3	1.5 bps/Hz	0.654	1/5	6.2 dB
5	4	3	1.5 bps/Hz	0.582	1/6	6.9 dB
6	4	3	1.5 bps/Hz	0.529	1/7	7.8 dB
7	4	3	1.5 bps/Hz	0.488	1/8	8.6 dB

Table 5.2 — Convergence thresholds obtained via EXIT chart analysis for Q3RC schemes with modulation index values ranging from $h = 2/5$ to $h = 1/8$ and attaining a TSE of 1.5 bps/Hz

From these tables, we can lay stress on two important observations:

- For all investigated families of CPM, the code rate increases with increasing modulation index.
- The best convergence thresholds are observed for the highest values of both h and R, as predicted in section 4.3.

Set number	M	L	Spectral efficiency	Code rate	h	Threshold
1	4	2	1.5 bps/Hz	0.923	1/4	-
2	4	2	1.5 bps/Hz	0.812	1/5	5.6 dB
3	4	2	1.5 bps/Hz	0.737	1/6	6.0 dB
4	4	2	1.5 bps/Hz	0.677	1/7	6.8 dB
5	4	2	1.5 bps/Hz	0.628	1/8	7.4 dB
6	4	2	1.5 bps/Hz	0.587	1/9	7.9 dB
7	4	2	1.5 bps/Hz	0.558	1/10	8.8 dB

Table 5.3 — Convergence thresholds obtained via EXIT chart analysis for Q2SRC schemes with modulation index values ranging from $h = 1/4$ to $h = 1/10$ and attaining a TSE of 1.5 bps/Hz

Set number	M	L	Spectral efficiency	Code rate	h	Threshold
1	4	3	1.5 bps/Hz	1.087	2/5	-
2	4	3	1.5 bps/Hz	0.829	2/7	5.0 dB
3	4	3	1.5 bps/Hz	0.752	1/4	5.1 dB
4	4	3	1.5 bps/Hz	0.645	1/5	5.8 dB
5	4	3	1.5 bps/Hz	0.573	1/6	6.3 dB
6	4	3	1.5 bps/Hz	0.521	1/7	6.8 dB
7	4	3	1.5 bps/Hz	0.481	1/8	7.6 dB

Table 5.4 — Convergence thresholds obtained via EXIT chart analysis for Q3SRC schemes with modulation index values ranging from $h = 2/5$ to $h = 1/8$ and attaining a TSE of 1.5 bps/Hz

Set number	M	L	Spectral efficiency	Code rate	h	Threshold
1	8	2	1.5 bps/Hz	1.108	1/4	-
2	8	2	1.5 bps/Hz	0.813	1/6	5.0 dB
3	8	2	1.5 bps/Hz	0.647	1/8	6.1 dB
4	8	2	1.5 bps/Hz	0.599	1/9	6.2 dB
5	8	2	1.5 bps/Hz	0.563	1/10	6.4 dB
6	8	2	1.5 bps/Hz	0.534	1/11	7.1 dB
7	8	2	1.5 bps/Hz	0.509	1/12	7.4 dB
8	8	2	1.5 bps/Hz	0.487	1/13	7.9 dB

Table 5.5 — Convergence thresholds obtained via EXIT chart analysis for O2RC schemes with modulation index values ranging from $h = 1/4$ to $h = 1/13$ and attaining a TSE of 1.5 bps/Hz

The best seven CPM schemes identified in terms of convergence threshold ($E_b/N_0 < 6.0$ dB) are:

1. Q3RC $h = 2/7$, $R = 0.839$: threshold at 4.7 dB
2. Q3RC $h = 1/4$, $R = 0.761$: threshold at 4.8 dB
3. Q3SRC $h = 2/7$, $R = 0.812$, and O2RC $h = 1/6$, $R = 0.813$: threshold at 5.0 dB
4. Q3SRC $h = 1/4$, $R = 0.752$: threshold at 5.1 dB
5. Q2RC $h = 1/5$, $R = 0.824$, and Q2SRC $h = 1/5$, $R = 0.812$: threshold at 5.6 dB

This short list should then be investigated in terms of performance in the error floor. To do so, the bounds on the frame error probability have to be computed. Nevertheless a problem exists: the (64,51) eBCH code does not achieve code rates higher than $R = 0.8$. For these cases, we should then switch to a longer eBCH code with the same error correcting power ($t = 2$ bits): the $(128, 113)$ code.

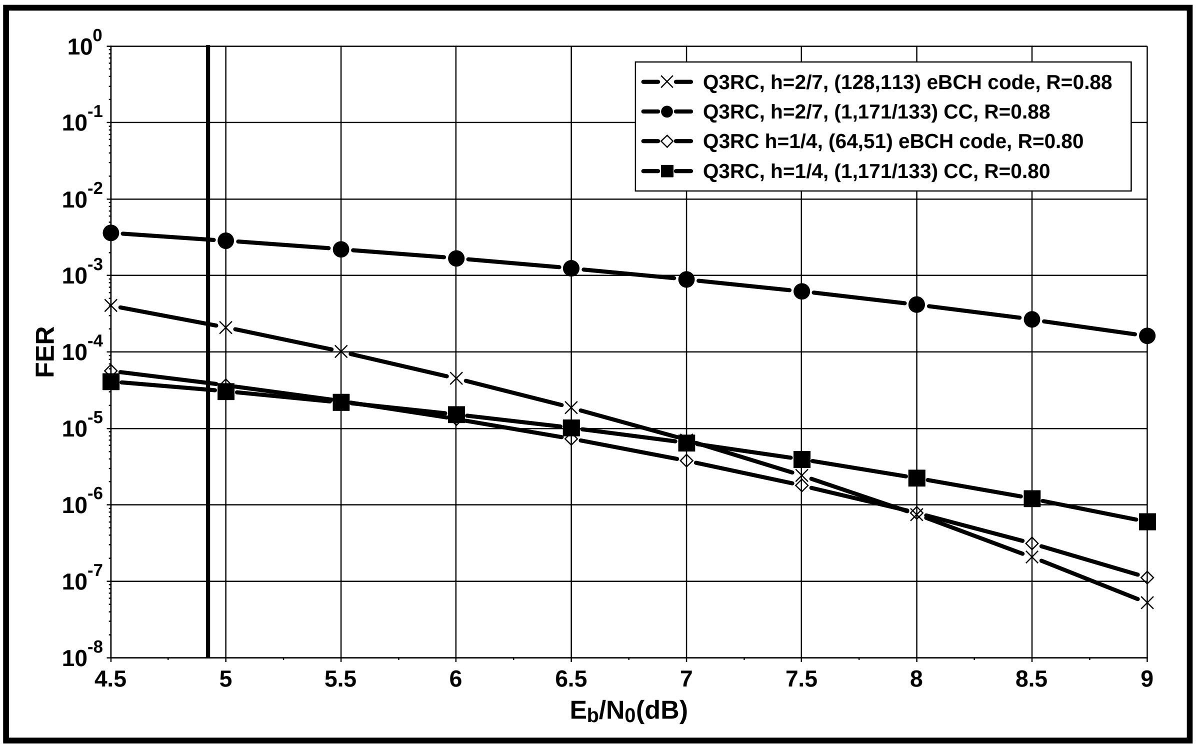

Figure 5.1 — FER bound comparison between the concatenation of a Q3RC $h = 1/4$ CPM with the $R = 0.8$ 64-state $(1, 171/133)$ CC and $(64, 51)$ eBCH code on one side and the concatenation of a Q3RC $h = 2/7$ CPM with the $R = 0.88$ 64-state (1,171/133) CC and (128,113) eBCH code on the other side.

Fig. 5.1 shows the bounds on the frame error rate for the $(128, 113)$ eBCH coded Q3RC with $h = 2/7$ compared to the $(64, 51)$ eBCH coded Q3RC with $h = 1/4$ CPM. The

$(1, 171/133)$ CC coded SCCPM bounds corresponding to identical simulation conditions have also been added for comparison purpose. The value of the probability of error predicted by the bound at an E_b/N_0 located 2.0 dB away from the threshold ($E_b/N_0 \simeq 7.0$) is around 10^{-5} for both eBCH coded SCCPM and the 64-state $R = 0.8$ SCCPM. However, the actual code rates taken for the computation of the bounds correspond to the non-shortened native code rates of the two BCH codes, that is $R \simeq 0.80$ for the $(64, 51)$ eBCH and $R \simeq 0.88$ for the $(128, 113)$ eBCH. Since the actual code rates for the application are lower ($R_{h=1/4} = 0.761 < 0.80$ and $R_{h=2/7} = 0.839 < 0.88$) and are obtained by the means of shortening, we would expect the error floors to be slightly lower than the ones plotted in fig. 5.1.

As the two sets of parameters display comparable floors with an eBCH outer code, the one with best iterative convergence properties should be chosen. Since two different codes are contemplated, EXIT charts should be computed for these particular cases. However, computing EXIT charts for the $(128, 113)$ eBCH code is of unaffordable complexity as the BCJR algorithm should operate on a trellis with up to 32,768 states. Then, the only alternative involves Monte Carlo FER simulations in order to both, evaluate the effect of the choice of the code on the convergence threshold and to verify the accuracy of error floor prediction via bounding techniques.

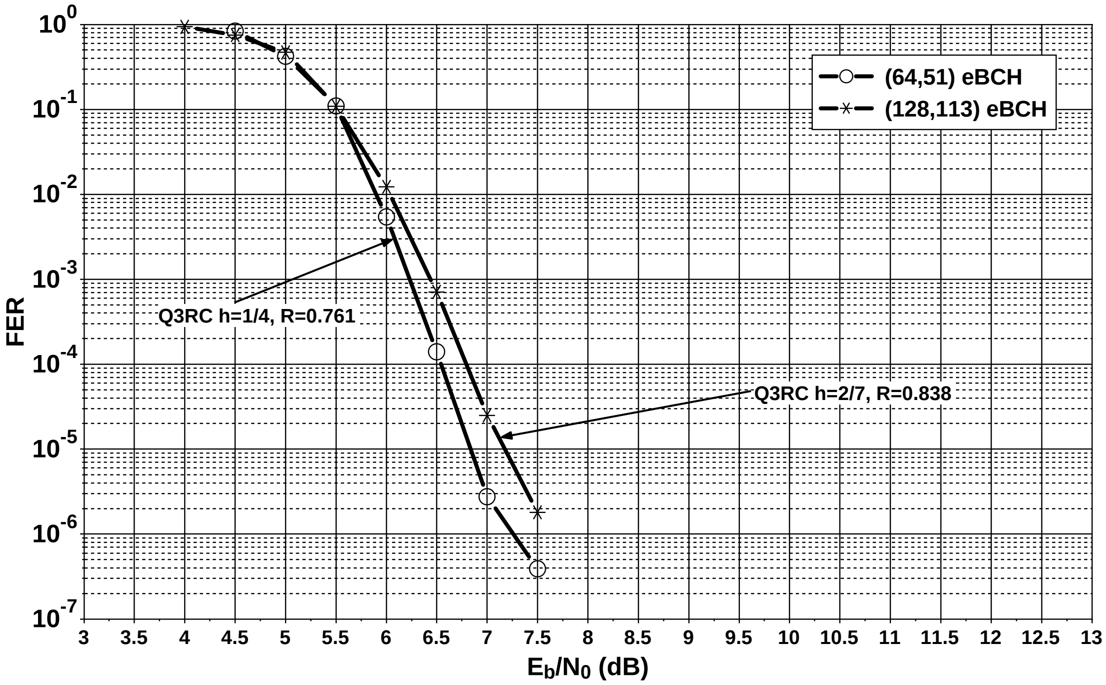

Figure 5.2 — FER comparison of the two competing schemes achieving a TSE of 1.5 bps/Hz for the transmission of 1024-information bit frames: $h = 1/4$ Q3RC with the $R = 0.761$ (64,51) eBCH code on one side and $h = 2/7$ Q3RC with the $R = 0.839$ (128,113) eBCH code on the other side. 30 iterations max.

Fig. 5.2 shows that the $(64, 51)$ eBCH coded Q3RC scheme with $h = 1/4$ and $R = 0.761$

performs slightly better in the waterfall region with a gain of 0.25 dB at 10^{-5} of FER and only displays a slight slope change at 10^{-6} of FER[1]. Moreover, since the computational complexity of both the CPM detector and the eBCH decoder is lower, this scheme has been definitely retained for the 1.5 bps/Hz TSE.

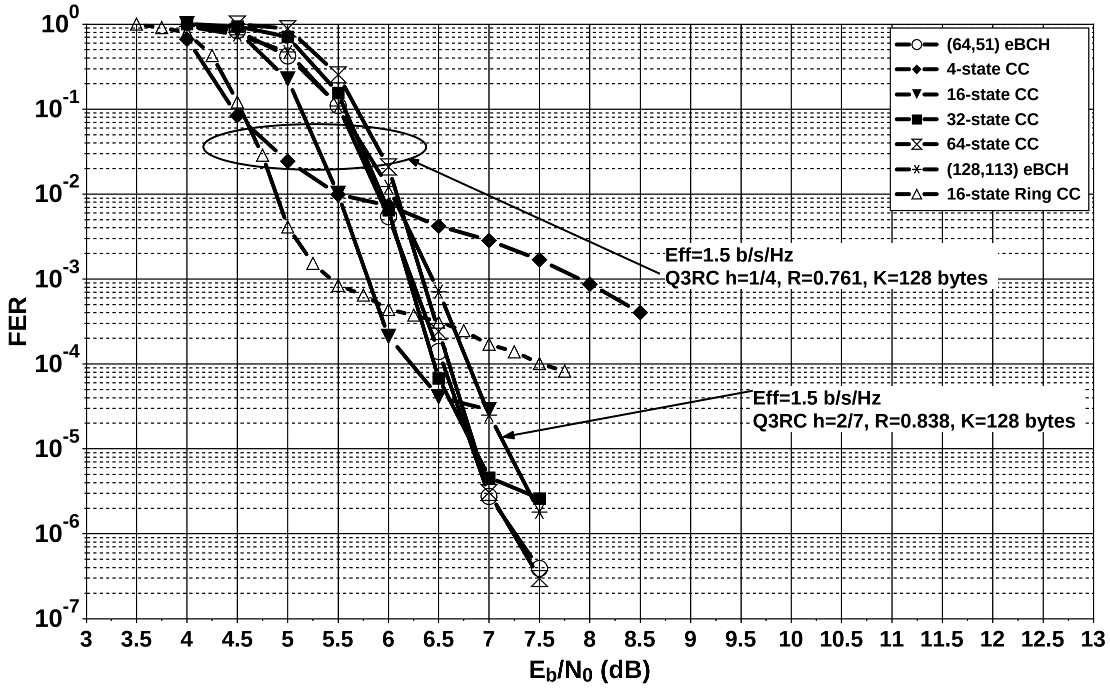

Figure 5.3 — FER performance of Q3RC, $h = 1/4$ associated with $R = 0.761$ (64,51) eBCH code, $R = 0.75$ 4, 16, 32, 64-state CC, $R = 0.75$ 16-state symbol based Ring CC and $R = 0.839$ (128,113) eBCH coded Q3RC, $h = 2/7$ for 1024-information bit frames and TSE of 1.5bps/Hz.

In order to perform an *a posteriori* validation of our SCCPM proposal for a TSE of 1.5 bps/Hz, we have also simulated the bit-interleaved SCCPM schemes using $(1, 5/7)$, $(1, 13/15)$, $(1, 35/23)$, $(1, 75/53)$, and $(1, 171/133)$ outer CC codes with $R = 0.75$ and Gray-mapped Q3RC $h = 1/4$ CPM. The simulation results are plotted in fig. 5.3. A symbol-interleaved SCCPM using the 16-state code over the ring $\mathcal{Z}_4$ of fig. 4.17(b) has also been simulated and the (128,113) eBCH coded Q3RC, $h = 2/7$ of the previous figure has also been reported for a broader comparison. Note that a slight code rate advantage exists for the convolutionally coded CPM as a code rate $R_{CC} = 0.75 < R_{eBCH} = 0.761$ was adopted in the undertaken simulations. Table 5.6 summarizes the main results regarding the compared convergence thresholds and the error floors for the simulated schemes.

We can observe that, despite the convergence threshold penalty reaching 1.2 dB for the 64-state CC and 1.0 dB for the $(64, 51)$ eBCH code, these two schemes represent the only solutions able to satisfy the error floor constraint of 10^{-6} of FER. Furthermore, the imple-

---

[1] The slope change can be lowered by introducing a high spread interleaver like the S-random.

TSE of 1.5 bps/Hz		
Outer code	$\Delta E_b/N_0$ at 10^{-1} of FER vs 16-state ring CC	Slope change at
16-state ring CC	-	$4.0{\cdot}10^{-3}$ of FER
4-state CC	-0.05 dB	$8.0{\cdot}10^{-2}$ of FER
16-state CC	+0.65 dB	$2.0{\cdot}10^{-4}$ of FER
32-state CC	+1.10 dB	$4.0{\cdot}10^{-6}$ of FER
64-state CC	+1.25 dB	$1.0{\cdot}10^{-6}$ of FER
(64,51) eBCH	+1.00 dB	$1.0{\cdot}10^{-6}$ of FER

Table 5.6 — Waterfall difference with respect to the 16-state code over ring $\mathcal{Z}_4$ and FER value corresponding to the change in the slope for all simulated SCCPM schemes. TSE of 1.5 bps/Hz.

mentation complexity of an eBCH SISO decoder using the Chase-Pyndiah algorithm is much lower than the complexity of 64-state CC Max-Log-MAP decoder[2]. As expected, the symbol-based 16-state ring CC offers the best waterfall performance, while it suffers from a critical error floor higher than 10^{-3} of FER.

In conclusion, the $(64, 51)$ eBCH coded bit-interleaved SCCPM represents the prevailing solution with best convergence threshold and lowest implementation complexity able to attain 10^{-6} of FER without marked error floors.

5.4 Selected SCCPM schemes

This section is intended to provide a summary of the main results stemming from the CPM and code selection process. First, we put forward the main trends regarding the CPM parameters and code rate effect that have been observed during the selection process and we provide a table summarizing the CPM parameters and the code rates selection result for the nine TSE values: 0.75, 1.0, 1.25, 1.5, 1.75, 1.875, 2.0, 2.125 and 2.25 bps/Hz. Then, some FER comparisons obtained with different outer codes are provided for 0.75 and 2.25 bps/Hz, representing the extreme TSE cases, for an *a posteriori* validation of the choice of the code. Finally, some additional simulation results are presented, in order to observe the effect of changing the frame size on the error correcting performance.

---

[2] The hardware complexity of a Chase-Pyndiah SISO decoder for the $(64, 51)$ eBCH code is comparable to the complexity of a 16-state CC Max-Log-MAP decoder.

5.4.1 General remarks about the selection procedure

The successive steps described in section 5.1 have been followed to choose the best SCCPM scheme for all values of target spectral efficiencies under study. The following observations regarding the set of parameters and their corresponding error correcting performance are worth mentioning:

- For spectral efficiencies lower than 1.0 bps/Hz, many systems with close (h, R) pair values show quasi-identical convergence thresholds. Consequently the preselection offers a wide set of parameters to choose from. The means of separation is thus mainly done via error floor comparison.

- For the remaining spectral efficiencies, the SCCPM system with the highest (h, R) values unambiguously shows the best convergence threshold respecting our proposed design guideline. Nevertheless, the investigation through the other sets of parameters offering the closest convergence thresholds has to be performed until the error floor requirement is met.

- All the TSEs can be achieved by octal schemes as well as by quaternary schemes. However, no error correcting performance improvement has been observed with octal schemes for spectral efficiencies lower than 1.75 bps/Hz. For higher efficiencies, octal schemes are competitive.

- For spectral efficiencies lower than 1.0 bps/Hz, partial response systems with smaller value of L $(L = 2)$ tend to offer superior error correcting capability than the ones with higher value of L.

- Apart from the 1.5 bps/Hz case, only one other spectral efficiency, 2.0 bps/Hz, leads to a set of CPM parameters dictating an outer code rate $R > 0.8$. Consequently a comparison between $(128, 113)$ and $(64, 51)$ eBCH codes has to be carried out again. Simulation results show that, similarly to the 1.5 bps/Hz case, the (64,51) eBCH code offers the best performance.

- The TSE of 1.5 bps/Hz represents the only case where the convergence threshold of the eBCH code is worse than the one of 32-state CC and quasi identical to the 64-state CC. For the remaining TSE, the eBCH always exhibits a convergence threshold improvement with respect to these two CC.

5.4.2 CPM selection for spectral efficiencies ranging from 0.75 to 2.25 bps/Hz

The selection of winning CPM parameters followed the steps enumerated in section 5.1 and applied to the 1.5 bps/Hz case of section 5.3. The resulting selected CPM schemes offer the earliest convergence thresholds when associated with an eBCH code while guaranteeing error floors lower than 10^{-6} of FER for the transmission of 1024-bit frames.

The results of the selection procedure are summarized in table 5.7.

CPM scheme selection				
TSE (bps/Hz)	Modulation	Modulation index h	Code rate R	Convergence Threshold
0.750	Q2RC	3/7	0.704	1.45 dB
1.000	Q2RC	2/7	0.688	2.25 dB
1.250	Q3RC	2/7	0.699	3.43 dB
1.500	Q3RC	1/4	0.761	4.89 dB
1.750	O2RC	1/8	0.755	7.54 dB
1.875	O2RC	1/9	0.749	8.15 dB
2.000	O2RC	1/9	0.799	9.40 dB
2.125	Q3RC	1/7	0.750	9.36 dB
2.250	Q3RC	1/7	0.794	9.97 dB

Table 5.7 — Selected CPM schemes and code rates. Convergence thresholds of the corresponding eBCH coded CPM for TSE of 0.75, 1.0, 1.25, 1.5, 1.75, 1.875, 2.0, 2.125 and 2.25 bps/Hz.

The results reported in table 5.7 show that the choice of the modulation order M and the pulse length L depends on the TSE value:

- for 0.75 bps/Hz $\leq$ TSE $\leq$ 1.0 bps/Hz, Q2RC schemes represent the best choice of CPM parameters.
- for 1.0 bps/Hz $\leq$ TSE $\leq$ 1.75 bps/Hz and 2.125 bps/Hz $\leq$ TSE $\leq$ 2.25 bps/Hz, Q3RC schemes represent the best choice of CPM parameters.
- for 1.75 bps/Hz $\leq$ TSE $\leq$ 2.0 bps/Hz, O2RC schemes represent the best choice of CPM parameters.

One can observe that no unambiguous strong conclusion on the choice of the CPM scheme family as a function of the TSE can be drawn, and a case by case study represents the only solution allowing the SCCPM to achieve both design constraints.

5.4.3 Code selection validation using FER Monte Carlo simulations

5.4.3.1 Simulation results for the 0.75 and 2.25 bps/Hz cases

In this section we report the FER simulation results for the two extreme TSE cases of 0.75 and 2.25 bps/Hz in order to validate the choice of the bit-interleaved SCCPM solution based on eBCH codes. Simulations were performed for the transmission of 1024-information bits frames for the single outer code symbol-interleaved and bit-interleaved SCCPM solutions studied in the previous chapter.

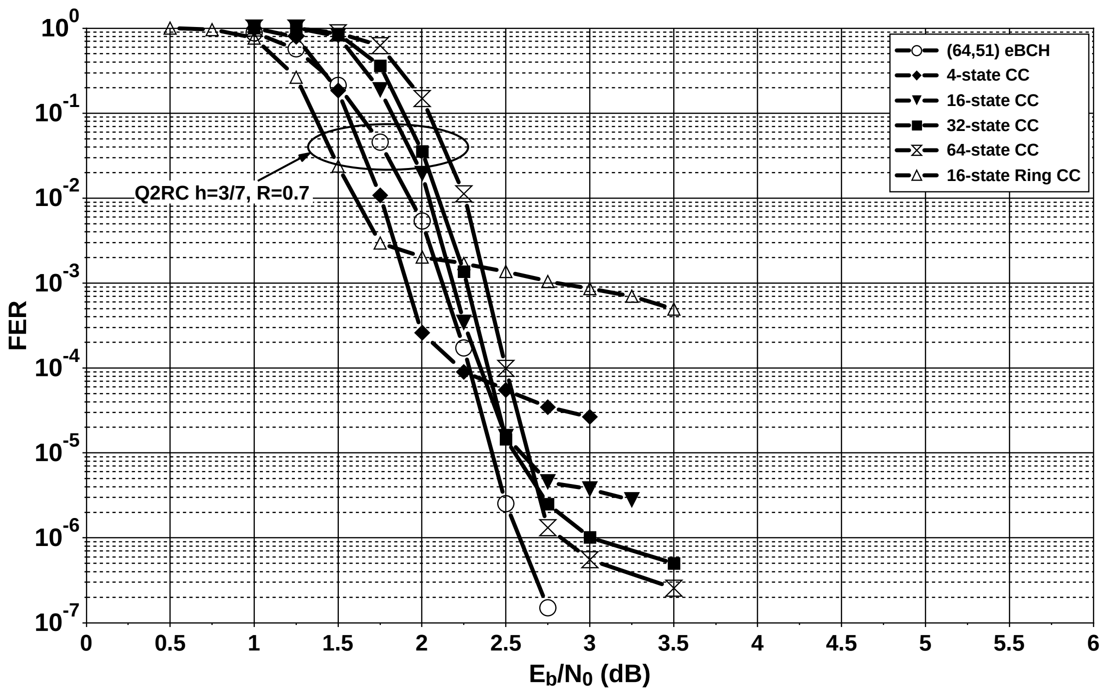

Figure 5.4 — FER performance of Q2RC, $h = 3/7$ associated with $R = 0.7$ (64,51) eBCH code, 4, 16, 32, 64-state CC and 16-state symbol based Ring CC for 1024-information bit frames and TSE of 0.75bps/Hz.

As already observed, the CC over ring $\mathcal{Z}_4$ displays the best convergence behaviour and can be taken as a reference for the waterfall region performance. However, it does not satisfy the floor constraint. Tables 5.8 and 5.9 recapitulate the E_b/N_0 gaps observed in the waterfall region between the different simulated schemes and the reference, as well as the position of their error floor.

In both cases, only two outer code solutions satisfy error floor requirement of 10^{-6} of FER consisting of the outer eBCH code and the 64-state CC. The block code shows 0.40 dB threshold gain with respect to the 64-state CC in the case of 0.75 and 2.25 bps/Hz while requiring a lower implementation complexity.

Although all the spectral efficiency cases have not been reported in this document, the

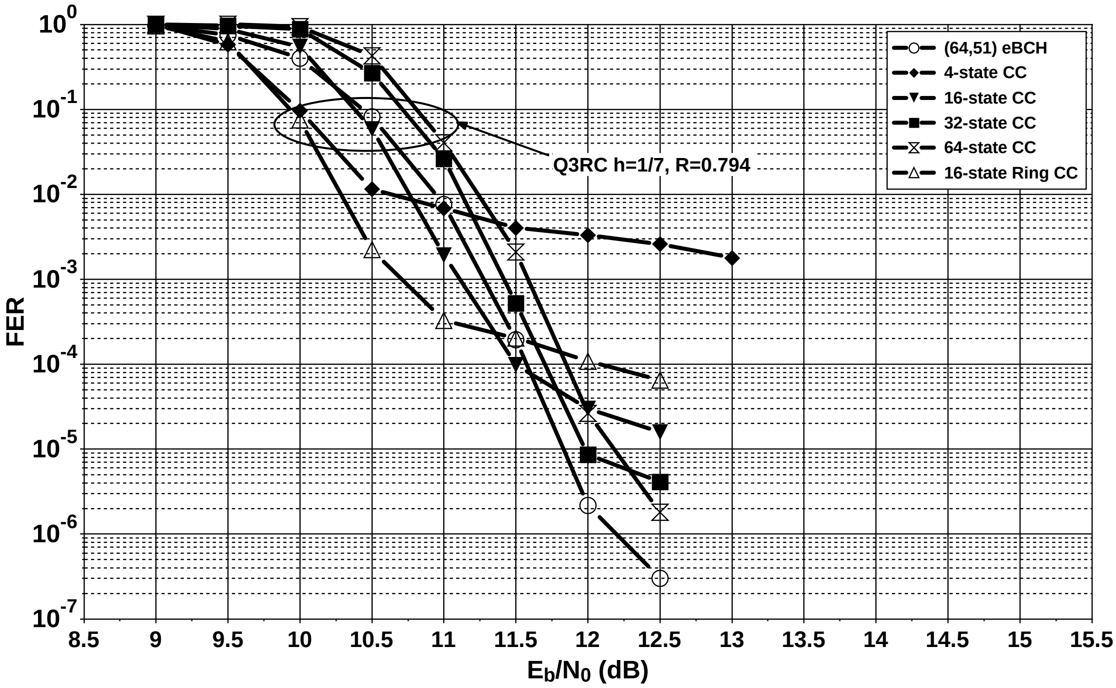

Figure 5.5 — FER performance of Q3RC, $h = 1/7$ associated with $R = 0.8$ (64,51) eBCH code, 4, 16, 32, 64-state CC and 16-state symbol based Ring CC for 1024-information bit frames and TSE of 2.25bps/Hz.

TSE = 0.75 bps/Hz - transmission of 1024-bit frames		
Outer code	$\Delta E_b/N_0$ at 10^{-1} of FER vs 16-state ring CC	Slope change at
16-state ring CC	-	$3.0{\cdot}10^{-3}$ of FER
4-state CC	+0.20 dB	$2.5{\cdot}10^{-4}$ of FER
16-state CC	+0.45 dB	$2.0{\cdot}10^{-5}$ of FER
32-state CC	+0.50 dB	$2.5{\cdot}10^{-6}$ of FER
64-state CC	+0.70 dB	$1.4{\cdot}10^{-6}$ of FER
(64,51) eBCH	+0.30 dB	$2.0{\cdot}10^{-6}$ of FER (slight slope change)

Table 5.8 — Gap in the waterfall region with respect to the 16-state code over ring $\mathcal{Z}_4$ and FER value corresponding to the change in the slope for all simulated SCCPM solutions. TSE = 0.75 bps/Hz.

TSE = 2.25 bps/Hz - transmission of 1024-bit frames		
Outer code	$\Delta E_b/N_0$ at 10^{-1} of FER vs 16-state ring CC	Slope change at
16-state ring CC	-	$3.0{\cdot}10^{-4}$ of FER
4-state CC	-	$1.0{\cdot}10^{-2}$ of FER
16-state CC	+0.35 dB	$1.0{\cdot}10^{-4}$ of FER
32-state CC	+0.75 dB	$9.0{\cdot}10^{-5}$ of FER
64-state CC	+0.80 dB	$3.0{\cdot}10^{-5}$ of FER (slight slope change)
(64,51) eBCH	+0.40 dB	$2.0{\cdot}10^{-6}$ of FER (slight slope change)

Table 5.9 — Gap in the waterfall region with respect to the 16-state code over ring and FER value corresponding to the change in the slope for all studied SCCPM solutions. TSE of 2.25 bps/Hz.

same relative behaviour between the different codes has also been observed for the set of TSE values under study where the proposed outer code solution (eBCH codes) still shows error correcting performance best suited for a broadband satellite link application at a reasonable complexity.

5.4.3.2 Effect of the frame length

Two frame sizes had to be investigated within the framework of the BSDT project: 1024 bits and 512 bits. Consequently, simulations were also undertaken for the short block size case for all considered spectral efficiencies. In this section, we report the corresponding results for SEs of 0.75 and 1.5 bps/Hz in fig. 5.6. The latter SE case has been chosen in order to observe the effect of changing the frame size on the relative error correcting performance of the 64-state CC with respect to the eBCH in the only TSE case (1.5 bps/Hz) where quasi-identical FER performance was observed for both codes.

The obtained FER simulation results for the transmission of 512-bit frames are in line with the ones previously presented for 1024-bit frames since no change in relative error correcting behaviour of the different studied SCCPM solutions have been observed. Particularly, the proposed SCCPM solution with an outer eBCH code remains the best compromise when the frame size decreases.

5.5 Conclusion

In this project, we have proposed a pragmatic method to optimise coded CPM schemes for a range of spectral efficiencies varying from 0.75 to 2.25 bit/s/Hz, targeting the return link

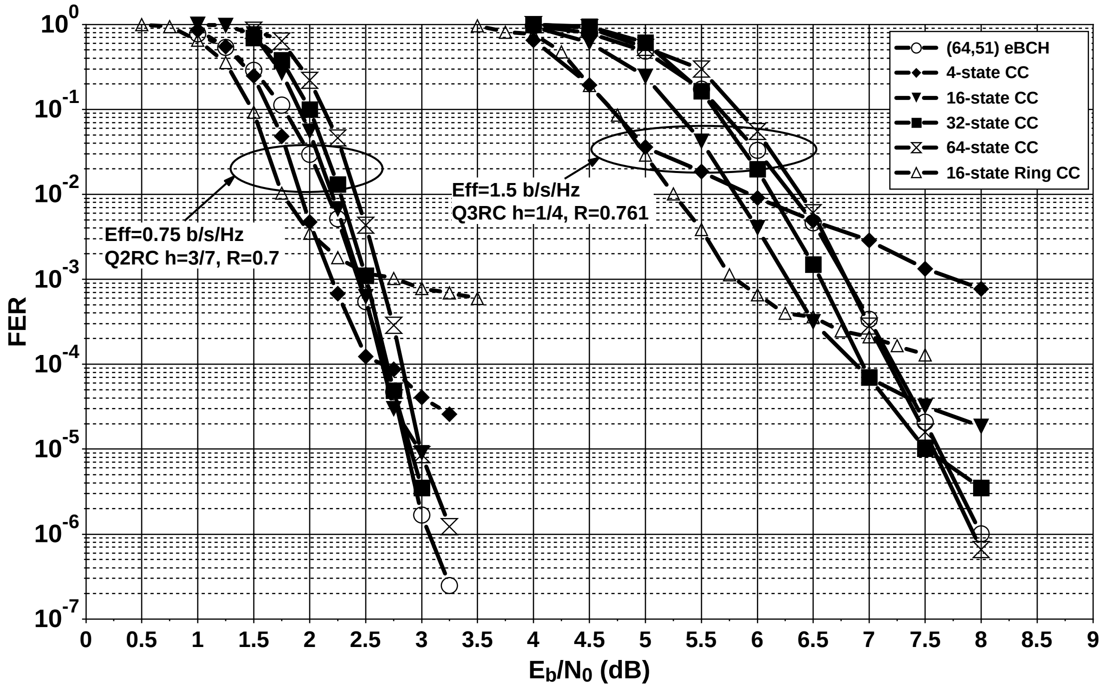

Figure 5.6 — FER performance of $R = 0.7$ Q2RC, $h = 3/7$ and $R = 0.761$ Q3RC, $h = 1/4$ associated with (64,51) eBCH code, 4, 16, 32, 64-state CC and 16-state symbol based Ring CC for 512-information bit frames and TSE of 0.75 and 1.5bps/Hz.

of broadband satellite communications. Innovative contributions have been proposed in this context namely a method for the choice of CPM parameters and the outer code solution. The resulting CPM system offers the best possible convergence threshold while achieving FER below 10^{-6} without change in the slope. This is due to the good distance properties of eBCH codes improving the joint performance of the concatenated SCCPM scheme and that for every value of the spectral efficiency.

In this second part of the manuscript, we have investigated SCCPM schemes in order to provide a technical solution to the design of a broadband satellite link. Some were inspired by previous works, the remaining others bear our marks. From our innovative contributions we would like to cite a method for choosing the set of CPM parameters, CPM precoding with convolutional codes over rings, a symbol based outer code solution using double binary convolutional codes, Flexi-like and eBCH outer code solutions. Some of these have proven to be particularly adapted to the targeted application, namely the contribution on optimizing the choice of CPM parameters and the proposition of eBCH as coding solution. Both allowed us to fully satisfy the design objectives in the context of the BSDT project.

Conclusion

THE work accomplished in the context of this PhD thesis spans the wide field of coded modulations while treating several aspects. The obtained results have found their way into implementation. They are divided into two main fields of interest:

In the first part, we have investigated linear high order modulation schemes such as QAM and PSK and their association with forward error correcting codes. After taking notice of the degradation in performance when transmitting over fading channels, we have defined the underlying reasons. Once depicted, factors acting on error correcting performance were clearly identified. In fact, diversity order represents the coded modulation parameter with the greatest influence.

Afterwards, we have proposed adequate solutions intended to increase the diversity order. This latter can be doubled by introducing minor modifications to the modulator and the demodulator inducing only a small increase in overall system complexity. A joint iterative demodulation and decoding process was carried out in order to fully take advantage of the increased diversity. Promising results have shown an improvement in error correcting performance on both fronts, waterfall and error floor, in most coded modulation cases. Floors lowered by two orders of magnitude or earlier convergence thresholds by 0.75 to 1.00 dB have been frequently obtained.

Future works on the subject are expected to treat three main aspects:

Results have been so far obtained while assuming a perfect channel estimation. The extension of the promising results to channels with partial CSI constitutes one of the steps to be made.

When very low error floors are targeted, Monte Carlo simulations represent time consuming operations. Consequently, adapting bounding techniques to the introduced modifications shall be investigated in order to propose an alternative to simulation.

Up until now, we have studied the association of turbo codes and modulations with signal space diversity. The extension to other types of strong outer codes namely LDPC is planned.

The diversity increase solution described in this part of the manuscript represents one of the contributions of the response to the DVB-T2 call for technology in June 2007. In this context, the work perspectives will be thouroughly investigated.

In the second part, we have investigated power and bandwidth efficient modulation schemes intended for a satellite link. Undertaken work is registered as a part of a European Space Agency funded project. Investigated schemes concern mainly continuous phase modulation where one of the existing families, namely MSK, has already been adopted in several standards and applications. High order CPM systems have yet to find their way into practical applications basically because of the high implementation complexity of the receiver. However, thanks to the great advancement made these recent years in computational power of integrated circuits and the advantages of this type of modulation, a renewed interest in CPM was born.

Our study provides answers to the choice of CPM parameters, the selection of the outer code solution, the mapping and the interleaving type for attaining FER in the order of 10^{-6} without change in the slope while operating at spectral efficiencies up to 2.25 bps/Hz. It includes innovative contributions that found their way into literature. Promising results satisfying design constraints for a broadband satellite link were obtained thanks to our proposed method for choosing CPM parameters on one side and our selection of the outer code solution on the other side.

This study does not have any foreseen technical follow up in the near future at the Electronics department of ENST Bretagne. However, obtained results are at the basis of prototype implementation at this time.

Additional work has been performed during this PhD thesis that has not been addressed in this manuscript. In 2004, we have participated in a project with partners from the Ecole Nationale des Télécommunications (ENST), the Institut National des Télécommunications (INT) and the EURECOM institute. The goal of this study was to conceive a low cost and power consumption wireless product using Ultra Wide Band (UWB) architectures for indoor high throughput short distance use. In this context, we have investigated the association of turbo codes and Pulse Position Modulation (PPM) over UWB channels. Innovative results with performance less than 1.0 dB from capacity have been published and set the road for a successful hardware prototyping.

List of Figures

List of Tables

List of acronyms

ARP	Almost Regular Permutation
ATM	Asynchronous Transfer Mode
AWGN	Additive White Gaussian Noise
BCJR	Bahl, Cocke, Jelinek and Raviv
BER	average Bit Error Rate
BICM	Bit-Interleaved Coded modulation
BICM-ID	Bit-Interleaved Coded Modulation with Iterative Demodulation
bpcu	bit per channel use
bps/Hz	bit per second per Hertz
BSDT	Study of enhanced digital transmission techniques for Broadband Satellite Digital Transmissions
CC	Convolutional Code
CPE	Continuous Phase Encoder
CPM	Continuous Phase Modulation
CSI	Channel State Information
DAB	Digital Audio Broadcasting
DVB-RCS	Digital Video Broadcasting Return Channel over Satellite (EN 301 790)
DVB-S2	Digital Video Broadcasting, Satellite, Second Generation (EN 302 307)
DVB-T	Digital Video Broadcasting, Terrestrial (EN 300 744)

DVB-T2	Digital Video Broadcasting, Terrestrial, Second Generation
eBCH	extended Bose, Ray-Chaudhuri, Hocquenghem
ENST	Ecole Nationale des Télécommunications
ESA	European Space Agency
ETSI	European Telecommunications Standard Institute
EXIT	EXtrinsic Information Transfer
FEC	Forward Error Correcting
FER	average Frame Error Rate
FHSS	Frequency-Hopping Spread Spectrum
GMSK	Gaussian Minimum Shift Keying
GSM	Global System for Mobile communications
HDTV	High Definition TV
IDMC	Independent Discrete Memoryless Channels
INT	Institut National des Télécommunications
IOWEF	Input-Output Weight Enumerating Function
IRA	Irregular Repeat Accumulate
LDPC	Low Density Parity Check
LOS	Line Of Sight
MHOMS	Modem for High Order Modulation Schemes
MIMO	Multiple-Input Multiple-Output
ML	Maximum Likelihood
MLSD	Maximum Likelihood Sequence Detection
MM	Memoryless Mapper
MSK	Minimum Shift Keying
NSED	Normalized Squared Euclidean Distance

OBP	Out of Band Power
OFDM	Orthogonal Frequency Division Multiplexing
OWEF	Output Weight Enumerating Function
PAM	Pulse Amplitude Modulation
PCCC	Parallel Concatenated Convolutional Codes
pdf	probability density function
PEP	Pairwise Error Probability
PPM	Pulse Position Modulation
PSD	Power Spectral Density
PSIR	Penalized Symmetric Information Rate
PSK	Phase Shift Keying
QAM	Quadrature Amplitude Modulation
RC	Raised Cosine
RQD-16-QAM	Rotated and Q-Delayed 16-Quadrature Amplitude Modulation
RSC	Recursive Systematic Convolutional
SCC	Serial Concatenation of Codes
SCCC	Serially Concatenated Convolutional Codes
SCCPM	Serially Concatenated Continuous Phase Modulation
SE	Spectral Efficiency
SI	Soft Input
SIR	Symmetric Information Rate
SISO	Soft Input Soft Output
SNR	average Signal To Noise Ratio
SP	Set Partitionning
SRC	Spectrally Raised Cosine frequency

SSD	Signal Space Diversity
S-SCP	Systematic with Serially Concatenated Parity
S/P	Serial to Parallel
SSP	Semi Set Partitionning
TBICM	Turbo Bit-Interleaved Coded Modulation
TBICM-ID	Turbo Bit-Interleaved Coded Modulation with Iterative Demodulation
TBICM-ID-SSD	Turbo Bit-Interleaved Coded Modulation with Iterative Demodulation and Signal Space Diversity
TBICM-SSD	Turbo Bit-Interleaved Coded Modulation with Signal Space Diversity
TCCPM	Trellis-Coded Continuous Phase Modulation
TCM	Trellis Coded Modulation
TLC	Turbo-Like Codes
TSE	Target Spectral Efficiency
TTCM	Turbo Trellis-Coded Modulation
UEP	Uniform Error Property
UWB	Ultra Wide Band
VoIP	Voice over Internet Protocol
WAN	Wide Area Networking
WiFi	Wireless Fidelity (IEEE 802.11)
WiMax	Worldwide Interoperability for Microwave Access (IEEE 802.16)
WLAN	Wireless Local Area Network

List of publications

[1] A. Graell i Amat, C. Abdel Nour, and C. Douillard, "Serially concatenated continuous phase modulation for satellite communications," *Submitted to IEEE Trans. Commun.*, 2007.

[2] ——, "Study of enhanced digital transmission techniques for broadband satellite digital transmissions (BSDT), Technical Note TN05: Code selection for the CPM return link," European Space Agency (ESA) funded Project, Tech. Rep., July 2007.

[3] ——, "Serially concatenated continuous phase modulation with extended BCH codes," in *IEEE Inf. Theory Workshop on Wireless Networks*, July 2007, pp. 1–6.

[4] C. Abdel Nour and C. Douillard, "On lowering the error floor of high order turbo BICM schemes over fading channels," in *IEEE Global Telecommun. Conf., GLOBECOM*, Nov. 2006, pp. 1–5.

[5] S. Chaillou, J. Boutros, and C. Abdel Nour, "Efficient iterative decoding of impulse radio based on energy detection," in *Int. Workshop on UWB Technologies*, Yokosuka, Japan, Dec. 2005.

[6] C. Abdel Nour and C. Douillard, "Performance improvement using turbo coded BICM-ID with 16-QAM over Gaussian and flat fading Rayleigh channels." in *IST Mobile & wireless commun. summit*, Dresden, Germany, June 2005.

Bibliography

[1] C. Shannon, “A mathematical theory of communication,” *Bell System Tech. J.*, vol. 27, pp. 379–423, 623–656, 1948.

[2] C. E. Shannon, “Probability of error for optimal codes in a Gaussian channel,” *Bell Syst. Tech. Journal*, vol. 38, pp. 611–656, 1959.

[3] C. Berrou, A. Glavieux, and P. Thitimajshima, “Near Shannon limit error-correcting coding and decoding: Turbo codes,” in *IEEE Int. Conf. Commun.*, vol. 2, May 1993, pp. 1064–1070.

[4] P. Robertson and T. Wörz, “Bandwidth-efficient turbo trellis-coded modulation using punctured component codes,” *IEEE J. Select. Areas Commun.*, vol. 16, no. 2, pp. 206–218, Feb. 1998.

[5] S. Le Goff, A. Glavieux, and C. Berrou, “Turbo-codes and high spectral efficiency modulation,” in *IEEE Int. Conf. Commun.*, vol. 2, New Orleans, LA, USA, May 1994, pp. 645–649.

[6] B. Sklar, “Rayleigh fading channels in mobile digital communication systems .I. characterization,” *IEEE Commun. Magazine*, vol. 35, no. 7, pp. 90–100, July 1997.

[7] J. D. Parsons, *The mobile radio propagation channel.* New York, USA: John Wiley & sons, 1992.

[8] R. S. Kennedy, *Fading dispersive communication channels.* New York, USA: John Wiley & sons, 1969.

[9] W. C. Jakes, *Microwave Mobile Communications.* Wiley-interscience, May 1994.

[10] J. M. Wozencraft and J. I. M., *Principles of Communication Engineering.* Waveland Press, 1965.

[11] E. Baccarelli and A. Fasano, “Some simple bounds on the symmetric capacity and outage probability for QAM wireless channels with Rice and Nakagami fadings,” *IEEE J. Select Areas Commun.*, vol. 18, no. 3, Mar. 2000.

[12] R. Bulirsch and J. Stoer, *Handbook Series Numerical Integration.* Numerische Mathematik, 1967.

[13] S. Dolinar, D. Divsalar, and F. Pollara, “Turbo code performance as a function of code block size,” in *IEEE Int. Symp. Inform. Theory*, Cambridge, USA, Aug. 1998.

[14] ——, *Code Performance as a Function of Block Size*, May 1998, jPL TMO Progress Report 42-133.

[15] C. Berrou and A. Glavieux, “Near optimum error correcting coding and decoding: Turbo-codes,” *IEEE Trans. Commun.*, vol. 44, no. 10, pp. 1261–1271, Oct. 1996.

[16] S. Vialle and J. J. Boutros, “Performance of optimal codes on Gaussian and Rayleigh fading channels: A geometrical approach,” in *37th Annual Allerton Conference*, Illinois, USA, Oct. 1999.

[17] S. Vialle, “Construction and analysis of new efficient channel coding structures for iterative decoding,” Ph.D. dissertation, ENST Paris, 2000.

[18] G. Ungerboeck, “Channel coding with multilevel/phase signals,” *IEEE Trans. Inform. Theory*, vol. 28, no. 1, pp. 55–66, 1982.

[19] S. H. Jamali and T. Le-Ngoc, *Coded-Modulation Techniques for Fading Channels.* Kluwer Academic Publishers, 1994.

[20] A. J. Viterbi, J. K. Wolf, E. Zehavi, and R. Padovani, “A pragmatic approach to trellis-coded modulation,” *IEEE Commun. Mag.*, vol. 27, no. 7, pp. 11–19, 1989.

[21] E. Zehavi, “8-PSK trellis codes for a Rayleigh channel,” *IEEE Trans. Commun.*, vol. 40, no. 5, pp. 873–884, May 1992.

[22] G. Caire, G. Taricco, and E. Biglieri, “Bit-interleaved coded modulation,” *IEEE Trans. Inform. Theory*, vol. 44, no. 3, pp. 927–946, May 1998.

[23] S. A. Al-Semari and T. Fuja, “Bit-interleaved I-Q TCM,” in *Int. Symp. Inform. Theory and its Applications*, Victoria, B.C., Canada, Sep. 1996.

[24] S. Benedetto and E. Biglieri, *Principles of Digital Transmission with Wireless Applications.* New York: Kluwer, 1999.

[25] M. K. Simon, J. K. Omura, R. A. Scholtz, and B. K. Levitt, “Spread spectrum communications,” *Rockville, MD, Computer Science press*, vol. 1, 1985.

[26] D. Divsalar and M. Simon, “Trellis coded modulation for 4800-9600 bits/s transmission over a fading mobile satellite channel,” *IEEE J. Select. Areas Commun.*, vol. SAC-5, pp. 162–175, 1987.

[27] A. Nilsson and T. Aulin, “On in-line bit interleaving for serially concatenated systems,” in *IEEE Int. Conf. Commun.*, Seoul, South korea, May 2005.

[28] S. Benedetto, D. Divsalar, G. Montorsi, and F. Pollara, “Serial concatenation of interleaved codes: Performance analysis, design, and iterative decoding,” *IEEE Trans. Inform. Theory*, vol. 44, no. 3, pp. 909–926, May 1998.

[29] C. Fragouli and R. D. Wesel, “Semi-random interleaver design criteria,” in *IEEE Global Telecommun. Conf., GLOBECOM*, Rio de Janeiro, Brazil, Dec. 1999, pp. 2352–2356.

[30] G. C. J. Clarke and C. Bibb, *Error correction coding for digital communications.* Plenum press, 1981.

[31] X. Li and J. Ritcey, “Bit-interleaved coded modulation with iterative decoding,” *IEEE Commun. Lett.*, vol. 1, no. 6, pp. 169–171, Nov. 1997.

[32] J. Lodge, R. Young, P. Hoeher, and J. Hegenauer, “Separable MAP filters for the decoding of product and concatenated codes,” in *IEEE Int. Conf. Commun.*, June 1993, pp. pp. 102–106.

[33] S. Benedetto, D. Divsalar, G. Montorsi, and F. Pollara, “A soft-input soft-output APP module for iterative decoding of concatenated codes,” *IEEE Commun. Lett.*, vol. 1, no. 1, pp. 22–24, Jan. 1997.

[34] X. Li, A. Chindapol, and J. Ritcey, “Bit-interleaved coded modulation with iterative decoding and 8 PSK signaling,” *IEEE Trans. Commun.*, vol. 50, no. 8, pp. 1250–1257, Aug. 2002.

[35] X. Li and J. Ritcey, “Trellis-coded modulation with bit interleaving and iterative decoding,” *IEEE J. Select. Areas Commun.*, vol. 17, no. 4, pp. 715–724, Apr. 1999.

[36] A. Chindapol and J. Ritcey, “Design, analysis, and performance evaluation for BICM-ID with square QAM constellations in Rayleigh fading channels,” *IEEE J. Select. Areas Commun.*, vol. 19, no. 5, pp. 944–957, May 2001.

[37] F. Schreckenbach, N. Görtz, J. Hagenauer, and G. Bauch, “Optimization of symbol mappings for bit-interleaved coded modulation with iterative decoding,” *IEEE Commun. Lett.*, vol. 7, no. 12, pp. 593–595, Dec. 2003.

[38] J. Tan and G. Stuber, “Analysis and design of symbol mappers for iteratively decoded BICM,” *IEEE Trans. Wireless Commun.*, vol. 4, no. 2, pp. 662–672, Mar. 2005.

[39] P. Junk, “Novel low complexity decoder for turbo codes,” *Electron. Lett.*, pp. 86–87, Jan. 1995.

[40] E. Hall and S. Wilson, “Design and analysis of turbo codes on Rayleigh fading channels,” *IEEE J. Select. Areas Commun.*, vol. 16, no. 2, pp. 160–174, Feb. 1998.

[41] C. Douillard and C. Berrou, “Turbo codes with rate-m/(m+1) constituent convolutional codes,” *IEEE Trans. Commun.*, vol. 53, no. 10, pp. 1630–1638, Oct. 2005.

[42] Y. Saouter, “Permutation models for B3G turbo codes,” in *Symp. Turbo Codes*, Muncih, Germany, April 2006.

[43] S. Barbulescu and W. Farrel, “Bandwidth efficient turbo coding for high speed mobile satellite communications.” in *Symp. Turbo Codes*, Brest, France, Sep. 1997, pp. 119–126.

[44] I. Abramovici and S. Shamai, “On turbo encoded BICM,” *Ann. Telecommun.*, vol. 54, no. 3, pp. 225–234, Mar. 1999.

[45] J. Boutros and E. Viterbo, “Signal space diversity: A power- and bandwidth-efficient diversity technique for the Rayleigh fading channel,” *IEEE Trans. Inform. Theory*, vol. 44, no. 4, pp. 1453–1467, July 1998.

[46] ——, “High diversity lattices for fading channels,” in *IEEE Int. Symp. Inform. Theory*, Whistler, Canada, Sep. 1995.

[47] ——, “Rotated multidimensional QAM constellations,” in *IEEE Workshop Inform. Theory*, Haifa, Israel, June 1996.

[48] J. Boutros, E. Viterbo, C. Rastello, and J.-C. Belfiore, “Good lattice constellations for both Rayleigh fading and Gaussian channels,” *IEEE Trans. Inform. Theory*, vol. 42, no. 2, pp. 502–518, Mar. 1996.

[49] S. Al-Semari and T. Fuja, “I-Q TCM: reliable communication over the Rayleigh fading channel close to the cutoff rate,” *IEEE Trans. Inform. Theory*, vol. 43, no. 1, pp. 250–262, 1997.

[50] M. K. Simon and M.-S. Alouini, *Digital communications over fading channels*, 2nd ed., J. Proakis, Ed. John Wiley & sons, 2005.

[51] S. ten Brink, “Convergence of iterative decoding,” *Electron. Lett.*, vol. 35, pp. 1117–1119, 1999.

[52] DVB-S2, "Second generation framing structure, channel coding and modulation systems for broadcasting, interactive services, news gathering and other broadband satellite applications," *ETSI EN 302 307 V1.1.2*, 2006.

[53] DVB-RCS, "Interaction channel for satellite distribution systems," *ETSI EN 301 790 V1.2.2*, 2000.

[54] SATMODE, "Modem layer specification," *available on the ESA Telecom web site at http://telecom.esa.int/telecom/www/object/index.cfm?fobjectid=13868*, 2005.

[55] J. B. Anderson, T. Aulin, and C.-E. Sundberg, *Digital Phase Modulation.* Springer, 1986.

[56] L. Bahl, J. Cocke, F. Jelinek, and J. Raviv, "Optimal decoding of linear codes for minimizing symbol error rate," *IEEE Trans. Inform. Theory*, vol. 20, no. 2, pp. 284–287, Mar 1974.

[57] B. Rimoldi, "A decomposition approach to CPM," *IEEE Trans. Inform. Theory*, vol. 34, no. 2, pp. 260–270, March 1988.

[58] F. Amoroso and J. Kivett, "Simplified msk signaling technique," *IEEE Trans. Commun.*, vol. Com-25, pp. pp. 433–441, April 1977.

[59] P. D. Welch, "The use of fast Fourier transforms for the estimation of power spectra: A method based on time averaging over short modified periodograms," *IEEE Trans. Audio and Electroacoustics*, vol. 15, no. 2, pp. 70–73, Mar 1967.

[60] T. M. Cover and T. J. A., *Elements of Information Theory.* Wiley-Interscience, 1991.

[61] C.-H. Kuo and K. Chugg, "On the bandwidth efficiency of CPM signals," in *IEEE Military Commun. Conf., MILCOM*, vol. 1, Monterey, CA, USA, Oct. 2004, pp. 218–224.

[62] M. Xiao and T. Aulin, "Serially concatenated continuous phase modulation with symbol interleavers: Performance, properties and design principles," in *IEEE Global Telecommun. Conf., GLOBECOM*, vol. 1, Dallas, USA, Nov. 2004, pp. 179–183.

[63] P. Moqvist and T. Aulin, "Serially concatenated continuous phase modulation with iterative decoding," *IEEE Trans. Commun.*, vol. 49, no. 11, pp. 1901–1915, Nov. 2001.

[64] A. Graell i Amat, G. Montorsi, and F. Vatta, "Analysis and design of rate-compatible serial concatenated convolutional codes," in *IEEE Int. Symp. Inf. Theory, ISIT*, Adelaide, Australia, Sep. 2005, pp. 607–611.

[65] P. Moqvist and T. Aulin, "Power and bandwidth efficient serially concatenated CPM with iterative decoding," in *IEEE Global Telecommun. Conf., GLOBECOM*, San Fransisco, CA, USA, Nov. 2000, pp. 790–794.

[66] S. ten Brink, "Convergence behavior of iteratively decoded parallel concatenated codes," *IEEE Trans. Commun.*, vol. 49, no. 10, pp. 1727–1737, 2001.

[67] J. Hagenauer, "The EXIT chart - introduction to extrinsic information transfer in iterative processing," in *European Signal Processing Conference, EUSIPCO*, Vienna, Austria, Sep. 2004, pp. 1541–1548.

[68] L. McPheters, S. McLaughlin, and K. Narayanan, "Precoded PRML, serial concatenation, and iterative turbo decoding for digital magnetic recording," *IEEE Trans. Magnetics*, vol. 35, no. 5, pp. 2325–2327, Sept. 1999.

[69] K. R. Narayanan and G. L. Stuber, "Performance of trellis coded CPM with iterative demodulation and decoding," *IEEE Trans. Commun.*, vol. 49, no. 4, pp. 676–687, April 2001.

[70] I. Altunbas and K. Narayanan, "A novel concatenated coding scheme for MSK," *Electron. Lett.*, Nov. 2001.

[71] V. Szeto and S. Pasupathy, "Iterative decoding of serially concatenated convolutional codes and MSK," *IEEE Commun. Lett.*, vol. 3, no. 9, pp. 272–274, Sept. 1999.

[72] P. Moqvist, "Serially concatenated systems: An iterative decoding approach with application to continuous phase modulation," *licentiate thesis, Chalmers University of Technology, Goteborg, Sweden*, Dec. 1999.

[73] M. Xiao and T. Aulin, "Serially concatenated continuous phase modulation with convolutional codes over rings," *IEEE Trans. Commun.*, vol. 54, no. 8, pp. 1387–1396, Aug. 2006.

[74] ——, "Irregular repeat continuous phase modulation," *IEEE Commun. Lett.*, vol. 9, no. 8, pp. 723–725, Aug 2005.

[75] M. Xiao, "Some concatenated and iterative decoding approaches for continuous phase modulation," *licentiate thesis, Chalmers University of Technology, Goteborg, Sweden*, Dec. 2004.

[76] A. Ganesan, "Capacity estimation and code design principles for continuous phase modulation CPM," Ph.D. dissertation, Texas A&M University, Sept. 2004, http://txspace.tamu.edu/handle/1969.1/53.

[77] A. Yilmaz and W. Stark, "Turbo coded continuous phase modulation," in *IEEE Military Commun. Conf., MILCOM*, vol. 2, Washington, USA, Oct. 2001, pp. 1405–1409.

[78] J. L. Massey and T. Mittelholzer, "Convolutional codes over rings," Gotland, Sweden, Sept. 1989, pp. 14–18.

[79] A. R. Hammons, P. V. Kumar, A. Calderbank, N. J. A. Sloane, and P. Sole, "The Z_4-linearity of Kerdock, Preparata, Goethals and related codes," *IEEE Trans. Inform. Theory*, vol. 40, p. 301, 1994.

[80] S. Benedetto, R. Garello, and G. Montorsi, "A search for good convolutional codes to be used in the construction of turbo codes," *IEEE Trans. Commun.*, vol. 46, no. 9, pp. 1101–1105, Sept. 1998.

[81] C. Berrou, C. Douillard, and S. Kerouédan, "The advantages of non-binary turbo codes," in *Inform. Theory Workshop*, Cairns, Australia, Sep. 2001.

[82] K. Chugg, P. Thiennviboon, G. Dimou, P. Gray, and J. Melzer, "New class of turbo-like codes with universally good performance and high-speed decoding," in *IEEE Military Commun. Conf. MILCOM*, vol. 5, Atlantic City, NJ, USA, Oct. 2005, pp. 3117–3126.

[83] S. Benedetto, D. Divsalar, G. Montorsi, and F. Pollara, "Analysis, design, and iterative decoding of double serially concatenated codes with interleavers," *IEEE J. Select. Areas Commun.*, vol. 16, no. 2, pp. 231–244, Feb. 1998.

[84] H. Jin, A. Khandekar, and R. McEliece, "Irregular repeat-accumulate codes," in *Symp. Turbo Codes*, Brest, France, Sept. 2000, pp. 1–8.

[85] A. Graell i Amat, G. Montorsi, and F. Vatta, "Design and performance analysis of a new class of rate compatible serial concatenated convolutional codes," *Submitted to IEEE Trans. Commun., available at arXiv:cs/0510035*, 2005.

[86] S. Benedetto, R. Garello, G. Montorsi, C. Berrou, C. Douillard, D. Giancristofaro, A. Ginesi, L. Giugno, and M. Luise, "MHOMS: high-speed ACM modem for satellite applications," *IEEE Wireless Commun.*, vol. 12, no. 2, pp. 66–77, Apr. 2005.

[87] P. A. Martin, M. Isaka, and M. P. C. Fossorier, "Serial concatenation of linear block codes and a rate-1 convolutional code," in *Symp. Turbo Codes*, Munich, Germany, April 2006.

[88] S. Lin and J. J. Costello, *Error control coding.* Prentice-Hall, 1983.

[89] R. Pyndiah, "Near-optimum decoding of product codes: Block turbo codes," *IEEE Trans. Commun.*, vol. 46, no. 8, pp. 1003–1010, Aug. 1998.